University of Leicester

Department of Engineering

Analytical and CFD Methods Investigating Shroud Blade Tip Leakage

By

Mohammed F. F. El-Dosoky

Thesis submitted to the University of Leicester in accordance with the requirements for the degree of Doctor of Philosophy

Supervisor: Dr. Aldo Rona
Co-supervisor: Dr. Shian Gao

April 2009

Analytical and CFD Methods Investigating Shroud Blade Tip Leakage

Mohammed F. F. El-Dosoky
Department of Engineering,
University of Leicester,
Leicester, LE1 7RH, UK.

Abstract

This study deals with the leakage flow over a shrouded turbine stage, its interaction with the main passage flow, and the associated losses. The study addressed these topics by providing an analytical correlation loss model and detailed CFD simulations.

An analytical model of leakage flow loss over a shrouded turbine stage has been developed. The analytical model uses directly measurable flow quantities to predict the effect of some of the over-shroud design parameters on stage performance. The model displays good predictive ability for the mass leakage fraction and the mixing losses. The model resolves the negative incidence angle induced by mixing the leakage flow with the main stream and predicts the increment in the total mixing loss coefficient at increasing leakage jet injection angles. The main contributions of this model to the leakage jet models documented in the open literature are the effect of the leakage jet injection angle on the mixing loss and the accounting of the effect of the number of fins on the leakage mass fraction in an explicit way. The present model exhibits a good qualitative and quantitative agreement with comparative benchmark data.

An in-house three-dimensional turbomachinery CFD code was developed and validated against six test cases, showing its ability to capture the salient flow features in each test case. This work makes an innovative use of Detached Eddy Simulation as an advanced Reynolds Averaged Navier-Stokes (RANS) model. A detailed leakage flow structure over the rotor shroud and its interaction with the main passage flow were modeled for seven test cases to investigate the effect of the number of fins, the clearance gap ratio, and the leakage jet injection angle on the flow. The results showed that reducing the injection 90^o to 30^o leads to a reduction in entropy mixing loss coefficient by up to 24.7% and gives a 0.2% increase in the rotor static to static efficiency and highlighted that reducing the leakage jet injection angle is a promising concept to control most of the adverse effects of the leakage flow.

Table of Contents

Acknowledgements

I would like to express my sincere gratitude and appreciation to my thesis supervisor, Dr. Aldo Rona for his continued guidance, support, enthusiasm and encouragement during the course of this research. He showed from the very beginning a superb willingness to help and advise me in whatever I do, clarifying all those concepts that happened to be obscure to me, while giving me the freedom I needed to study and work at a comfortable pace. Thanks to his very high standards.
I would like also to thank Prof. J. P. Gostelow for his support and invaluable advices. I am grateful to Dr. Shian Gao for being my co-supervisor.
My deepest gratitude goes to Dr. Nadier Ince for his advice and support. Alstom UK, for providing the model geometry of the shrouded turbine of chapter 6, is gratefully acknowledged.

I would like to acknowledge Mathematical Modelling Centre for granting computer time and the support provided by Mr. Stuart Poulton and his colleagues. Thanks also go to Tom Robotham, Andrew Norman, Surjit Kaur, and all the other support staff at the University of Leicester.
My special thanks go to my colleagues in the CFD group, Dr. William Paul Bennett, Marco Grottadaurea, Ivan Spisso, Manule Monti, Davide Di Pasquale, Pietro Ghillani, and Ozzi Oaikhiena. My special thanks go to my friend Farhad for his endless friendship and support. I thank my office roommates who made my time as a postgraduate student so enjoyable. I will miss this place.
I would like to acknowledge the Educational and Cultural Bureau of the Embassy of the Arab Republic of Egypt for their support.
I am thankful to all my teachers, especially Prof. A. K. S. Ayaad, Prof. M. M. Abdelghany, and Prof. O. M. E. Abdel-Hafez.
Finally, I am indebted so much to my family who have supported me for a long time and waited patiently through the course of my research.

Nomenclature

English Symbols

a	Speed of sound
A	Area
$\boldsymbol{A}$	Conservative variable Jacobian matrix for the Euler equations
C	Turbine blade chord
C_c	Contraction coefficient
Cd	Discharge coefficient
C_d, C_s	Yoshizawa constants
C_D	Dissipation coefficient
c_p	Specific heat at constant pressure
C_{Smag}	Smagorinsky constant
c_v	Specific heat at constant volume
Cp	Coefficient of pressure
e	Specific internal energy
e_0	Stagnation specific internal energy
$\boldsymbol{E}$	Eigenvector
f_{β^*}	Dimensionless cross-diffusion parameter
F	Conservative flux vector
F_c	Convective flux vector
F_t	Turbulent flux vector
h	Specific enthalpy
h_0	Stagnation specific enthalpy
H	Blade height
$\boldsymbol{I}$	Unit tensor
k	Specific turbulence kinetic energy
k_t	Turbulent thermal conductivity
ℓ_x, ℓ_y, ℓ_z	Spectral radii
M	Mach number
$\dot{m}$	Mass flow rate
M_t	Turbulence Mach number
M_{to}	Compressibility correction closure coefficient
n	Number of fins
$\boldsymbol{n}$	Unit normal vector
N	Rotational shaft speed, r.p.m
N_f	Number of faces in a unit control volume
p	Pressure
P_k	Turbulent production term
P_0	Stagnation pressure
P_{0r}	Relative stagnation pressure
Pr	Prandtl number
Pr_t	Turbulent Prandtl number
p_t	Turbulent pressure

$\boldsymbol{q}$	Molecular heat flux vector
$\boldsymbol{q_t}$	Turbulent heat flux vector
r	Static to total pressure ratio
$\boldsymbol{r}$	Radius vector
R	Gas constant
R^-, R^+	Negative and positive Riemann invariant
$\boldsymbol{\mathcal{R}}$	residual vector
Re	Reynolds number
s	Specific entropy
S	Control volume surface area
$\mathbf{S}$	Source terms vector
S_{ij}	Strain-rate tensor
t	Time
$\boldsymbol{t_1}, \boldsymbol{t_2}$	Tangent and binormal Unit normal vectors
T	Temperature
T_0	Stagnation temperature
T_{0r}	Relative stagnation temperature
Tu	Turbulence intensity
u_g	Gird rotational velocity
$\boldsymbol{u}$	Velocity vector
$\boldsymbol{u}_i$	Cartesian velocity in index notation
u_n, u_{t1}, u_{t2}	velocity components in the ortho-normal directions
u,v,w	Cartesian Velocity components in x, y, z direction
$\boldsymbol{u}^+$	Velocity normalized by friction velocity
$\boldsymbol{u_r}$	Velocity vector in rotating frame of reference.
$\boldsymbol{u_\tau}$	Friction velocity
$\mathbf{U}$	Conservative variables vector
U_r	Relative contravariant velocity
V	Volume
x, y, z	Physical space Cartesian coordinates
x_j	Cartesian coordinate in index notation
y^+	Dimensionless surface normal coordinate

Greek Symbols

α	Characteristic wave strength or absolute flow angle
β	$k-\omega$ model closure coefficient or relative flow angle
β^*	$k-\omega$ model closure coefficient
β_o, β_o^*	$k-\omega$ dissipation term closure coefficients
γ	Specific heat ratio c_p/c_v
Γ	Blending function
δ_{ij}	Kronecker delta
Δ	LES filter width
ε	Specific dissipation
ε^*	Entropy modification parameter
η	Efficiency or MUSCL extrapolation parameter
κ	Karman constant, 0.41

Λ	Degree of reaction
λ	Eigenvalue of Jacobian matrix
μ_l	Dynamic or laminar viscosity
μ_t	Turbulent (eddy) viscosity
ξ^*	$k-\omega$ dissipation term compressibility correction coefficient
ρ	Density
σ	$k-\omega$ model closure coefficient for turbulent transport of ω
σ^*	$k-\omega$ model closure coefficient for turbulent transport of k
τ	Sealing gap ratio
$\boldsymbol{\tau}$	Viscous stress tensor
τ_{ij}	Turbulent stress tensor
$\boldsymbol{\tau_r}$	Reynolds stress tensor
τ_w	Surface (wall) shear stress
Φ	Non-linear limiting function
ϕ	Stage flow coefficient
φ	model closure coefficient
χ_k	Dimensionless cross-diffusion parameter
ω	Specific turbulence dissipation rate
$\boldsymbol{\omega}$	Angular velocity vector

Other Symbols

$\otimes$	Tensor product
$:$	Double scalar product

Subscripts

∞	Freestream state
b	Boundary state
h	Rotor hub states
int	Interior state
L	Over-shroud leakage flow states
LES	Large Eddy Simulation
r	Relative frame of reference
$RANS$	Reynolds Averegaed Navier-Stokes
$ref, 0$	Reference state
ss	Isentropic expansion through the rotor
t	Rotor tip states
T	turbulent hybrid $RANS/LES$ model
th	Over-shroud throat flow states
x	Axial component
θ	Tangential component

Superscripts

T	Transpose operator
$'$	Fluctuating component

Accents

^	Roe averaged variable
$-$	Short-time averaged or large-scale value

Chapter 1

Context and Aim

1-1 Introduction

Turbines can be broadly classified into shrouded and unshrouded. The loss of performance due to tip leakage over unshrouded blades has been intensively studied, more than the leakage flow over shrouded blades. Shrouded turbines have seals at rotor tips called labyrinth seals. Labyrinth seals represent one of the most important areas of development of the turbomachinery aerodynamics community. The flow past a labyrinth rotor seal in a typical shrouded turbine stage is hot, has high vorticity and a low axial momentum. This leads to unwanted heat transfer to the shroud and casing, endwall losses, and mixing losses. Therefore, the tip leakage flow has significant detrimental effects on the performance of a turbine stage. Generally, the related losses can be grouped into losses of the leakage flow itself and losses caused by its interaction with the main flow. Although the turbomachinery designers have a lot of information concerning the flow field through these seals, there is a need for relatively straight-forward models to predict the effects of the seals on the stage performance. Also there is a need for more CFD work to understand the interaction between the leakage flow and the main blade passage flow downstream of the trailing edge. To improve on the design of contemporary turbine stages, it would be useful to have:

- A simple correlation loss model to evaluate the expected turbine stage performance.
- A deeper insight of the loss mechanisms to give feedback design recommendations.

This study tackles both aspects by providing:

1- An analytical model of leakage flow loss over a shrouded turbine stage.

2- A CFD prediction of flow through a shrouded turbine stage.

1-2 Analytical model

Most of the literature reviewed by the author focuses on the physics of leakage flow over an unshrouded turbine and its interaction with the main flow. This study aims to build an analytical model [chapter 3] to estimate the losses in a shrouded stage and the effects of leakage on the shrouded turbine performance.

The key questions motivating this part of the study are:

1- How much the tip leakage loss contributes to the overall loss?
2- What are the effects of labyrinth seal geometries on the turbine performance at different flow conditions?
3- How much does the injection angle affect the mixing flow loss coefficient?
4- What is the value of incidence angle induced by mixing and how does this affect the subsequent blade row?

The analytical model results will be calibrated against experimental results from a shrouded stage tested by Pfau [2003].

1-3 CFD Model

The review of previous work has shown that almost all researches have investigated the loss mechanisms and the unsteady flow structures from the endwall flow, the secondary flow, the leakage flow, the downstream blade passage interaction and blade rows interaction separately, while a few investigations have considered a combination of two or more of these flow loss mechanisms. Most of the CFD models reported in available literature have been applied to unshrouded turbine stages. Therefore, there is a paucity of investigations in the literature that are directed towards understanding the leakage flow structure over a shrouded blade and its interaction with the main passage flow. This study deals with the leakage flow over a shrouded turbine stage, its interaction with the main passage flow, and the associated losses.

The main objectives motivating this part of the study are:

1. Identify the leakage flow structure over a representative shrouded blade and the intensity of its interaction with the main passage flow downstream.
2. Understand the loss mechanisms through and downstream of a shrouded blade.
3. Identify the leakage jet effects on the main passage flow.
4. Quantify the associated leakage losses and compare them with the results from the analytical model of chapter 3.
5. Draw recommendations from this study to improve the design and performance of commercial turbine stages.

These objectives will be met by:

a. Developing an in-house three-dimensional turbomachinery CFD code.
b. Validating the code against available experimental and numerical data.
c. Solving the leakage problem following the flowchart sequence shown in figs. 1-1 to 1-4.

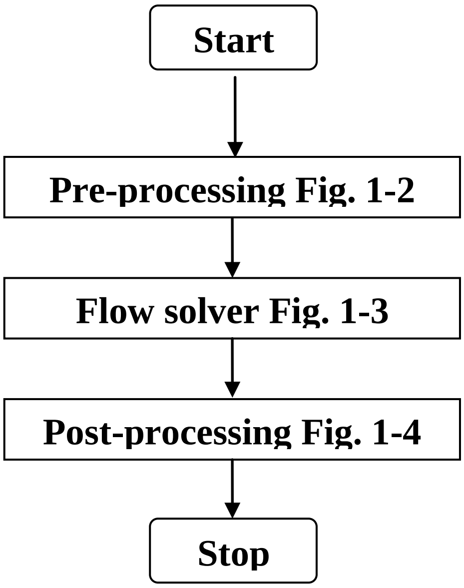

Fig. 1-1 The hierarchy structure of a CFD Code.

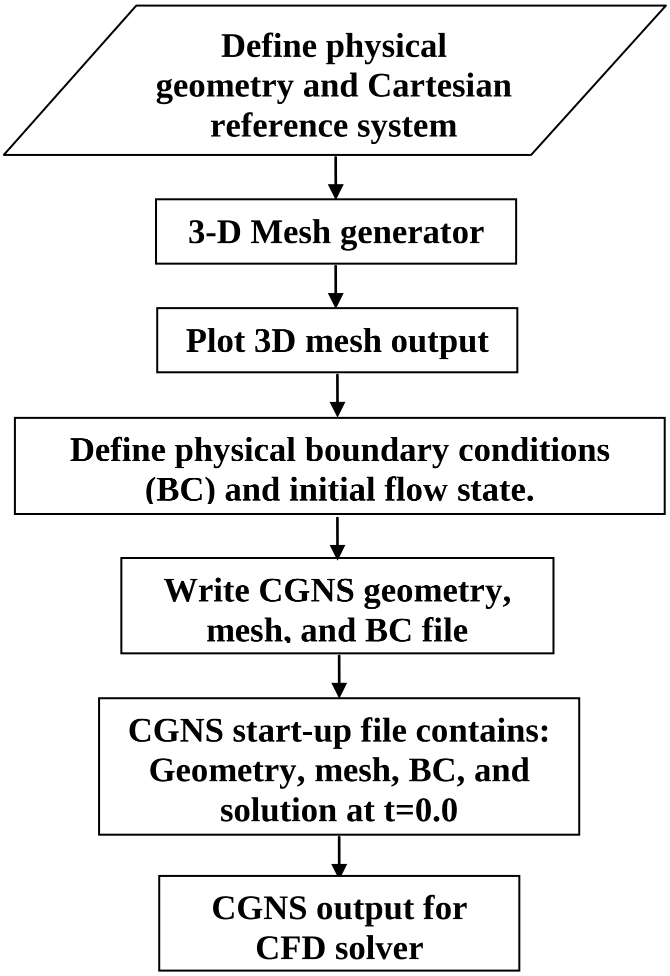

Fig. 1-2 Tasks order in the code pre-processor stage.

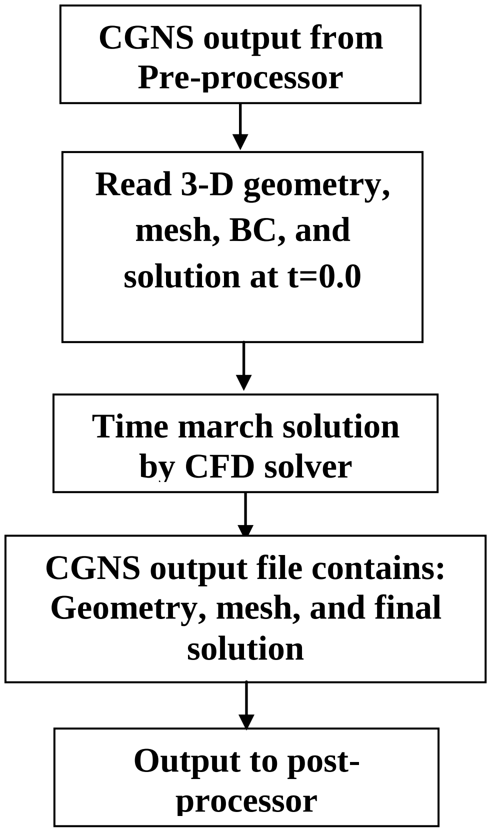

Fig. 1-3 Sequence of processes in the code solver stage.

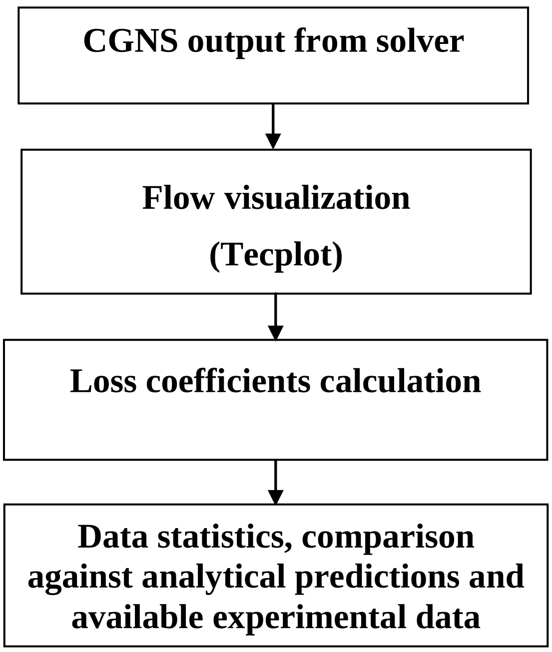

Fig. 1-4 The post-processor stages.

1-4 Thesis Outline

Chapter 1 shows the aims of the thesis and gives the methods to tackle them.

Chapter 2 reviews the Main sources of loss in turbomachines. This chapter also reviews the effects of some new design aspects such as lean, partial shrouded blade tip and endwall contouring on the performance of a turbine stage. Finally, a review of available analytical models for flow simulation through the turbomachines is presented.

Chapter 3 presents the analytical model that addresses a) the calculation of the mass leakage fraction for the through flow labyrinth seal with any number of fins b) the contribution of the tip leakage loss to the overall loss c) the effects of the injection angle on the mixing loss d) the effects of the tip leakage jet on the incidence angle that affects the subsequent row.

Chapter 4 documents the numerical scheme that was developed to obtain the three-dimensional turbomachinery flow solver used to investigate the shroud blade tip leakage.

Chapter 5 contains the numerical results from six test cases to validate the in-house flow solver. The six cases, classified according to their respective frame of reference, are:

- Fixed frame of reference test cases are shock tube, supersonic flow over 10 degree ramp, spherical explosion, and wing-body junction.
- Rotating frame of reference test cases are turbulent flow in a rotating square duct, and unshrouded axial turbine rotor cascade.

Chapter 6 presents the results of the CFD simulation of the leakage flow over a shrouded turbine stage, its interaction with the main passage flow, and the associated losses. Seven cases are modelled to study the effect of the number of fins, the clearance gap ratio, and the leakage jet injection angle on the flow. In addition to these cases, a reference case with zero mass leakage fraction and a clean end wall is simulated for comparison purposes.

Chapter 7 summarises the conclusions from the analytical model, the CFD flow solver validation, and the over-shroud leakage predictions and makes suggestions for further research.

Chapter 2

Literature Review

2-1 Introduction

The aim of this chapter is to provide an overview of the published work that is related to the current investigation. Significant research effort and design advances have led to thermal efficiencies of up to 60% in power station combined cycles that use modern gas turbines. A contemporary compressor stage has an isentropic efficiency of about 90% and a contemporary turbine stage has an isentropic efficiency of up to 95%, as reported by Chernobrovkin and Lakshminarayana [1999]. Further improvements in stage efficiency become more and more difficult and require a much deeper understanding of the flow field inside turbomachines.

The present chapter focuses on the loss generation mechanisms and on the development of secondary flows in turbine blade passages. A review of the available literature gives a brief discussion of the sources of unsteady flow and of the accompanied losses, as well as the interaction between the blade rows. This chapter also presents the effects of some new design aspects such as lean, partial shrouded blade tip and endwall contouring on the performance of a turbine stage. Finally, a review of available analytical models for flow simulation through the turbomachines is presented.

2-2 Main sources of loss in turbomachines

The paper of Denton [1993] reviews the origins of loss mechanisms in turbo-machines. Denton [1993] encourages the use of entropy generation as the convenient way to evaluate the loss generation in a turbomachine. The advantage of using the entropy generation to investigate loss is that it is independent from the frame of reference. The stage efficiency (η) can be calculated by knowing the stage pressure ratio p_r from equation 2-1.

$$\eta = \frac{1-\left(p_r e^{(s_2-s_1)/R}\right)^{\frac{(\gamma-1)}{\gamma}}}{1-(p_r)^{\frac{(\gamma-1)}{\gamma}}} \qquad (2-1)$$

where γ is the specific heat ratio and R is the specific gas constant, $R = C_p - C_v$. However entropy cannot be measured directly, it is calculated by using the measurements of both temperature and pressure of the working fluid.

Several mechanisms present in turbomachines create entropy, namely viscous effects in boundary layers, mixing processes in free shear layers, heat transfer across a finite temperature difference, throttling action across labyrinth seals, and non-equilibrium processes such as shock waves. The loss sources can be classified as follows (Denton [1993], and Payne et al. [2003]):

Two-dimensional losses:

- Boundary layer loss: Entropy is generated by the shear stress in the boundary layer, and the related entropy production depends on the state of the boundary layer.
- Shock loss: Entropy creation occurs due to heat conduction and high viscous normal stresses within the shock wave.
- Mixing out of a wake behind a trailing edge: this loss represents at least 1/3 of the total two-dimensional loss in subsonic flow with a trailing edge blockage of 6.3 percent.

Three-dimensional losses:

- Endwall loss: Entropy generation occurs due to secondary flow structures mainly at the endwall boundary layer. This sort of loss represents about 1/3 of a typical total turbine stage loss.
- Tip leakage loss: the losses can be grouped into losses of the leakage flow itself and losses caused by its interaction with the main flow.
- Unsteady loss: the wakes, vortices, and separations generated from one blade row mix-out downstream of that blade row. This mixing occurs in an unsteady environment and generates an unsteady loss component.

2-2.1 Loss generation in the boundary layer

Boundary layers are regions of profiled velocity gradients and shear stress. In most boundary layers, the velocity changes are most rapid near the surface and so most of the entropy generation is concentrated in the inner part of the layer. Boundary layers are found on both sides of a turbine blade, but the suction side is dominant in producing loss. The rate of entropy generation in the boundary layer up to a specified point x can be evaluated, using the drag coefficient on the blade surface, as $\dot{S} = \int_0^x \frac{\rho V_\delta^3 C_d}{T_\delta} dx$, Denton [1993], where V_δ and T_δ are the velocity and temperature at the edge of the boundary layer. Fig. 2.1 shows the values of dissipation coefficient against Reynolds number. This figure shows that transition should be kept as far downstream as possible to minimize loss. Denton [1993] stated that the dissipation coefficient for turbulent boundary layers is much less dependent on the shape factor of the boundary layer.

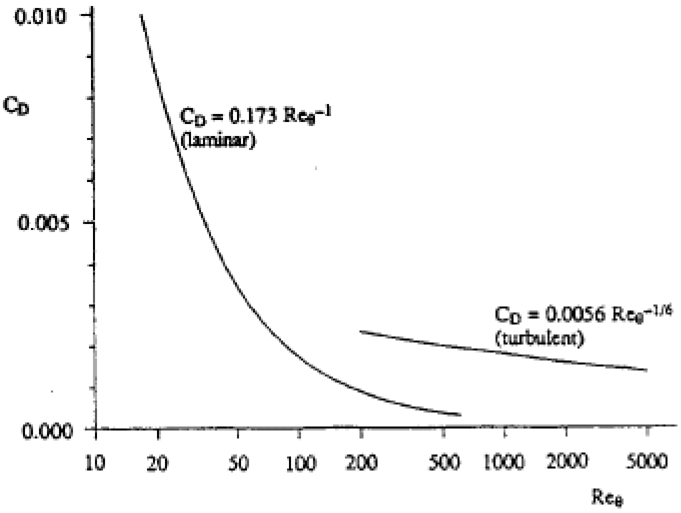

Fig. 2-1 Dissipation factor for laminar and turbulent boundary layers, Denton [1993].

The influence of free stream turbulence levels on the aerodynamic entropy generation rate in the boundary layer was investigated experimentally by Griffin and Davies [2004]. The authors mentioned that an increase in the free stream turbulence level from 0.8% to 5.0% results in almost a 45% increase in suction surface boundary layer loss for a comparable Reynolds number. Laminar and transitional losses were most influenced by the free stream turbulence level. In contrast, the local turbulent boundary layer loss was unaffected by the five fold increase in free stream turbulence level.

Boundary layer separation, transition and reattachment have been studied experimentally under low-pressure turbine airfoil conditions by Volino [2002(a)**,** 2002(b)]. The author carried out his study at Reynolds numbers ranging from 25,000 to 300,000 (based on suction surface length and the exit velocity) at low (0.5%) and high (9%) inlet free stream turbulence levels. A high Reynolds number or free stream turbulence level moves transition upstream and leads to rapid boundary layer reattachment. At the lowest Reynolds number, transition did not occur before the trailing edge, and the boundary layer did not reattach. The author stated that the beginning of a significant rise in the turbulent shear stress signals the beginning of transition. A separated layer creates a significant wake and its mixing pressure loss is often higher than the boundary layer loss of the corresponding attached turbulent boundary layer.

2-2.2 Loss generation in mixing processes

The flow through a turbine stage contains many aspects generating mixing loss, such as trailing edge wakes, leakage jets, endwall and passage vortices, and separated shear layers. Denton's model [1993], which addresses the effects of wake acceleration before mixing, showed that where a total pressure wake was accelerated, mixing loss diminished, and vice-versa. Concerning the total temperature of the wake, this is shown to exhibit a reverse trend, according to the Rose and Harvey model, [2000]. In this model the authors evaluate the effects of acceleration of a turbomachinery wake before mixing using a simple analytical model. It is concluded that the rotodynamic work process tends to reduce total pressure wake depths in turbines and compressors and therefore mixing losses. The mixing loss due to a total temperature wake is less strongly affected by the differential work process. If cold wakes are accelerated before they mix out, the large mixing losses are increased, and if diffusion occurred before mixing, there is modest loss reduction. This trend is the reverse of the trend observed for total pressure wakes as shown in fig. 2-2. The other aspects of mixing loss are discussed in sections 2.2.3 and 2.2.4.

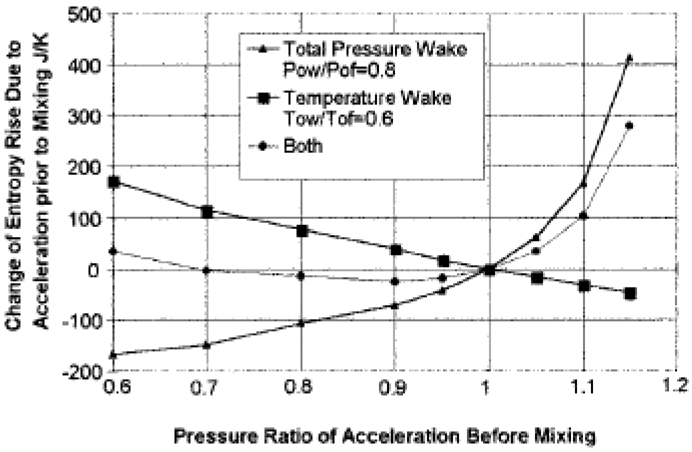

Fig. 2-2 Effect of acceleration on mixing loss, Rose and Harvey [2000].

2-2.3 Endwall loss

Endwall loss is a major source of lost efficiency, contributing approximately one third of the total loss, according to Denton [1993]. Endwall loss refers to all the loss arising on the annulus walls within and outside the blade passage. A semi-empirical model for estimating secondary flows and endwall loss for an axial flow turbomachine cascade was developed by Sharma and Butler [1987]. They gave an expression for predicting the streamwise extent of the secondary flow region at the trailing edge. They split the passage losses into a two-dimensional profile loss, calculated using a two-dimensional boundary layer calculation method, and an endwall secondary loss, calculated using a semi-empirical expression based on a pitch-averaged boundary layer. The previous two sorts of loss with inlet losses gave predictions for cascade losses within ±10 % of the measured values. The flow patterns near the endwalls are determined by the secondary flow whose strength depends mainly on the thickness of the upstream boundary layer, the pitch to chord ratio, the aspect ratio, the inlet vorticity, and the amount of turning in the blade row. Because of the importance of the secondary flow influencing factors, the secondary flow characteristic will be later reviewed in more detail.

2-2.4 Tip leakage loss

Turbines can be broadly classified into shrouded and unshrouded. Shrouded turbines have seals at rotor tips called labyrinth seals. Labyrinth seals represent one of the most important areas of development of the turbomachinery aerodynamics community. Although the turbomachinery designers have a lot of information concerning the flow field through these seals, there is a need for relatively straight-forward models to predict the effects of the seals on the stage performance. The loss of performance due to tip leakage over unshrouded blades has been intensively studied, more than the leakage flow over shrouded blades. Also there is a need for more CFD work to understand the interaction between the leakage flow and the main blade passage flow downstream of the trailing edge.

A detailed measurement of the tip leakage flow structure and its effect on the blade loading near the blade tip was obtained by Sjolander and Amrud [1987]. Xiao et al. [2001] carried out an experimental investigation of the effects of the tip clearance flow in an unshrouded axial turbine rotor. They investigated the structure of the tip leakage flow and the development of the loss, the pressure, the velocity and the turbulence fields. They found that the highest total pressure loss was observed in the region of the tip leakage vortex. Part II of this paper presented the vorticity, velocity and turbulence fields at several axial locations. The results indicated that the relative motion between blades and the casing leads to the development of a scraping vortex that, along with secondary flow, reduces the propagation of the tip leakage flow into the main flow.

Yaras and Sjolander [1990, 1992] carried out a series of studies on the tip leakage flow field and its losses. The relative motion between the shroud and the casing was simulated in a linear cascade test by using a moving belt. They verified the formation of the scraping vortex and discussed the changes in the structure of tip leakage and passage vortex due to the relative motion. The results indicated that the distortion of the surface pressure field near the tip was reduced with increasing wall speed because of the reduced strength of the tip leakage vortex. Yaras and Sjolander [1992] reviewed the existing methods for predicting the tip leakage loss in turbomachinery and they concluded that the present methods are based on a variety of assumptions, many of which have not been fully verified experimentally. These methods neglect the additional viscous loss production on the endwall due to the existence of the tip-leakage vortex. Heyes et al. [1992] studied the tip geometry effects on the loss generation process. They reported the effects of using plane tips, a suction side squealer, and a pressure side squealer. The results showed that the use of a squealer could provide a benefit, in particular with a suction side squealer, because it reduces the leakage flow through the tip gap. Tallman and Lashminarayana [2001] used a 3D Reynolds averaged Navier-Stokes CFD code to simulate the effects of turbine parameters on the tip leakage flow and vortex in a linear cascade. The authors showed the effects of reduced tip clearance height on the leakage flow, on the leakage vortex, and highlighted the additional secondary flows present in the near casing region of the axial turbine. An experimental and analytical investigation was carried out by Helmers et al. [2003] to study the performance of turbines at large tip clearance of unshrouded rotor cascades. They aimed to establish a parametric description of losses related to tip clearance effects. A survey of the flow angle downstream of the rotor yielded the following two aspects:

a) Intense secondary flow and tip leakage flow cause significant spanwise variation of the outlet flow angle.

b) The deficit of flow turning due to tip gap flow is drastically increased by increasing tip gap size.

Gbadebo et al. [2006] showed that the tip leakage vortex can reattach the otherwise separated tip trailing edge flow in a highly loaded rotor. Therefore, the optimal gap tip clearance to minimise the stage loss is about twice the casing stage inflow boundary layer thickness.

The structure of a labyrinth seal cavity flow has been experimentally investigated by Pfau et al. [2001]. They studied the nature of the mixing of the labyrinth leakage flow and the main core flow to identify the disturbances in the flow entering the next blade row. The authors showed that the fluid leaving the cavity is broken up into distinct oblique jets of low momentum embedded in the channel flow, causing a negative incidence angle and additional loss at the inlet of the subsequent row. Denecke et al. [2003] investigated experimentally the effects of rub-groove geometries on a labyrinth seal leakage at different seal clearances. Figure 2-3a shows three relative position of rub-groove to labyrinth seal knife commonly used in a gas turbine with one of the following labyrinth seal types: a) straight-through labyrinth seals b) stepped labyrinth seals with forward facing steps shown in fig. 2-3b c) stepped labyrinth seals with backward facing steps. The results indicated that the minimum discharge coefficient was found at clearances in the range of

$$0.3 < \frac{seal\,clearance}{(seal\,clearance + rub\,groove\,depth)} < 0.7.$$

The interaction between the shroud leakage flow and the main flow in a three stage low pressure turbine was investigated by Gier et al.[2003]. The study aimed at reducing the impact of the leakage flow and shroud design related losses by understanding the leakage loss characteristics, especially the losses connected to the strengthening of the secondary flow and other main flow interaction. The results specified the contribution of the major sources of leakage related loss to the total shrouded leakage related loss as follow: the mixing loss is about 50%, the bypass and step losses are about 20%, and the losses due to incidence and secondary flows were estimated to have a smaller fraction. Bindon and Morphis [1992] showed that radiusing and contouring the leakage gap geometry prevent the formation of the separation bubble and significantly reduce the internal gap loss but unfortunately create a higher mixing loss to give an almost unchanged overall loss coefficient.

However, the leakage jet entering the flow did not show the high loss concentration that had been previously associated with the separation bubble.

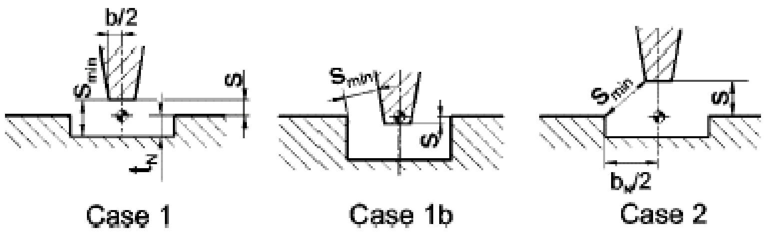

Fig. 2-3a Geometry definition of rectangular grooves, Denecke et al. [2003].

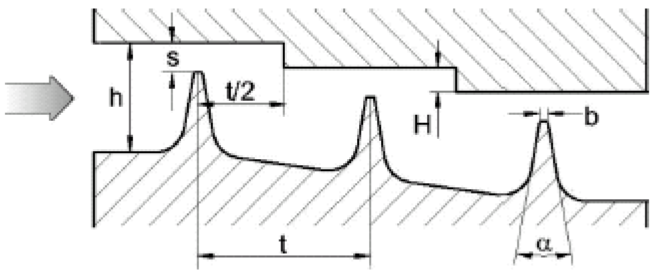

Fig. 2-3b Labyrinth seal geometry definition, Denecke et al. [2003].

Dishart and Moore [1990] investigated the tip leakage effect on loss production in a large–scale linear turbine cascade. The flow fraction passed through the gap was 5.7% developing a mass-averaged total pressure loss coefficient of 0.071, based on the inlet dynamic pressure. The measurements at 0.4 axial chord downstream of the trailing edge showed that the tip leakage effects were limited. At this location, the introduced loss due to the tip leakage jet was found to be equal to the sum of the measured loss at the tip gap exit plane and the value of the tip gap secondary kinetic energy that was dissipated by that downstream location. Another way to control the leakage flow over the shroud of an axial flow turbine was used by Wallis et al. [2001]. The authors used turning vanes supported on the shroud of the rotor blades aiming to reduce the aerodynamic losses associated with leakage re-injected into the mainstream flow. They tried to reduce the tangential velocity of the leakage flow and consequently reduce the magnitude of downstream leakage losses and improve the incidence onto following blade rows. The authors obtained the desired objectives to the expense of overall performance (3.5% reduction in brake efficiency). The authors recommended that, before developing any new method of managing the leakage flow, the unsteady three-dimensional flow phenomenon occurring in the shroud region should be understood.

2-2.5 Unsteady loss

The real flow in a turbomachinery stage is highly three-dimensional and unsteady, Martelli [2000]. The relative motion of rotor and stator blade rows causes the movement of circumferential and spanwise gradients in total pressure and temperature. The tip leakage vortex, secondary flow vortices, and vortex shedding at the trailing edge interact with the downstream blade flow.

- The potential field interaction at the rotor-stator interface causes noise, blade vibration and strong pulsation, especially when the axial inter-blade gap is less than 30% of the blade pitch.
- The two-dimensional wake stretching inside the downstream blade passage, as shown in Fig. 2-4 from Hodson and Howel [2005], increases its secondary kinetic energy. Thereafter, the dissipation of this energy due to viscosity increases the loss.
- The periodically changing of the upstream flow drives an early unsteady boundary layer transition.

Payne et al. [2003] performed an experimental investigation into unsteady losses in a high-pressure turbine stage. The measurements have shown that there are four major loss mechanisms: the tip leakage vortex, the upper passage vortex, the trailing edge wake, and the lower passage vortex. These results were obtained without examining the blade row interaction. The latter aspect will be discussed in detail in section 2-3.6.

2-3 Secondary flows in turbomachines

2-3.1 Flow field characteristics

Secondary flow is produced when a streamwise component of vorticity is developed from the deflection of an initially sheared flow. Secondary flows occur, for example, when a developed pipe flow enters a bend, when a sheared flow passes over an aerofoil of finite thickness or an aerofoil of finite lift, or when a boundary layer faces an obstacle normal to the surface over which it is flowing.

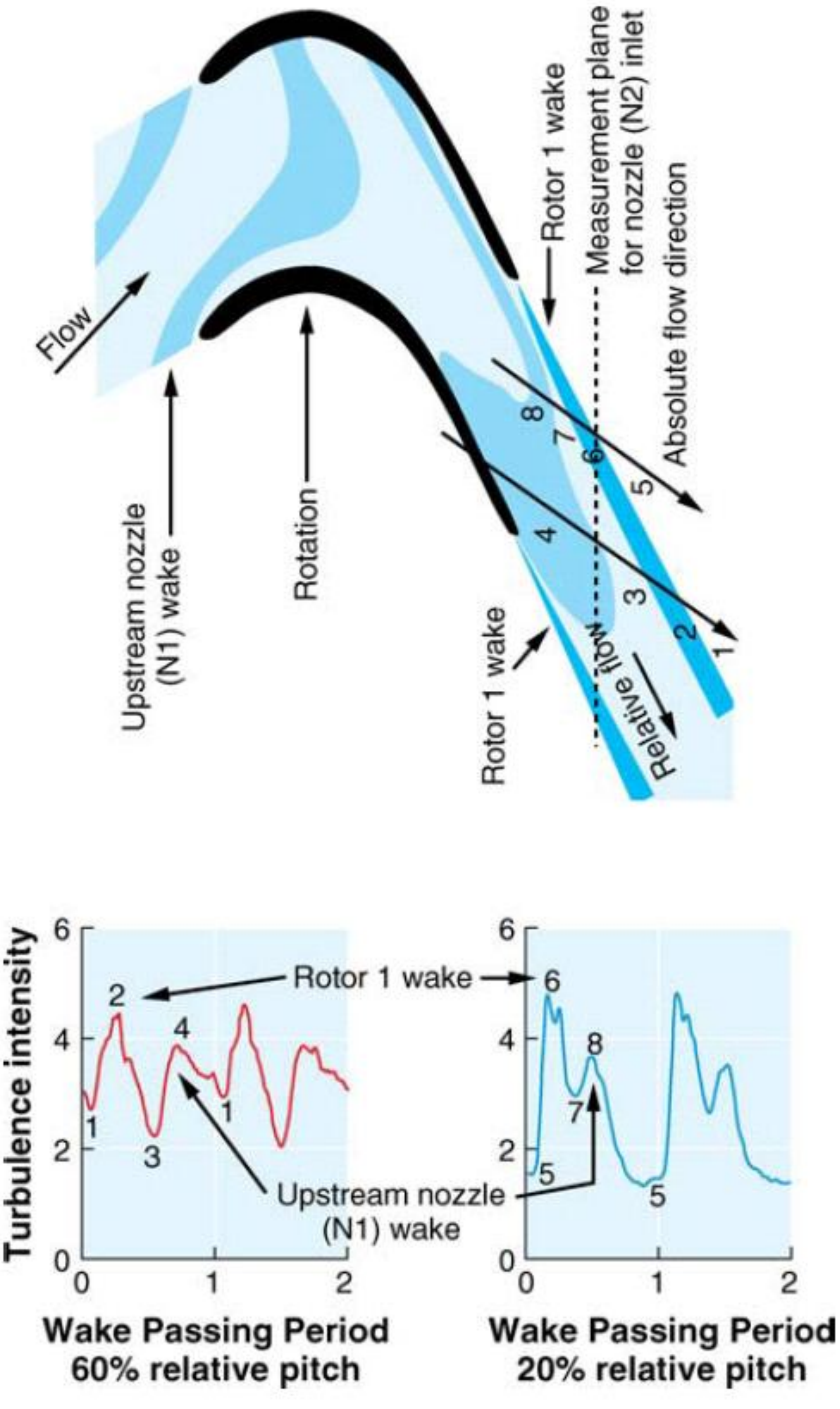

Fig. 2-4 Variation with time of the turbulence intensity at inlet to stage 2 at two circumferential positions, from Hodson and Howell [2005].

Surface flow visualization of the secondary flow past a rotor blade hub was performed by Aunapu et al. [2000] using the ink dots, solvent, and black powder techniques. These visualization methods enabled the capture of secondary flow aspects such as the horseshoe vortex and its migration across the passage to impinge on the neighbouring blade, endwall cross flow, and the endwall saddle point as shown in figs. 2-5 and 2-6. Gregory-Smith and Cleak [1992] carried out measurements of the turbulent flow field in a cascade of high turning turbine rotor blades. They placed a grid upstream of the cascade to raise the inlet turbulence level to 5 percent. They observed that the main flow field is not affected greatly by the high inlet turbulence level, Reynolds stresses are very high in the loss core, and the flow close to the endwall is highly skewed. However, the effect of the high inlet turbulence level on the kinetic energy of the secondary flow is limited.

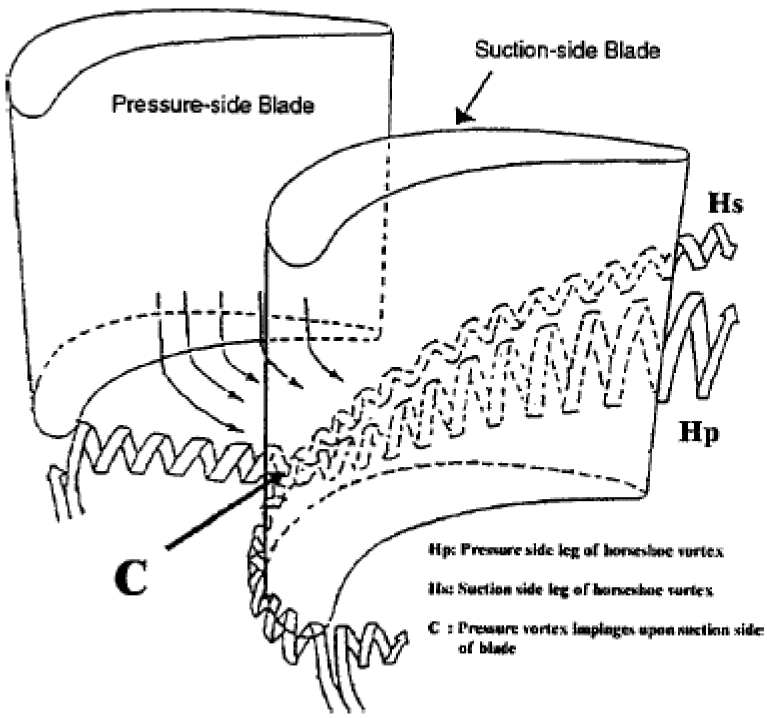

Fig. 2-5 Schematic of horseshoe vortex impinging upon suction-side blade, Goldstein and Spores [1988], from Aunapu et al. [2000].

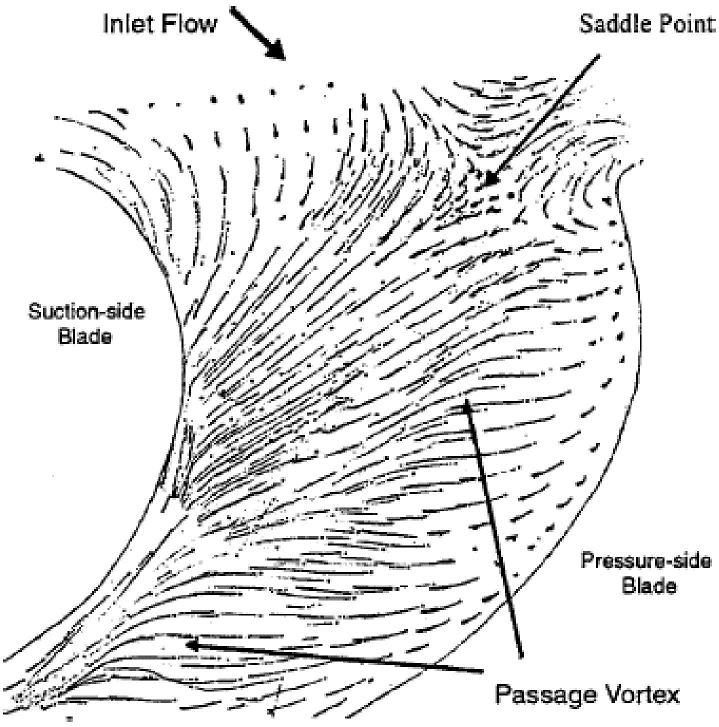

Fig. 2-6 Ink dot flow visualization on the endwall, from Aunapu et al. [2000].

Walsh and Gregory-Smith [1990] examined the effect of inlet skew on the flow field of a large-scale axial flow turbine cascade experimentally. They found that the inlet skew has a significant effect on the distribution and magnitude of the generated losses and the conventional number of correlation factors used to compute secondary losses are not adequate for an accurate loss prediction under inlet skew conditions. The experimental results showed that the presence of inlet skew modifies the whole of the flow field and in particular modifies the distribution of vorticity at exit from the cascade. The authors claimed that the effects of inlet skew appear to be more significant than the variation in inlet boundary layer thickness or the reduction in loss that can be obtained by endwall profiling.

Brear et al. [2002] investigated the behaviour of the pressure surface separation and its interaction with the secondary flow on low-pressure turbine blades tested at +10 deg, 0, -10 deg incidence. Numerical simulation showed strong incidence dependence around the leading edge of the profile. Experiments showed that all characteristics of the pressure surface separation are controlled mainly by the incidence. As the incidence is reduced, the increasing blockage of the pressure surface separation then increases the velocity in the separated shear layer to levels at which the separation can create significant loss. Another observation is that the effects of wake passing, free stream turbulence, and Reynolds number on pressure separation are of secondary importance. The results suggested that the pressure surface separation is highly dissipative through the action of its strong turbulent shear. In the second part of this paper, Brear et al. [2002] studied the interaction between the pressure surface separation and the secondary flow experimentally and numerically. They concluded that the interaction of the pressure surface separation with the secondary flow could affect the development of the secondary flow and the loss that it creates. Using this argument, the secondary flow strength and loss production could be reduced by raising the momentum of the fluid near the endwall.

This wealth of experimental and numerical work on secondary flows in turbomachines has been absorbed in literature reviews on this subject, that have tried to reconcile the evidence and produce an integrated picture of the turbomachinery secondary flows.

Sieverding [1985] reviewed the results of experimental secondary flow research over the previous twelve years. He started from the classical secondary flow model described by Hawthorne [1955]. Figure 2-7 shows the proposed model which includes the vortex system and the so-called passage vortex. The flow with inlet vorticity is deflected through the cascade and this distortion of the vortex filaments of the inlet boundary layer passes with the flow through the curved passage. Also, there is a vortex sheet at the trailing edge, which models the trailing filament vortices and the trailing edge shed vorticity. This model has since been evolved into more comprehensive models such as the one by Vogt and Zippel [1996]. This model accounts for several of the secondary flow phenomena that are present in a typical turbine cascade flow visualization, as shown in fig. 2-8.

Langston [2000] presented a review for the research works pre-1985 and made a survey of the open literature on secondary flow investigations published since Sieverding [1985]. Langston [2000] described the basic secondary flow structure past a turbine passage, examined the secondary flow vortices and the work on secondary flow loss reduction involving aerofoil geometry and endwall contouring. The review reported that the endwall vortex secondary flow is responsible for a loss of lift and an increase in aerodynamic loss when compared to a two-dimensional cascade flow. The lift loss, which translates into loss in turbine work, is shown in fig. 2-9. The lift coefficient is given by the circular integral of the pressure coefficient distribution, which is the area enclosed by the solid line. The results show that this area shrinks with reducing spanwise distance from the cascade side wall.

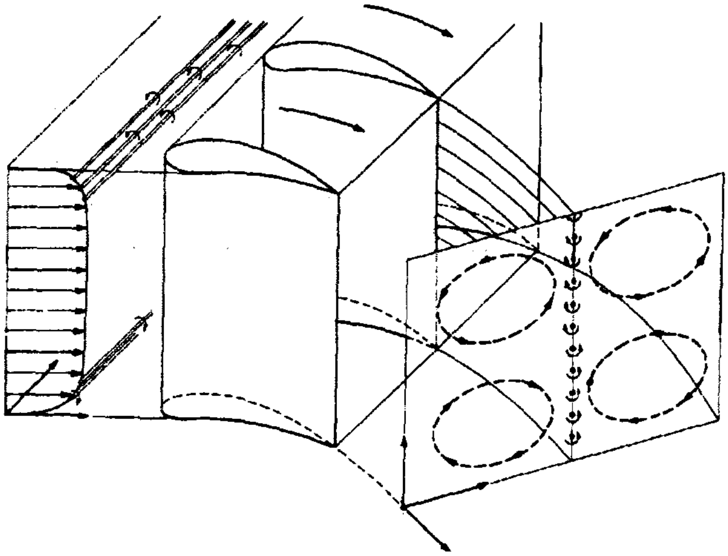

Figure 2-7 Secondary flow model, from Hawthorne [1955].

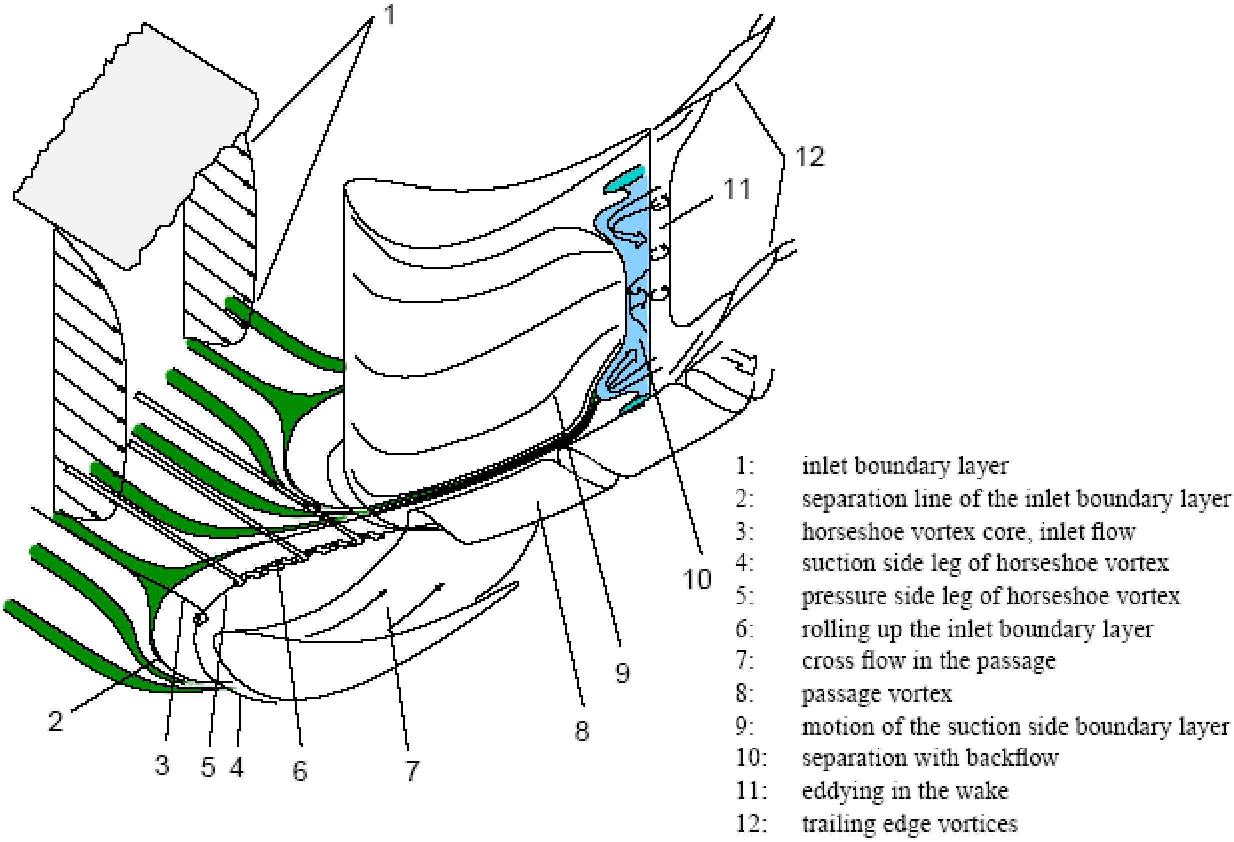

Fig. 2-8 Secondary flow phenomena in a turbine cascade, Vogt and Zippel [1996].

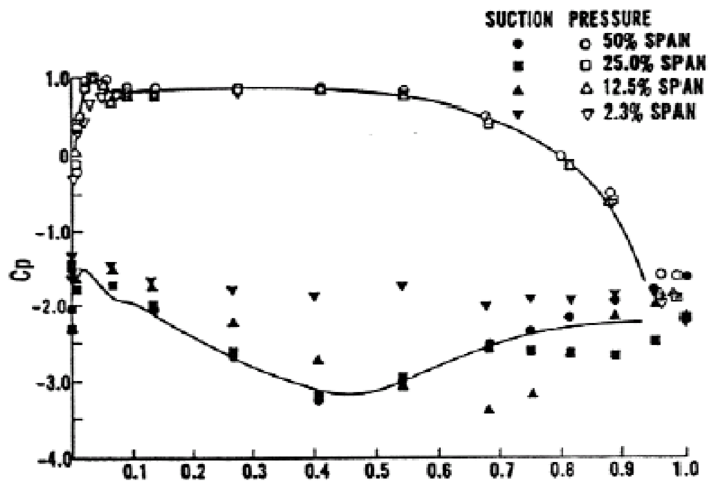

Fig. 2-9 Static pressure distribution on aerofoil surface compared with potential flow, Langston [2000].

2-3.2 Horseshoe vortex

A horseshoe vortex most often develops at the hub of a typical turbine half stage due to the separation of the inlet boundary layer at the saddle point. This has been recorded by surface flow visulization by Aunapu [2000]. One of the earliest turbine passage flow description includes a horseshoe vortex was developed by Klein [1966] who introduced a cascade vortex model with both the passage and the horseshoe vortices. In 1980, another model was derived from the measurements in three dimensions by Langston. The difference between the Klein and Langston models, as reported by Sieverding, are:

i. Langston clearly postulates that the pressure side leg of the leading edge horseshoe vortex, which has the same sign of rotation as the passage vortex, merges with it and becomes part of the passage vortex.
ii. The suction side leg of the leading edge horseshoe vortex, which rotates in the opposite direction to the passage vortex, according to the Langston model continues along the suction side endwall corner, while according to Klein's model it is gradually dissipated as it comes in contact with the passage vortex.

Sieverding and Van den Bosch visualized of the horseshoe vortex and passage vortex evolutions by using a coloured smoke wire technique. Figure 2-10 shows the streamwise evolution of the horseshoe and passage vortices. This figure shows that the reduction and elimination of the leading edge horseshoe vortex would have little effect on the shape and position of the passage vortex.

2-3.3 Endwall boundary layer

The endwall boundary layer characteristic is an important aspect of secondary flow research. Senoo [1958] carried out boundary layer measurements in a turbine blade passage. The author concluded that the endwall boundary layer in the throat is laminar, regardless of the state and thickness of upstream boundary layer. In general, boundary layer profiles are presented under the form of streamwise and cross-flow velocity profiles. Sieverding [1985] summarized the typical velocity profiles that occur in a turbine blade passage:

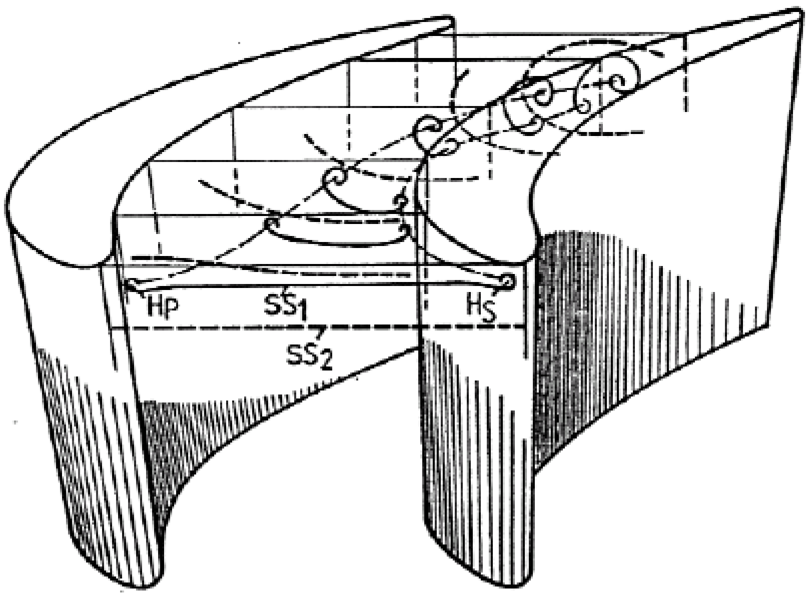

Fig. 2-10 Streamwise evolution of horseshoe and passage vortices, Sieverding and Van den Bosch [1985].

- Flow field upstream of the stage inlet: the streamwise boundary layer over the endwall is assumed to have a two-dimensional character, as shown in fig. 2-11.
- Passage entrance flow field up to the primary separation line S_{1s}: The cross-flow components are reinforced and the streamwise component remains two-dimensional in character.

- Region between separation lines S_{1p} and S_{2p}: the stagnation separation bubble is formed due to the adverse pressure gradient approaching the leading edge. The bubble has a radial extension of about one fifth of the boundary layer thickness at this point (mid way between the separation lines).
- Downstream of separation line S_{2p}: the vortical motion of the horseshoe and/or passage vortices convects fluid from the outer boundary layer or free stream toward the endwall and this depends on the intensity of the passage vortex. The foregoing described profiles are presented in fig. 2-12. Langston found that the cross-flow behaviour of the profiles a and b in fig. 2-12 could be correlated by the following expression $\frac{V_n}{V_s} = \tan\left(\left(\in_w - \alpha z\right) \; e^{-\gamma z}\right)$ where $\in_w$, α, and γ are constants determined experimentally and represent the yaw angle with respect to the free stream, the wall distance at which the yaw angle changes its sign, and γ is related to the maximum underturning.

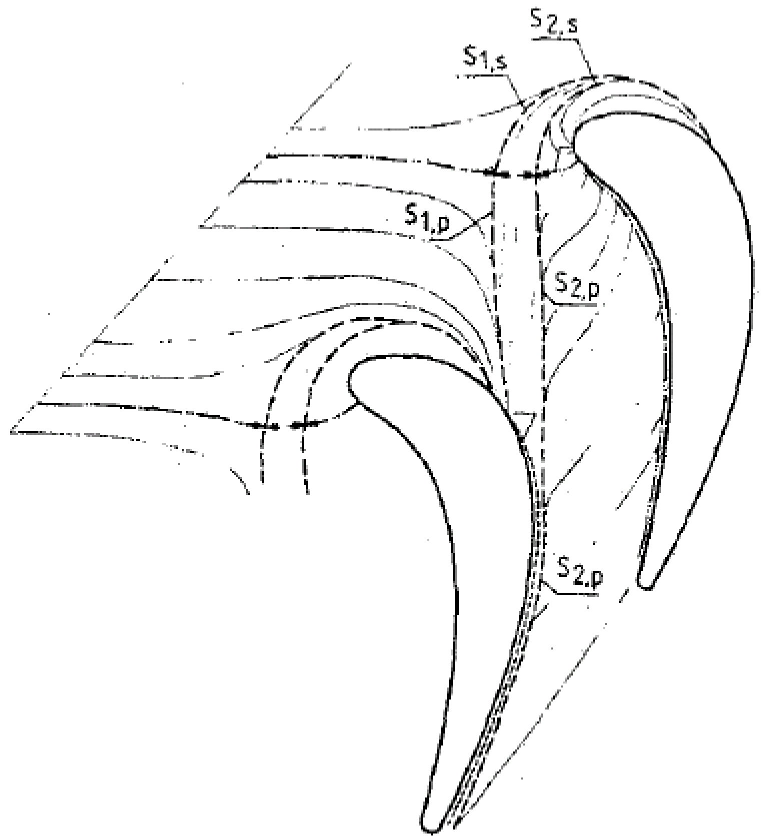

Fig. 2-11 General representation of endwall flow characteristics, from Sieverding [1985].

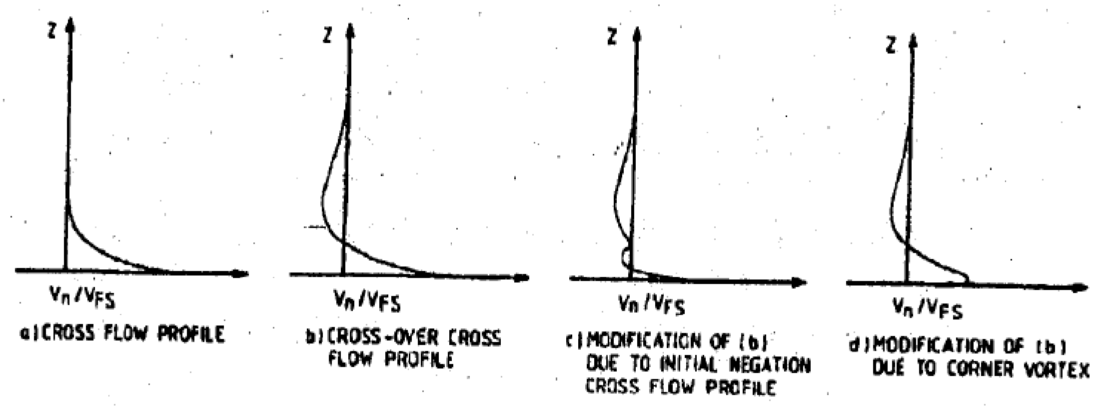

Fig. 2-12 Various types of endwall boundary layer profiles, Sieverding [1985].

Langston [2000] reviewed the progress that had been made in understanding the flow conditions that occur when the inlet endwall boundary layer separates at the saddle point and rolls up into a horseshoe vortex, as shown in fig. 2-13. The saddle point location occurs in a region of streamwise adverse pressure gradient and strongly depends on the incidence angle of the cascade flow. The separation at the saddle point does not depend on the radius of curvature of the aerofoil leading edge, but depends on the pressure field generated by the overall shape and size of the pressure and suction surfaces of the aerofoil. The author stated that the non-dimensional parameter E generated by Eckerle and Awad [1991] is the important parameter to predict the initiation of the swirl flow.

$E = (\mathrm{Re}_D)^{\frac{1}{3}}(D/\delta^*)$, where Re_D is the cylinder Reynolds number, D is the cylinder diameter of leading edge, and δ^* is the displacement thickness of the endwall boundary layer at the position of leading edge. For E > 1000, there is no swirling motion in the plane of symmetry upstream of the cylinder. For E < 1000, the swirling motion of the vortex is initiated. The identification of these two regimes gives a good way to predict the saddle point, the inception of the horseshoe vortex and thus the effects of the separating flow on heat transfer.

Measurements at five planes within the cascade (x/C_x =0.03, 0.22, 0.45, 0.67, 0.83) and at two downstream locations (x/C_x =1.03, 1.22) were conducted by Harrison [1990]. The author measured the endwall shear stress and traced the generation of stagnation pressure loss in the cascade passage of high turning turbine blades. The study showed that the passage vortex lies over the endwall lift-off line and acts to thin the endwall boundary layer upstream as well as downstream of the line. Although there is a laminar boundary layer over much of the endwall within the blade passage and the wall shear stress is high, this boundary layer is not the dominant cause in the generation of secondary loss.

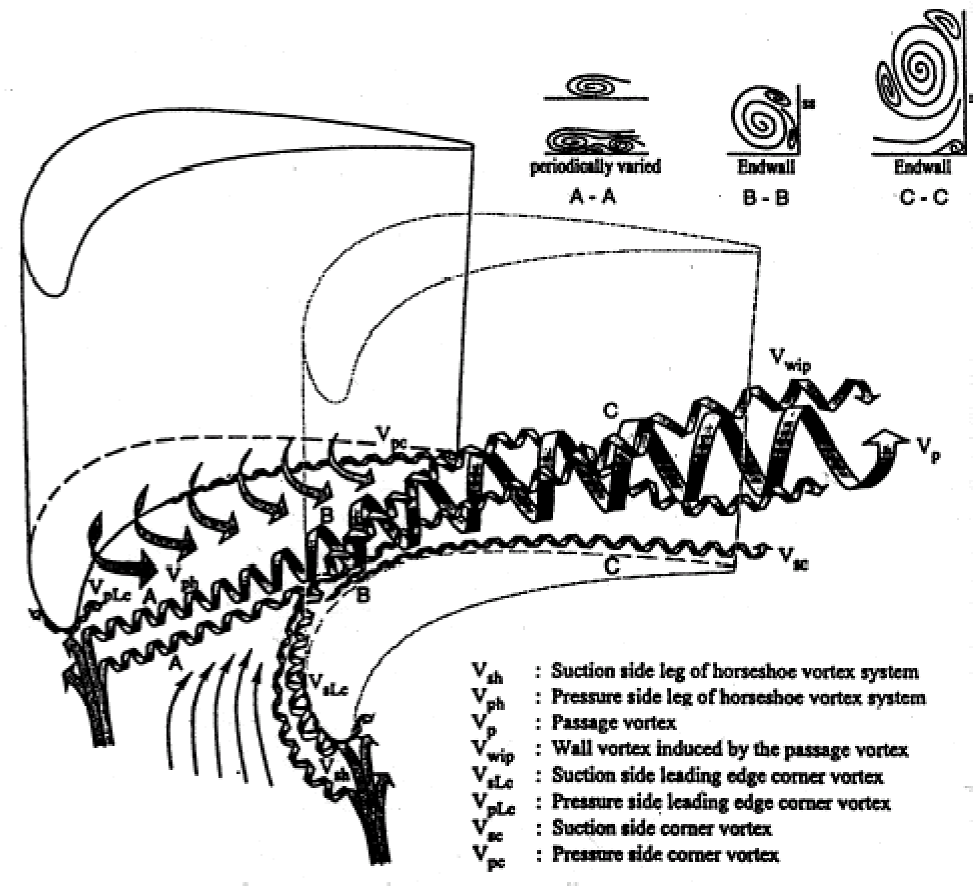

Fig. 2-13 Secondary flow development, Wang et al. [1997].

Moore and Gregory-Smith [1996] investigated the turbulence and transition in secondary flows in a turbine cascade experimentally. The authors measured the mean velocity components and the six components of the Reynolds stresses using hot-wire anemometry. They concluded that the endwall and suction surface corner are high turbulence flow regions associated with the corner vortex. The transition in the suction surface boundary layer occurred between 0.55 and 0.71 axial chord (C_x) downstream of the cascade leading edge. The thick turbulent endwall boundary layer is then rolled up into a loss core and replaced by a thin skewed boundary layer.

Aunapu et al. [2000] tried to modify the endwall secondary flow by using different numbers of endwall jets, which were installed at a location downstream of the saddle point near the leading edge of the pressure side. These jets diverted the path of the passage vortex and were expected to improve the film cooling on the suction side blade, but the aerodynamic losses increased in the passage. A boundary layer fence was effective in altering the path, reducing the strength, and minimizing the harmful effects of the pressure side leg of the horseshoe vortex in the turbine passage. Total pressure losses appear to be generated primarily near the suction surface-endwall corner. A comparison between the development of the endwall characteristics with and without modification was presented.

2-3.4 The interactions of secondary flows generating losses

By analysing the vortex structure and their effect on the endwall boundary layer, Sieverding [1985] gave a summary of the most important factors contributing to the generation of loss through a turbine cascade:

- The natural increase of the inlet endwall boundary layer momentum thickness up to the separation lines S_{1s} and S_{1p} in fig. 2.11.
- The stagnant separation bubble in the leading edge region between the two separation lines (S_{1s} and S_{2s}) and (S_{1p} and S_{2p}) in fig. 2.11.
- The growth of a new boundary layer downstream of the separation line S_{2p}.
- The corner vortex in both the pressure side and suction side endwall corners. These become the dominant loss factors downstream.
- The shear stress effects along all three-dimensional separation lines.
- The losses due to the shear action of the passage vortex on the blade suction side.
- The mixing process between the cross-flow and the blade flow along the three-dimensional separation line S_4.
- The dissipation of all vortices and complete mixing of the non-uniform outlet flow downstream of the cascade.

Langston [2000] stated that the secondary or endwall flow losses could reach 30-50% of the total loss; therefore there are many attempts and studies to reduce them. Some of these studies used fences and grooves on the endwall and suction side aerofoil surfaces to reduce secondary flow losses. Other researches changed the endwall contouring from planar configuration to S shape and the results showed a significant reduction in the full passage loss. This reduction reaches 17% of full passage mass averaged loss compared to a full planar endwall configuration, Kopper and Milano [1981]. The plane turbine cascade endwall with a bulb leading edge shown in fig. 2-14 exhibited a 47% reduction in net secondary loss, sauer et al. [2000].

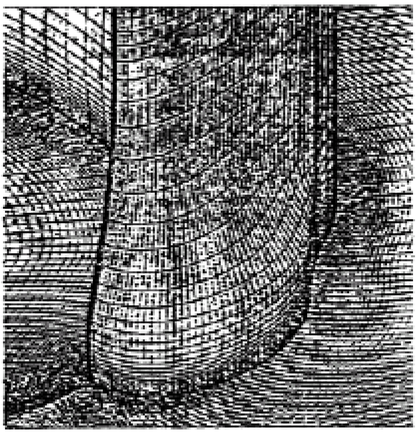

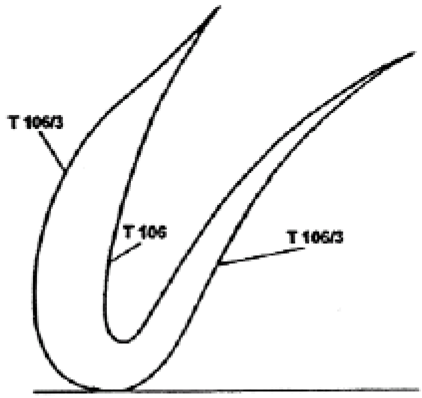

Fig. 2-14 a- Turbine endwall modification
b- Leading endwall bulb, Sauer et al. [2000].

Hodson and Dominy [1987] studied the off-design performance of a low-pressure turbine cascade experimentally. They investigated the effects of incidence angle, Reynolds number, pitch-chord ratio, and inlet boundary layer thickness on the secondary flow losses. The authors found that the production of secondary loss is greatest at lower Reynolds numbers, positive incidence, and at higher pitch-chord ratios.

Yamamoto [1987] carried out measurements of secondary flow and total pressure loss before, within, and after a straight stator cascade with a turning angle of about 65^{o}. He did these measurements in fourteen planes normal to the streamwise direction their positions ranged from –0.25 to 1.28 axial chord. Further measurements were taken parallel to the streamwise plane near the suction blade surface. Yamamoto [1987] mentioned that the counter vortex at the suction surface / endwall intersection is weak and has no significant effect on the passage loss. A high loss region was found on the endwall near the pressure side and the majority of the loss was produced due to the interaction of the passage vortices with the suction surface downstream of the cascade throat at a distance of 0.74 axial chord, approximately. In the second part of this paper, Yamamoto repeated the above measurements in a straight rotor cascade with a turning angle of about 102^o. He got similar results to the stator case except the secondary flows are stronger than those in stator blade cascade.

An experimental investigation of the flow within and downstream of a turbine blade cascade of high aspect ratio was carried out by Adjlout and Dixon [1992]. They showed that the turbulence level of the free stream does not affect the total pressure loss coefficient. Flow unsteadiness with a discrete dominant frequency downstream of the trailing edge was observed in the position of the core vortex using oil flow visualization.

2-3.5 Leading edge and endwall contouring

The influence of the leading edge geometry on secondary losses in a turbine cascade at the design incidence was presented by Benner et al. [2004] using two cascades with the same inlet and outlet conditions and different leading edges. The results from this experiment suggest that the strength of the passage vortex plays an important role in the downstream flow field and in generating stage loss. It was concluded also that the aerofoil loading distribution has a significant influence on the strength of this vortex. In contrast, the leading edge geometry has only a minor influence on the secondary flow field and the corresponding secondary losses at the blade design incidence, as concluded by the authors. The effect of leading edge fillet and inlet swirl angle on the secondary flow structure was studied by Shih and Lin [2003] using ensemble-averaged compressible Navier-Stokes equations with the shear stress transport (SST) turbulence closure model. The authors aimed to control the secondary flow structure using the leading edge fillet and the inlet swirl. The results obtained showed that both leading edge fillet and inlet swirl can reduce significantly the aerodynamic loss and the surface heat transfer. The size and intensity of the secondary flows alone are not able to account for the stage aerodynamic losses and its heat transfer characteristics. The swirl and fillets investigated increased the stagnation region size on the endwall about the aerofoil leading edge.

Harvey et al. [2000] used a non-axisymmetric turbine endwall to investigate the secondary flow through a turbine rotor profile in linear cascade. They showed numerically, using a three-dimensional RANS code, that using a non-axisymmetric endwall profile can significantly reduce secondary flows especially the secondary kinetic energy and the exit angle under-turning. The effects of the non-axisymmetric endwall profiling are comparable with those of the exiting techniques of lean and skew. Hartland et al. [2000] carried out experimental work to validate the numerical predictions done by Harvey et al. [2000]. The authors concluded that the experimental results show a reduction in the strength of the secondary flow at the cascade exit and a more uniform exit flow angle profile. The comparison with a planar endwall showed a reduction in the overall loss by 30% at the downstream exit plane. Ingram et al. [2005] investigated the endwall boundary layer separation induced by a non-axisymmetric endwall profile. They investigated the flow in detail theoretically and experimentally with pressure probe traverses and surface flow visualization. They reported that the inlet boundary layer locally separates, generating extra loss, which feeds directly into the core of the passage vortex. They summarized that the application of non–axisymmetric endwall profiling can give rise to adverse features, although it has shown to be highly beneficial.

The influence of the blade lean on turbine losses was investigated by Harrison [1992] using a blade without lean, with a straight simple lean, and with a compound lean. The author mentioned that the lean has an observable effect upon the blade loading, on state of the boundary layer on both suction and endwall surfaces, and on the distribution of loss generation. Blade lean also has a small effect on the overall loss coefficient. However, a compound lean can reduce the downstream mixing loss and the spanwise variations of mean exit flow angle. The simple lean substantially reduces velocities and hence loss generation at one endwall and increases them at the opposite wall. On the other hand, a compound lean reduces endwall losses but at the expense of midspan loss. The compound lean increased flow turning, reduced downstream mixing losses, and substantially reduced spanwise variations in mean flow angle, as reported by the author. Another study on the effect of the blade compound lean at the stator root on the performance of the low-pressure turbine stage was presented by Lampart [2000]. The results indicated that compound lean induces additional blade force, streamwise curvature, and redistributes the pressure and mass flow rate along the blade spanwise direction. This could improve the efficiency, particularly in low load regions.

2-3.6 Blade row interaction

Sections 2-2.1 to 2-2.5 reviewed in some detail the losses through an isolated blade. As turbomachines consist of more than one blade row, it is necessary to study the effect of interaction between blade rows, since blade rows are typically placed close to each other to reduce the engine size and increase the power to weight ratio. The importance of this phenomenon is due to the flow exiting one blade row does not mix out completely before reaching the next blade row.

Walraevens and Gallus [1995] carried out measurements to investigate the stator-rotor-stator interaction in an axial flow turbine. The time-dependent three-dimensional velocity vector field was measured using a hot-wire with double and triple wire probes behind a rotor and the following stator. The results obtained showed that the upstream stator wakes strongly influence the rotor passage flow, causing a high turbulence level and a strong cross-flow towards the suction side. These contribute to the development of the upper and lower trailing edge vortices. Due to the passage vortices in adjacent passages, the suction side boundary layer flow close to the trailing edge points radially inwards, whereas the pressure side boundary layer flow of the same blade points radially outwards. Both boundary layers leave the blade surface and form a shear layer with strong mixing due to local pressure gradient. Downstream of the trailing edge, the mixing process continues and forms the trailing edge vortex as explained schematically in fig. 2-15.

Measurements in the rotor region of a single-stage turbine were analysed by Binder et al. [1987]. These measurements relate to the unsteady blade row interaction caused by secondary vortices. This study captured the following features:

- The stator secondary vortices aligned parallel to the stator wake are chopped by the rotor blades as shown in fig. 2-16.
- After the vortex is chopped, the vortex motion breaks up and its energy is converted into turbulence.

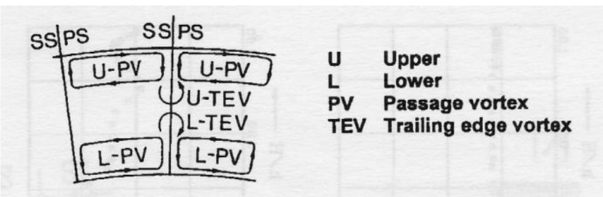

Fig. 2-15 Development of trailing edge vortices, Walraevens and Gallus [1995].

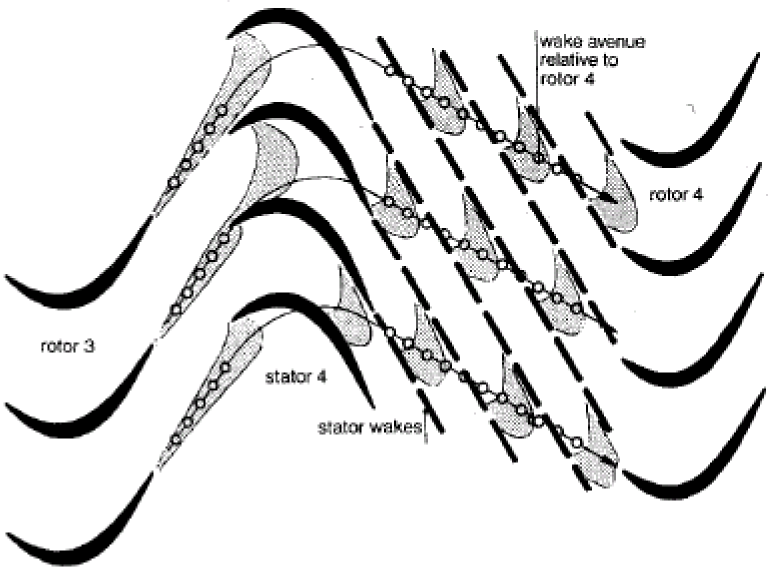

Fig. 2-16 Blade wakes interaction flow, Binder et al [1989].

Miller et al. [2003] carried out an experimental investigation on the wake, shock, and the potential flow interaction in a 1.5 stage turbine and compared the results with the predictions of a time resolved computational model. They studied the main interaction (vane-rotor and rotor-vane interactions) in addition to the vane-vane interaction.

The flow through a turbo-machine is highly unsteady due to the blade relative motion and wake interaction with the downstream row, especially with the suction side boundary layer, because the suction side boundary layer is responsible for most of the energy loss due to its tendency to separate. The process of wake induced boundary layer transition in low pressure turbines and the loss generation processes that results are reviewed by Hodson and Howell [2005] with emphasis on how the effect of the wakes may be exploited to control the loss generation.

A three-dimensional unsteady viscous Navier-Stokes solver was used for the prediction of the vane-rotor interaction in a high-pressure turbine stage by Miller et al. [2003]. Numerical results were compared with the experimental data acquired using a fast response aerodynamic probe. The authors summarize the following conclusions:

- The four main flow features of the rotor exit flow are the rotor tip leakage, the rotor hub secondary flow, the rotor trailing edge shock, and the rotor wake.
- There are two significant vane periodic changes in the rotor exit flow field. The first occurs close to the rotor suction surface at all radial heights, and the

second, which is dominant, occurs close to hub wall. Specifically, wakes at vane passing frequency amplify their vorticity over the suction side of the rotor profile close to the leading edge.

- The tip leakage flow was found to be largely unaffected by vane-rotor interaction.

Chaluvadi et al. [2003, 2004] examined the impact of the upstream vortices on the performance of the downstream blade row, the transport mechanism of the passage vortices inside the downstream blade row, and the unsteady mixing of the passage vortices in the downstream blade row. In this study, the authors concluded that, at the exit of the rotor, the pressure side leg of the stator passage vortex was radially displaced upward and the suction side leg was entrained into the rotor passage vortex. A large variation in the stator flow field was observed between 8.4% C_x and 25.2% C_x downstream of the stator trailing edge, due to the downstream rotor potential field.

The effect of blade loading on the propagation of unsteady flow was investigated by Korakianitis [1992] in an axial-turbine-blade rotor cascade. The potential flow field of the rotor cuts into the potential flow field of the upstream stator. After the potential flow field is cut, it propagates as a flow disturbance superimposed on the rotor flow field. At the rotor leading edge, the potential flow field of the rotor cuts into the wake. The wake then is sheared into the rotor passage and results in a region of increased and decreased unsteady pressure upstream and downstream of the convecting wake respectively. The wake interaction is more pronounced in highly loaded cascades and at a lower outlet stator angle. The potential flow interaction dominates the unsteadiness for high values of R (stator-to-rotor-pitch ratio) and wake interaction dominates the unsteadiness for low values of R as shown in fig. 2-17. The previous argument could be used to determine locations of local unsteady pressure regions.

The influence of the turbine stator wake on the rotor flow field was investigated experimentally by Matsunuma and Tustusi [2000] using a LDV system. The authors measured velocity distribution, the flow angle, and the turbulence intensity, and the obtained data were analyzed with respect to the absolute and relative frame of reference. Figure 2-18 shows the time dependent distributions of the absolute velocity, absolute flow angle, relative velocity, relative flow angle, and turbulence intensity. It shows the low velocity area caused by the stator wake, which affects the flow field around the rotor.

The exit combustor flow field entering the stator vane passages in a gas turbine is typically nonuniform and significantly affects the development of the secondary flows in the turbine passages. The effects of varying total pressure profiles in both the radial and circumferential direction on the secondary flow fields in a first-stage stator vane were analyzed by Hermanson and Thole [2002] using computational fluid dynamics. These CFD simulations were compared with flow field data measured in a large-scale, linear turbine vane cascade. The authors concluded that the application of a temperature gradient in combination with an inlet boundary layer reduced the streamwise vorticity and the spanwise velocity associated with the secondary flows. Applying a temperature gradient at the inlet with a constant velocity resulted in a large vortex with very little streamwise vorticity rotating in the opposite direction with respect to the passage vortex with flow moving away from the endwall up the vane surface. Secondary flow patterns were predicted for two cases with pitchwise and spanwise total pressure gradients. The former was found to be the driving factor for determining the magnitude of secondary flows in the passage.

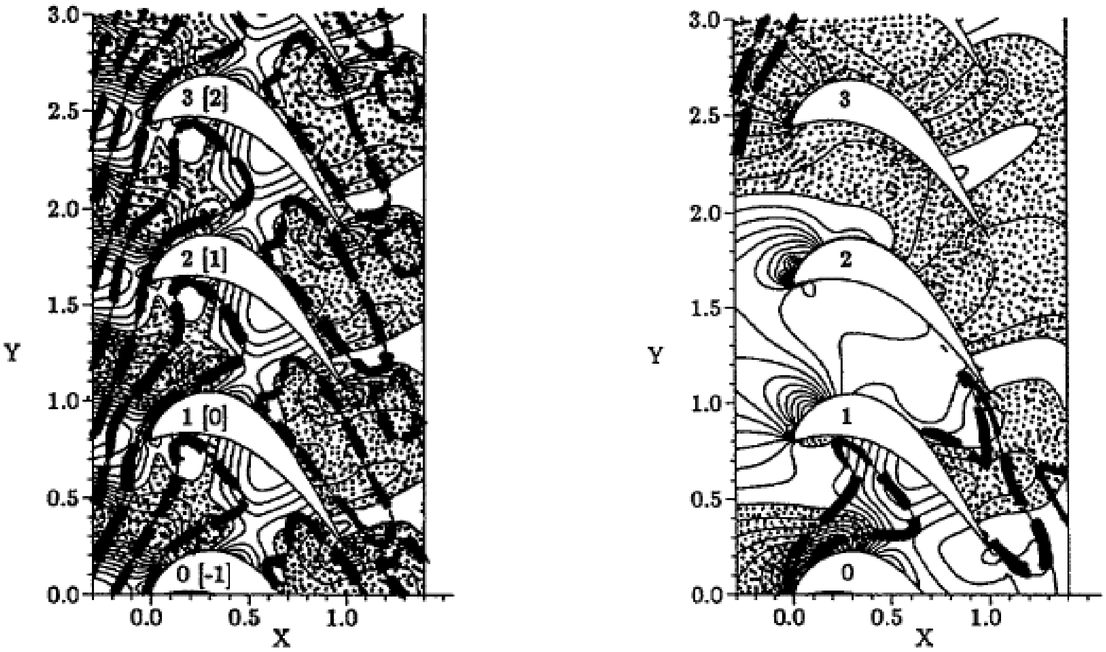

Fig. 2-17 Unsteady flow fields with both interactions on the cascade, Korakianitis [1992].
Left the wake interaction dominates for R = 1.
Right the potential-flow interaction dominates for R = 4.

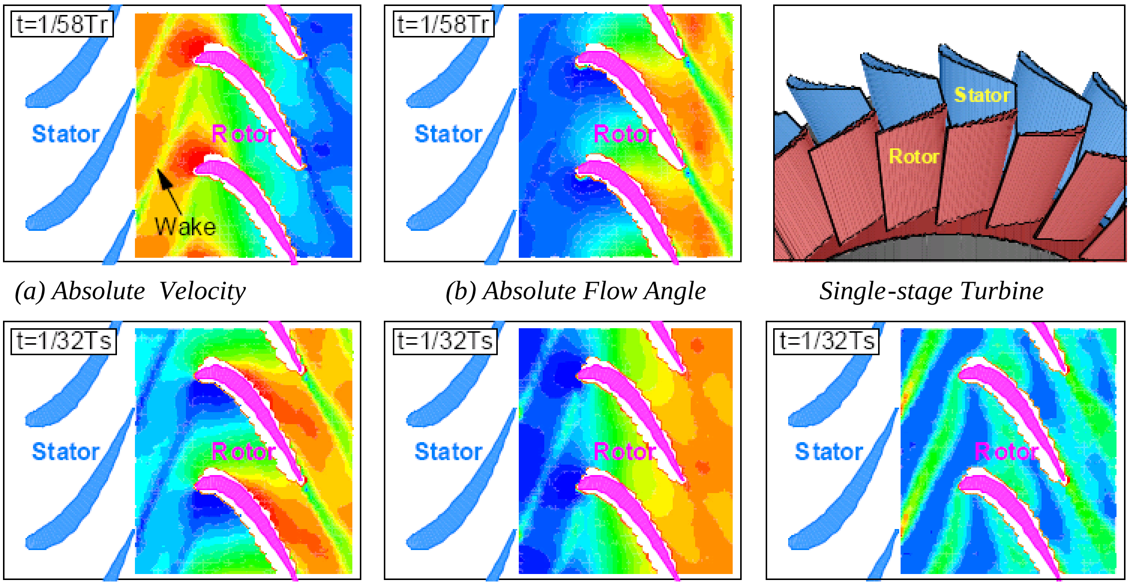

(a) Absolute Velocity *(b) Absolute Flow Angle* *Single-stage Turbine*

(c) Relative Velocity *(d) Relative Flow Angle* *(e) Turbulence Intensity*

Fig. 2-18 Time-dependent flow distributions around turbine rotor cascade, Matsunuma and Tustusi [2000].

2-4 Overview of turbomachinery flow simulation

Computational models of turbine stages are widely used to understand the flow structure and the loss sources. In this section, there is a review of the open literature CFD of turbine cascades, single stage, and multi stages.

A time-dependent solution of the Euler equations was obtained by the application of a difference scheme on a grid consisting of quadrilateral elements, Denton [1983]. The multi grid method was used to accelerate the solution. In 1990, Denton and Dawes introduced independently the mixing plane technique to enable the simulation of the flow through multistage turbomachines. A three-dimensional numerical method to predict the viscous flow through multistage turbomachines has been developed by Denton [1992]. To avoid calculating the unsteady flow, which is inherent in any machine containing both rotating and stationary blade rows, a mixing process is modelled at a calculating station between adjacent blade rows. The effects of this mixing on the flow within the blade rows are minimized by using extrapolated boundary conditions at the mixing plane.

Kunz and Lakshminarayana [1992] developed and applied an explicit, three-dimensional, coupled Navier-Stokes $/k - \varepsilon$ technique to internal turbomachinery flow computations. The code is developed based on the extension of previous two-dimensional work. The discretization scheme avoids the metric ambiguity problem associated with standard finite difference spatial discretization at the interface between periodic and solid boundaries and retains the accuracy and stability properties of a compact differencing scheme. Tallman and Lakshminarayana [2001] used a pressure-correlation based three-dimensional Navier-Stokes CFD code to simulate the effect of the turbine geometry and inflow conditions on the tip leakage flow and vortex in a linear turbine cascade. The effects of realistic tip clearance spacing, inlet condition, and relative endwall motion were simulated to understand the detailed flow physics.

Chima [1998] modified a multiblock Navier-Stokes turbomachinery code to allow the analysis of a multistage turbomachine. A steady averaging-plane approach was used to pass information between blade rows. Averaging-plane methods solve all blade rows simultaneously, exchanging spanwise distributions of averaged flow quantities at a common grid interface between the blade rows. The averaging plane method maintains the spanwise consistency between blade rows. The method splits the flow into a steady component (periodic component), and an unsteady random (turbulent) component. The flow equation is integrated in time using procedures analogous to Reynolds averaging to predict the passage pitch averaged flow. The method requires that the computational grids for each blade overlap at least one neighbouring blade row on each side. The author stated several conclusions regarding the characteristic boundary conditions and the averaging-plane method as follow:

- The use of characteristic boundary conditions ensures that information propagates correctly between blade rows, although the boundary conditions are non-reflecting.
- The well-known mixed-out average that represents the flow far downstream, and a new kinetic energy average that represents the local flow were used with the averaging-plane method.
- The averaging-plane method ignores physical processes such as wake mixing and migration, acoustic interaction, and other unsteady effects that may be important in a real turbine.

Another computational study on the tip leakage flow was carried out by Harvey and Ramsden [2001]. The authors used a steady flow Reynolds averaged Navier-Stokes CFD code to qualitatively determine the benefits of a turbine rotor partial shroud. They concluded that the use of a partially shrouded high pressure turbine rotor improves the turbine efficiency by 1.2% to 1.8% at 2 percent tip gap clearance/span.

Many three-dimensional flow solvers for simulating rotating machinery are documented in the literature. These include the work by Adamczyk [1985], Ni and Bogoian [1989], Dawes [1990], Denton [1990], and Hall [1997]. Most of the multistage solvers in the design process are steady. The main reasons for a lack of wide-spread use of the unsteady numerical methods are the large computational requirements necessary to calculate the flow solution and the long integration times necessary to achieve significant time averages. However, some of the current turbomachinery flow solvers are unsteady, such as Giles [1988], Jorgenson and Chima[1988], Rao and Delaney [1990], and Arnone and Pacciani [1995], but the unsteady solvers are still impractical to be used as a standard design tool for a multistage turbomachine.

2-5 Summary remarks on the literature survey

The literature review highlighted the following areas where further investigation is required:

- The leakage flow structure over a shrouded turbine blade.
- The effect of labyrinth seal geometry on the loss quantification.
- The mixing loss due leakage jet injection into the blade passage flow.
- The unsteadiness generated downstream the rotor blade due to the interaction between the main flow and the jet leakage flow.
- The loss mechanisms through and downstream of the shrouded blade.

The specific review of turbulent turbomachinery flow models highlighted that current RANS methods are able to reproduce some of the flow physics relating to loss production in a turbine stage. In the present study, the author intends to use compressible RANS in addition to a hybrid RANS/LES method to specifically address:

- The structure of the over shroud leakage flow in a turbine stage.
- The interaction between the tip leakage flow and the main passage flow.
- The steady loss mechanisms in a turbine stage.

Chapter 3

Tip Leakage and Mixing Losses Analytical Model

3-1 Introduction

The flow past a labyrinth rotor seal in a typical shrouded turbine stage is hot, has high vorticity and a low axial momentum. This leads to unwanted heat transfer to the shroud and casing, endwall losses, and mixing losses. Although turbomachinery designers have a lot of information concerning the flow through labyrinth seals, there is a need for a relatively straightforward model to predict the adverse effects of the leakage flow on the stage performance. The loss of performance due to tip leakage over unshrouded blades has been intensively studied, more than the leakage flow over shrouded blades. Therefore this part of the study aims to contribute to the building up of appropriate knowledge of the impact of the leakage flow on shrouded turbine stage performance.

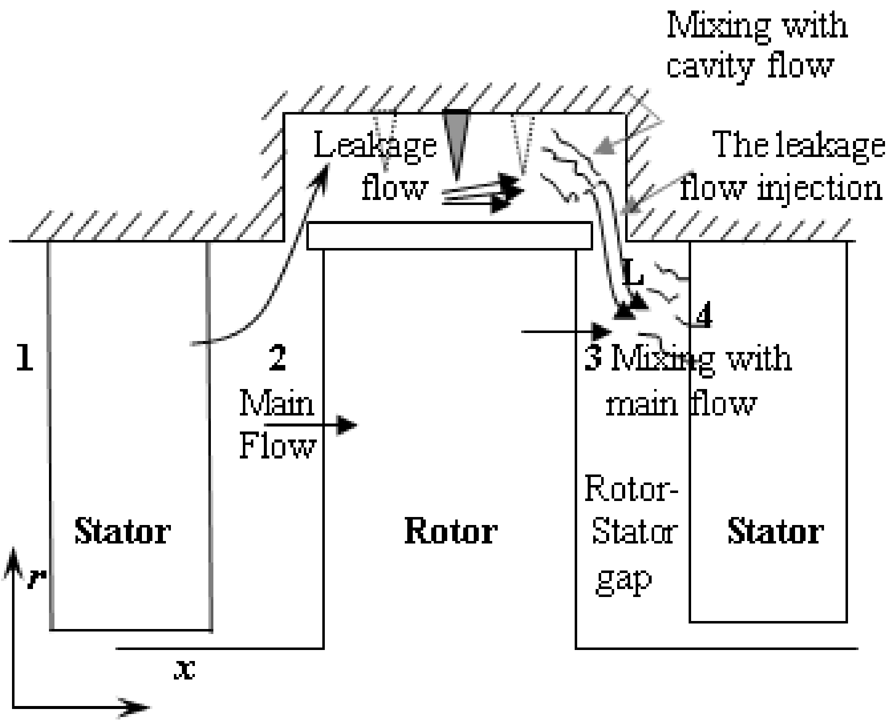

Figure 3-1. Schematic of a shrouded stage with secondary flows. Meridional plane (x; r).

Figure 3-1 shows a simplified geometry of a shrouded rotor stage with a labyrinth seal in a typical HP turbine stage. The structure of the labyrinth seal cavity flow has been experimentally investigated by Pfau et al. [2001]. They studied the nature of the mixing of the labyrinth leakage and the main passage flows to identify the disturbances in the flow entering the next blade row. The authors showed that the fluid leaving the shroud is broken up into distinct oblique jets of low momentum embedded in the channel flow, causing a negative incidence angle and additional loss at the inlet of the subsequent blade row.

Wallis et al. [2001] tested a way to control the leakage flow over the shroud of an axial flow turbine. The authors used turning vanes supported on the shroud of the rotor blades aimed at reducing the aerodynamic losses associated with the leakage flow re-injected into the main passage flow. They tried to reduce the tangential velocity of the leakage flow and consequently reduce the magnitude of the downstream leakage losses and improve the incidence onto the following blade row. The authors obtained the desired objectives at the expense of the overall performance, reporting a 3.5% reduction in brake thermal efficiency. Schlienger et al. [2003] installed inserts to redirect the leakage flow where it mixes with the main flow. They reported that the inserts reduced the stage efficiency, although they improved the endwall flow structure. Rhode et al. [1997a, 1997b] investigated experimentally the effects of the annular groves and sloping surfaces upon the leakage flow resistance using leakage flow measurements and flow visualization technique. They concluded that such features can increase the leakage flow resistance.

An attempt to quantify the mass leakage flow through the labyrinth seal is presented by Egli [1935]. He assumed that the leakage flow approaches the labyrinth fins with zero kinetic energy. The leakage flow suffers from a series of throttling actions through the labyrinth seal and then the flow recovers part of its kinetic energy as it expands downstream of the last fin. He assumed that the leakage flow through the labyrinth seal follows the Fanno line by assuming a completely dissipated kinetic energy before approaching the next fin and that no heat is exchanged with the surroundings. Under the above assumptions the mass leakage flow is estimated as Egli [1935]:

$$\dot{m}_L = A_{fin}\, c_c \psi_{th} \sqrt{p_{02}\rho_{02}} \qquad (3-1)$$

where ψ_{th} is the theoretical expansion number defined as:

$$\psi_{th} = \sqrt{2\frac{\gamma}{\gamma-1}r^{\frac{2}{\gamma}}\left(1-r^{\frac{\gamma-1}{\gamma}}\right)} \qquad (3-2)$$

Traupel [1973] developed a loss correlation model to evaluate the leakage mass flow. The model is based on an extensive amount of empirical data obtained on an impulse turbine test rig, Fridh [2002]. According to the model, the leakage mass flow is given by

$$\dot{m}_L = A_{fin}\,\varepsilon\sqrt{p_2\rho_2} \qquad (3-3)$$

where ε is the discharge characteristic that is evaluated empirically for a specific labyrinth seal configuration.

While Egli's model is applicable to adiabatic flows only, in Traupel's model the empirical correlation coefficients are determined from real configurations and within the limits of the parameter space spanned by Traupel, its predictions account for heat transfer and a non-zero approaching velocity to the fins.

Denton and Johnson [1976] developed a seal leakage flow model. The leakage flow was estimated based on the pressure difference across the seal. Denton [1993] derived a simple tip leakage loss model assuming that the leakage flow swirl component does not change across the labyrinth seal. The ratio of the leakage flow to the main flow is estimated by

$$\frac{\dot{m}_L}{\dot{m}_m} = \tau C_c\sqrt{sec^2\beta_3 - tan^2\beta_2} \qquad (3-4)$$

where τ is the sealing gap ratio, C_c contraction coefficient, β_2 is the rotor inlet angle, and β_3 is the rotor exit angle. Denton's model does not account for the number of fins in the labyrinth seal and ignores the temperature difference between the leakage flow and the main flow streams in the mixing loss calculation, Eqn. (3-32), so that the entropy generation is underestimated by up to 20% of the overall mixing entropy generation, Pfau [2003].

Song and Song [2004] built a concentric and eccentric model to predict the lateral forces and the flow response to the labyrinth seal in turbines. The model estimated the leakage flow for a two-fin labyrinth seal using the sealing gap ratio and the pressure drop across the rotor.

This part of this study aims to add to the above usable models with a focus on quantifying the over-shroud leakage effects on stage performance, for turbine design purposes. The study addresses a) the calculation of the mass leakage fraction for the through flow labyrinth seal with any number of fins b) the contribution of the tip leakage loss to the overall loss c) the effects of the injection angle on the mixing loss d) the effects of the tip leakage jet on the incidence angle that affects the subsequent row. A new analytical model is formulated that accounts for (a-d), El-Dosoky et al. [2007]. This is a contribution that has both scientific and industrial relevance, for the benefit of the turbomachinery community. The limitations of the new model are that it does not account for some of seal design parameters and viscous effects such as the fin shape, stepped design, and skin friction. Addressing these limitations is an interesting line of model development for further work.

3-2 Steady tip leakage flow mixing model

Downstream of the rotor blade trailing edge, the over-shroud leakage flow re-enters the main passage, as sketched in Fig. 3-1. This flow has a different velocity with respect to that from the main passage. The mixing of these two streams increases the entropy in the flow. This section describes an analytical model to predict the single stage entropy loss coefficient due to this mixing process.

The present model assumed that the flow through the labyrinth seal is adiabatic and the pressure of the leakage jet at mixing stage is roughly equal to the pressure downstream of the rotor trailing edge, assuming that there is no significant restriction except at the seal fins, Denton [1993]. The pressure drop across each labyrinth seal fin is roughly equal, as reviewed by Denton [1993]. The leakage jet mixes with the major downstream main flow where secondary flows have a significant effect on stage loss and this is of particular interest to low aspect ratio, high pressure stages.

The analytical model is presented in two steps. The first step predicts the flow conditions at the rotor trailing edge and at the exit from the labyrinth seal, states 3 and L in Fig. 3-1, using the given stage inflow conditions, state 1 in Fig. 3-1, and the stage design pressure ratio. The second step extends the modelling further downstream, through the rotor-stator gap, Fig. 3-1, and estimates the mass-averaged entropy mixing loss coefficient.

The first step starts by considering the stage inlet stagnation temperature T_{o1}, the stage inlet stagnation pressure p_{o1}, the flow coefficient ϕ, and the rotational speed. The inlet velocity triangle at state 2 can be drawn by calculating the blade circumferential velocity and the flow velocity component and knowing the stator exit blade angle. Using the first law of thermodynamics, the temperature at state 2 is estimated. From the stator (or nozzle) stagnation pressure p_{01} and the total pressure loss coefficient Y_{tN}, from Horlock [1966], the stagnation pressure at the rotor inlet is estimated as

$$p_{02} = p_{01}\left[Y_{tN}\left(1-\frac{p_2}{p_{02}}\right)+1\right] \tag{3-5}$$

The static temperature distribution through the stage is determined from the degree of reaction Λ,

$$\Lambda = \frac{T_2 - T_3}{T_1 - T_3} \tag{3-6}$$

The specific work W developed by the turbine and the stagnation temperature at the rotor exit,

$$W = V_b \Delta V_\theta = C_p(T_{01} - T_{03}) \tag{3-7}$$

where ΔV_θ is the absolute tangential flow velocity change across the rotor.

$$C_p T_{03} = C_p T_3 + \frac{V_{\theta 3}^2 + V_{x3}^2}{2} \tag{3-8}$$

By solving the Eqns. (3-7) and (3-8) simultaneously, the absolute velocity components $V_{\theta 3}$ and V_{x3} are calculated. Consider the dashed line control volume Cv_1 defined in Fig. 3-2.

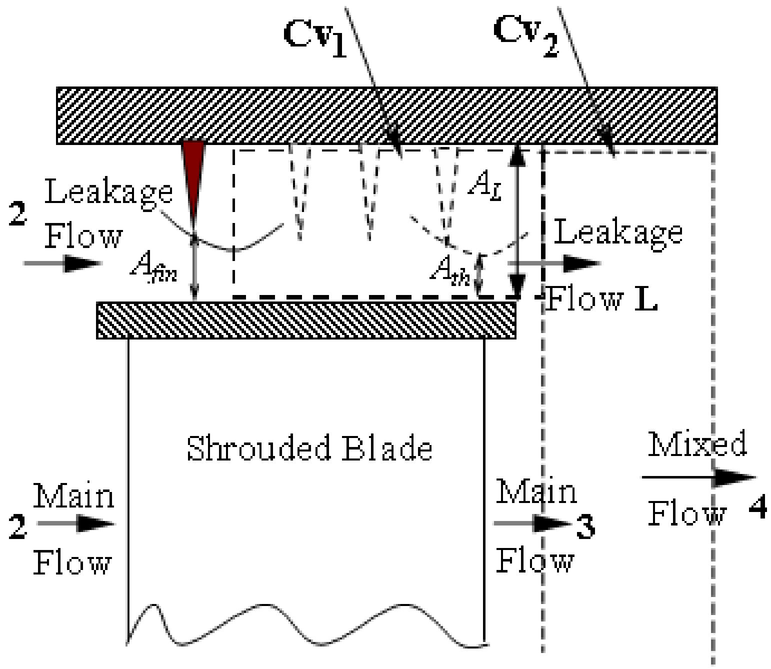

Figure 3-2. Shrouded stage control volumes. Meridional plane (*x*; *r*).

It is assumed that the leakage flow does not suffer any significant losses with constant tangential velocity before it reaches the throat A_{th}, Denton [1993]. From the conservation of mass, momentum and energy in the control volume Cv_1,

$$p_{th} + \frac{\dot{m}_L}{A_L} V_{thx} = p_L + \frac{\dot{m}_L}{A_L} V_{Lx} \qquad (3-9)$$

In Eqn. (3-9), subscripts th and L refer, respectively, to conditions at the shroud throat and at the shroud exit, as shown in Fig. 3-2. V_{thx} and V_{Lx} are the axial velocities of the leakage flow at the throat and at the exit, respectively. The exit leakage pressure from the last fin, p_L, is

$$p_L = p_3 \qquad (3-10)$$

The pressure drop across each fin roughly equals the total pressure drop across the blade row divided by the number of fins, as reported by Denton [1993].

$$p_{th} = p_2 \left(\frac{T_{th}}{T_2}\right)^{\frac{\gamma}{\gamma-1}} \qquad (3-11)$$

The throat static pressure p_{th} and static temperature T_{th} are estimated from Eqns. (3-9) and (3-11), respectively. From the equation of state, the density at the throat is calculated using the throat pressure and temperature. The actual leakage mass flow rate is

$$\dot{m}_L = \mathrm{Cd}(\rho V A)_{th} \qquad (3-12)$$

where Cd is the leakage flow discharge coefficient, A_L is the overshroud annular exit area, ρ is the fluid density, and γ is its ratio of specific heats. Re-arranging Eqn. (3-9) gives that the leakage mass flow rate

$$m_L = \mathrm{Cd}\rho_{th} A_{th} \sqrt{2 \frac{\gamma}{\gamma-1} \frac{p_{02}}{\rho_{02}} r^{\frac{2}{\gamma}} \left(1 - r^{\frac{\gamma-1}{\gamma}}\right)} \qquad (3-13)$$

There is no significant difference between the theoretical expansion function ψ_{th} of the sharp edged orifice used by Egli and the well-rounded opening orifice for pressure ratio across the orifice higher than 0.5, as reported by Egli [1935]. Since the pressure ratio across each labyrinth fin is higher than 0.5, the discharge coefficient Cd is estimated from Urner's equation, Urner [1997]

$$\mathrm{Cd} = \sqrt{\frac{C_c(1-\beta^4)}{1 - C_c^2 \beta^4}} \qquad (3-14)$$

in which the diameter ratio β and the contraction coefficient C_c are

$$\beta = \sqrt{\frac{A_{fin}}{A_L}} \qquad (3-15)$$

$$C_c = \left(1 + \sqrt{\frac{1-\beta^2}{2}}\right)^{-1} \qquad (3-16)$$

$$C_c = \frac{A_{th}}{A_{fin}} \qquad (3-17)$$

In Eqns. (3-15) and (3-17), A_{fin}, A_L, and A_{th} are, respectively, the area of the annular gap between the fin edge and the casing, the shroud annular cross-sectional area and the throat annular cross sectional area , as shown in Fig. 3-2.

The system of equations (3-5) to (3-17) are solved to obtain (i) the flow conditions at the exit plane from the rotor, which is location 3 in Fig. 3-2, and (ii) the tip clearance exit flow conditions, at location *L* in Fig. 3-2.

The second step of the analytical model is obtained by considering the dashed line control volume Cv_2 in Fig. 3-3. Within this control volume, the leakage flow mixes with the main passage flow.

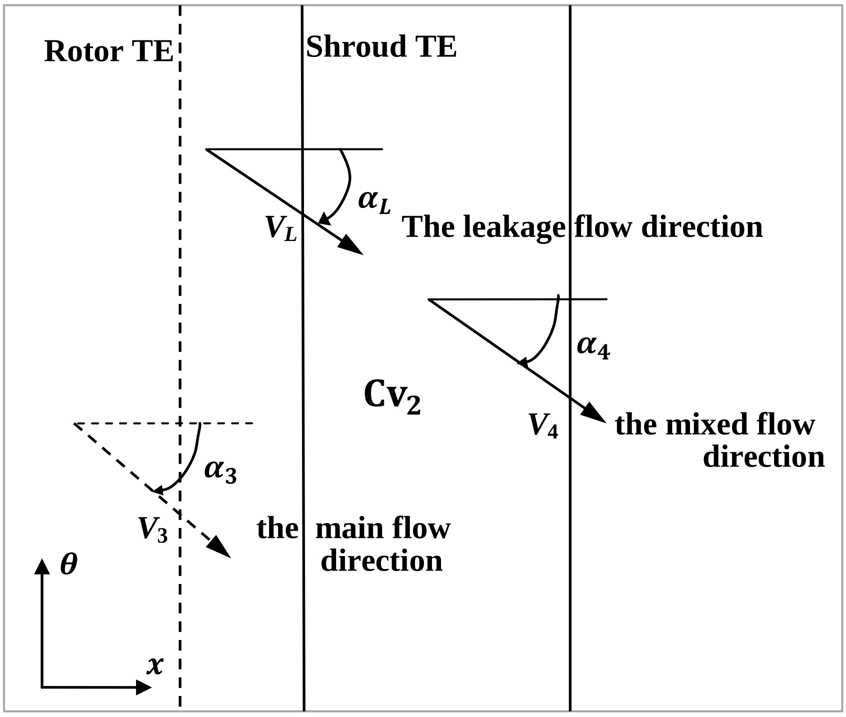

Figure 3-3. Schematic diagram for control volume Cv_2. Cascade plane (x; θ).

By continuity of mass,

$$\rho_4 V_4 cos\alpha_4 A_4 = \rho_L V_L cos\alpha_L A_L + \rho_3 V_3 cos\alpha_3 A_3 \qquad (3-18)$$

The force-momentum balance in the circumferential direction is

$$\rho_4 V_4^2 cos\alpha_4 sin\alpha_4 A_4 = \rho_L V_L^2 cos\alpha_L sin\alpha_L A_L + \rho_3 V_3^2 cos\alpha_3 sin\alpha_3 A_3 \qquad (3-19)$$

Similarly, the force-momentum balance in the axial direction is

$$(\rho_4 V_4^2 cos^2\alpha_4 + p_4)A_4 = (\rho_L V_L^2 cos^2\alpha_L + p_L)A_L + (\rho_3 V_3^2 cos^2\alpha_3 + p_3)A_3 \quad (3-20)$$

From the conservation of specific stagnation energy in the control volume Cv_2,

$$\dot{m}_4 h_{o4} = \dot{m}_L h_{oL} + \dot{m}_3 h_{o3} \qquad (3-21)$$

where

$$h_0 = C_p T + \frac{V^2}{2} \qquad (3-22)$$

The entropy s of a perfect gas relative to a reference condition s_{ref} is a function of its temperature and pressure. Assuming the turbine flow discharge is a perfect gas, the entropy increment through the mixing region can be calculated using either

$$s - s_{ref} = C_p ln\frac{T}{T_{ref}} - Rln\frac{p}{p_{ref}} \qquad (3-23)$$

or

$$s - s_{ref} = C_v ln\frac{T}{T_{ref}} - Rln\frac{\rho}{\rho_{ref}} \qquad (3-24)$$

where subscript ref indicates the reference state, which is commonly taken as the turbine stage inflow state, which is state 1 in Fig. 3-1. The second law of thermodynamics applied to the mixing process states that the rate of increase of entropy inside a control volume is equal to the net entropy flux difference across the control volume boundaries. Therefore, in Cv_2,

$$\Delta\dot{S}_{mix} = \dot{m}_4 S_4 - (\dot{m}_L S_L + \dot{m}_3 S_3) \qquad (3-25)$$

from which the mass averaged entropy mixing loss coefficient equals

$$\left(\frac{T_4 \Delta\dot{S}}{0.5\dot{m}_4 V_2^2}\right) \qquad (3-26)$$

The mixing loss model has been applied to a turbine stage with the following dimensions: The mean diameter/tip diameter ratio = 0.85, the stator exit angle $\alpha_2 = 69.7^o$, the rotor exit angle $\beta_3 = 69.6^o$, the rotational speed N = 10500rpm, the stage inflow stagnation temperature $T_0 = 1200$K, and the stage inflow stagnation pressure $p_0 = 400$kPa. The working fluid is air with specific gas constant R = 287 J/kgK and specific heat ratio $\gamma = 1.4$. Unfortunately, there is a lack in the available experimental measurements for this shrouded turbine. However, the model predictions are compared against measurements by Pfau [2003] and the other theoretical models were verified against experimental data such as Denton and Johnson [1976]. The turbine non-dimensional parameters are the Reynolds number $Re = \frac{\rho \omega D_m^2}{\mu} = 1.1 \times 10^7$, where $D_m = 0.5(D_t + D_h)$ is the stage mean diameter, the discharge pressure coefficient $C_p = \frac{\Delta p}{0.5\rho(\omega D_m/2)^2} = 4.3$, where Δp is the pressure difference across the stage, and the degree of reaction $\Lambda = 0.5$. The model predictions are compared against the experimental measurements by Pfau [2003] from a two-stage laboratory air turbine at the same set of non-dimensional parameters as the selected test case. The comparison is done at the same flow coefficient ϕ, the same gap sealing ratio τ, which is the tip clearance height normalized by the blade height $H = 0.5(D_t - D_h)$, and for the same number of fins $n = 3$.

3-3 Model predictions

3-3.1 The Leakage Mass Fraction

The most apparent effect of the leakage flow over the tip of a shrouded blade is the reduction in the mass flow rate through the blade passage, which leads to a reduction in work. In addition, the mixing of the leakage flow with the main passage flow in the stator-rotor gap is an irreversible process that leads to a loss in total pressure. This raises the back pressure at the rotor blade exit, altering the pressure drop through the rotor with respect to its design value, Denton [1993].

Figure 3-4 shows the variation of the leakage mass fraction $\frac{\dot{m}_L}{\dot{m}_m}$, where $\dot{m}_m$ is the main stream flow rate, against the sealing gap ratio τ. The relationship between the mass leakage fraction and the sealing gap ratio τ is approximately linear and very sensitive to the value of τ. This trend agrees well with the trend predicted by both the concentric model of Song & Song [2004] and by the model of Denton & Johnson [1976]. Also, the predicted values are in good agreement with the experimental measurements by Pfau [2003] at $\tau = 0.3\%$ and $\tau = 1.0\%$, especially with the measured leakage mass fraction across the second rotor, which is reported by the diamonds (♦) in Fig. 3-4. The predictions from an empirical correlation by Traupel [1973], as reported in Pfau [2003], also exhibit a good agreement with the results from the present model. The variation of the leakage flow mass fraction has been studied versus the number of labyrinth seals. The pressure drop across one of the seals roughly equals the total pressure drop across the blade row divided by the number of seals, Denton [1993]. The leakage mass fraction varies with the number of fins (n) according to

$$\frac{\dot{m}_L}{\dot{m}_m} \propto n^x \qquad (3-27)$$

where the exponent x is not a fixed value but is directly related to the flow coefficient $\phi = \frac{V_x}{U}$, where V_x and U are, respectively, the axial velocity component and the rotor blade speed at the mean diameter $D_m = 0.5(D_t + D_h)$. For the flow coefficient range plotted in Fig. 3-5, $0.3 \leq \phi \leq 0.5$, the exponential fitting of the results shows that the values of x varied from 0.491 to 0.359. This variation of the exponent x with stage flow rate demonstrates why Came changed the power of n from 0.5 to 0.42 in unpublished data, as reported by Denton [1993]. The inverse variation of the leakage mass fraction with the number of seals implies that the majority of the decrement in the leakage mass flow rate takes place by the first three seals and any additional seal adds little flow resistance, so the further reduction in $\dot{m}_L$ is limited.

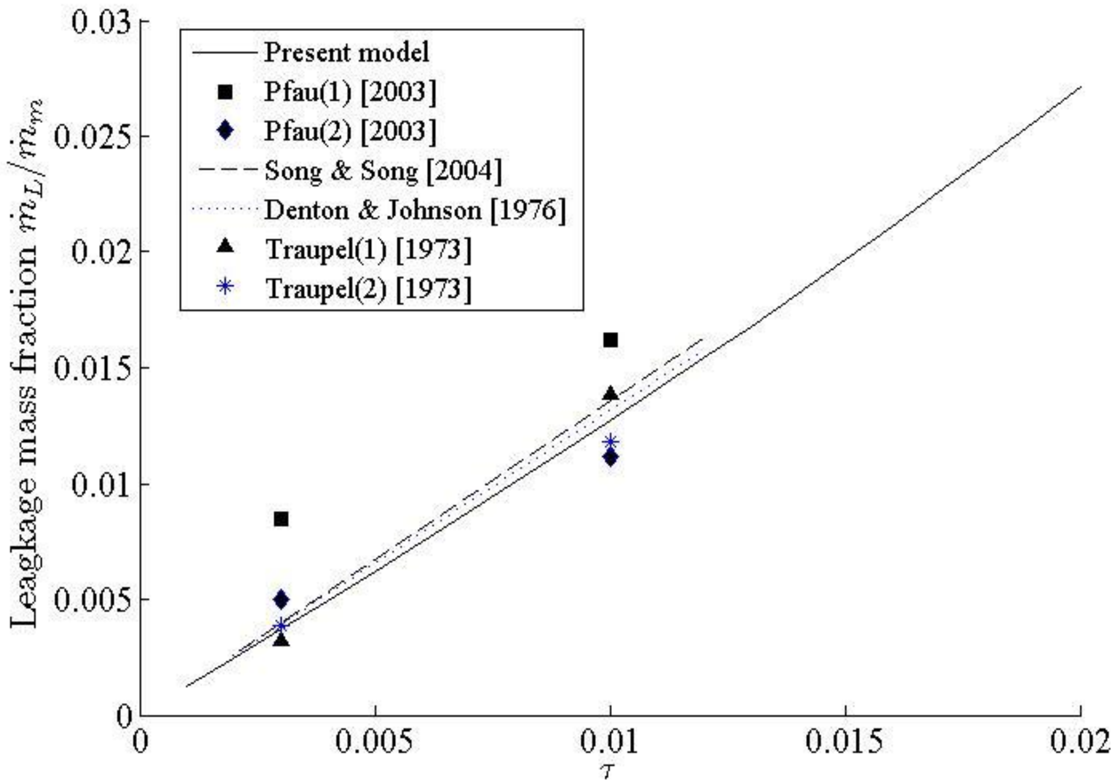

Figure 3-4. Leakage mass flow fraction versus sealing gap ratio.

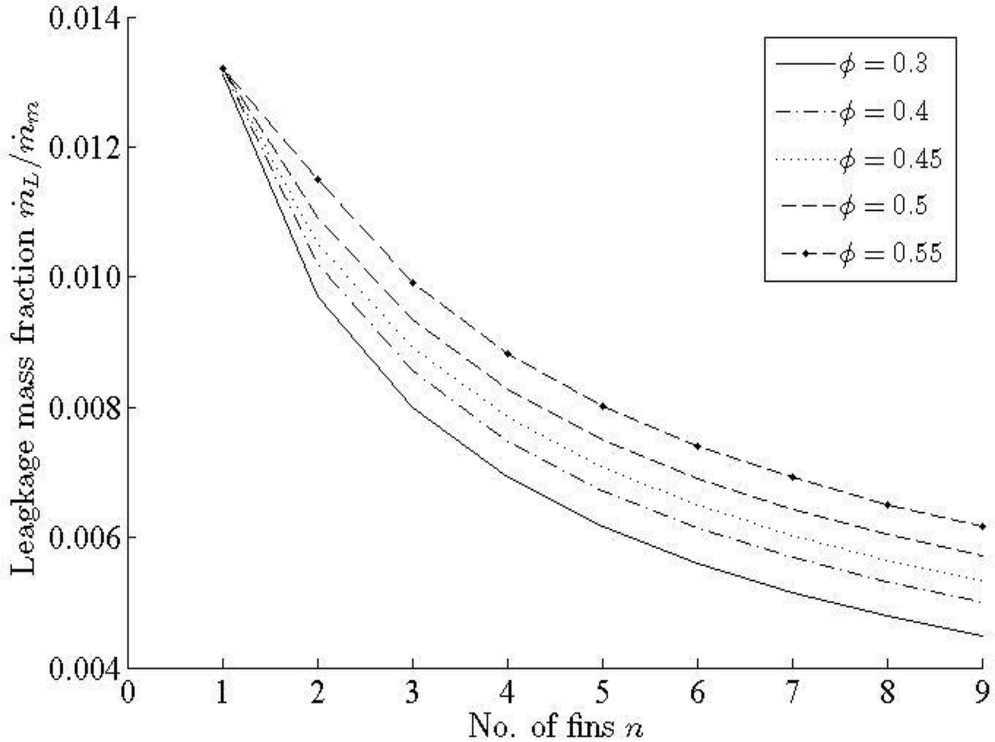

Figure 3-5. Leakage mass fraction versus the number of labyrinth fins at varying flow coefficient ϕ.

3-3.2 The Stage Efficiency

The stage total-to-total efficiency is, from Horlock [1966]

$$\eta_{tt} = \frac{T_{01} - T_{03}}{T_{01} - T_{03ss}} \qquad (3-28)$$

Figure 3-6 shows the reduction in the total-to-total efficiency versus the sealing gap ratio over a range of flow coefficients. The total-to-total efficiency drop was calculated relative to the η_{tt} at zero gap width. η_{tt} decreases as the sealing gap ratio τ increases because of the increasing leakage mass flow rate $\dot{m}_L$. The average total-to-total efficiency drop $(d\eta_{tt}/d\tau)$varies from 1.7% to 4.0% over the range of flow coefficients reported in Fig. 3-6. According to Denton [1993], $(d\eta_{tt}/d\tau)$ varies between 1.4% and 2.5% with higher values for higher stage loadings and degrees of reaction. This is in broad agreement with the present model and this range was verified experimentally by Pfau [2003].

The relationship between the reductions in total-to-total efficiency and the fin gap width is approximately linear and the slope is variable, depending on the flow coefficient. The reduction in total-to-total efficiency at $\phi = 0.9$ and n = 3 is compared to the experimental results obtained by Pfau [2003] and against predictions from the model of Denton [1993] as reported by Pfau [2003]. This comparison shows a good agreement between the present model and the experimental results at both sealing gap ratio clearances. The model by Denton [1993] predicts lower values because this model does not account for the temperature difference between the leakage flow and the main flow, Pfau [2003]. Helmers et al. [2003] carried out experimental measurements and CFD simulations on an unshrouded rotor and they obtained the same trend for the reduction in total-to-total efficiency with sealing gap ratio in the unshrouded configuration.

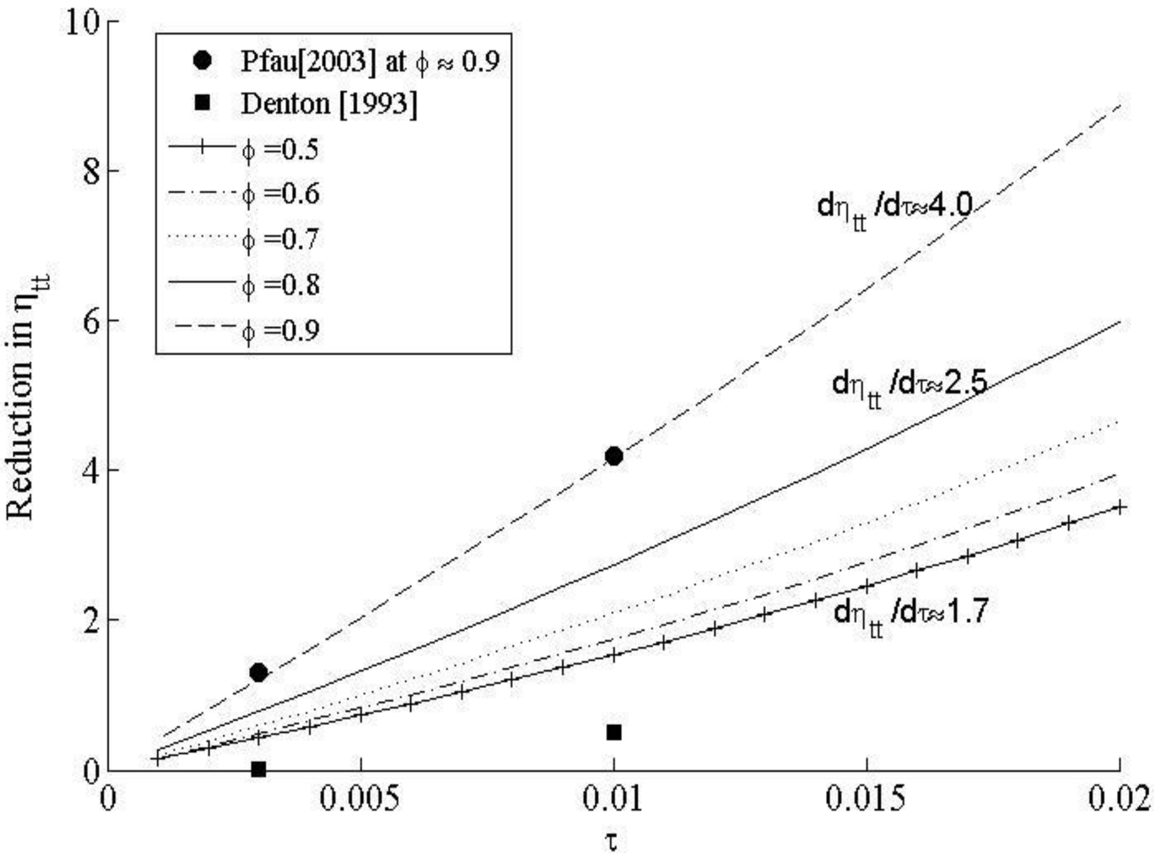

Figure 3-6. The stage total-to-total efficiency drop versus the sealing gap ratio at different flow coefficients ϕ.

The practical way to evaluate the losses associated with tip leakage flow and its interaction with the main flow is to compare the efficiency of the stage with and without tip clearance. Figure 3-7 shows the total-to-total efficiency of the 50% degree of reaction turbine stage of section 3-2 with and without tip clearance versus the flow coefficient. Figure 3-7 shows that the difference between the stage efficiency at $\tau = 0$ and at $\tau \neq 0$ increases as the flow coefficient increases, because of the increasing strength of the leakage jet. Specifically, increasing ϕ increases the conversion of potential energy, represented by the stage inlet total pressure, into the leakage jet kinetic energy. The jet is under-turned with respect to the rotor blade outlet angle, therefore it adversely affects the passage flow turning through the stator-rotor gap, reducing the stage specific work output.

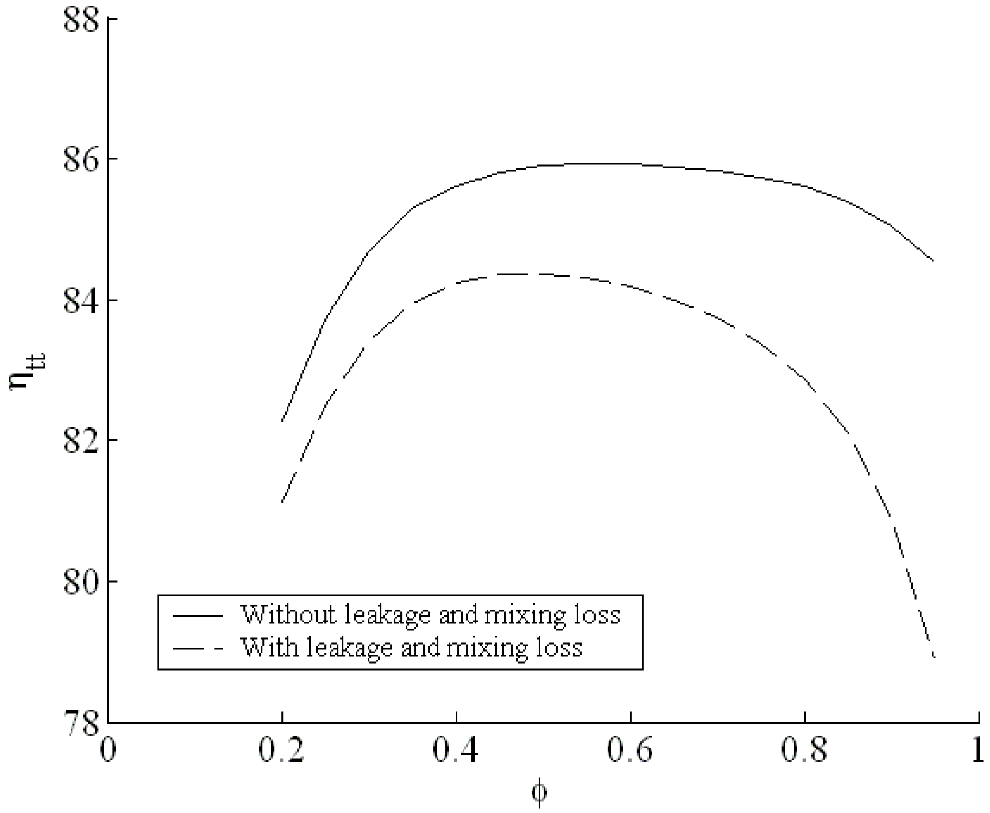

Figure 3-7. Variation of the stage total-to-total efficiency with flow coefficient.

3-3.3 Under-turning of the stage outflow

Intense tip leakage flow causes a significant change in the stage outlet flow angle. The deficit in flow turning angle due to the tip gap flow increases exponentially with increasing tip gap width. This deficit in flow turning angle has two main consequences. The first is a decrement in the tangential velocity component, which reduces the stage loading, and the other is an increment in the axial velocity component, which increases the axial mass flow. An interpretation of the latter effect can be that an increment in gap size significantly reduces the blockage of flow through the rotor blade passages, Helmers et al. [2003].

$\delta\beta_3$ is the difference between the flow relative angle before and after mixing. The change of rotor relative exit angle $\delta\beta_3$ versus the change of sealing gap ratio width is plotted in Fig. 3-8 and is compared against the results obtained by Pfau [2003]. Close to zero sealing gap ratio, the change in relative flow angle due to the leakage jet vanishes. In an unshrouded rotor, the reduction in the turning angle with tip gap clearance follows the same trend, as reported by Helmers et al. [2003]. The change in relative flow angle results in a change of incidence angle in the downstream stage. The calculation of this change, which represents the deviation of the absolute inlet flow angle from the next stator design inlet blade angle, is shown in Fig. 3-9. This figure shows that the negative incidence angle increases as the tip gap width increases. This increase is due to an increase in leakage mass flow fraction and in the strength of the leakage jet. In addition, the leakage jet has a large whirl velocity component that causes the main flow to spiral, especially if a large axial gap is available downstream of the rotor exit. Consequently, the losses caused by the leakage jet downstream of the shroud are increased.

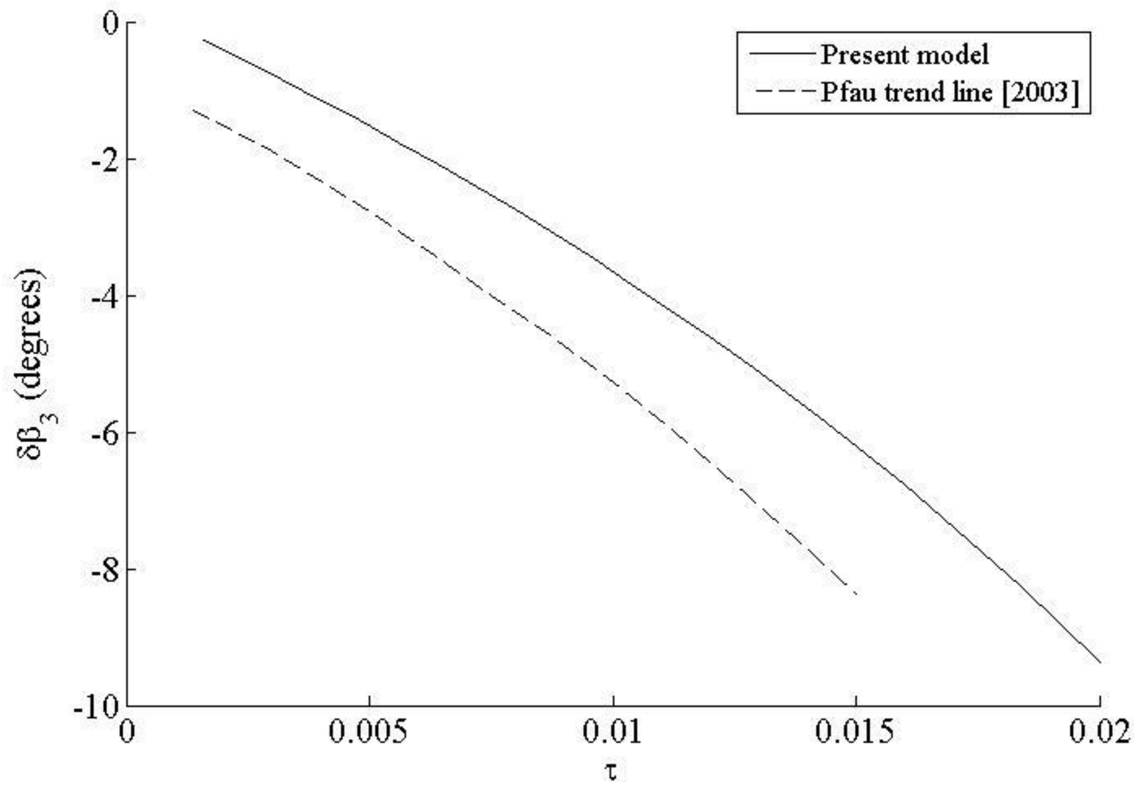

Figure 3-8. Variation of relative flow outlet angle with the sealing gap ratio.

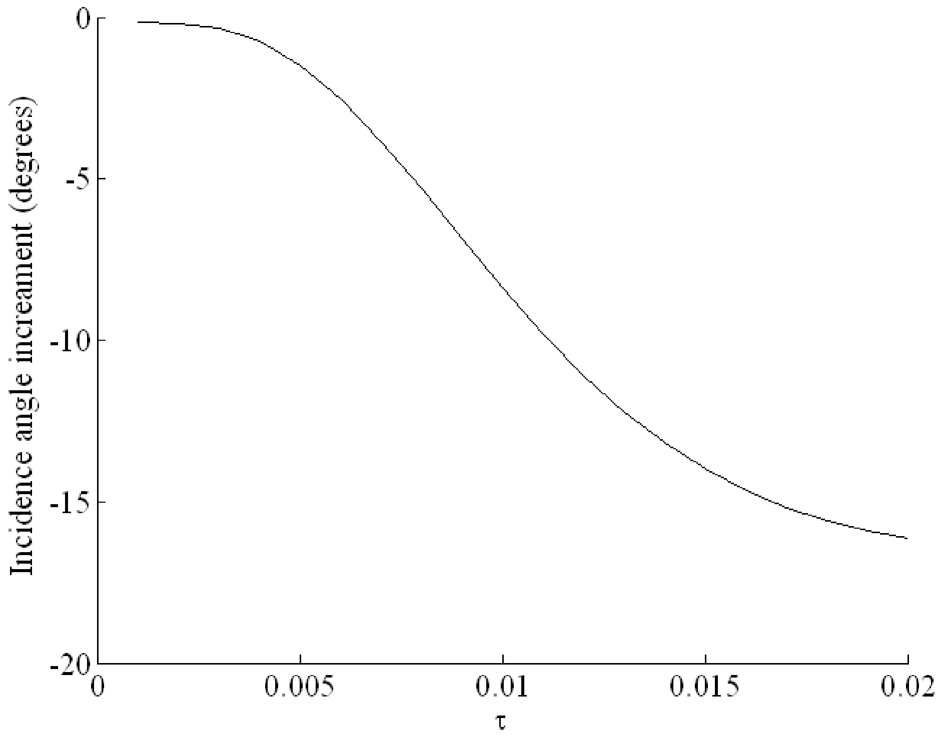

Figure 3-9. Change in incidence angle due to mixing with the sealing gap ratio.

3-3.4 Entropy Generation

Several mechanisms in turbomachines create entropy, specifically, viscous effects in boundary layers, the mixing process in free shear layers, heat transfer across finite temperature differences, throttling actions, and non-equilibrium processes, such as shock waves, Denton [1993]. Of particular interest to this part of study is the throttling action across the labyrinth seals, accompanied by flow mixing between the casing and the shroud, and the mixing process between the leakage jet and the main flow in the stator-rotor gap, as shown in Fig. 3-1. The leakage jet shortly downstream of the last labyrinth fin mixes with the cavity flow and thereafter re-enters into the main passage flow. This mixing continues through the rotor-stator gap. Most of the entropy generation during the mixing process takes place by the time the leakage jet has mixed with five times its own flow rate in the main passage, Pfau [2003]. This mixing occurs within a few jet diameters downstream of the jet injection, Denton [1993], so it affects mainly the region close to the end wall. The mass averaged tip leakage loss coefficient, due to diffusion and mixing with the cavity fluid, is

$$\left(\frac{T_4\Delta s}{0.5V_2^2}\right)_L = -T_L R\frac{\dot{m}_L}{\dot{m}_m}ln\frac{p_{oL}}{p_{o2}} \qquad (3-29)$$

The sum of the passage mixing loss coefficient, Eqn. (3-26), and the tip leakage mixing loss coefficient, Eqn. (3-29), gives the total mass averaged single stage mixing loss coefficient

$$\left(\frac{T_4\Delta s}{0.5V_2^2}\right)_{tot} = \left(\frac{T_4\Delta\dot{S}}{0.5\dot{m}_4V_2^2}\right)_{mix} + \left(\frac{T_4\Delta s}{0.5V_2^2}\right)_L \qquad (3-30)$$

The Shapiro [1953] mass averaged mixing loss coefficient, which is used for comparison purposes, is

$$\left(\frac{T_4\Delta s}{0.5V_2^2}\right) = \frac{T_4C_p}{0.5V_2^2}\frac{\dot{m}_L}{\dot{m}_m}\left[\left(1+\frac{\gamma-1}{2}M_3^2\right)\frac{T_{oL}-T_{o3}}{T_{o3}}\right.$$

$$\left. + (\gamma-1)M_3^2\left(1-\frac{V_L cos\alpha_L}{V_3}\right)\right] \qquad (3-31)$$

where M_3, T_{o3} and V_3 are the absolute Mach number, the stagnation temperature and the absolute flow velocity at the rotor trailing edge, state 3 in Fig. 3-2, T_{oL}, V_L and α_L are the leakage flow stagnation temperature, absolute velocity and tangential angle at the shroud outlet, as shown in Fig. 3-3.

Comparative predictions of the mass averaged mixing loss coefficient have been obtained from a model by Denton [1993],which assumes that the leakage flow and the main passage flow have the same temperature. This gives the rate of entropy creation as

$$\left(\frac{T_4\Delta s}{0.5V_2^2}\right) = 2\frac{\dot{m}_L}{\dot{m}_m}\left(1-\frac{V_{\theta L}}{V_{\theta 3}}sin^2\beta_3\right) \qquad (3-32)$$

where $V_{\theta L}$ and $V_{\theta 3}$ are, respectively, the tangential flow velocities at the rotor trailing edge and that at the shroud outlet.

Figure 3-10 shows the variation of the total mixing entropy coefficient with the sealing gap ratio. The solid line is the prediction from Eqn. (3-30), the symbols are mixing entropy loss coefficient values based on experimental measurements by Pfau [2003] and the dashed lines are the mixing loss coefficient predictions calculated using the models by Shapiro [1953] and by Denton [1993]. The current predictions show a closer agreement with the experimental data with respect to the other models. However, there is still a significant difference between the present predictions and the experimental results. This difference is due to the present model not accounting for some sources of loss, such as windage loss and wake mixing loss. The measurements suggest that the mixing entropy loss does not go to zero for a vanishing gap width. Such effect may be driven by unsteady cavity flow interaction, the wall skin friction inside the shroud cavity, and other viscous effects. There is therefore room for improvement in all three models to better describe the contributions to the loss coefficient that are independent of the sealing gap ratio.

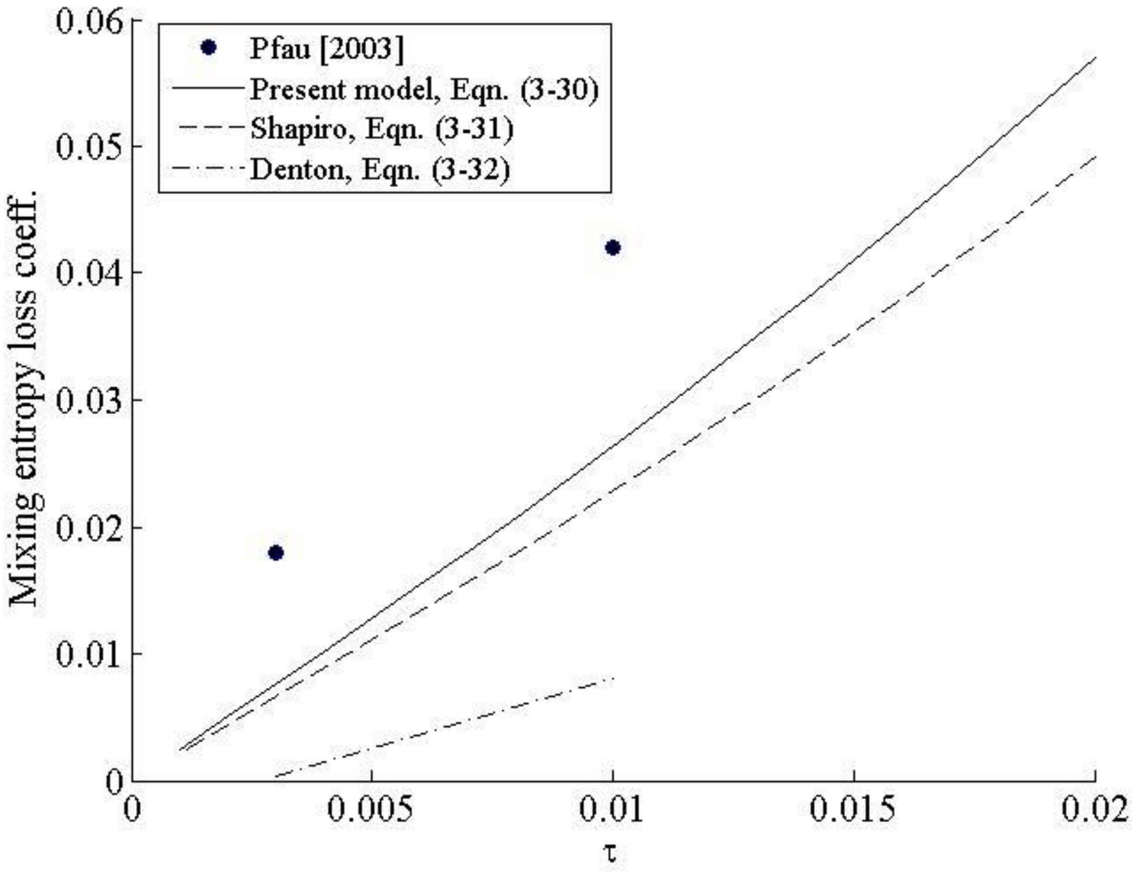

Figure 3-10. Change in the total entropy mixing loss coefficient with the sealing gap ratio.

The variation of the total entropy mixing loss coefficient against the turning angle is shown in Fig. 3-11. It appears that the total entropy mixing loss coefficient decreases as the turning angle increases and the stage loading increases. This effect will be generated in a lower degree of reaction turbine, because the lower pressure drop across the rotor reduces the mass leakage fraction. However, lowering the degree of reaction increases the total losses per unit mass flow rate, which reduces the overall stage isentropic efficiency, Denton [1993]. Although there are some analytical studies to evaluate the different sources of loss in shrouded turbine blades, none of them studied the effect of the injection angle at which the leakage flow mixes with the main flow, as shown in Fig. 3-12. In the present study, the effect of the leakage flow injection angle on the total entropy mixing loss coefficient was investigated. Figure 3-13 shows that the total entropy mixing loss coefficient increases as the injection angle increases from 0^o to 90^o. The predicted percent rise in mixing loss coefficient at increasing injection angles reaches 28%. This is a considerable value, given that the mixing loss represents about 42% of the labyrinth seal loss and about 10% of the stage loss, according to estimates by Pfau [2003]. The above percentages are not constant and depend on the stage operating conditions and the labyrinth seal geometry.

Figure 3-14 shows a comparison between the total mixing loss coefficient at injection angles 0^o and 90^o versus the tip gap ratio. The mixing loss at a given injection angle increases as the sealing gap ratio increases.

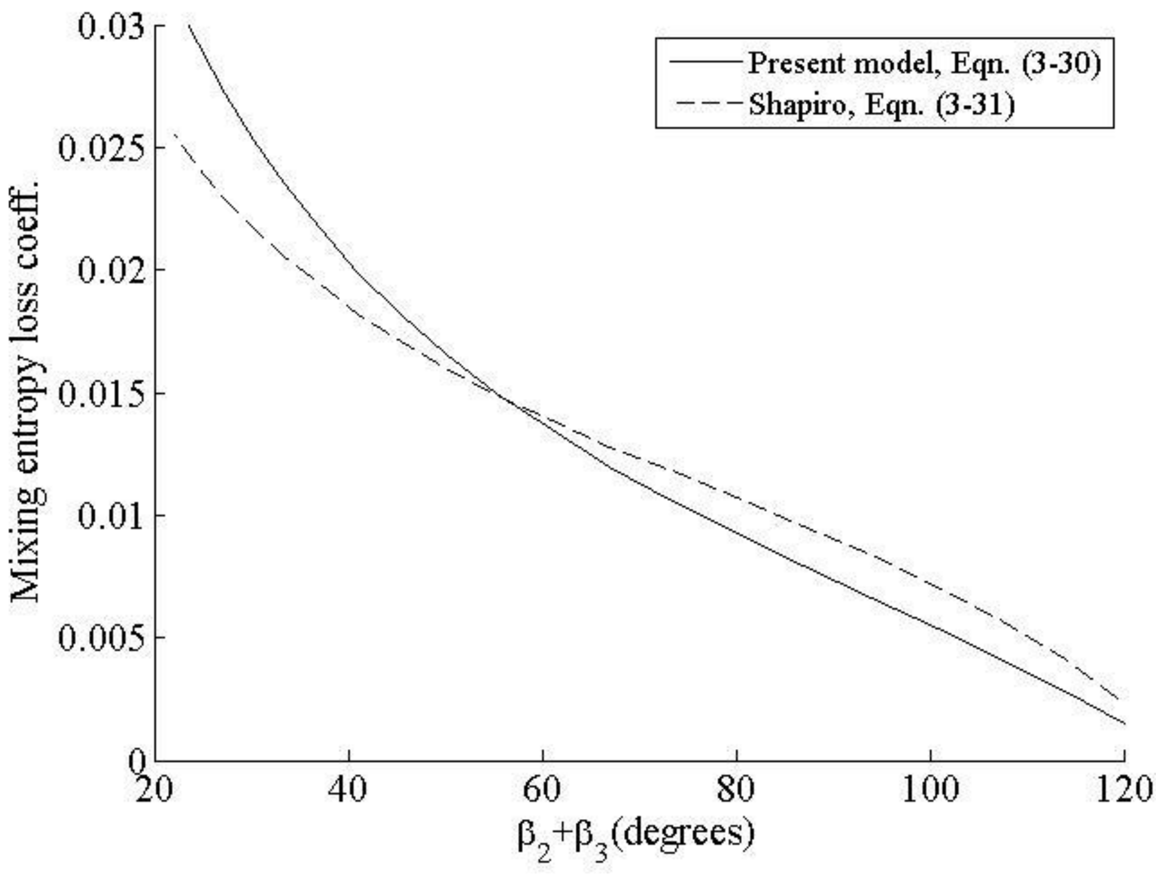

Figure 3-11. Total entropy mixing loss coefficient versus the flow turning angle through the rotor.

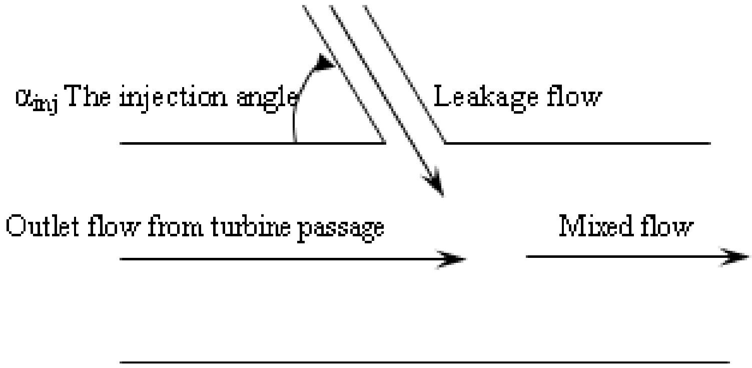

Figure 3-12. Leakage flow injection downstream of the turbine rotor. Meridional plane (x; r).

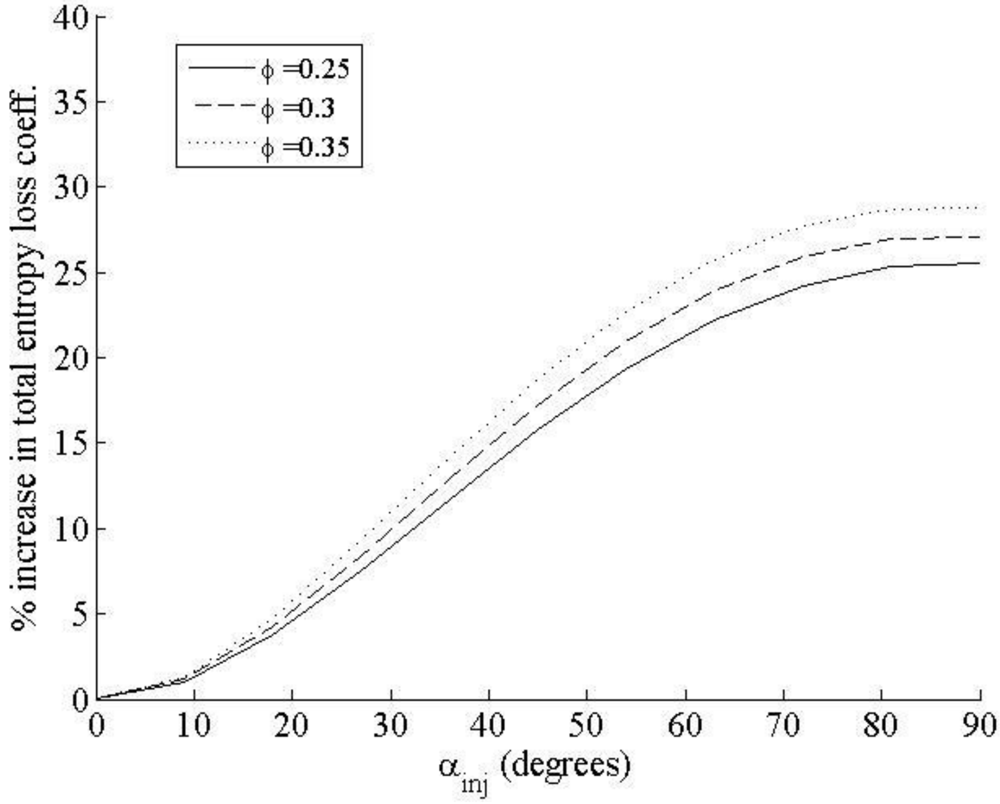

Figure 3-13. Increase in mixing loss coefficient versus leakage injection angle at different flow coefficients ϕ.

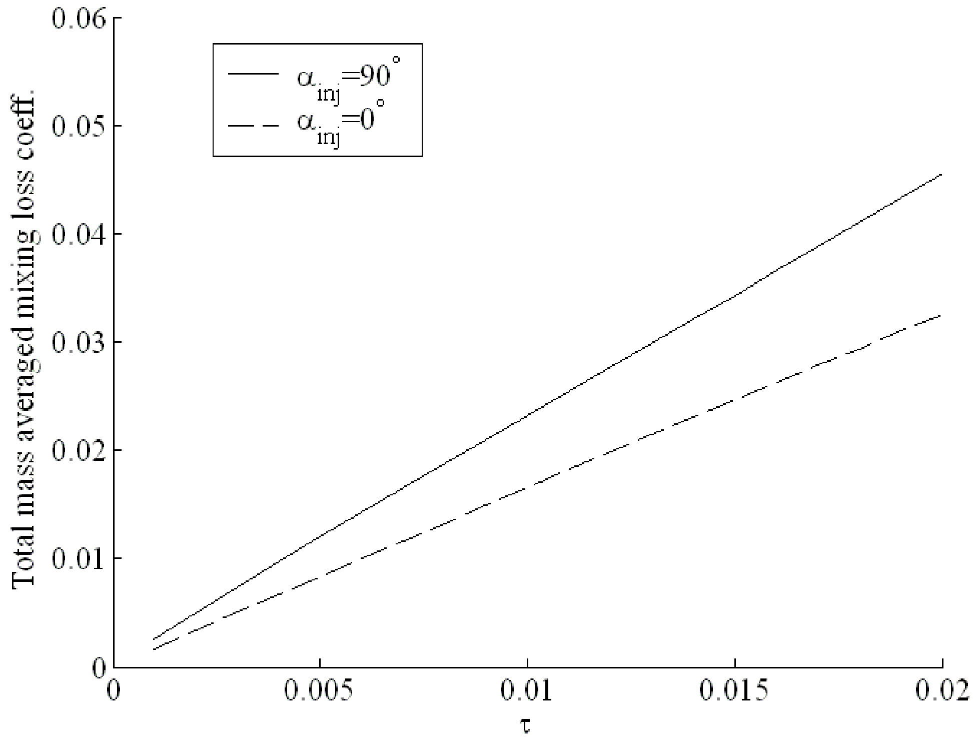

Figure 3-14. Variation of the total mass averaged mixing loss coefficient with sealing gap ratio at 0^o and 90^o injection angles.

3-4 Conclusions

Chapter 3 presented an analytical model to evaluate the effect of shroud leakage flow on turbine stage performance. The results from the present model have been compared against experimental data and benchmark analytical model predictions. The present model exhibited a good qualitative and quantitative agreement with these data. The following conclusions are drawn from the analytical model predications:

a) The mass leakage fraction, the reduction in total-to-total efficiency, and total mixing loss coefficient increase linearly as the sealing gap ratio increases.

b) The effectiveness of reducing the leakage flow by increasing the number of fins in the labyrinth seal decreases as the number of fins increases. Little benefit is seen with more than three fins.

c) The stage outflow under-turning induced by the mixing process increases as the tip gap width increases, so its adverse effect on flow field structure and on the subsequent blade row performance increases.

d) The injection angle at which the leakage flow mixes with the main stream increases the mixing entropy loss coefficient by a considerable amount, it affects the end wall loss and may increase the stage outflow unsteadiness.

The last two conclusions are going to be discussed further in chapter 6 using the numerical modelling results of the leakage flow structure and its interaction with the main passage flow.

Chapter 4

Numerical Flow solver

Computational Fluid Dynamic (CFD) is a widely used tool to predict internal and external flows. CFD enables the user to model flows with complex physics and geometries. CFD is a powerful technique to predict how a flow develops with time without using any additional equipment.

The goal of this chapter is to document the numerical scheme that was developed to obtain the three-dimensional turbomachinery flow prediction of chapter 6. The three-dimensional scheme extends the two-dimensional numerical method of Bennett [2005]. The next sections give an overview of the governing equations and numerical methods used to construct this scheme.

4-1 Governing equations

The governing equations of a continuous Newtonian fluid flow are the Navier-Stokes equations. These partial differential equations represent the conservation laws of physics, and can be used to describe all properties of a continuous flow system, Hirsch [1990].

The equation generated by applying the conservation of mass to a fluid flow is called the continuity equation. The second equation derived from applying Newton's second law is called the conservation of momentum. The last one is the conservation of energy which represents the application of the first law of thermodynamics. The unsteady compressible three dimensional Navier-Stokes equations can be written in Cartesian tensor form as follow:

$$\frac{\partial \rho}{\partial t} + \nabla \cdot (\rho \boldsymbol{u}) = 0 \qquad (4-1)$$

$$\frac{\partial}{\partial t}(\rho \boldsymbol{u}) + \nabla \cdot (\rho \boldsymbol{u} \otimes \boldsymbol{u} + p\boldsymbol{I} - \boldsymbol{\tau}) = 0 \qquad (4-2)$$

$$\frac{\partial}{\partial t}\rho(e_0 + k) + \nabla \cdot \rho \boldsymbol{u}(h_0 + k) = \nabla \cdot (-\boldsymbol{q} + \boldsymbol{\tau} \cdot \boldsymbol{u}) \qquad (4-3)$$

The variables $\boldsymbol{\tau}, e_o,\ h_0$, and $\boldsymbol{q}$ are the viscous stress tensor, the specific stagnation energy, the stagnation enthalpy, and the heat flux vector. These can be expressed in terms of the magnitude and gradient of velocity and temperature vectors as follow:

$$\boldsymbol{\tau} = \mu_l \left(\nabla \boldsymbol{u} + \boldsymbol{u} \nabla \frac{2}{3} \boldsymbol{I} \nabla \cdot \boldsymbol{u} \right) \qquad (4-4)$$

where $\mu_l$is the molecular viscosity estimated from Sutherlands law

$$\mu_l = 1.458 \times 10^{-6} \frac{T^{\frac{3}{2}}}{(T + 110.4)} \qquad (4-5)$$

$$e_o = e + \frac{\boldsymbol{u} \cdot \boldsymbol{u}}{2} = c_v T + \frac{\boldsymbol{u} \cdot \boldsymbol{u}}{2} \qquad (4-6)$$

$$h_o = e_o + \frac{p}{\rho} \qquad (4-7)$$

$$\boldsymbol{q} = -\frac{c_p \mu_l}{P_r} \nabla T \qquad (4-8)$$

where c_p, c_v, and P_r are the gas constant pressure specific heat, constant volume specific heat, and Prandtl number respectively. To complete a closed set of equations, the static pressure is estimated, assuming a calorically perfect gas, as follow:

$$p = \rho R T \qquad (4-9)$$

where R is the gas constant

$$R = c_p - c_v \qquad (4-10)$$

From equations (4-6) and (4-9) the pressure can be related to the total energy and velocity as follow:

$$p = (\gamma - 1\,)\rho \left[e_o - \frac{\boldsymbol{u} \cdot \boldsymbol{u}}{2} \right] \qquad (4-11)$$

4-1.1 Averaging Navier-Stokes equations

In case of laminar flow, the governing equations are closed by specifying the algebraic relations for the viscosity and the heat conductivity coefficient as functions of pressure and temperature. Therefore, the final solution is strongly dependent on the accuracy of these empirical relations.

In case of turbulent flow, most CFD codes do not solve the instantaneous equations directly due to limitations in RAM capacity and processor time. So, the flow variables, varying with time, are divided into mean and fluctuating components. The principle of this technique is called Reynolds-averaging and applies to a given vector variable as follow:

$$\boldsymbol{u} = \overline{\boldsymbol{u}} + \boldsymbol{u}' \qquad (4-12)$$

The mean component $\overline{\boldsymbol{u}}$ is defined to be

$$\overline{\boldsymbol{u}} = \frac{1}{\Delta t}\int_{(n-1)\Delta t}^{n\Delta t} \boldsymbol{u}(x, y, z, t)dt \qquad (4-13)$$

where n and Δt are the time level in the CFD computation and the time interval chosen long enough with respect to the fluctuations of the turbulent flow and short compared to the time of variations not related to turbulence. By applying this technique to Navier-Stokes equations, the short-time Reynolds averaged Navier-Stokes equations can be written as follow, Bennett [2005]:

$$\frac{\partial \bar{\rho}}{\partial t} + \nabla \cdot (\bar{\rho}\overline{\boldsymbol{u}}) = 0 \qquad (4-14)$$

$$\frac{\partial}{\partial t}(\bar{\rho}\overline{\boldsymbol{u}}) + \nabla \cdot (\bar{\rho}\overline{\boldsymbol{u}}\otimes\overline{\boldsymbol{u}} + \bar{p}\boldsymbol{I} - \overline{\boldsymbol{\tau}} + \bar{\rho}\overline{\boldsymbol{u}'\otimes\boldsymbol{u}'}) = 0 \qquad (4-15)$$

$$\frac{\partial}{\partial t}\bar{\rho}\left(\bar{e}_0 + \bar{k}\right) + \nabla \cdot \bar{\rho}\overline{\boldsymbol{u}}\left(\bar{h}_0 + \bar{k}\right) = \nabla \cdot \left(-\overline{\boldsymbol{q}} - \rho\overline{\boldsymbol{u}'h'} + \overline{\boldsymbol{\tau}} \cdot \overline{\boldsymbol{u}} - \bar{\rho}\overline{\boldsymbol{u}'\otimes\boldsymbol{u}'} \cdot \overline{\boldsymbol{u}}\right) \quad (4-16)$$

The short-time averaged turbulence kinetic energy, $\bar{k}$, and the turbulent pressure, p_t, are defined as:

$$\bar{k} = \frac{1}{2}\overline{\boldsymbol{u}' \cdot \boldsymbol{u}'} \qquad (4-17)$$

$$p_t = p + \frac{2}{3}\bar{\rho}\bar{k} \qquad (4-18)$$

The form of the continuity equation has not changed after averaging, but the momentum equation has an additional term $-\bar{\rho}\overline{\boldsymbol{u}'\otimes\boldsymbol{u}'}$ which is the Reynolds stress tensor $\overline{\boldsymbol{\tau}}_{\boldsymbol{r}}$. This term represents the influence of turbulence on the momentum equations, and depends on the unknown fluctuating velocity components. Therefore, the short-time Reynolds averaged Navier-Stokes equations with equation of state become an open set of equations, and it is necessary to develop a turbulence closure model. The purpose of this model is to replace the Reynolds stress $\overline{\boldsymbol{\tau}}_{\boldsymbol{r}}$ with an equation related to the mean flow variable components. Using Boussinesq relationship, the Reynolds stress $\overline{\boldsymbol{\tau}}_{\boldsymbol{r}}$ can be written by analogy with viscous stress as:

$$\overline{\boldsymbol{\tau}}_{\boldsymbol{r}} = -\bar{\rho}\overline{\boldsymbol{u}'\otimes\boldsymbol{u}'} = \mu_t\left(\nabla\overline{\boldsymbol{u}} + \overline{\boldsymbol{u}}\nabla\frac{2}{3}\boldsymbol{I}\nabla \cdot \overline{\boldsymbol{u}}\right) - \frac{2}{3}\boldsymbol{I}\bar{\rho}\bar{k} \qquad (4-19)$$

where μ_t is the eddy viscosity estimated from a turbulence model.

Short-time Reynolds averaging introduces a new term in energy equation due to the influence of turbulence, which is the turbulent heat flux $-\rho\overline{\boldsymbol{u}'h'}$. The turbulent enthalpy, transport by turbulent motion $-\rho\overline{\boldsymbol{u}'h'}$ is modelled as being proportional to the short-time averaged temperature gradient, Wilcox [1993]. In the short-time Reynolds averaged Navier-Stokes equation, the turbulent heat flux, $\boldsymbol{q}_t$, is modelled by:

$$-\rho\overline{\boldsymbol{u}'h'} = \boldsymbol{q}_t = -\frac{\mu_t c_p}{Pr_t}\nabla T \tag{4-20}$$

where Pr_t is the turbulent Prandtl number $Pr_t = \frac{\mu_t c_p}{k_t}$ and k_t is the thermal eddy conductivity.

4-1.2 $\boldsymbol{k-\omega}$ Turbulence models

Subsection 4-1.1 showed that the Reynolds averaged Navier-stokes equations contain unknown variables such as $-\rho\overline{\boldsymbol{u}'h'}$ as a consequence of averaging. Therefore, additional mathematical relations are needed to close the system of mean flow equations (4-14 to 4-16) with the equation of state. The mathematical relations can be algebraic, such as the Baldwin and Lomax model, or differential, such as the $k-\omega$ or $k-\varepsilon$ models.

In this flow solver, the $k-\omega$ model of Wilcox [2002] is used as the main turbulence closure model. A brief description of this turbulence model is given in this section. The Wilcox $k-\omega$ turbulence model was originally formulated by Wilcox [1993] for the Reynolds averaged Navier-Stokes equations, in which the flow averaged variables $\overline{\boldsymbol{u}}$ of Equation (4-12) are constant in time and $\Delta t \to \infty$ in Equation (4-13). This model has since been applied to the short-time averaged Navier-Stokes equations to model time dependent flows characterized by large-scale coherent instabilities embedded in a background flow of small scale random turbulence. These applications show that it is possible to apply the Wilcox [1993] $k-\omega$ turbulence closure to the short-time Reynolds averaged Navier-\stokes equations, provided the time scale of the resolved motion is much greater than that associated with the fluctuations in the small scale turbulence. This is the driving principle for selecting Δt in Equation (4-13).

In addition to the $k-\omega$ model, an unconventional turbulence model using the hybrid RANS/LES technique is added to enhance the prediction of complex flows. The details of this numerical approach are described later in section 4-7.

The derivation of the turbulent kinetic energy transport equation starts by replacing the scalar product of the Navier-Stokes momentum equations with the fluctuating component of the velocity vector $\boldsymbol{u}'$. By Reynolds averaging the result and rearranging the notation, the turbulent kinetic energy transport equation is obtained.

$$\frac{\partial}{\partial t}\left(\bar{\rho}\overline{k}\right) + \nabla \cdot \left(\bar{\rho}\overline{\boldsymbol{u}}\overline{k}\right) =$$
$$\overline{\boldsymbol{\tau}_{\boldsymbol{r}}} : \nabla\overline{\boldsymbol{u}} - \overline{\boldsymbol{\tau}' : \nabla\boldsymbol{u}'} + \overline{p'\nabla \cdot \boldsymbol{u}'} + \overline{\boldsymbol{u}}'\nabla\bar{p} + \nabla \cdot \left(\overline{\boldsymbol{\tau}' \cdot \boldsymbol{u}'} - \overline{p'\boldsymbol{u}'} - \bar{\rho}\overline{\boldsymbol{u}'\otimes\boldsymbol{u}'.\boldsymbol{u}'/\boldsymbol{2}}\right)$$
$$(4-21)$$

The turbulent kinetic energy consists of the following terms from left to right:

1) The unsteady term 2) The convection term 3) Production
4) Dissipation 5) Pressure dilatation 6) Pressure work
7) Molecular diffusion 8) Pressure diffusion 9) Turbulent transport

The first two terms i.e., the unsteady and the convective terms are the derivatives of the turbulent kinetic energy fluctuation that are treated like other Eulerian derivatives. Terms 1 and 2 can be rearranged by the use of the continuity equation into the material transport of turbulent kinetic energy $D\left(\bar{\rho}\overline{k}\right)/Dt$, with $\overline{\boldsymbol{u}}$ being the transport velocity in the material operator D. Some terms represent additional unknowns and must be modelled. Following the analysis of Wilcox [2002], the dissipation term $\overline{\boldsymbol{\tau}' : \nabla\boldsymbol{u}'}$, which represents the viscous dissipation of turbulence shear stresses, can be written in terms of the averaged dissipation per unit mass, $\bar{\varepsilon}$, as follow: $\overline{\boldsymbol{\tau}' : \nabla\boldsymbol{u}'} = \bar{\rho}\bar{\varepsilon}$. The specific dissipation is modelled as:

$$\bar{\varepsilon} = \nu\overline{\frac{\partial u_i'}{\partial x_j}\frac{\partial u_i'}{\partial x_j}} \qquad (4-22)$$

Wilcox (1994) related the specific dissipation to the dissipation per unit turbulence kinetic energy, $\overline{\omega}$, by the following form:

$$\overline{\boldsymbol{\tau}' : \nabla\boldsymbol{u}'} = \bar{\rho}\bar{\varepsilon} = \bar{\rho}\beta^*\overline{k}\overline{\omega} \qquad (4-23)$$

Equation (4-23) models the term 4 in Equation (4-21). Unfortunately, there is no straightforward analogy for the pressure diffusion term, term 8 in Equation (4-21). So, the pressure diffusion and turbulent transport terms, terms 8 and 9 in Equation (4-21), are grouped together and assumed to behave as a gradient-transport process, from Wilcox [2002]. A recent Direct Numerical simulation shows that the term is quite small as stated by Wilcox. Thus, the pressure diffusion and turbulent transport are modelled as:

$$\overline{p'\boldsymbol{u}'} - \bar{\rho}\overline{\boldsymbol{u}'\otimes\boldsymbol{u}'.\boldsymbol{u}'/\boldsymbol{2}} = \sigma^*\mu_t\nabla\overline{k} \qquad (4-24)$$

where σ^*, and μ_t are the model closure coefficient and the eddy viscosity respectively.

The molecular diffusion term represents the mixing and transport of energy by natural fluid molecular motion, and is related to the spatial gradient of the turbulent kinetic energy as:

$$\overline{\boldsymbol{\tau}' \cdot \boldsymbol{u}'} = \mu_l \nabla \bar{k} \qquad (4-25)$$

The Pressure work is omitted because of the definition of $\overline{\boldsymbol{u}}' = 0$, while the Pressure dilatation term is dropped because of the lack of a widely accepted model for this term, Wilcox [2002]. Also, the Mach number in this study is below the hypersonic range which gives the possibility to neglect the pressure dilatation, Wilcox [2002].

The dissipation term in turbulent kinetic energy equation is modelled as a function of the dissipation per unit turbulence kinetic energy, ω, which is an additional unknown in the Reynolds averaged Navier-Stokes equations. Therefore, another partial differential equation similar to the turbulent kinetic energy equation must be derived to find ω. The derivation of the transport equation for the specific dissipation rate is similar to the derivation of the turbulent kinetic energy transport equation. It starts with spatial gradient $\frac{\partial}{\partial x_j}$ of the Navier-Stokes momentum equation with $2\nu \frac{\partial u_i'}{\partial x_j}$, more details are available in McKeel [1996].

The complete set of partial differential equations, which consists of Reynolds averaged Navier-Stokes equations and $k-\omega$ turbulence model, can be written as:

$$\frac{\partial \bar{\rho}}{\partial t} + \nabla \cdot (\bar{\rho}\overline{\boldsymbol{u}}) = 0 \qquad (4-26)$$

$$\frac{\partial}{\partial t}(\bar{\rho}\overline{\boldsymbol{u}}) + \nabla \cdot (\bar{\rho}\overline{\boldsymbol{u}} \otimes \overline{\boldsymbol{u}} + \bar{p}\boldsymbol{I}) = \nabla \cdot (\overline{\boldsymbol{\tau}} + \overline{\boldsymbol{\tau}}_{\boldsymbol{r}}) \qquad (4-27)$$

$$\frac{\partial}{\partial t}\bar{\rho}\left(\bar{e}_0 + \bar{k}\right) + \nabla \cdot \bar{\rho}\overline{\boldsymbol{u}}\left(\bar{h}_0 + \bar{k}\right)$$
$$= \nabla \cdot \left[-(\overline{\boldsymbol{q}} + \overline{\boldsymbol{q}}_{\boldsymbol{t}}) + (\overline{\boldsymbol{\tau}} + \overline{\boldsymbol{\tau}}_{\boldsymbol{r}}) \cdot \overline{\boldsymbol{u}} + (\mu_l + \sigma^* \mu_t)\nabla \bar{k}\right] \qquad (4-28)$$

$$\frac{\partial}{\partial t}\left(\bar{\rho}\bar{k}\right) + \nabla \cdot \left(\bar{\rho}\overline{\boldsymbol{u}}\bar{k}\right) =$$
$$\overline{\boldsymbol{\tau}}_{\boldsymbol{r}} : \nabla \overline{\boldsymbol{u}} - \beta^* \bar{\rho}\bar{k}\bar{\omega} + \nabla \cdot \left[(\mu_l + \sigma^* \mu_t)\nabla \bar{k}\right] \qquad (4-29)$$

$$\frac{\partial}{\partial t}(\bar{\rho}\bar{\omega}) + \nabla \cdot (\bar{\rho}\overline{\boldsymbol{u}}\bar{\omega}) =$$
$$\frac{\varphi \bar{\omega}}{\bar{k}} \overline{\boldsymbol{\tau}}_{\boldsymbol{r}} : \nabla \overline{\boldsymbol{u}} - \beta \bar{\rho}\bar{\omega}^2 + \nabla \cdot [(\mu_l + \sigma \mu_t)\nabla \bar{\omega}] \qquad (4-30)$$

The following closure coefficients, cross diffusion modification, compressibility correction and auxiliary relations of Wilcox $k-\omega$ model, Wilcox [2000] are defined as follows:

$$\varphi = \frac{13}{25}\,, \qquad \sigma = \frac{1}{2}\,, \qquad \sigma^* = \frac{1}{2} \qquad (4-31)$$

$$\mu_t = \frac{\bar{\rho}\bar{k}}{\bar{\omega}} \qquad (4-32)$$

$$\beta^* = \beta_o^* f_{\beta^*}[1 + \xi^* F(M_t)] \qquad (4-33)$$

$$\beta = \beta_o - \beta_o^* f_{\beta^*} \xi^* F(M_t) \qquad (4-34)$$

$$\beta_o^* = \frac{9}{100}, \beta_o = \frac{9}{125}, \xi^* = \frac{3}{2} \qquad (4-35)$$

$$f_{\beta^*} = \begin{cases} 1 & \forall \chi_k \le 0 \\ (1 + 680{\chi_k}^2)/(1 + 400{\chi_k}^2) & \forall \chi_k > 0 \end{cases} \qquad (4-36)$$

$$\chi_k = \frac{1}{\bar{\omega}^3} \nabla\bar{k}\nabla\bar{\omega} \qquad (4-37)$$

$$F(M_t) = \left[{M_t}^2 - {M_{t_o}}^2\right] H\left(M_t - M_{t_o}\right) \qquad (4-38)$$

$$M_{t_o} = \frac{1}{4} \qquad (4-39)$$

$$M_t = \frac{2\bar{k}}{a^2} \qquad (4-40)$$

where $H\left(M_t - M_{t_o}\right)$ is the Heaviside step function defined as follow: the function value is zero for $M_t < M_{t_o}$, and is 1 for $M_t \ge M_{t_o}$. a is the speed of sound

The system of partial differential equations for the conservation of mass, momentum, and energy, along with the partial differential equations for the transport of turbulent kinetic energy and specific dissipation rate, can be written in the following compact form:

$$\frac{\partial \mathbf{U}}{\partial t} + \nabla \cdot [\boldsymbol{F}_{\mathbf{c}}(\mathbf{U}) + \mathbf{F}_{\mathbf{t}}(\mathbf{U})] = \mathbf{S} \qquad (4-41)$$

where $\mathbf{U}$ is the vector of conservative variables

$$\mathbf{U} = \begin{bmatrix} \bar{\rho} \\ \bar{\rho}\,\bar{\boldsymbol{u}} \\ \bar{\rho}\left(\bar{e}_o + \bar{k}\right) \\ \bar{\rho}\bar{k} \\ \bar{\rho}\,\bar{\omega} \end{bmatrix} \qquad (4-42)$$

$\boldsymbol{F}_{\mathbf{c}}$ is the inviscid flux vector

$$\boldsymbol{F_c} = \begin{bmatrix} \bar{\rho}\,\bar{\boldsymbol{u}} \\ \bar{\rho}\,\bar{\boldsymbol{u}}\otimes\bar{\boldsymbol{u}} + \bar{p}\boldsymbol{I} \\ \bar{\rho}\,\bar{\boldsymbol{u}}\left(\bar{h}_o + \bar{k}\right) \\ \bar{\rho}\bar{\boldsymbol{u}}\bar{k} \\ \bar{\rho}\,\bar{\boldsymbol{u}}\,\bar{\omega} \end{bmatrix} \qquad (4-43)$$

$\mathbf{F_t}$ is the viscous flux vector

$$\mathbf{F_t} = \begin{bmatrix} 0 \\ -(\bar{\boldsymbol{\tau}} + \bar{\boldsymbol{\tau}}_{\boldsymbol{r}}) \\ \bar{\boldsymbol{q}} + \bar{\boldsymbol{q}}_t - (\bar{\boldsymbol{\tau}} + \bar{\boldsymbol{\tau}}_{\boldsymbol{r}})\cdot\bar{\boldsymbol{u}} - (\mu_l + \sigma^*\mu_t)\nabla\bar{k} \\ -(\mu_l + \sigma^*\mu_t)\nabla\bar{k} \\ -(\mu_l + \sigma\mu_t)\nabla\bar{\omega} \end{bmatrix} \qquad (4-44)$$

and $\mathbf{S}$ is the source term, defined by:

$$\mathbf{S} = \begin{bmatrix} 0 \\ 0 \\ 0 \\ s_k \\ s_\omega \end{bmatrix} = \begin{bmatrix} 0 \\ 0 \\ 0 \\ \bar{\boldsymbol{\tau}}_{\boldsymbol{r}} : \nabla\bar{\boldsymbol{u}} - \beta^*\bar{\rho}\bar{k}\bar{\omega} \\ \frac{\varphi\bar{\omega}}{\bar{k}}\bar{\boldsymbol{\tau}}_{\boldsymbol{r}} : \nabla\bar{\boldsymbol{u}} - \beta\bar{\rho}\bar{\omega}^2 \end{bmatrix} \qquad (4-45)$$

For simplicity, the over line to indicate cell averaged values will be omitted in the next sections, also $\boldsymbol{\tau}$ will indicate the total shear stresses (viscous and turbulent stresses).

4-2 Space discretization

The governing equation (4-41) is discretized on a structured non-orthogonal multi-block boundary fitted mesh. There are several available techniques to discretize the governing equations, such as finite difference methods, finite element methods, and finite volume methods. The finite volume discretization method is used in this work for its ability to handle near discontinuous flow features, such as shock waves. The integration of the governing equations (4-41) over a control volume V gives:

$$\int_V \frac{\partial\mathbf{U}}{\partial t}dV + \int_V \nabla\cdot[\mathbf{F_c} + \mathbf{F_t}]\,dV = \int_V \mathbf{S}\,dV \qquad (4-46)$$

By using the Gauss divergence theorem making the assumption that the control volume V is time invariant to bring the time derivative outside the first term, the equation (4-46) can be rewritten as:

$$\frac{\partial}{\partial t}\int_V \mathbf{U}dV + \oint_S \mathbf{F_c}\cdot\boldsymbol{n}dS + \oint_S \mathbf{F_t}\cdot\boldsymbol{n}dS = \int_V \mathbf{S}\,dV \qquad (4-47)$$

where $\boldsymbol{n}$ is the inward normal unit vector to the closed surface S bounding the control volume V. The circular integral $\oint$ in equation (4-47) is taken anticlockwise positive.

$$\mathbf{U}_i = \frac{1}{V_i}\int_V \mathbf{U} dV \qquad (4-48)$$

$$\mathbf{F_c}(\mathbf{U}_{\boldsymbol{n}}) = \mathbf{F_c}\cdot\boldsymbol{n} = \begin{bmatrix} \rho\,\boldsymbol{u}\cdot\boldsymbol{n} \\ \rho\,\boldsymbol{u}\otimes\boldsymbol{u}\cdot\boldsymbol{n} + p\boldsymbol{I}\cdot\boldsymbol{n} \\ \rho\,\boldsymbol{u}\,(h_0 + k)\cdot\boldsymbol{n} \\ \rho\,\boldsymbol{u}k\cdot\boldsymbol{n} \\ \rho\,\boldsymbol{u}\,\omega\cdot\boldsymbol{n} \end{bmatrix} \qquad (4-49)$$

$$\mathbf{F_t}(\mathbf{U}_{\boldsymbol{n}}) = \mathbf{F_t}\cdot\boldsymbol{n} = \begin{bmatrix} 0 \\ -\boldsymbol{\tau}\cdot\boldsymbol{n} \\ (\boldsymbol{q} - \boldsymbol{\tau}\cdot\boldsymbol{u})\cdot\boldsymbol{n} - (\mu_l + \sigma^*\mu_t)\nabla k\cdot\boldsymbol{n} \\ -(\mu_l + \sigma^*\mu_t)\nabla k\cdot\boldsymbol{n} \\ -(\mu_l + \sigma\mu_t)\nabla\omega\cdot\boldsymbol{n} \end{bmatrix} \qquad (4-50)$$

where $\mathbf{F_c}$ and $\mathbf{F_t}$ are the convective fluxes and the diffusive fluxes respectively. The normal velocity to the surface $\mathbf{U}_{\boldsymbol{n}}$ is defined as:

$$\mathbf{U}_{\boldsymbol{n}} = \begin{bmatrix} \rho \\ \rho\,u_n \\ \rho\,u_{t1} \\ \rho\,u_{t2} \\ \rho\ \ (e_0 + k) \\ \rho\,k \\ \rho\ \ \omega \end{bmatrix} \qquad (4-51)$$

where u_n, u_{t1}, u_{t2} are the normal, tangential, and binormal velocity components on the closed surface of the control volume given later by equation (4-63). Let the physical space in which the flow develops be divided into an assembly of control volumes and let V_i be the i^{th} control volume in this assembly. The convective and diffusive flux integrations can be considered as the summation of the contributions over all discrete faces, N_f, bounding the computational control volume V_i.

$$\oint_S \mathbf{F_c}\cdot\boldsymbol{n}\,dS = \sum_{k=1}^{N_f}(\mathbf{F_c}_k S_k)_i \qquad (4-52)$$

$$\oint_S \mathbf{F_t}\cdot\boldsymbol{n}\,dS = \sum_{k=1}^{N_f}(\mathbf{F_t}_k S_k)_i \qquad (4-53)$$

$$\mathbf{S}_i = \frac{1}{V_i}\int_{V_i} \mathbf{S}\,dV \qquad (2-54)$$

Substituting (4-48), (4-52), (4-51), and (4-52) in (4-46), the discretized short-time Reynolds averaged Navier-Stokes equations are obtained as:

$$V_i \frac{d}{dt}\mathbf{U}_i + \sum_{k=1}^{N_f} (\mathbf{F_c}_k S_k)_i + \sum_{k=1}^{N_f} (\mathbf{F_t}_k S_k)_i = V_i \mathbf{S}_i \qquad (4-55)$$

The interpretation of equation (4-55) states that the rate of change of the volume averaged conservative variable $\mathbf{U}_i$ in the i^{th} control volume is equal to the summation of the area averaged convective and diffusive fluxes through the discrete boundary faces, k, plus the source term. Equation (4-55) shows that the spatial discretization and time integration are independent and this represents one of the advantages of the finite volume method. In the following sections, the numerical method to solve equation (4-55) is presented. Firstly, the convective flux is evaluated, then diffusive flux and source term are computed, and last the conservative variables are integrated in time.

4-3 Calculation of Inviscid fluxes

An upwind numerical method is used to determine the interface fluxes according to the direction of the propagation of the information on that mesh. Basically, there are two techniques to identify the upwind directions, the Flux Vector Splitting [FVS] technique, and the Flux Difference Splitting [FDS] technique or Godunov method. The merits and demerits of the Flux Vector Splitting [FVS] technique compared with the Flux Difference Splitting [FDS] technique are discussed in Toro [1999] and are:

- FVS requires less effort needed to achieve the upwind direction than FDS technique.
- FVS is simpler, popular, and well suited for implicit methods.
- The resolution of flow discontinuities by FVS is poor compared with FDS, particularly for stationary contact and shear waves.
- FVS results, when applied to the Navier-Stokes equations, are less accurate than FDS, as reported by van Leer, Thomas, and Roe.

More details of both upwind techniques can be found in Hirsch [1990] and Toro [1999].

4-3.1 Roe's Approximate Riemann Solver

In this study, the FDS approach is used. The FDS calculates the fluxes at cells interface by determining an approximate solution to a Riemann problem. The scheme is built based on Roe's approximate Riemann solver which is a popular approximate Riemann solver among the CFD community. Roe's scheme provides a method of calculating the convective fluxes across a face of a control volume using the eigensystem of a Jacobian matrix, **A**. Since the Reynolds averaged Navier-Stokes equations are nonlinear, and Roe's scheme is based on a linear one dimensional formulation, the equations are linearized through the Jacobian matrix, **A**. For a multi-dimensional problem, the convective fluxes are calculated in each independent spatial direction using the 1-D method, solving the Riemann problem across each cell interface along the interface normal direction $\boldsymbol{n}$. Referring to equation (4-41), the Jacobian matrix can be defined as follows:

$$\mathbf{A(U)} = \frac{\partial \mathbf{F_c(U)}}{\partial \mathbf{U}} . \boldsymbol{n} \qquad (4-56)$$

Let $\mathbf{U_L}$ and $\mathbf{U_R}$ be the conservative variables vectors (i.e. the flow states) to the left and to the right of any cell interface $S_{k,i}$. Roe's approximate Riemann solver replaces the Jacobian matrix $\mathbf{A(U)}$ by a constant matrix $\widehat{\mathbf{A}}(\mathbf{U_L}, \mathbf{U_R})$ that satisfies the following properties:

- The matrix $\widehat{\mathbf{A}}(\mathbf{U_L}, \mathbf{U_R})$ maintains the hyperbolicity nature of the system, and has real eigenvalues and a complete set of eigenvectors.
- The matrix $\widehat{\mathbf{A}}(\mathbf{U_L}, \mathbf{U_R})$ is consistent with the exact Jacobian, **A** (i.e. as $\mathbf{U_L} \rightarrow \mathbf{U_R} \rightarrow \mathbf{U}$, then, $\widehat{\mathbf{A}}(\mathbf{U_L}, \mathbf{U_R}) \rightarrow \mathbf{A}$)
- For any $\mathbf{U_L}$ and $\mathbf{U_R}$ $\mathbf{F(U_L)} - \mathbf{F(U_R)} = \widehat{\mathbf{A}}(\mathbf{U_L} - \mathbf{U_R})$ (i.e. the conservation is maintained)

Let eigenvectors of $\widehat{\mathbf{A}}(\mathbf{U_L}, \mathbf{U_R})$ be $\hat{e}_k$ and the corresponding eigenvalues be $\hat{\lambda}_k$. By projecting the difference in the flow states onto the eigenvectors, the following equations can be written.

$$\mathbf{U_R} - \mathbf{U_L} = \sum_k \hat{\alpha}_k \hat{e}_k \qquad (4-57)$$

$$\mathbf{F_R} - \mathbf{F_L} = \sum_k \hat{\alpha}_k \hat{\lambda}_k \hat{e}_k \qquad (4-58)$$

where $\hat{\alpha}_k$is the wave strength of the k^{th} wave of wave shape $\hat{e}_k$ and characteristic speed $\hat{\lambda}_k$. By considering the interface between two cells at $i + \frac{1}{2}$ as shown in fig. 4-1, the fluxes at the interface are computed by the summation over the negative and positive wave speed starting from either the right or the left flow state.

$$\mathbf{F}_{i+\frac{1}{2}} = \mathbf{F}_{\mathrm{R}} - \sum_{k}^{\hat{\lambda}_k \geq 0} \hat{\alpha}_k \hat{\lambda}_k \hat{e}_k \qquad (4-59)$$

$$\mathbf{F}_{i+\frac{1}{2}} = \mathbf{F}_{\mathrm{L}} + \sum_{k}^{\hat{\lambda}_k \leq 0} \hat{\alpha}_k \hat{\lambda}_k \hat{e}_k \qquad (4-60)$$

By taking the arithmetic mean of equations (4-59) and (4-60), a first order estimate of the interface fluxes is obtained as

$$\mathbf{F}_{i+\frac{1}{2}} = \frac{1}{2}(\mathbf{F}_{\mathrm{L}} + \mathbf{F}_{\mathrm{R}}) - \sum_{k=1}^{m} \hat{\alpha}_k \left|\hat{\lambda}_k\right| \hat{e}_k \qquad (4-61)$$

where m is the number of the eigenvalues of $\widehat{\mathbf{A}}$ which equals the rank of this square matrix. The Riemann problem at any cell interface $S_{k,i}$ will be solved in the interface normal direction, see fig. 4-1. The unit vectors are denoted by $\boldsymbol{n}$,$\boldsymbol{t_1}$, and $\boldsymbol{t_2}$ which represent the unit normal to the interface surface, the first tangential unit vector, and the second tangential unit vector to the interface surface respectively. The ortho-normal unit vectors must satisfy the following cross product, Manna [1992]:

$$\boldsymbol{n} \times \boldsymbol{t_1} = \boldsymbol{t_2},\ \boldsymbol{t_1} \times \boldsymbol{t_2} = \boldsymbol{n},\ \text{and}\ \boldsymbol{t_2} \times \boldsymbol{n} = \boldsymbol{t_1} \qquad (4-62)$$

The velocity components in the ortho-normal directions are:

$$\begin{aligned} u_n &= \boldsymbol{u} \cdot \boldsymbol{n} \\ u_{t_1} &= \boldsymbol{u} \cdot \boldsymbol{t_1} \\ u_{t_2} &= \boldsymbol{u} \cdot \boldsymbol{t_2} \end{aligned} \qquad (4-63)$$

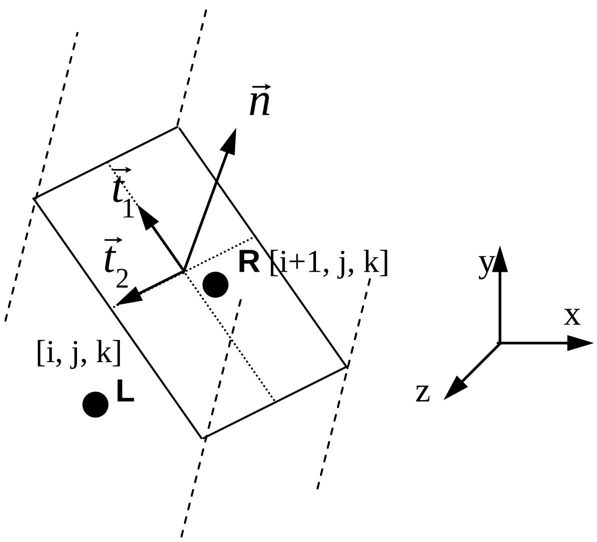

Fig. 4-1 The interface between two adjacent cells

In the present study, Roe's approximate Riemann solver is used to calculate the convective fluxes for three dimensional Reynolds averaged Navier-Stokes equations with $k-\omega$ turbulence closure. So, the eigenvalues of the approximate Jacobian matrix can be obtained by solving the linear system of equations $|\widehat{\boldsymbol{A}}-\hat{\lambda}\mathbf{I}| = \mathbf{0}$ where $\mathbf{I}$ is the identity matrix. The resulting eigenvalues are:

$$\begin{aligned}
\hat{\lambda}_1 &= \hat{u}_n - \hat{a}_t \\
\hat{\lambda}_2 &= \hat{u}_n \\
\hat{\lambda}_3 &= \hat{u}_n \\
\hat{\lambda}_4 &= \hat{u}_n \\
\hat{\lambda}_5 &= \hat{u}_n + \hat{a}_t \\
\hat{\lambda}_6 &= \hat{u}_n \\
\hat{\lambda}_7 &= \hat{u}_n
\end{aligned} \qquad (4-64)$$

By substituting the eigenvalue $\hat{\lambda}_k$ into $\widehat{\boldsymbol{A}}\hat{e}_k = \hat{e}_k\hat{\lambda}_k$ and solving for the eigenvector $\hat{e}_k$, the corresponding eigenvectors are to be found:

$$\begin{aligned}
\hat{e}_1 &= \begin{bmatrix}1 & \hat{u}_n - \hat{a}_t & \hat{u}_{t_1} & \hat{u}_{t_2} & \hat{h}_o + \frac{2}{3}\hat{k} - \hat{u}_n\hat{a}_t & \hat{k} & \widehat{\omega}\end{bmatrix}^T \\
\hat{e}_2 &= \begin{bmatrix}1 & \hat{u}_n & \hat{u}_{t_1} & \hat{u}_{t_2} & \hat{h}_o + \frac{2}{3}\hat{k} - \frac{\hat{a}_t^2}{(\gamma-1)} & \hat{k} & \widehat{\omega}\end{bmatrix}^T \\
\hat{e}_3 &= [0 \quad 0 \quad 1 \quad 0 \quad \hat{u}_{t_1} \quad 0 \quad 0]^T \\
\hat{e}_4 &= [0 \quad 0 \quad 0 \quad 1 \quad \hat{u}_{t_2} \quad 0 \quad 0]^T \\
\hat{e}_5 &= \begin{bmatrix}1 & \hat{u}_n + \hat{a}_t & \hat{u}_{t_1} & \hat{u}_{t_2} & \hat{h}_o + \frac{2}{3}\hat{k} + \hat{u}_n\hat{a}_t & \hat{k} & \widehat{\omega}\end{bmatrix}^T \\
\hat{e}_6 &= \begin{bmatrix}0 & 0 & 0 & 0 & \frac{3\gamma-5}{3(\gamma-1)} & 1 & 0\end{bmatrix}^T \\
\hat{e}_7 &= [0 \quad 0 \quad 0 \quad 0 \quad 0 \quad 0 \quad 1]^T
\end{aligned} \qquad (4-65)$$

The symbols with hat indicate that their values are computed using the Roe averaging method, Roe [1981]:

$$\hat{u}_n = \frac{\sqrt{\rho_{\mathrm{L}}}u_{n\mathrm{L}} + \sqrt{\rho_{\mathrm{R}}}u_{n\mathrm{R}}}{\sqrt{\rho_{\mathrm{L}}} + \sqrt{\rho_{\mathrm{R}}}}$$

$$\hat{u}_{t_1} = \frac{\sqrt{\rho_{\mathrm{L}}}u_{t_1\mathrm{L}} + \sqrt{\rho_{\mathrm{R}}}u_{t_1\mathrm{R}}}{\sqrt{\rho_{\mathrm{L}}} + \sqrt{\rho_{\mathrm{R}}}}$$

$$\hat{u}_{t_2} = \frac{\sqrt{\rho_{\mathrm{L}}}u_{t_2\mathrm{L}} + \sqrt{\rho_{\mathrm{R}}}u_{t_2\mathrm{R}}}{\sqrt{\rho_{\mathrm{L}}} + \sqrt{\rho_{\mathrm{R}}}}$$

$$\hat{h}_o = \frac{\sqrt{\rho_{\mathrm{L}}}h_{o\mathrm{L}} + \sqrt{\rho_{\mathrm{R}}}h_{o\mathrm{R}}}{\sqrt{\rho_{\mathrm{L}}} + \sqrt{\rho_{\mathrm{R}}}}$$

$$\hat{k} = \frac{\sqrt{\rho_{\mathrm{L}}}k_{\mathrm{L}} + \sqrt{\rho_{\mathrm{R}}}k_{\mathrm{R}}}{\sqrt{\rho_{\mathrm{L}}} + \sqrt{\rho_{\mathrm{R}}}} \qquad (4-66)$$

$$\hat{\omega} = \frac{\sqrt{\rho_{\mathrm{L}}}\omega_{\mathrm{L}} + \sqrt{\rho_{\mathrm{R}}}\omega_{\mathrm{R}}}{\sqrt{\rho_{\mathrm{L}}} + \sqrt{\rho_{\mathrm{R}}}}$$

$$\hat{p} = \frac{\sqrt{\rho_{\mathrm{L}}}p_{\mathrm{L}} + \sqrt{\rho_{\mathrm{R}}}p_{\mathrm{R}}}{\sqrt{\rho_{\mathrm{L}}} + \sqrt{\rho_{\mathrm{R}}}}$$

$$\hat{\rho} = \sqrt{\rho_{\mathrm{L}}\rho_{\mathrm{R}}}$$

$$\hat{a}_t = \sqrt{\left(\frac{\gamma\hat{p}}{\hat{\rho}} + \frac{2}{3}\hat{k}\right)}$$

In order to calculate the Roe numerical flux $\mathbf{F}_{i+\frac{1}{2}}$ using equation (4-61) the wave strengths $\hat{\alpha}_k$ must be evaluated. The relations to calculate the wave strengths can be derived by projecting the conservative variables difference $\mathbf{U}_{\mathrm{R}} - \mathbf{U}_{\mathrm{L}}$ onto the eigenvectors as follow:

$$\begin{bmatrix} \Delta\rho \\ \Delta\rho u_n \\ \Delta\rho u_{t_1} \\ \Delta\rho u_{t_2} \\ \Delta\rho e_o \\ \Delta\rho k \\ \Delta\rho\omega \end{bmatrix} = \sum_{k=1}^{m} \hat{\alpha}_k \hat{e}_k \qquad (4-67)$$

where Δ represents the difference across the cell interface, for example $\Delta\rho = \rho_{\mathrm{R}} - \rho_{\mathrm{L}}$. By solving the above linear system of simultaneous equations for $\hat{\alpha}_k$, the characteristic wave strengths found to be:

$$\hat{\alpha}_1 = \frac{1}{2\hat{a}_t^{\,2}}\left[\Delta p + \frac{2}{3}\left(\hat{\rho}\Delta k + \hat{k}\Delta\rho\right) - \hat{\rho}\hat{a}_t\Delta u_n\right]$$

$$\hat{\alpha}_2 = \Delta\rho - \frac{1}{\hat{a}_t{}^2}\left[\Delta p + \frac{2}{3}\left(\hat{\rho}\Delta k + \hat{k}\Delta\rho\right)\right]$$

$$\hat{\alpha}_3 = \hat{\rho}\Delta u_{t_1}$$

$$\hat{\alpha}_4 = \hat{\rho}\Delta u_{t_2}$$

$$\hat{\alpha}_5 = \frac{1}{2\hat{a}_t{}^2}\left[\Delta p + \frac{2}{3}\left(\hat{\rho}\Delta k + \hat{k}\Delta\rho\right) + \hat{\rho}\hat{a}_t\Delta u_n\right]$$

$$\hat{\alpha}_6 = \hat{\rho}\Delta k$$

$$\hat{\alpha}_7 = \hat{\rho}\Delta\omega \qquad (4-68)$$

4-3.2 MUSCL Data Reconstruction

In the finite-volume approximation, the continuous change in flow state in the physical domain is replaced by an assembly of control volumes V_i with a constant flow state volume averaged in each volume and a discontinuous step changes in flow state across the volume average boundaries$S_{k,i}$. A zeroth order approach in interpreting the flow state inside each control volume V_i is to take the flow state as uniform and equal to the finite-volume average. The evolution in time of the flow is obtained by solving a Riemann problem across each all interface $S_{k,i}$. The Roe's approximate Riemann solver, used to estimate the convective fluxes at the cell interface, is first order space accurate because the solution is projected on each cell as a piecewise constant state, Hirsch [1990]. Using of this order spatial discretization leads to excessive diffusion. Following van Leer [1979], second order spatial accuracy or higher can be achieved in regions of smooth flow by using more upwind points and replacing the piecewise constant by a linear or quadratic reconstruction of the conservative variables distribution in each cell. This method is known as the Monotone Upwind Schemes for Conservation Laws (MUSCL) approach. In the present study, up to a third order spatial accuracy is achieved in the evaluation of the flow variables at cell interfaces by using a four-cell stencil, as shown in fig. 4-2.

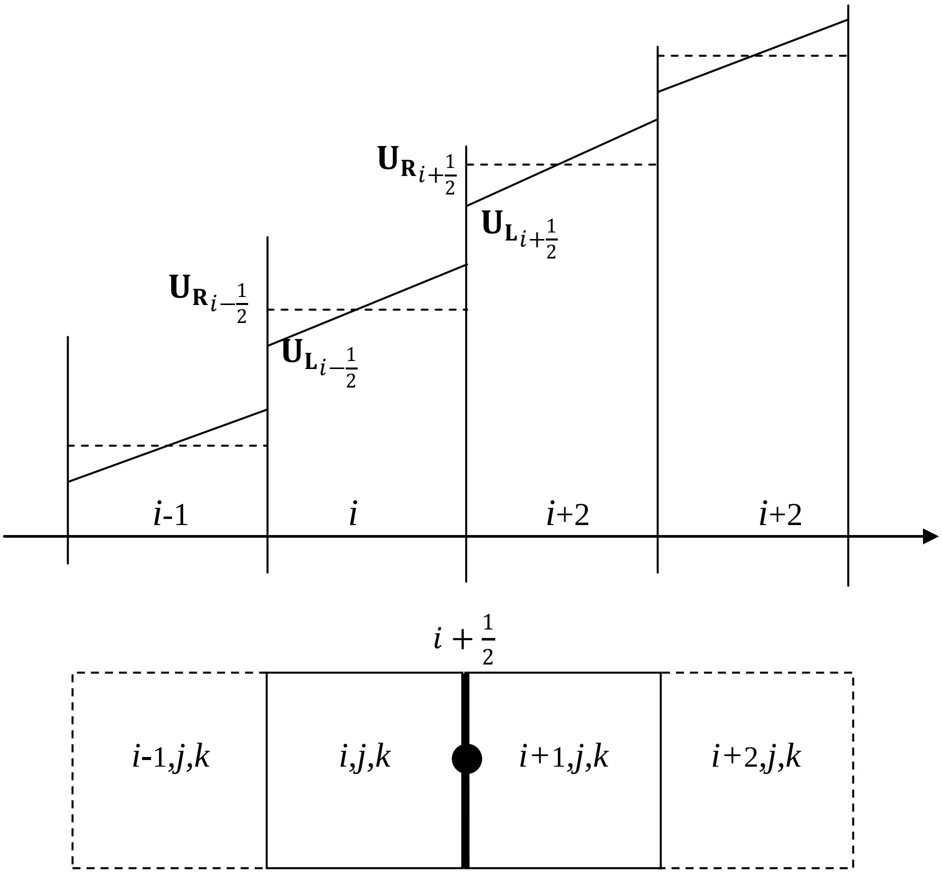

Fig. 4-2 The four-cell stencil used to build the MUSCL scheme.

Based on a simple Taylor expansion, any scalar variable in $\mathbf{U}$ can be interpolated at the cell interface $i+\frac{1}{2}$ with an accuracy up to third-order on a uniform mesh. The cell interface interpolated variables at left and right of the location $i+\frac{1}{2}$ are defined as:

$$\mathbf{U_L}_{i+\frac{1}{2}} = \mathbf{U}_i + \frac{\varepsilon}{4}\left[(1-\eta)\Delta\mathbf{U}_{i-\frac{1}{2}} + (1+\eta)\Delta\mathbf{U}_{i+\frac{1}{2}}\right] \qquad (4-69)$$

$$\mathbf{U_R}_{i+\frac{1}{2}} = \mathbf{U}_{i+1} - \frac{\varepsilon}{4}\left[(1-\eta)\Delta\mathbf{U}_{i+\frac{3}{2}} + (1+\eta)\Delta\mathbf{U}_{i+\frac{1}{2}}\right] \qquad (4-70)$$

where $\Delta\mathbf{U}$, the volume averaged flow variable differences, are defined as:

$$\Delta\mathbf{U}_{i-\frac{1}{2}} = \mathbf{U}_i - \mathbf{U}_{i-1},$$

$$\Delta\mathbf{U}_{i+\frac{1}{2}} = \mathbf{U}_{i+1} - \mathbf{U}_i,$$

$$\Delta\mathbf{U}_{i+\frac{3}{2}} = \mathbf{U}_{i+2} - \mathbf{U}_{i+1} \qquad (4-71)$$

The parameter ε is the switch between the first order and the higher spatial discretization accuracy, if $\varepsilon = 0$ the piecewise constant (first order) interpolation is recovered, if $\varepsilon = 1$ the higher spatial discretization order is obtained. The other parameter η specifies the order of MUSCL scheme. Table 4-1 shows the description corresponding to each η value, Lee [2006]. For the present study, the values of ε and η are 1 and $\frac{1}{3}$ respectively.

ε	η	The scheme
0	N/A	First order piece-wise constant
1	-1	Second order fully upwind biased scheme
	0	Second order upwind biased scheme
	1/2	'QUICK' method of Leonard
	1/3	3^{rd} order Asymmetric biased method
	1	Three point central difference method

Table 4-1 The values of MUSCL parameters.

4-3.3 TVD Scheme

Although the upwind schemes appear to appropriately account for the flow physics more than central difference schemes, the numerical results show that the higher order spatial discretization schemes exhibit instabilities when in regions of rapidly changing flow, such as across shock waves. These instabilities derive from a lack of monotonicity preservation in the scheme. To preserve the numerical stability, a total variation concept is applied. The total variation of the conservative variables vector is given by:

$$TV(\mathbf{U}) = \int_{-\infty}^{\infty} \left|\frac{\partial \mathbf{U}}{\partial x}\right| dx \qquad (4-72)$$

where the integration extends over the full physical domain. The total variation for the discrete case is

$$TV(\mathbf{U}^n) = \sum_i |\mathbf{U}_{i+1}^n - \mathbf{U}_i^n| \qquad (4-73)$$

where n is the time level. The numerical scheme is called to be total variation diminishing (TVD) if

$$TV(\mathbf{U}^{n+1}) \leq TV(\mathbf{U}^n) \qquad (4-74).$$

Harten [1983] proved that

1. All monotone schemes are TVD

2. All TVD schemes are monotonicity preserving

To construct a high resolution upwind TVD scheme, one of the slope limiters should be applied to the dependent variables or fluxes. After applying the non-linear limiters on the MUSCL approach, the fluxes at cell interface can be defined as:

$$\mathbf{U}_{\mathbf{L}_{i+\frac{1}{2}}} = \mathbf{U}_i + \frac{\varepsilon}{4}\left[(1-\eta)\mathbf{\Phi}_{\mathbf{R}_{i-\frac{1}{2}}}\Delta\mathbf{U}_{i-\frac{1}{2}} + (1+\eta)\mathbf{\Phi}_{\mathbf{L}_{i+\frac{1}{2}}}\Delta\mathbf{U}_{i+\frac{1}{2}}\right] \qquad (4-75)$$

$$\mathbf{U}_{\mathbf{R}_{i+\frac{1}{2}}} = \mathbf{U}_{i+1} - \frac{\varepsilon}{4}\left[(1-\eta)\mathbf{\Phi}_{\mathbf{L}_{i+\frac{3}{2}}}\Delta\mathbf{U}_{i+\frac{3}{2}} + (1+\eta)\mathbf{\Phi}_{\mathbf{R}_{i+\frac{1}{2}}}\Delta\mathbf{U}_{i+\frac{1}{2}}\right] \qquad (4-76)$$

where $\mathbf{\Phi}$ is the limiting function, which is dependent on the gradient slope r as follow:

$$\mathbf{\Phi}_{\mathbf{R}_{i-\frac{1}{2}}} = \mathbf{\Phi}\left(\frac{\mathbf{U}_{i+1}-\mathbf{U}_i}{\mathbf{U}_i-\mathbf{U}_{i-1}}\right) = \mathbf{\Phi}(r_{\mathbf{L}})$$

$$\mathbf{\Phi}_{\mathbf{L}_{i+\frac{1}{2}}} = \mathbf{\Phi}\left(\frac{\mathbf{U}_{i}-\mathbf{U}_{i-1}}{\mathbf{U}_{i+1}-\mathbf{U}_{i}}\right) = \mathbf{\Phi}\left(\frac{\mathbf{1}}{r_{\mathbf{L}}}\right)$$

$$\mathbf{\Phi}_{\mathbf{L}_{i+\frac{3}{2}}} = \mathbf{\Phi}\left(\frac{\mathbf{U}_{i+1}-\mathbf{U}_i}{\mathbf{U}_{i+2}-\mathbf{U}_{i+1}}\right) = \mathbf{\Phi}(r_{\mathbf{R}})$$

$$\mathbf{\Phi}_{\mathbf{R}_{i+\frac{1}{2}}} = \mathbf{\Phi}\left(\frac{\mathbf{U}_{i+2}-\mathbf{U}_{i+1}}{\mathbf{U}_{i+1}-\mathbf{U}_{i}}\right) = \mathbf{\Phi}\left(\frac{\mathbf{1}}{r_{\mathbf{R}}}\right) \qquad (4-77)$$

The limiting functions should be selected to satisfy the following TVD condition, Sweby [1984]:

$$\begin{array}{lcc} \mathbf{\Phi}(r) = 0 & \forall & r \le 0 \\ r \le \mathbf{\Phi}(r) \le min[1,2r] & \forall & 0 < r \le 1 \\ 1 \le \mathbf{\Phi}(r) \le min[2,r] & \forall & r > 1 \end{array} \qquad (4-78)$$

, that represents the confined area (the area between the solid and dashed line) in fig. 4-3. There are several limiter functions used by CFD community. The most common limiter functions applied to the Roe method are:

The MinMod limiter,

$$\Phi(r) = \mathbf{minmod}(1,r) = \max[0,\min(1,r)] \qquad (4-79)$$

and the Super Bee limiter

$$\Phi(r) = \max[0,\min(1,2r),\min(2,r)] \qquad (4-80)$$

In the present study, the minmod limiter function, which represents the lower bounds (the dash line) of the TVD region as shown in fig. 4-3, is used to calculate the cell interface fluxes. The formulations for the cell interface fluxes, after applying the minmod limiter function, are

$$\mathbf{U}_{\mathbf{L}_{i+\frac{1}{2}}} = \mathbf{U}_i + \frac{\varepsilon}{4}\left[(1-\eta)\overline{\overline{\Delta\mathbf{U}}}_{i-\frac{1}{2}} + (1+\eta)\overline{\overline{\Delta\mathbf{U}}}_{i+\frac{1}{2}}\right] \qquad (4-81)$$

$$\mathbf{U}_{\mathbf{R}_{i+\frac{1}{2}}} = \mathbf{U}_{i+1} - \frac{\varepsilon}{4}\left[(1-\eta)\overline{\overline{\Delta\mathbf{U}}}_{i+\frac{3}{2}} + (1+\eta)\overline{\Delta\mathbf{U}}_{i+\frac{1}{2}}\right] \quad (4-82)$$

where

$$\overline{\overline{\Delta\mathbf{U}}}_{i-\frac{1}{2}} = \mathbf{\Phi}_{\mathbf{R}_{i-\frac{1}{2}}}\Delta\mathbf{U}_{i-\frac{1}{2}} = \mathbf{minmod}\left(\Delta\mathbf{U}_{i-\frac{1}{2}}, \Delta\mathbf{U}_{i+\frac{1}{2}}\right)$$

$$\overline{\overline{\Delta\mathbf{U}}}_{i+\frac{1}{2}} = \mathbf{\Phi}_{\mathbf{L}_{i+\frac{1}{2}}}\Delta\mathbf{U}_{i+\frac{1}{2}} = \mathbf{minmod}\left(\Delta\mathbf{U}_{i+\frac{1}{2}}, \Delta\mathbf{U}_{i-\frac{1}{2}}\right)$$

$$\overline{\overline{\Delta\mathbf{U}}}_{i+\frac{3}{2}} = \mathbf{\Phi}_{\mathbf{L}_{i+\frac{3}{2}}}\Delta\mathbf{U}_{i+\frac{3}{2}} = \mathbf{minmod}\left(\Delta\mathbf{U}_{i+\frac{3}{2}}, \Delta\mathbf{U}_{i+\frac{1}{2}}\right)$$

$$\overline{\Delta\mathbf{U}}_{i+\frac{1}{2}} = \mathbf{\Phi}_{\mathbf{R}_{i+\frac{1}{2}}}\Delta\mathbf{U}_{i+\frac{1}{2}} = \mathbf{minmod}\left(\Delta\mathbf{U}_{i+\frac{1}{2}}, \Delta\mathbf{U}_{i+\frac{3}{2}}\right) \quad (4-83)$$

$$\mathbf{minmod}(\boldsymbol{a},\boldsymbol{b}) = sign(\boldsymbol{a}).\max[0,\min(|\boldsymbol{a}|, sign(\boldsymbol{a}).\boldsymbol{b})] \quad (4-84)$$

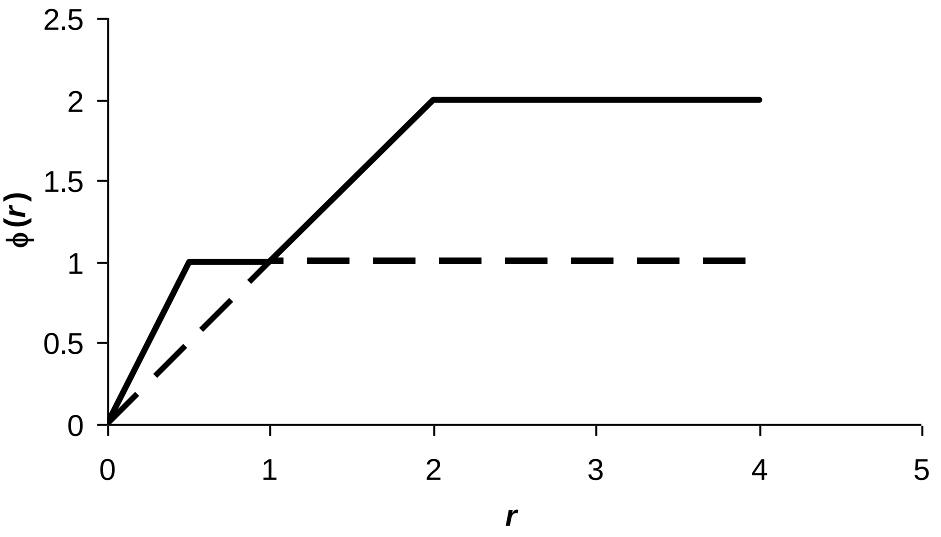

Fig. 4-3 The TVD second order scheme region.

4-3.4 Entropy correction for the Roe scheme

The Roe scheme has a very low amount of diffusion on oblique grids and it is considered a non-diffusive scheme for grid aligned flows, Kermani and Plett [2001]. So, the scheme can exhibit non-physical solutions such as expansion shocks. To avoid these, the entropy condition must be satisfied. A lot of effort has been devoted toward the solution of the entropy violation inherent in the Roe scheme. A numerical solution to this problem is given by Harten and Hyman [1983]. They noted that the entropy violation is due to the vanishing of numerical viscosity value. Therefore, they replaced the small values of numerical viscosity with larger values through the following formulation:

$$\begin{cases} \hat{\lambda} \rightarrow \dfrac{{\varepsilon^*}^2 + \hat{\lambda}^2}{2\varepsilon^*} \qquad |\lambda| < \varepsilon^* \\ \varepsilon^* = \max\left[0, \left(\hat{\lambda} - \lambda_{\mathrm{L}}\right), \left(\lambda_{\mathrm{R}} - \hat{\lambda}\right)\right] \end{cases} \qquad (4-85)$$

Kermani and Plett [2001] modified the above equation by enlarging the applicable band over which the entropy fix formulation is applied. The modified formulation is

$$\begin{cases} \hat{\lambda} \rightarrow \dfrac{{\varepsilon^*}^2 + \hat{\lambda}^2}{2\varepsilon} \qquad |\lambda| < \varepsilon^* \\ \varepsilon^* = 2.0 \max[0, (\lambda_{\mathrm{R}} - \lambda_{\mathrm{L}})] \qquad \text{or} \\ \varepsilon^* = 4.0 \max\left[0, \left(\hat{\lambda} - \lambda_{\mathrm{L}}\right), \left(\lambda_{\mathrm{R}} - \hat{\lambda}\right)\right] \end{cases} \qquad (4-86)$$

This modification was made to prevent the occurrence of expansion shocks in the vicinity of a sonic expansion and is entropy fix used in the Roe scheme.

4-4 Calculation of viscous fluxes

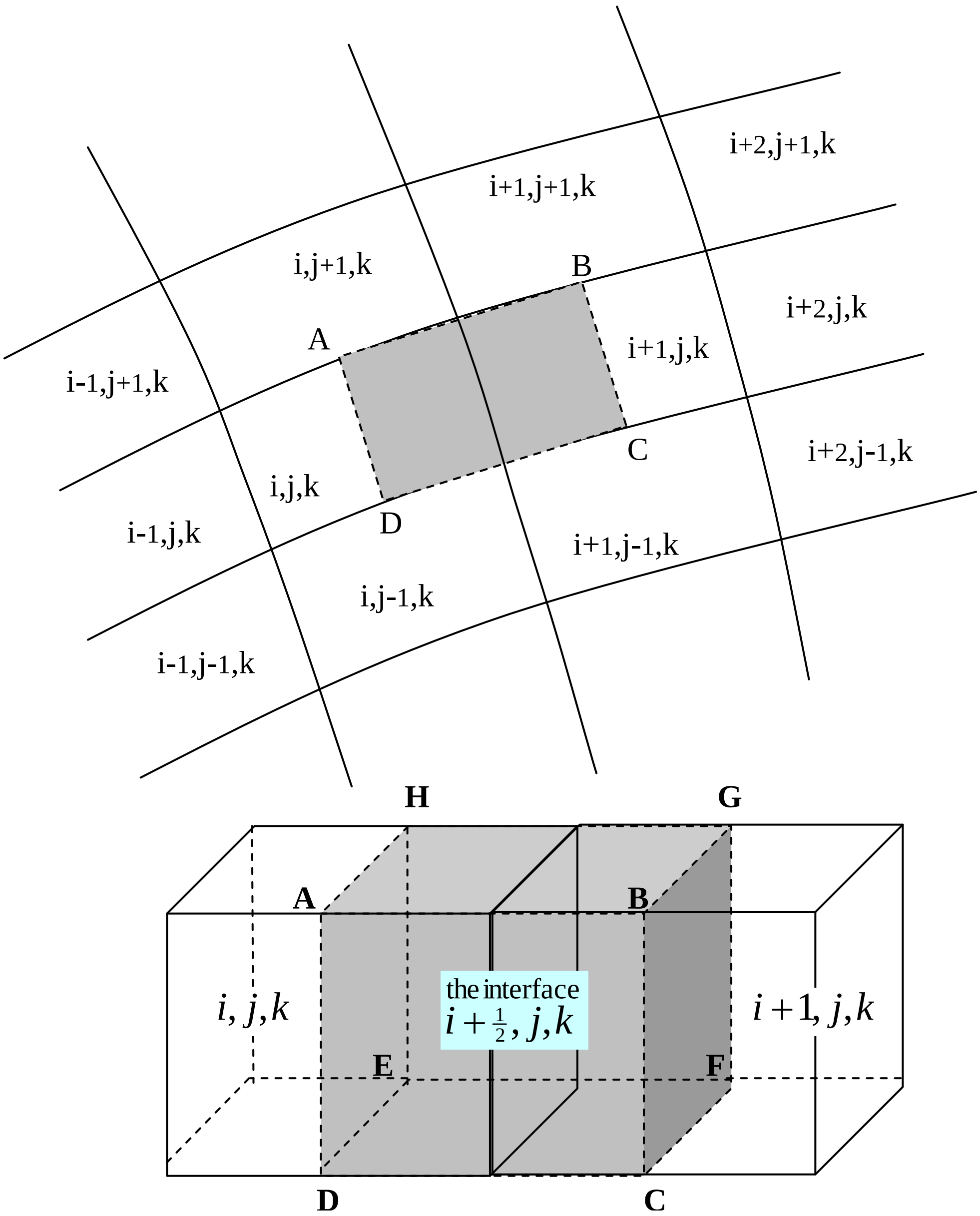

Fig. 4-4 The constructed control volume for the diffusive fluxes calculation

The calculation of the convective fluxes in the Reynolds averaged Navier Stokes equations coupled with $k-\omega$ model is done on a (i, j, k) structured topological orthogonal mesh that discretises the computational domain. The conservative flow variables are defined as the finite volume averges in each volume V_i. at the cell centre. The convective fluxes calculation is carried out over the six faces $S_{k,i}$ of each control volume V_i bounded by solid lines in fig. 4-4. In the case of the diffusive fluxes calculation, a staggered control volume is generated across cell interfaces, where the viscous fluxes need to be estimated. The new control volume is shaded and bounded by dash lines as shown in fig. 4-4. By considering for example the interface $i+\frac{1}{2}$ between the cells *i,j,k* and *i+1,j,k*, the new control volume ABCDEFGH has eight vertices located at the mid position on the four faces of the two cells containing the interface $i+\frac{1}{2}$. The coordinates of theses vertices are unknown and they are calculated from the coordinates of the original cell vertices. After calculating the coordinates of the vertices of the new control volume, the volume, the surface areas, and the normal to its faces are calculated. Next, the primitive flow variables $\boldsymbol{u}, T, k,$ and ω along each face are estimated by

$$u_{ABCD} = \frac{1}{4}\left(u_{i,j,k} + u_{i+1,j,k} + u_{i,j,k+1} + u_{i+1,j,k+1}\right)$$

$$u_{BGFC} = u_{i+1,j,k}$$

$$u_{EFGH} = \frac{1}{4}\left(u_{i,j,k} + u_{i+1,j,k} + u_{i,j,k-1} + u_{i+1,j,k-1}\right)$$

$$u_{ADEH} = u_{i,j,k}$$

$$u_{ABGH} = \frac{1}{4}\left(u_{i,j,k} + u_{i+1,j,k} + u_{i,j+1,k} + u_{i+1,j+1,k}\right)$$

$$u_{CDEF} = \frac{1}{4}\left(u_{i,j,k} + u_{i+1,j,k} + u_{i,j-1,k} + u_{i+1,j-1,k}\right) \qquad (4-87)$$

The other variables are evaluated similarly. Now, the gradients of the flow variables are calculated by applying the Gauss divergence theorem on the generated control volume as follow:

$$\nabla \boldsymbol{u} = \frac{1}{V}\oint_S \boldsymbol{u} \cdot \boldsymbol{n}\, dS \qquad (4-88)$$

The diffusive fluxes, which represent the third term in equation (4-55), can be estimated by substituting these gradients into the viscous flux vector equation (4-44).

4-5 Source term

The source term vector defined in equation (4-45) includes the production and destruction terms of the $k-\omega$ equations. The production term is evaluated using equation (4-19) to calculate the Reynolds stress tensor $\boldsymbol{\tau}$ and by applying divergence theorem to calculate the velocity gradients. The coefficients β^* and β of the turbulence model including this compressibility correction are defined by equations (4-33) and (4-34). Evaluating the source term completes the estimation of the linear terms in equation (4-52) and the final step to evaluate the solution of the volume-averaged conservative variables vector $\mathbf{U}_i$ is by the time integration of the differential $\frac{\partial \mathbf{U}_i}{\partial t}$.

4-6 Time integration.

The explicit numerical scheme used in the present study first estimates the finite volume fluxes of both the Euler and the Reynolds averaged Navier-Stokes equation and then advances the flow solution in time. This method gives the flexibility to adopt different levels of spatial approximation for the convective and diffusive fluxes, independently from the time integration. The governing equations (4-55) can be written in the following compact form by replacing the discretized spatial differential terms and the source term by $\mathcal{R}_i$.

$$V_i \frac{\partial \mathbf{U}_i}{\partial \mathrm{t}} + \mathcal{R}_i = 0 \qquad (4-89)$$

where $\mathcal{R}_i$ denotes the residual vector generated from the summation of the discretized spatial differential terms and the source term. The numerical method leads to a set of first order ordinary differential equations that can be advanced in time using an explicit time integration scheme. An explicit multistage time stepping scheme is used because it is computationally cheap and requires a small amount of computer memory. The explicit multi stage Runge-Kutta time stepping scheme integrates in equation (4-89) in time and preserves the properties of the TVD scheme. This scheme is:

$$\mathbf{U}_i{}^0 = \mathbf{U}_i{}^n$$

$$do\ k = 1, m$$

$$\mathbf{U}_i{}^k = \mathbf{U}_i{}^0 - \alpha_k \frac{\Delta t}{V_i} \mathcal{R}_i^{k-1}$$

$$end\ do$$

$$\mathbf{U}_i{}^{n+1} = \mathbf{U}_i{}^m \qquad (4-90)$$

where m and n denote the number of stages of Runge-Kutta scheme and the time level respectively. The weighting coefficients α_1 to α_m are defined according to:

$$\alpha_1 = \frac{1}{m-k+1}, \qquad k = 1, 2, \cdots\cdots, m \qquad (4-91)$$

The results are obtained using a two step Runge-Kutta scheme in which $\alpha_{m-1} = \frac{1}{2}$, $\alpha_m = 1$, which gives a second order accurate time integration, as reported by Bennett [2005]. The stability of the explicit scheme is restricted by the time step. The scheme remains stable up to a certain value of the time step that satisfies the Courant-Friedrichs-Lewy (CFL) condition, Blazek [2001].

$$\Delta t \leq CFL \frac{V_i}{\ell_x + \ell_y + \ell_z} \tag{4-92}$$

$$\ell_x = (|u_i| + a_i)S_i^x$$
$$\ell_y = (|v_i| + a_i)S_i^y$$
$$\ell_z = (|w_i| + a_i)S_i^z \tag{4-93}$$

where CFL is Courant number, V_i is the cell volume, a_i is the local speed of sound, and S_i^x, S_i^y, and S_i^z are the projected areas of cell i in the x, y, and z directions.

4-7 Hybrid RANS/LES turbulence model

A significant element in the predictive ability of the DES is the switching between RANS and LES, for which zonal and non-zonal techniques are available. The zonal technique works by pre-defining the regions where RANS and LES turbulence closures apply, which is not a convenient approach for modelling unknown flows. The other technique avoids the pre-defined regions by automatically choosing the turbulence closure, based on local mesh and flow properties.

This study uses this latter technique to switch between RANS and LES turbulence closure. The switch ensures that a RANS layer is always present near a wall and delivers a gradual transition between RANS and LES closure by using an appropriate blending function. This technique prevents one of the DES problems known as grid induced separation, which is due to the activation of the LES model inside the attached boundary layer because of an excessive grid refinement used near the wall.

The RANS portion of the flow is modelled using the Menter $k - \omega - SST$, which is a widely used turbulence model. The $k - \omega - SST$ turbulence closure combines the standard $k - \omega$ model of Wilcox with the Jones-Launder $k - \varepsilon$ model to benefit from the finite value of ω near the walls and avoid the strong dependency of predictions on the values of k and ω prescribed at the outer boundaries of the computational domain as stated by Menter [1992]. The model shows a good ability to reproduce the transport of the dominant shear stress in adverse pressure gradient boundary-layers, Menter[1992]. In this study, the Menter $k-\omega-SST$ is coupled with the one equation Sub-Grid-Scale (SGS) LES model by Yoshizawa that provides the LES turbulence closure.

4-7.1 The Menter SST model

The shear stress transport (SST) model, developed by Menter [1992], combines the best qualities of k-ω and k-ε models. Menter showed that the SST model exhibits an improved agreement with experiments compared to other two-equation RANS turbulence models for a variety of test cases. The SST model gives more accurate predictions in regions of separation in complex flow with a strong adverse pressure gradient, Menter [1992]. The transport equations for k and ω are:

$$\frac{D\rho k_{RANS}}{Dt} = \tau_{ij}\frac{\partial u_i}{\partial x_j} - \beta^* \rho\omega k_{RANS} + \frac{\partial}{\partial x_j}\left[\left(\mu + \sigma_k \mu_{t,RANS}\right)\frac{\partial k_{RANS}}{\partial x_j}\right] \qquad (4-94)$$

$$\frac{D\rho\omega}{Dt} = \frac{\gamma\rho}{\mu_{t,RANS}}\tau_{ij}\frac{\partial u_i}{\partial x_j} - \beta\rho\omega^2 + \frac{\partial}{\partial x_j}\left[\left(\mu + \sigma_\omega \mu_{t,RANS}\right)\frac{\partial \omega}{\partial x_j}\right] + \underbrace{2\rho[1-F_1]\sigma_{\omega 2}\frac{1}{\omega}\frac{\partial k_{RANS}}{\partial x_j}\frac{\partial \omega}{\partial x_j}}_{\text{cross-diffusion}} \qquad (4-95)$$

where τ_{ij} is the turbulent shear stress and is modelled by:

$$\tau_{ij} = \mu_t\left(\frac{\partial u_i}{\partial x_j} + \frac{\partial u_j}{\partial x_i} - \frac{2}{3}\frac{\partial u_k}{\partial x_k}\delta_{ij}\right) - \frac{2}{3}\rho k_{RANS}\delta_{ij} \qquad (4-96)$$

The coupling function F_1 is given by:

$$F_1 = \tanh({arg_1}^4),$$

$$arg_1 = \min\left[\max\left(\frac{\sqrt{k_{RANS}}}{0.09\omega y};\frac{500\mu}{\rho\omega y^2}\right);\frac{4\rho\sigma_{\omega 2}k_{RANS}}{CD_{k\omega}y^2}\right] \qquad (4-97)$$

$$CD_{k\omega} = max\left[2\rho\sigma_{\omega 2}\frac{1}{\omega}\frac{\partial k_{RANS}}{\partial x_j}\frac{\partial \omega}{\partial x_j};10^{-20}\right] \qquad (4-98)$$

where y is the distance to the nearest wall and $CD_{k\omega}$ represents the positive part of the cross-diffusion term in equation (4-95). The constants of the model are obtained by blending the constants in the k-ω and k-ε models using the coupling function F_1 as follows:

$$\begin{bmatrix}\sigma_k\\ \sigma_\omega\\ \beta\\ \gamma\end{bmatrix} = F_1\begin{bmatrix}\sigma_{k1}\\ \sigma_{\omega 1}\\ \beta_1\\ \gamma_1\end{bmatrix} + (1-F_1)\begin{bmatrix}\sigma_{k2}\\ \sigma_{\omega 2}\\ \beta_2\\ \gamma_2\end{bmatrix} \qquad (4-99)$$

The $k-\omega$ constants are $\sigma_{k1}=0.85$, $\sigma_{\omega 1}=0.5, \beta_1=0.075$, $\beta^*=0.09$, $\gamma_1=\frac{\beta_1}{\beta^*}-\frac{\sigma_{\omega 1}\kappa^2}{\sqrt{\beta^*}}$, and $\kappa=0.41$ while the $k-\varepsilon$ constants are $\sigma_{k2}=1.0$, $\sigma_{\omega 2}=0.856, \beta_2=0.0828, \beta^*=0.09, \gamma_2=\frac{\beta_2}{\beta^*}-\frac{\sigma_{\omega 2}\kappa^2}{\sqrt{\beta^*}}$, and $\kappa=0.41$.

By enforcing the Bradshaw's assumption that the turbulent shear stress in the boundary layer is equal to $\rho\alpha_1 k_{RANS}$, Menter's SST turbulent eddy viscosity can be obtained from $\mu_{t,RANS}=\frac{\rho\alpha_1 k_{RANS}}{max\,[\alpha_1\omega;|S_{ij}|F_2]}$ where $\alpha_1=0.31$, S_{ij} is the strain rate tensor $S_{ij}=\frac{1}{2}\left(\frac{\partial u_i}{\partial x_j}+\frac{\partial u_j}{\partial x_i}\right)$, and its magnitude $|S_{ij}|=\sqrt{2S_{ij}S_{ij}}$.

$$F_2=\tanh({arg_2}^4),\qquad arg_2=\max\left(2\frac{\sqrt{k_{RANS}}}{0.09\omega y};\frac{400\mu}{\rho\omega y^2}\right) \qquad (4-100)$$

Menter suggested using a limiter P_k for the turbulent production term to prevent the unrealistic build up of eddy viscosity in the stagnation regions. The limiter bounds the production term up to 20 times the destruction term and replaces $\tau_{ij}\frac{\partial u_i}{\partial x_j}$ in the k transport equation by.

$$P_k=\min\left[\tau_{ij}\frac{\partial u_i}{\partial x_j};20\beta^*\rho\omega k_{RANS}\right] \qquad (4-101)$$

Menter tested this limiter carefully and reported that this limiter does not change the predicted flow field of well-developed turbulent flows because the maximum level for the ratio of production term to destruction term reaches only up to two inside a shear layer. Therefore, this limit has been implemented in the current CFD scheme.

4-7.2 Large eddy simulation

To get a large eddy simulation solution, the filtered Navier-Stokes equations closed by a one-equation Sub-Grid-Scale (SGS) kinetic energy model are solved. In this study, the one equation SGS model by Yoshizawa is adopted. The SGS transport equation for the kinetic energy k_{SGS}, as shown in Dahlström and Davidson [2003], is given by

$$\frac{D\rho k_{SGS}}{Dt}=\tau_{ij}\frac{\partial u_i}{\partial x_j}-C_d\frac{\rho {k_{SGS}}^{\frac{3}{2}}}{\Delta}+\frac{\partial}{\partial x_j}\left[\left(\mu+\sigma_k\mu_{t,LES}\right)\frac{\partial k_{SGS}}{\partial x_j}\right] \qquad (4-102)$$

where τ_{ij} is the SGS stress tensor, Δ is the filter width and is set to the cube root of the volume of the cell i $\left(\Delta = \sqrt[3]{V_i}\right)$, $\mu_{t,LES} = \rho C_s \Delta \sqrt{k_{SGS}}$, and $\sigma_k = 1.0$.

The Yoshizawa constants C_d and C_s are problem dependent and can be evaluated from the corresponding Smagorinsky constant for that problem. In the equilibrium conditions, where the production and dissipation are in balance, the SGS model recovers the Smagorinsky subgrid eddy viscosity model, so that

$$\mu_{t,LES} = \rho \sqrt{\frac{C_s}{C_d}} C_s \Delta^2 \left|S_{ij}\right| = \rho C_{Smag}^2 \Delta^2 \left|S_{ij}\right| \qquad (4-103)$$

The Smagorinsky constant is related to the Yoshizawa constants by the given equation $C_{Smag} = \left(\frac{C_s^3}{C_d}\right)^{0.25}$ and its value is flow dependent and ranges from 0.065 to 0.2 for many flow problems.

4-7.3 Hybrid RANS/LES model

The present hybrid RANS/LES model combines the RANS turbulent kinetic energy equation with the LES turbulent kinetic energy equation using a weighting function Γ. The resulting transport equation for the turbulent kinetic energy k_T is

$$\frac{D\rho k_T}{Dt} = \tau_{ij}\frac{\partial u_i}{\partial x_j} - \left(\Gamma \rho \beta^* k_T \omega + (1-\Gamma) C_d \frac{\rho k_T^{\frac{3}{2}}}{\Delta}\right) + \frac{\partial}{\partial x_j}\left[(\mu + \sigma_k \mu_t)\frac{\partial k_T}{\partial x_j}\right] \qquad (4-104)$$

The hybrid eddy viscosity is given by

$$\mu_t = \Gamma \mu_{t,RANS} + (1-\Gamma)\mu_{t,LES} \qquad (4-105)$$

The blending function Γ is defined as

$$\Gamma = \tanh(\xi^4) \qquad (4-106)$$

where $\xi = \max\left[\frac{L_{RANS}}{y}; \frac{500\nu\beta^* L_{RANS}}{\sqrt{k_T}y^2}\right]$ and $L_{RANS} = \frac{\sqrt{k_T}}{\beta^*\omega}$.

The hybrid technique solves the resulting turbulent kinetic energy equation in combination with the transport equation for ω. Close to the wall, $y \to 0$ and the blending function approaches unity $(\Gamma \to 1.0)$, as can be shown by applying de l'Hopital's theorem to the blending function equation in the $\lim_{y\to 0}\Gamma$. The LES component of the turbulence closure model becomes less important as $y \to 0$,

$k_T \to k_{RANS}$, and the RANS solution is recovered. Conversely, away from the wall, the blending function approaches zero ($\Gamma \to 0.0$), $k_T \to k_{LES}$, and the LES solution becomes dominant.

4-8 Convergence Acceleration

To reduce the computational cost, two techniques were implemented to accelerate the solution of the governing equations. These are:

1- Local time stepping

2- Implicit residual smoothing.

The discussion of these methods is presented in the following two subsections.

4-8.1 Local time stepping

Local time stepping accelerates the convergence by calculating Δt at each cell based on the local numerical stability limit. The expression for the local time step is, Blazek [2001]:

Inviscid flow calculations

$$\Delta t_i \leq CFL \frac{V_i}{\ell_x + \ell_y + \ell_z} \qquad (4-107)$$

where *CFL* is the Courant number, and V_i is the volume of cell i, and ℓ_x, ℓ_y, and ℓ_z are the spectral radii of the convective flux Jacobian matrix. The spectral radii for three dimensional structured grids are calculated as follow:

$$\ell_x = (|u_i| + a_i)S_i^x$$
$$\ell_y = (|v_i| + a_i)S_i^y$$
$$\ell_z = (|w_i| + a_i)S_i^z \qquad (4-108)$$

Where a_i is the local speed of sound, and S_i^x, S_i^y, and S_i^z are the projected areas of the cell i in the x, y, and z directions.

This method allows the solution to advance at each cell using its maximum Δt_i, instead of using Δt_i which is equal to the minimum Δt_i calculated all over the control volumes. However, if a time accurate solution is required, the Δt must be fixed and taken equal to the minimum Δt_i over all the control volumes to maintain numerical stability.

Viscous flow calculations

The local time stepping for a steady viscous flow calculation is computed using the spectral radii of the viscous flux Jacobians as well as the convective ones. The local time step can be determined from Blazek [2001] as.

$$\Delta t_i \leq CFL \frac{V_i}{\left(\ell_x + \ell_y + \ell_z\right) + c\left(\ell_{xv} + \ell_{yv} + \ell_{zv}\right)} \qquad (4-109)$$

Where c is a constant that has been set to 4.0, and ℓ_{xv}, ℓ_{yv}, and ℓ_{zv} are the spectral radii of the viscous flux Jacobians which calculated from:

$$\ell_{xv} = max\left(\frac{4}{3\rho}, \frac{\gamma}{\rho}\right)\left(\frac{\mu_l}{Pr_l} + \frac{\mu_t}{Pr_t}\right)\frac{(S_i^x)^2}{V_i} \qquad (4-110)$$

and similarly for ℓ_{yv}, and ℓ_{zv}.

4-8.1 Implicit residual smoothing.

The maximum Courant number can be further increased by using implicit smoothing of the residuals. The unsteady flow simulation is computationally more expensive than the steady flow simulation for the same computational grid, and the local time stepping cannot be applied to an unsteady flow simulation, so it becomes valuable to use this technique for the time-dependent flow simulations. Jorgensen and Chima [1989] concluded that the implicit residual smoothing can be used with a time accurate explicit scheme without adversely affecting the results of the unsteady flow solution. Also, Rao and Delaney [1990] demonstrated that the errors introduced by using the implicit residual smoothing method are very local in nature and are smaller than the discretization error. This technique adds an implicit quality to the explicit schemes to overcome the Courant-Friedrichs-Lewy condition by damping the high frequency error components of the residual.

The implicit residual smoothing formulation for three-dimensional flow can be written as:

$$\left(1 - \beta_\xi \nabla_\xi \Delta_\xi\right)\left(1 - \beta_\zeta \nabla_\zeta \Delta_\zeta\right)\left(1 - \beta_\eta \nabla_\eta \Delta_\eta\right)\check{\mathcal{R}}_{i,j,k} = \mathcal{R}_{i,j,k} \qquad (4-111)$$

where the operator $\Delta\nabla$ is the standard second-order central difference operator, for instance

$$\nabla_\xi \Delta_\xi \check{\mathcal{R}}_{i,j,k} = \check{\mathcal{R}}_{i-1,j,k} - 2\check{\mathcal{R}}_{i,j,k} + \check{\mathcal{R}}_{i+1,j,k} \qquad (4-112)$$

and $\check{\mathcal{R}}_{i,j,k}$ is the residual after smoothing in the ξ, ζ, and η directions with coefficients β_ξ, β_ζ, and β_η. The later are defined by Swanson and Turkel [1997] as:

$$\beta_\xi = \max\left\{0, \frac{1}{4}\left[\left(\frac{CFL}{CFL^*}\frac{\lambda_\xi}{\lambda_\xi + \lambda_\zeta + \lambda_\eta}\Phi_\xi\right)^2 - 1\right]\right\}$$

$$\beta_\zeta = \max\left\{0, \frac{1}{4}\left[\left(\frac{CFL}{CFL^*}\frac{\lambda_\zeta}{\lambda_\xi + \lambda_\zeta + \lambda_\eta}\Phi_\zeta\right)^2 - 1\right]\right\}$$

$$\beta_\eta = \max\left\{0, \frac{1}{4}\left[\left(\frac{CFL}{CFL^*}\frac{\lambda_\eta}{\lambda_\xi + \lambda_\zeta + \lambda_\eta}\Phi_\eta\right)^2 - 1\right]\right\} \quad (4-113)$$

where CFL and CFL^* are the Courant numbers of the smoothed and unsmoothed schemes respectively, the coefficients Φ_ξ, Φ_ζ, and Φ_η are

$$\Phi_\xi = 1 + \left(\frac{\lambda_\zeta}{\lambda_\xi}\right)^{\frac{1}{2}} + \left(\frac{\lambda_\eta}{\lambda_\xi}\right)^{\frac{1}{2}}$$

$$\Phi_\zeta = 1 + \left(\frac{\lambda_\xi}{\lambda_\zeta}\right)^{\frac{1}{2}} + \left(\frac{\lambda_\eta}{\lambda_\zeta}\right)^{\frac{1}{2}}$$

$$\Phi_\eta = 1 + \left(\frac{\lambda_\xi}{\lambda_\eta}\right)^{\frac{1}{2}} + \left(\frac{\lambda_\zeta}{\lambda_\eta}\right)^{\frac{1}{2}} \quad (4-114)$$

and $\lambda_\xi, \lambda_\zeta$, and λ_η are the spectral radii of the convective flux Jacobian matrix. In a Cartesian grid, $\lambda_\xi = \lambda_x$, $\lambda_\zeta = \lambda_y$, and $\lambda_\eta = \lambda_z$, as defined in equation (4-108).

The sufficient condition for unconditionally stable Runge-Kutta scheme, as stated by Jorgensen and Chima [1989], is

$$\beta \geq \frac{1}{4}\left[\left(\frac{CFL}{CFL^*}\right)^2 - 1\right] \quad (4-115)$$

The smoothing formulation is applied sequentially in each coordinate direction, the results of which are three sets of tri-diagonal systems of algebraic equations as follows:

In the i direction,

$$-\beta_\xi \check{\mathcal{R}}^*{}_{i-1,j,k} + (1 + 2\beta_\xi)\check{\mathcal{R}}^*{}_{i,j,k} - \beta_\xi \check{\mathcal{R}}^*{}_{i+1,j,k} = \mathcal{R}_{i,j,k} \quad (4-116)$$

In the j direction,

$$-\beta_\zeta \check{\mathcal{R}}^{**}{}_{i,j-1,k} + (1 + 2\beta_\zeta)\check{\mathcal{R}}^{**}{}_{i,j,k} - \beta_\zeta \check{\mathcal{R}}^{**}{}_{i,j+1,k} = \check{\mathcal{R}}^*{}_{i,j,k} \quad (4-117)$$

In the k direction,

$$-\beta_\eta \check{\mathcal{R}}^{***}{}_{i,j,k-1} + (1 + 2\beta_\eta)\check{\mathcal{R}}^{***}{}_{i,j,k} - \beta_\eta \check{\mathcal{R}}^{***}{}_{i,j,k+1} = \check{\mathcal{R}}^{**}{}_{i,j,k} \quad (4-118)$$

where $\mathcal{R}_{i,j,k}$ is the calculated convective and diffusive residuals before smoothing and $\check{\mathcal{R}}^*{}_{i,j,k}, \check{\mathcal{R}}^{**}{}_{i,j,k}$, and $\check{\mathcal{R}}^{***}{}_{i,j,k}$ denote the smoothed residuals in i, j, and k directions respectively. The above sets of tri-diagonal system of algebraic equations are solved by using the Thomas algorithm.

By using the implicit residual smoothing, the scheme is able to handle approximately three times the unsmoothed Δt.

4-9 Navier-Stokes equations in rotational frame of reference

The simulation of fluid flow in a rotating frame of reference is very important to many engineering fields such as gas turbines, compressors, pumps, propellers, and centrifugal separators. The simulation gives information about the flow structure, heat transfer characteristics, and machine performance under rotating forces where performing experimental measurements is difficult especially at high rotational speed.

Towards developing a turbomachinery flow solver, the governing equations are solved in a rotating frame of reference. Two numerical methods are integrated to the in house code to solve the RANS equations in the rotating frame of reference. The first numerical scheme gives the solution of the finite-volume averaged conservative vector $\mathbf{U}_i$ in terms of the relative velocities and relative total internal energy, while the other gives the solution of the finite-volume averaged conservative vector $\mathbf{U}_i$ in terms of the absolute velocities and absolute total internal energy. Both numerical schemes are tested using an unshrouded turbine rotor cascade and they give approximately the same results.

Relative conservative variable vector scheme

The first numerical method solves the RANS equations in a rotating frame of reference using the finite-volume averaged conservative variables vector $\mathbf{U}_i = [\rho, \rho \boldsymbol{u}_r, \rho E_r, \rho k, \rho\omega]^T$ in terms of the relative velocities and relative total internal energy per unit mass.

To briefly describe the adapted method, the rotation of the system with constant angular velocity vector $\boldsymbol{\omega}$ around any fixed axis of rotation is considered. The relative velocity results from subtracting the rotational velocity of the rotating grid from the absolute velocity, $\boldsymbol{u}$, as follow:

$$\boldsymbol{u}_r = \boldsymbol{u} - (\boldsymbol{\omega} \times \boldsymbol{r}) \qquad (4-119)$$

The convective and diffusive fluxes for the RANS equations are written the same as in Eqns (4-43) and (4-44) in terms of relative velocity components and relative total internal energy instead of the absolute ones taking into account the effects due to the Coriolis force as well as the centrifugal force by adding them to the source term. The Coriolis force and the centrifugal force are defined as:

$$\boldsymbol{f_{co}} = -2(\boldsymbol{\omega} \times \boldsymbol{u}_r) \qquad \boldsymbol{f_{ce}} = -\boldsymbol{\omega} \times (\boldsymbol{\omega} \times \boldsymbol{r}) \qquad (4-120)$$

Then source term $\boldsymbol{S}$ can be written as

$$\mathbf{S} = [0, \quad (\boldsymbol{f_{co}} + \boldsymbol{f_{ce}}), \quad 0, \quad \mathrm{S}_k, \ \mathrm{S}_\omega]^T \qquad (4-121)$$

where S_k and $\mathbf{S}_\omega$ are the source terms of the transport turbulence model equations, given by equation (4-45). The perfect gas equation of state is given as:

$p = \rho RT$ where $T = \frac{1}{c_v}(e_o - \frac{|\boldsymbol{u}_r|^2}{2} + \frac{|\boldsymbol{\omega}\times\boldsymbol{r}|^2}{2})$.

By solving the RANS equations similarly as described above, the solution in the relative frame of reference is obtained. More details can be found in Kunz and Lakshminarayana [1992].

Absolute conservative variable vector scheme

The integral form of the RANS equations in a rotating frame of reference, using the finite-volume averaged conservative variables vector $\mathbf{U}_i$ in terms of the absolute variables is

$$V_i \frac{d}{dt}\mathbf{U}_i + \sum_{k=1}^{N_f}(\mathbf{F_c}_k S_k)_i + \sum_{k=1}^{N_f}(\mathbf{F_t}_k S_k)_i = V_i \mathbf{S}_i \qquad (4-122)$$

$$\mathbf{U}_i = \begin{bmatrix} \rho \\ \rho \boldsymbol{u}_i \\ \rho\,(e_o + k) \\ \rho k \\ \rho\omega \end{bmatrix} \qquad (4-123)$$

$$(\mathbf{F_c})_i = \begin{bmatrix} \rho \boldsymbol{u}_r \cdot \boldsymbol{n} \\ (\rho \boldsymbol{u}_i \boldsymbol{u}_r + p\boldsymbol{I}) \cdot \boldsymbol{n} \\ (\rho \boldsymbol{u}_r (h_o + k) + (\boldsymbol{\omega} \times \boldsymbol{r})p) \cdot \boldsymbol{n} \\ \rho \boldsymbol{u}_r k \cdot \boldsymbol{n} \\ \rho \boldsymbol{u}_r \omega \cdot \boldsymbol{n} \end{bmatrix} \qquad (4-124)$$

$$(\mathbf{F_t})_i \;=\; \begin{bmatrix} 0 \\ -\boldsymbol{\tau}\cdot\boldsymbol{n} \\ (\boldsymbol{q}-\boldsymbol{\tau}\cdot\boldsymbol{u})\cdot\boldsymbol{n}-(\mu_l+\sigma^*\mu_t)\nabla k\cdot\boldsymbol{n} \\ -(\mu_l+\sigma^*\mu_t)\nabla k\cdot\boldsymbol{n} \\ -(\mu_l+\sigma\mu_t)\nabla\omega\cdot\boldsymbol{n} \end{bmatrix} \qquad (4-125)$$

$$\mathbf{S} = [0, -\rho\,(\boldsymbol{\omega}\times\boldsymbol{u}),\quad 0,\quad \mathrm{S}_k,\ \mathrm{S}_\omega]^T \qquad (4-126)$$

where $\boldsymbol{u}_i$ is the absolute velocity vector, p is the static pressure, e_o is the absolute specific total energy, k is the specific turbulent kinetic energy and ω is the specific turbulent dissipation rate.

where $\boldsymbol{u}_r = \boldsymbol{u}-(\boldsymbol{\omega}\times\boldsymbol{r})$ is the relative velocity

The normal component of the gird rotational velocity is

$$u_g = (\boldsymbol{\omega}\times\boldsymbol{r}).\boldsymbol{n} \qquad (4-127)$$

The equation of state of a perfect gas to calculate the pressure is

$$p = (\gamma-1)e \qquad (4-128)$$

where

$$e = e_o - \frac{|\boldsymbol{u}_i|^2}{2} \qquad (4-129)$$

The inviscid fluxes using Roe's approximate Riemann solver are calculated in terms of the left and right states across a median-dual cell interface as shown in fig. 4-3.

$$\mathbf{F}_{i+\frac{1}{2}} = \frac{1}{2}(\mathbf{F_L}+\mathbf{F_R}) - \sum_{k=1}^{m} \hat{\alpha}_k\left|\hat{\lambda}_k\right|\hat{e}_k \qquad (4-130)$$

The Roe-avaraged relative contravariant $U_r = \boldsymbol{u}_r\cdot\boldsymbol{n}$ is

$$\widehat{U}_r = \frac{\sqrt{\rho_\mathrm{L}}U_{r\mathrm{L}}+\sqrt{\rho_\mathrm{R}}U_{r\mathrm{R}}}{\sqrt{\rho_\mathrm{L}}+\sqrt{\rho_\mathrm{R}}} \qquad (4-131)$$

The other Roe-averaged variables are computed from the absolute left and the absolute right state using equation (4-66).

The summation of the product of the eigenvalues, the eigenvectors and the wave strengths can be evaluated as follows:

$$\sum_{k=1}^{m} \hat{\alpha}_k |\hat{\lambda}_k| \hat{e}_k =$$

$$(\widehat{U}_r - \hat{a}) \left(\frac{1}{2\hat{a}_t{}^2} \left[\Delta p + \frac{2}{3} (\hat{\rho} \Delta k + \hat{k} \Delta \rho) - \hat{\rho} \hat{a}_t \Delta u_n \right] \right) \begin{bmatrix} 1 \\ \hat{u}_n - \hat{a}_t \\ \hat{u}_{t_1} \\ \hat{u}_{t_2} \\ \hat{h}_o + \frac{2}{3} \hat{k} - \hat{u}_n \hat{a}_t \\ \hat{k} \\ \widehat{\omega} \end{bmatrix} +$$

$$(\widehat{U}_r + \hat{a}) \left(\frac{1}{2\hat{a}_t{}^2} \left[\Delta p + \frac{2}{3} (\hat{\rho} \Delta k + \hat{k} \Delta \rho) + \hat{\rho} \hat{a}_t \Delta u_n \right] \right) \begin{bmatrix} 1 \\ \hat{u}_n + \hat{a}_t \\ \hat{u}_{t_1} \\ \hat{u}_{t_2} \\ \hat{h}_o + \frac{2}{3} \hat{k} + \hat{u}_n \hat{a}_t \\ \hat{k} \\ \widehat{\omega} \end{bmatrix} +$$

$$(\widehat{U}_r) \left(\Delta \rho - \frac{1}{\hat{a}_t{}^2} \left[\Delta p + \frac{2}{3} (\hat{\rho} \Delta k + \hat{k} \Delta \rho) \right] \right) \begin{bmatrix} 1 \\ \hat{u}_n \\ \hat{u}_{t_1} \\ \hat{u}_{t_2} \\ \hat{h}_o + \frac{2}{3} \hat{k} - \frac{\hat{a}_t{}^2}{(\gamma - 1)} \\ \hat{k} \\ \widehat{\omega} \end{bmatrix} +$$

$$(\widehat{U}_r) \rho \begin{bmatrix} 0 \\ 0 \\ \Delta u_{t_1} \\ \Delta u_{t_2} \\ \hat{u}_{t_1} \Delta u_{t_1} + \hat{u}_{t_2} \Delta u_{t_2} \\ 0 \\ 0 \end{bmatrix} + (\widehat{U}_r) \rho \begin{bmatrix} 0 \\ 0 \\ 0 \\ 0 \\ \frac{3\gamma - 5}{3(\gamma - 1)} \Delta k \\ \Delta k \\ \Delta \omega \end{bmatrix} \qquad (4-132)$$

The calculation method of the other terms (i.e. the diffusive fluxes, the source term, and the time integration) of equation (4-122) is carried out as described in sections 4-4 to 4-6 respectively.

Both numerical methods for a rotating frame of reference, recover to the fixed frame of reference scheme for $\boldsymbol{\omega} = 0$.

The code has been validated for a turbulent flow in a rotating and non-rotating square duct in section 5-4.1 and for an unshrouded turbine rotor blade in section 5-4.2.

4-10 Boundary conditions

Boundary conditions have a crucial role in the numerical accuracy of any CFD scheme. Their role differentiates one case study from another, in the flow fields of both are governed by the same fluid equations. Therefore, the ill-treatment of the boundary conditions has a negative effect on the scheme stability and convergence speed, and finally leads to inaccurate solution. The imposed boundary conditions are defined using an exterior frame one cell deep all around the physical domain of each block, as shown in fig. 4-5. The boundary condition values are function of the first interior cell variables and the imposed variables on the exterior ghost cell. This function is specified according to the physical boundary condition defined at the interface between the first interior and the ghost cell. In this study, many types of boundary condition are used in the numerical solution of both Euler and RANS equations such as inflow, outflow, solid wall, far-field, symmetry, periodic boundary, and inter-block boundary. The next subsections describe the numerical treatment of the boundary conditions used in this study.

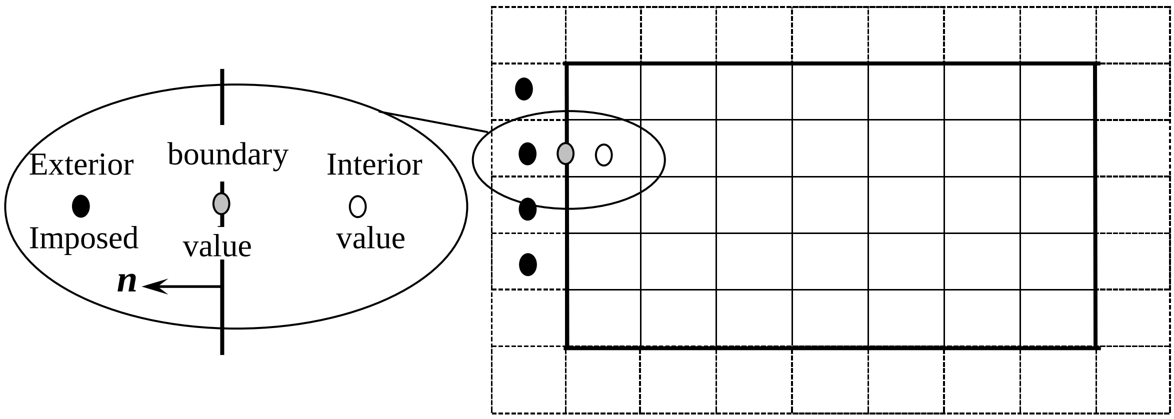

Fig. 4-5 The ghost cells (dashed line) around the computational domain (the solid thick line).

4-10.1 Inflow boundary condition

The inflow boundary condition can either be subsonic inflow or supersonic inflow based on the component of the inlet Mach number normal to the boundary $\boldsymbol{M} \cdot \boldsymbol{n}$. The numerical treatment of both categories is defined as follow:

Subsonic inflow

In case of three dimensional inviscid flows, since there are four characteristic waves (λ_2 to λ_5) moving towards the domain interior, the number of variables to be defined is four. The selected variables imposed at the boundary interface depend on the available experimental data. Commonly, the imposed variables are the stagnation temperature T_0, stagnation pressure P_0, and two inlet flow angles $\alpha,$ and β. The imposed conditions are used in addition to the interior flow variables to calculate the intermediate boundary states following these steps:

The negative Riemann invariant is defined as

$$R^- = \left[\boldsymbol{u}_i.\boldsymbol{n} - \frac{2a}{(\gamma-1)}\right]_{int} \tag{4-133}$$

where $\mathbf{n}$, a are the normal unit vector to the boundary cell face and the speed of sound based on the interior conditions. The interior tangential velocity component is

$$u_t = |\boldsymbol{u}_i - \boldsymbol{u}_i.\boldsymbol{n}|_{int} \tag{4-134}$$

The entropy value at the boundary and the total enthalpy using the imposed conditions are

$$s = \frac{P_0}{(\rho_0)^\gamma} \ , \qquad h_0 = \frac{\gamma R T_0}{\gamma - 1} \tag{4-135}$$

The positive Riemann invariant is defined as

$$R^+ = \frac{1}{\gamma-1}\left[(\gamma-3)R^- + 4\sqrt{h_0 - \frac{{V_t}^2}{2} - \frac{\gamma-1}{2}(R^-)^2}\right] \tag{4-136}$$

Now, the normal velocity and the speed of sound at the boundary can be calculated using the Riemann invariants

$$u_{nb} = \frac{R^+ + R^-}{2} \ , \qquad a = \frac{\gamma-1}{4}(R^+ - R^-) \tag{4-137}$$

The boundary velocity is $u_b = \sqrt{{u_{nb}}^2 + {u_t}^2}$

The velocity components at the inlet are obtained by decomposing the boundary velocity u_b according to the two prescribed flow angles

$$u_b = u_b cos(\alpha)$$

$$v_b = u_b \sin(\alpha) cos(\beta)$$

$$w_b = u_b \sin(\alpha) sin(\beta) \tag{4-138}$$

The density, static pressure, and temperature at the boundary are evaluated as follows:

$$\rho_b = \left(\frac{a^2}{\gamma s}\right)^{\frac{1}{\gamma-1}} \tag{4-139}$$

$$p_b = \frac{\rho_b a^2}{\gamma} \tag{4-140}$$

$$T_b = T_0 \left(\frac{p_b}{P_0}\right)^{\frac{\gamma-1}{\gamma}} \tag{4-141}$$

Supersonic inflow

For supersonic inflow, all the characteristic waves are directed into the interior of the computational domain, therefore a complete set of boundary variables should be defined at the inlet. In this study, the stagnation pressure P_0, stagnation temperature T_0, and the inlet Mach number vector $\boldsymbol{M}$ are imposed at the inlet boundary condition. The boundary primitive variables are calculated from the imposed variables using the following relations:

$$T_b = \frac{T_0}{\left[1 + \frac{\gamma - 1}{2}\left({M_x}^2 + {M_y}^2 + {M_z}^2\right)\right]} \tag{4-142}$$

$$p_b = p_0 \left(\frac{T_b}{T_0}\right)^{\frac{\gamma}{\gamma-1}} \tag{4-143}$$

$$\rho_b = \frac{p_b}{RT_b} \tag{4-144}$$

$$a_b = \sqrt{\gamma R T_b} \tag{4-145}$$

$$\boldsymbol{u} = \boldsymbol{M} a_b \tag{4-146}$$

4-10.2 Subsonic outflow

In subsonic outflow, only one boundary condition should be imposed because there is only one characteristic wave directed toward the interior of the computational domain. The static pressure p_b at exit is defined and the remaining primitive variables are extrapolated from interior domain. The back pressure equation, as a function of normal Mach number component, is obtained from Manna [1992]:

$$c_1 M_{nb}^3 + c_2 M_{nb}^2 + c_3 M_{nb} + c_4 = 0 \tag{4-147}$$

where the coefficients c_1, c_2, c_3, and c_4 are:

$$c_1 = \gamma - 1 \tag{4-148}$$

$$c_2 = 2\gamma \tag{4-149}$$

$$c_3 = \gamma + 3 \tag{4-150}$$

$$c_4 = 2 - \left[\left(\rho a (1 + M_n)^2 \left(\frac{\gamma - 1}{\gamma} V_n + \frac{2a}{\gamma} \right) \right)_{int} \right] / p_b \qquad (4-151)$$

The normal component of the boundary condition Mach number M_{nb} can be obtained by solving the first equation using a Newton-Raphson method. By substituting the value of M_{nb} into the following equation $[\frac{\rho a}{4}(1 + M_n^2)]_{int} = [\frac{\rho a}{4}(1 + M_n^2)]_{boundary}$, the speed of sound at the boundary a_b can be obtained:

$$a_b = \frac{[\gamma p_b (M_{nb} + 1)^2]}{[\rho a (M_n + 1)^2]_{int}} \qquad (4-152)$$

Then, the boundary condition primitive variables are determined as follows:

$$\rho_b = \frac{\gamma p_b}{{a_b}^2} \qquad (4-153)$$

$$u_{nb} = M_{nb}\, a_b \qquad (4-154)$$

$$\boldsymbol{u}_b = (\boldsymbol{u}_i - (\boldsymbol{u}_i . \boldsymbol{n})\boldsymbol{n})_{int} + u_{nb}\,\boldsymbol{n} \qquad (4-155)$$

4-10.3 Supersonic outflow

In this case, the waves leave the computational domain. The boundary condition conservative variable must be extrapolated from the solution inside the domain. In this study, a zero order extrapolation approach is used to calculate the boundary condition variables, so $\boldsymbol{u}_b = \boldsymbol{u}_{int}$.

4-10.4 Inflow/outflow boundary conditions for turbomachinery

The inflow/outflow boundary conditions for turbomachinery are written in terms of perturbations about the mean flow from the upstream/downstream blade row. This boundary condition is developed by Chima [1998] based on Giles' non-reflecting characteristic-based boundary condition. More details are available in Chima [1998].

4-10.5 Solid wall boundary condition

Inviscid flow

The inviscid wall boundary condition means that the flow slips over the surface. Due to this condition, the velocity vector must be tangent to the surface. In other words, the wall normal velocity component must vanish.

$$\boldsymbol{u_b} \cdot \boldsymbol{n} = 0 \qquad (4-156)$$

Therefore, the velocity components of the boundary cell are:

$$u_n = (\boldsymbol{u}_i . \boldsymbol{n})_{int} \qquad (4-157)$$

$$\boldsymbol{u}_b = (\boldsymbol{u}_i - 2u_n \boldsymbol{n})_{int} \qquad (4-158)$$

The imposed pressure gradient is equal to zero by setting $\frac{\partial p}{\partial \boldsymbol{n}} = 0$. Accordingly, the pressure at the boundary cell is put equal to the first interior cell. Also, the temperature is set equal to the interior temperature by assuming adiabatic wall $\frac{\partial T}{\partial \boldsymbol{n}} = 0$. Since the pressure and temperature of the boundary cell is equal to the interior values, the density is taken equal the interior, by the equation of state $p = \rho RT$.

Viscous flow

For viscous flows, the fluid at the solid surface has a zero relative velocity. Then, for a stationary surface, the boundary velocity vector is defined as $\boldsymbol{u}_b = -\boldsymbol{u}_{int}$ to impose a zero velocity vector at the solid surface. By imposing a zero pressure gradient normal to the wall and no heat flux through the wall (adiabatic solid wall), the pressure and temperature can be set equal to the interior variables,$p_b = p_{int}$ and $T_b = T_{int}$.

4-10.6 Far-field boundary condition

The domain of the simulation of the flow around bodies such as wings, airfoils, vehicles requires a boundary far enough from these configurations so that free stream conditions can be assumed at this boundary. The far-field boundary condition is applied in such cases. The far-field boundary condition should be far enough from the body to suppose that the unperturbed field is reached. The far-field boundary should prevent outgoing waves from reflecting back in the interior domain. The numerical treatment of the far-field boundary is based upon the locally fixed and extrapolated Riemann invariants. The Riemann invariants are defined normal to the boundary and they are evaluated as follows:

- The incoming Riemann invariant R^- is calculated from the free stream conditions.

$$R^- = \left[\boldsymbol{u}.\boldsymbol{n} - \frac{2a}{(\gamma - 1)}\right]_\infty \qquad (4-159)$$

- The outgoing Riemann invariant R^+ is calculated from the interior conditions.

$$R^+ = \left[\boldsymbol{u}.\boldsymbol{n} - \frac{2a}{(\gamma - 1)}\right]_{int} \qquad (4-160)$$

The local normal velocity and speed of sound at the boundary are given by:

$$u_{nb} = \frac{R^+ + R^-}{2}\ , \qquad a_b = \frac{\gamma - 1}{4}(R^+ - R^-) \qquad (4-161)$$

The boundary is classified as inflow or outflow according to the sign of u_{nb}. Since the unit normals to the boundary are directed to the exterior of the physical domain, the positive sign of u_{nb} means outflow and the negative sign means inflow.

At an outflow boundary, the set of boundary condition variables are:

$$\boldsymbol{u}_b = (\boldsymbol{u}_i - (\boldsymbol{u}_i.\boldsymbol{n})\boldsymbol{n})_{int} + u_{nb}\boldsymbol{n} \tag{4-162}$$

$$s_b = s_{int} \tag{4-163}$$

$$\rho_b = \left(\frac{\rho_{int}^{\gamma} {a_b}^2}{\gamma p_{int}}\right)^{\frac{1}{\gamma-1}} \tag{4-164}$$

$$p_b = \frac{\rho_b {a_b}^2}{\gamma} \tag{4-165}$$

At an inflow boundary, the set of boundary condition variables are:

$$\boldsymbol{u}_b = (\boldsymbol{u}_i - (\boldsymbol{u}_i.\boldsymbol{n})\boldsymbol{n})_{\infty} + u_{nb}\boldsymbol{n} \tag{4-166}$$

$$s_b = s_{\infty} \tag{4-167}$$

$$\rho_b = \left(\frac{\rho_{\infty}^{\gamma} {a_b}^2}{\gamma p_{\infty}}\right)^{\frac{1}{\gamma-1}} \tag{4-168}$$

$$p_b = \frac{\rho_b {a_b}^2}{\gamma} \tag{4-169}$$

4-10.7 Symmetry plane

A symmetry plane can be created if the model exhibits no flux across that plane. Using a symmetry plane reduces the size of the computational domain and consequently the computational cost and time. The symmetry plane has the following conditions:

- The gradients of the pressure and density normal to the plane are zero, $\nabla p.\boldsymbol{n} = 0$, $\nabla \rho.\boldsymbol{n} = 0$, therefore.

$$p_b = p_{int} \tag{4-170}$$

$$\rho_b = \rho_{int} \tag{4-171}$$

- The gradient of the tangential velocity normal to the plane is zero.

$$\partial(\boldsymbol{u} \times \boldsymbol{n})/\partial \boldsymbol{n} = 0 \tag{4-172}$$

$$u_{t\,b} = u_{t\,int} \tag{4-173}$$

- The normal velocity should vanish at the symmetry plane

$$\boldsymbol{u} \cdot \boldsymbol{n} = 0 \tag{4-174}$$

4-10.8 Periodic boundary condition

Translational periodicity

The periodic boundary condition is applicable on a model that consists of a number of repeated basic units. This gives the opportunity to truncate the computational domain to one basic unit to study the flow through the entire model. The interchangeable effects between the repeated units are enforced by using periodic boundary conditions. Figure 4-6 shows the domain of the flow through the passage between two adjacent blades which is repeated to form the flow through a linear cascade. The figure shows the system of data exchange between the ghost cells and the first interior cells adjacent to the periodic boundary. The periodicity in the example of fig. 4-6 is implemented by imposing $[\mathbf{U}(i,1)]_b = \mathbf{U}(i,j\,\max-1)$ and $[\mathbf{U}(i,j\max)]_b = \mathbf{U}(i,2)$.

Some problems have a pressure gradient in the direction of the periodicity, such as the study of the fully developed flow in a stationary duct. In this case, the pressure gradient needs to be evaluated and added to the momentum equation in that direction. Then the transitional periodicity can be treated as described in the preceding paragraph.

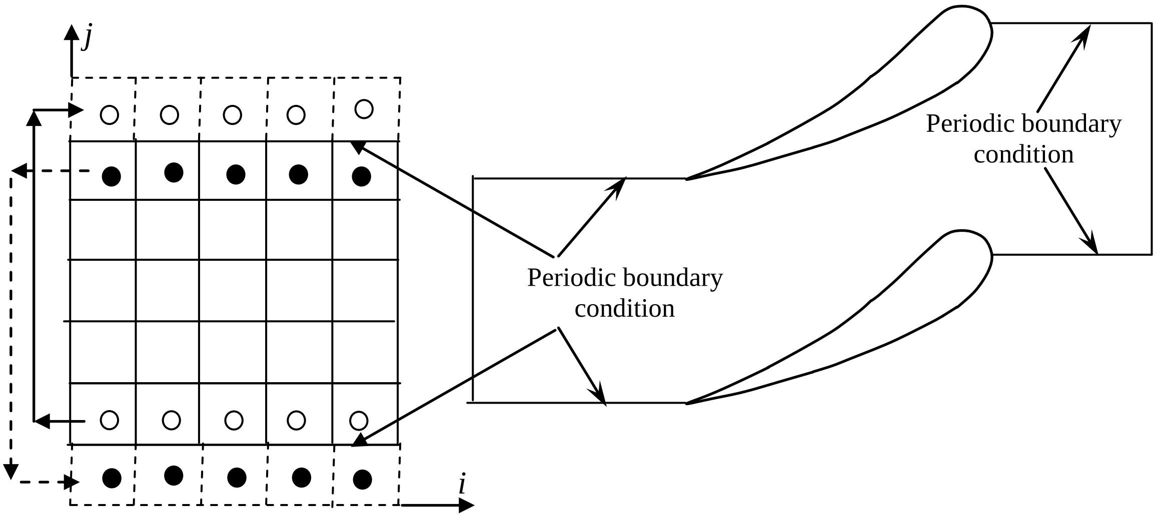

Fig.4-6 Transitional periodic boundary condition

Rotational periodicity

The rotational periodicity is applicable in many CFD problems when the physical model exhibits geometric periodicity by rotating about the axis associated with the geometry. The flows in fluid machinery such as pumps, compressors, and turbines are examples in which to use the rotational periodicity boundary conditions. Figure 4-7 shows the rotational periodic boundaries. The rotational axis is assumed to coincide with the x-axis. Between rotationally periodic planes, the vector quantities such as the velocity vector should be transformed through a rotation matrix **R** while the scalar quantities such as the pressure and density remain unchanged (i.e. $p_{b1} = p_1$ and $\rho_{b1} = \rho_1$). The boundary value of the velocity vector $\boldsymbol{u}_{b1}$ is determined from:

$$\boldsymbol{u}_{b1} = \mathrm{R}\boldsymbol{u}_1 \qquad (4-175)$$

where

$$\mathrm{R}=\begin{bmatrix} 1 & 0 & 0 \\ 0 & cos\phi & -sin\phi \\ 0 & sin\phi & cos\phi \end{bmatrix} \qquad (4-176)$$

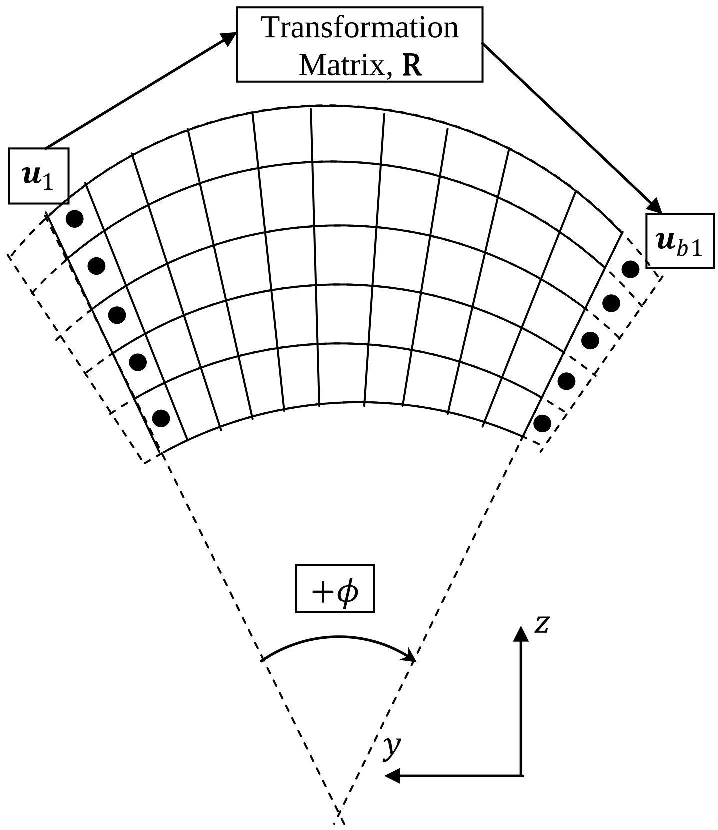

Fig.4-6 Rotational periodic boundary condition.

4-10.9 Inter-block boundary condition

The multiblock approach is used to construct the numerical mesh for a geometrically complex domain. In this approach, the physical domain is divided into a finite number of parts called zones. The border between two neighbouring zones is called connectivity interface. The flow inside one zone exchanges information with its neighbours through the connectivity interface. The mechanism of communication between two neighbouring zones is shown in fig. 4-8. The conservative variables of the first interior cells adjacent to the connectivity interface are copied to the ghost cells of the neighbouring zone.

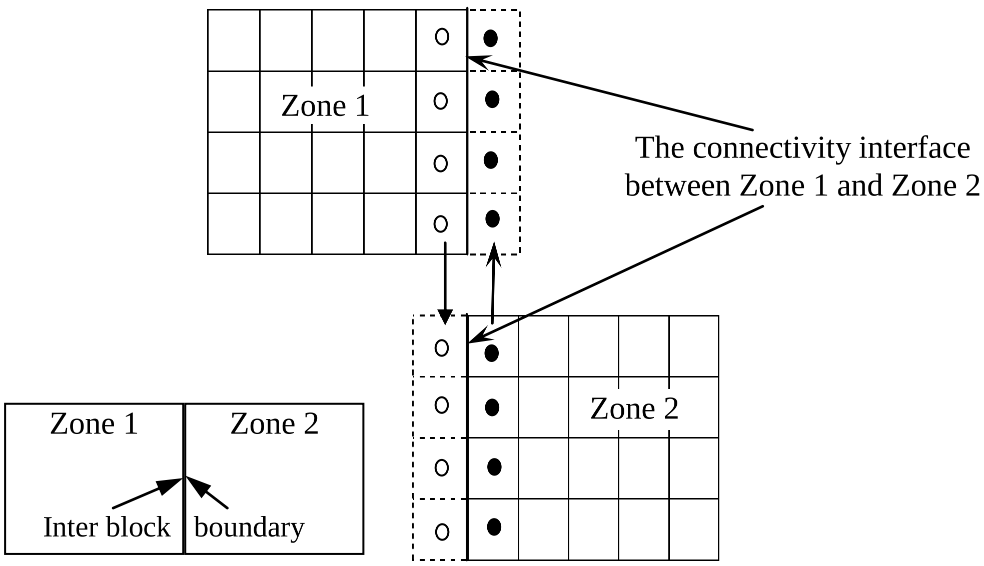

Fig. 4-8 The data exchange in the inter-block boundary condition.

4-11 CGNS input/output

While developing the 3D in house solver, it was decided to adapt an input output format that makes it compatible with commercial pre and post-processors. For this, the CFD General Notation System (CGNS) was used as the input/output standard, Rumsey et al. [2005]. The CGNS file includes the information required by the flow solver such as the grid, the flow solution, the connectivity, the boundary conditions, and auxiliary information. Also, Using the CGNS database structure saves time, prevents the potential errors in setting up the information, and facilitates the exchange of data between the CFD users. Therefore a CGNS reader and writer are built to read and write to input/output the test cases in the flow solver. The CGNS format enables to post-process the solution file by reading it directly into Tecplot 360 2008, using the CGNS reader that is built-in into Tecplot 360 2008. The CGNS reader and writer have been tested using commonly available test cases provided by Alstom and were shown to be able to read in, time-march, and output the numerical solution.

Chapter 5

The Flow Solver Validation

5-1 The code validation strategy

This chapter contains the numerical results from six test cases to validate the in-house flow solver. The test cases are arranged in the order of increased flow complexity. The six cases, classified according to their respective frame of reference, are:

- Fixed frame of reference.
    1- Shock tube.
    2- Supersonic flow over 10 degree ramp.
    3- Spherical Explosion.
    4- Wing-body junction.
- Rotating frame of reference.
    1- Turbulent flow in a rotating square duct.
    2- Unshrouded axial turbine rotor cascade.

The test cases have been validated against the available experimental and numerical data. The following steps were carried out for all the cases:

1- An in-house CFD pre-processor for a 3D multiblock structured mesh was written in FORTRAN 90 (except the last test case in which the grid was only rewritten with generating a halo of ghost cells that surrounds every block to be compatible with the flow solver structure).
2- Using the CFD pre-processor, CGNS input file was written, containing the grid, the initial solution, and a proper set of boundary conditions.
3- The in-house flow solver was then applied to the CGNS test case and the solution written in a CGNS.

4- The CGNS output, containing the grid, the flow solution, and the boundary conditions, was post-processed using Tecplot 360 2008 and the results compared with the experimental (whenever available) and numerical data.

5-2 Fixed frame of reference test cases

5-2.1 Test case 1: Shock tube problem (1D inviscid flow)

A shock tube is used as the first test case to validate the three-dimensional extension of the two-dimensional numerical method of Bennett [2005]. This test uses a sub-set of the flow solver software, specifically the Euler equations are solved instead of the full $k - \omega$ time dependent RANS. This test case models the essentially one-dimensional inviscid flow inside a shock tube of rectangular cross-section. The shock tube duct is 8.0 m long and has a rectangular cross-section 1.0 x 0.165 m^2. The top, bottom and side walls are rigid. The duct is open at both ends lengthwise. A structured mesh of four blocks discretizes the flow domain, as shown in Fig. 5-1. Blocks 1 and 4 use a uniform mesh of 102 x 19 x 3 computational cells. Blocks 2 and 3 use a streamwise longer mesh of 154 x 19 x 3 cells. The purpose of using meshes of unequal length is to construct inter-block boundaries in a region of smoothly changing flow, to test the performance of the multi-block three-dimensional scheme connectivity.

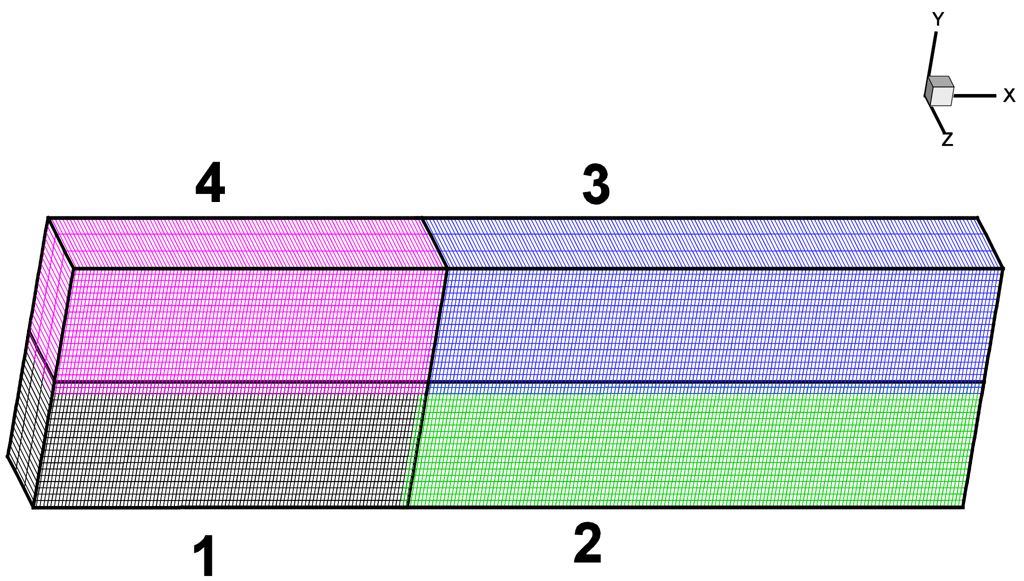

Fig. 5-1 Shock tube mesh geometry.

The shock tube flow is represented diagrammatically in Fig. 5-2a. Initially, a diaphragm splits the flow domain into two compartments containing air at different density and pressure, at rest in a rigid walled rectangular tube. The initial flow state (ρ,|**u**|, p) is (2.881, 0, 4.4) and (1, 0, 1), in the left and right compartments respectively, where ρ and p are the normalized static density and pressure and **u** is the normalized velocity vector. The flow variables are normalized with respect to the initial flow state in the right compartment, where the density ρ_r = 1.125 kg/m^3, the pressure $p_r = 1.0(\rho_r\ a_r\ ^2)$, and the speed of sound a_r = 390 m/s. Velocities are normalized by the rightwards propagating shock tube velocity $u_{shock} = 1.486a_r$, lengths are normalized by the computational domain length l = 8 m and time is normalized by l/a_r.

After removing the diaphragm, a shock wave and a contact surface discontinuity travel from X/L = 0.0 through the low-pressure section (right side). A rarefaction wave travels from X/L = 0.0 through the high-pressure section (left side). The flow field at any time t > 0.0 is divided into five distinct regions. These are numbered 1 to 5 in Fig. 5-2b. The first and last regions are undisturbed by the compression and rarefaction waves and maintain their initial left and right flow states. The flow properties in regions 2 to 4 at t > 0.0 are given in Bennett [2005], following the analytical solution in Hirsch [1990].

The inviscid compressible flow of test case one is modelled by the in-house three-dimensional CFD method, with zero turbulent kinetic energy, k = 0, and zero laminar viscosity, μ_l = 0. Under these conditions, the flow governing equations reduce to the discrete short-time averaged Euler equations. At the beginning of the computation, the left half of the modelled domain is primed with the left compartment flow state from Fig. 5-2a. The right half of the computational domain is primed with the right compartment flow state. Inviscid wall boundary conditions are imposed along the shock tube sides, to model the rigid boundaries, using flow symmetry about the plane of each wall. At the shock tube open ends, the flow state is zero order extrapolated from the interior.

The flow develops from its initial state at t = 0.0 to a time of $t = 0.1906l/a_\infty$ seconds. The analytical solution and the predictions from the 2D scheme of Bennett [2005] are compared against the three-dimensional method predictions in Figures 5-3 to 5-5. Figures 5-3, 5-4, and 5-5 show respectively the normalized static density, pressure and velocity profiles along the length of the shock tube. The 2D prediction is traversed along the shock tube centreline, at $Y = 0.5m$. The 3D prediction is traversed at ($Y = 0.5m$; $Z = 0.055m$). In these figures, the analytical solution, the two-dimensional model predictions, and the three-dimensional prediction are shown by the solid-green, dotted-black, and dashed-blue lines, respectively. Figures 5-3, 5-4, and 5-5 show the 3D prediction overlapping the two-dimensional one and in good agreement with the analytical solution. There is no significant deterioration between the 3D solution and 2D solution, confirming that the shock-capturing characteristics of the two-dimensional scheme have been preserved in its three-dimensional extension. Figure 5-6 shows the normalized static density distribution in the Y direction at $X/L = -0.18$ and $X/L = 0.18$. In Fig. 5-6, the predicted density is spanwise constant. There is no evidence of any numerical error generated at the $Y/L = 0.06$ plane, which is the inter-block boundary between blocks 1-4 and 2-3 shown by a dotted line in fig. 5-6. Therefore the flow prediction is unaffected by the multi-block discretization of the computational domain and the inter-block boundaries work properly in the 3D scheme.

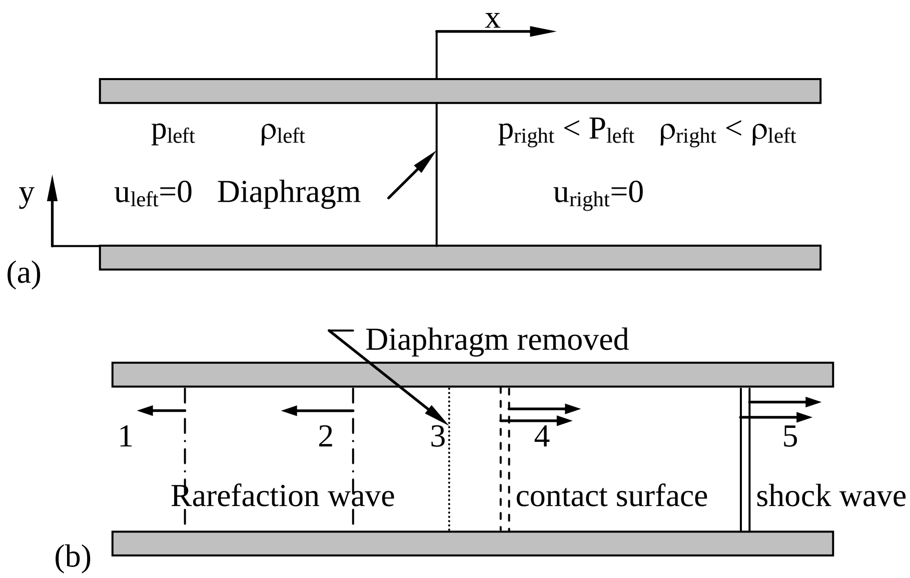

Fig. 5-2 Shock tube flow geometry. (a) Initial flow conditions before removing the diaphragm (b) flow field regions at time t > 0 after the diaphragm removal, Bennett [2005].

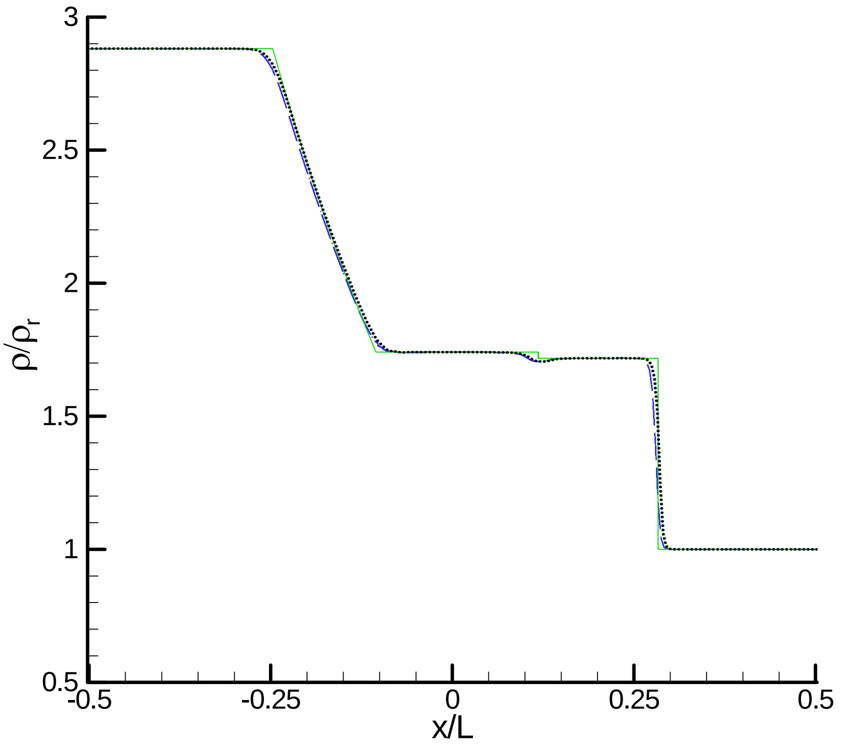

Fig. 5-3 Static density distribution normalized by the right compartment density at t = 0.1906l/a_∞ seconds. (—) Analytical solution. (···) Bennett [2005]. (---) the present solver.

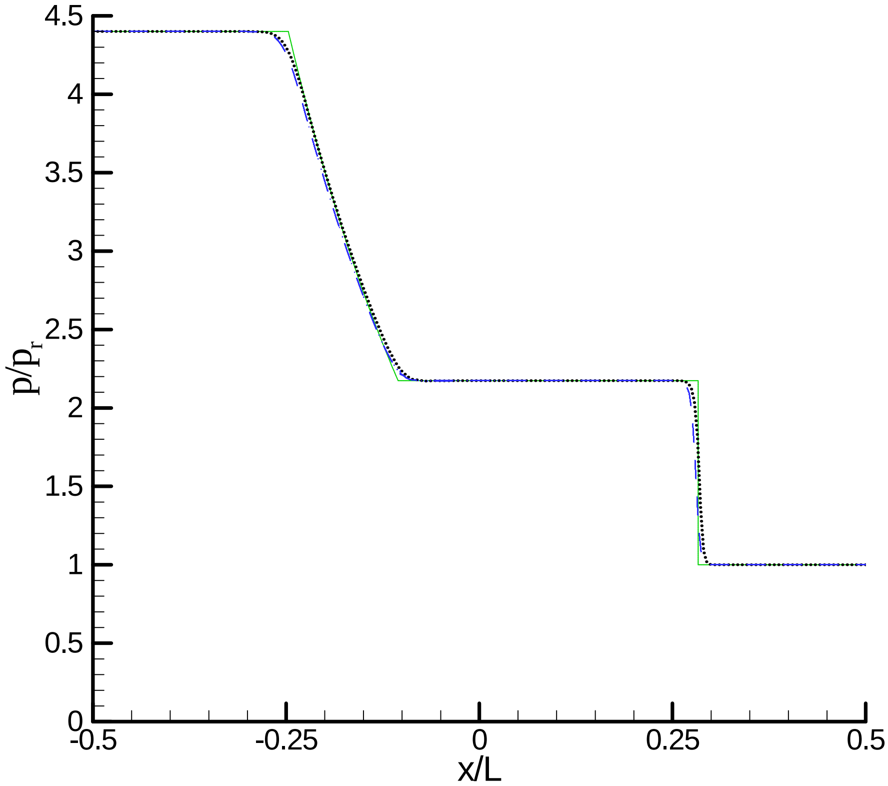

Fig. 5-4 Static pressure distribution Normalized by the right compartment pressure at t = 0.1906l/a_∞ seconds. (—) Analytical solution. (···) Bennett [2005]. (---) the present solver.

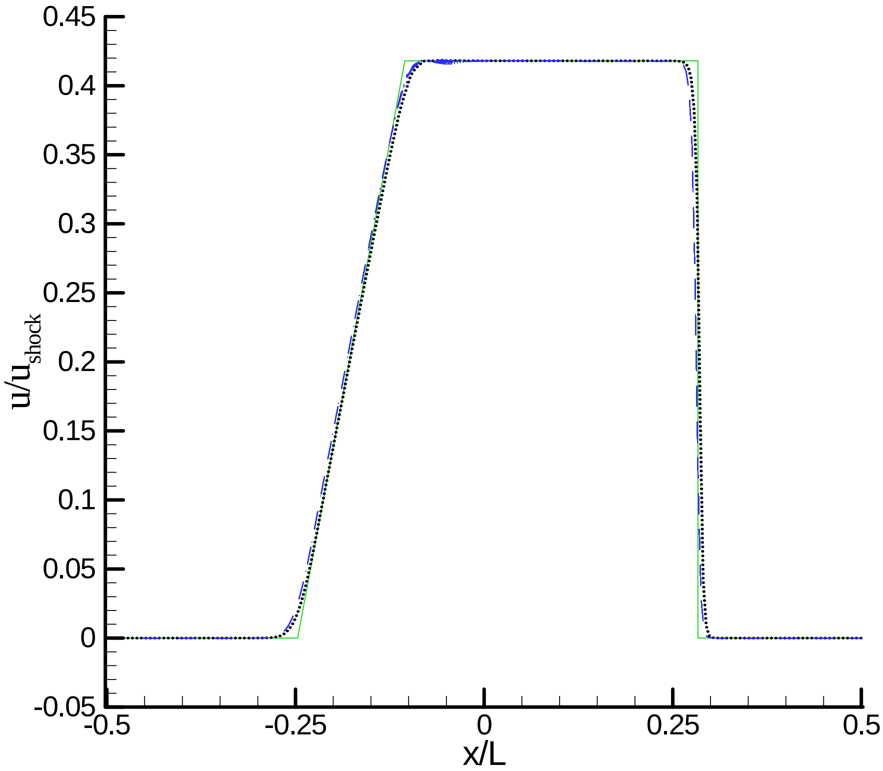

Fig. 5-5 Velocity distribution normalized by shock wave velocity at t = 0.1906l/a_∞ seconds. (—) Analytical solution. (···) Bennett [2005]. (---) the present solver.

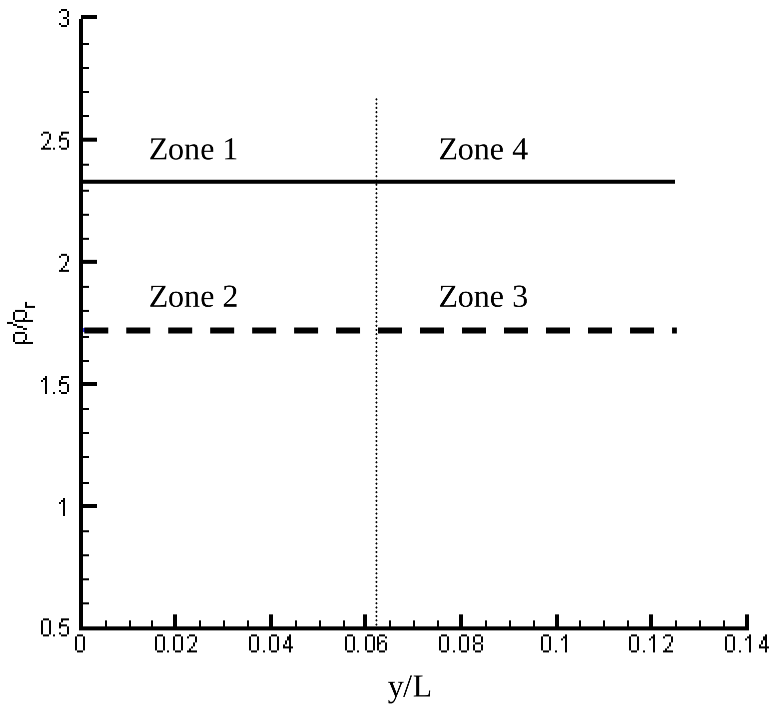

Fig. 5-6 The normalized static density along Y direction at X/L = -0.18 (continuous line) and X/L = 0.18 (dashed line) at t = 0.1906l/a_∞ seconds.

5-2.2 Test case 2: Supersonic flow over a 10^o ramp (2D inviscid flow)

The multiblock flow over ramp test case consists of two blocks as shown diagrammatically in Fig. 5-7a. The lower wall of the geometry consists of a 1m long horizontal plate, a 1.0154m long inclined plate at 10 degrees, representing a compression ramp, followed by a 10 degree expansion edge, and a 3m long horizontal flat plate thereafter along x axis. The duct is 5m long in x and has a rectangular cross-section. The inlet cross-sectional area is 1x0.25m^2. The two blocks are meshed using the structured mesh shown in fig. 5-7b. The first block has 300x75x10 computational cells in x, y, and z. The second block has 75x75x10 computational cells along x, y, z directions. Special care was paid when meshing along the x axis to create a mesh that is orthogonal to the wall. The curvilinear section of the mesh starts slightly upstream the compression ramp and continues to the duct end. Supersonic inflow, supersonic outflow, and inviscid wall boundary conditions are used. Since the entire flow is supersonic, the inflow state is fixed at the free stream conditions of Mach number M=2.0, stagnation pressure p_0=270kPa, and stagnation temperature T_0=288 K. The outflow is extrapolated from the interior cells. An inviscid wall boundary condition is applied to the wall of the domain.

The numerical results of the supersonic flow over a10 degree ramp are shown in Fig. 5-8. Figure 5-8a shows the contours of static pressure. The figure shows the oblique shock wave due to 10 degree compression ramp, separating zones (a) and (b), the shock reflection, separating zones (b) and (c), and a Prandtl-Mayer expansion fan, separating zones (b) and (d). In figure 5-8b, the solution is smooth across the inter-block boundary between zone 1 and zone 2. In table 5-1, the flow conditions across the first oblique shock and shock wave angle are compared with the analytical values obtained from the Rankine-Hugoniot equations. Also, the numerical Mach numbers in four regions marked (a - d) on fig. 5-8a are compared with the corresponding analytical values in table 5-2. Tables 5-1 and 5-2 show that the results are in good agreement with the analytical solution and the numerical predictions are within 1.0 % of the analytical values.

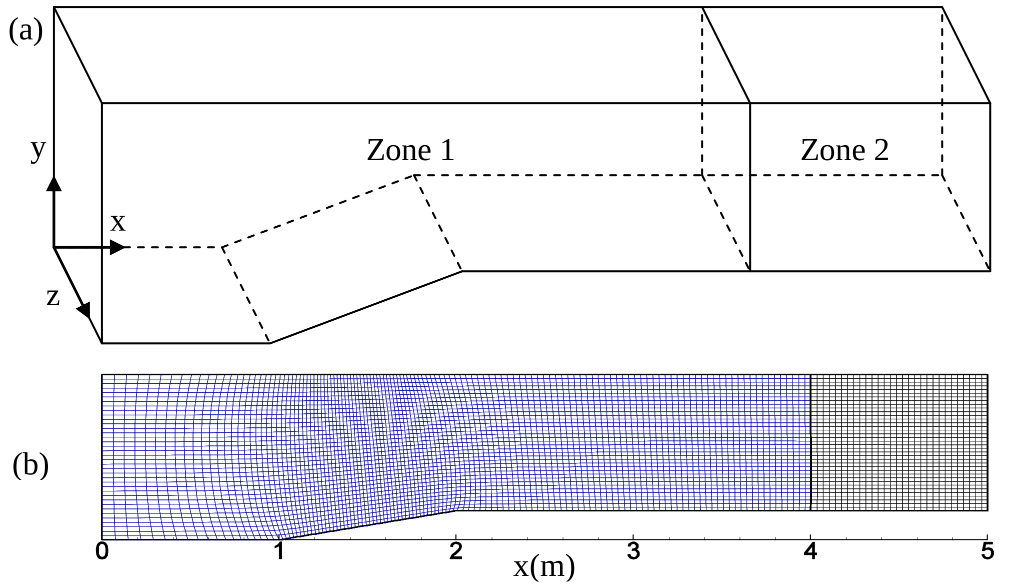

Fig. 5-7 a) A diagrammatic sketch for the duct and 10 degree ramp geometry.

Fig. 5-7 b) the test case structured mesh (28125 cells in each z plane).

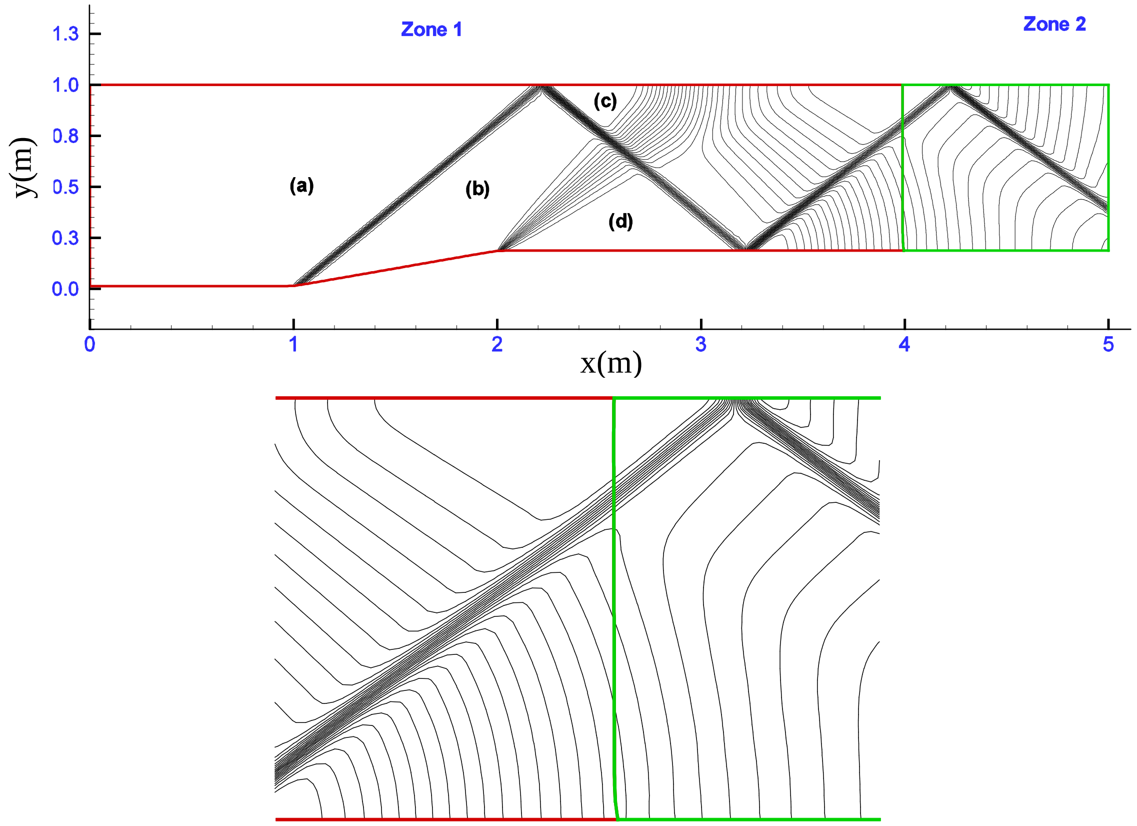

Fig. 5-8 M_∞=2.0 inviscid 2D flow over a 10^o ramp.

a) Isobar contours $\Delta p = 2.0$ kPa.

b) Details across blocks 1 and 2, showing a smooth solution transfer across the inter block boundary.

Figure 5-9 shows the plot of the pressure coefficient Cp of the lower duct wall against the x axis. The pressure coefficient $p = \frac{p - p_\infty}{\frac{1}{2}\rho_\infty u_\infty^2}$, where p is the local static pressure, p_∞ is the inlet static pressure, ρ_∞ is the inlet static density, and u_∞ is the inlet velocity. At x =1m the flow is compressed by a 39.3^o oblique shock, increasing the wall static pressure coefficient to Cp =0.2525. At x=2m the flow is expanded by a Prandtl-Mayer expansion fan. This reduces the Cp to 0.0010. At x=3.224m, the 39.3^o shock reflected from the upper duct wall impinges on the lower duct wall whereupon it is reflected away from the floor. This doubles the compression action and raises the pressure coefficient Cp to 0.6428. The pressure coefficient profile in the range $0 \leq x \leq$ 3.223m can be obtained analytically from the Rankine-Hugoniot equations. The analytical solution is shown in fig. 5-9 by the dotted line. Figure 5-9 shows a good agreement between the numerical and analytical pressure coefficients along the lower wall in the range $0 \leq x \leq 3.223$m, with minor numerical difference across the shocks and at the end of the Prandtl-Mayer expansion. By increasing the number of cells or using multi-level adaptive meshes, the slope deviation between the numerical and analytical Cp across the compression shock and expansion fan could be reduced.

Variable	Analytical value	Numerical value
Shock wave angle	39.3^o	39.43^o
Pressure ratio $\frac{p_b}{p_a}$	1.7070	1.7070
Density ratio $\frac{\rho_b}{\rho_a}$	1.4580	1.4586
Mach ratio $\frac{M_b}{M_a}$	0.8204	0.8203

Table 5-1. Comparison between numerical and analytical flow states across the oblique shock. Subscripts (a) and (b) refer to the states in regions (a) and (b) in fig. 5-8a.

Flow region	Analytical Mach number	Numerical Mach number
(a)	2.0000	2.0000
(b)	1.6408	1.6406
(c)	1.3000	1.2880
(d)	2.0000	1.9860

Table 5-2. Comparison between numerical and analytical Mach numbers in regions (a - d) in fig. 5-8a.

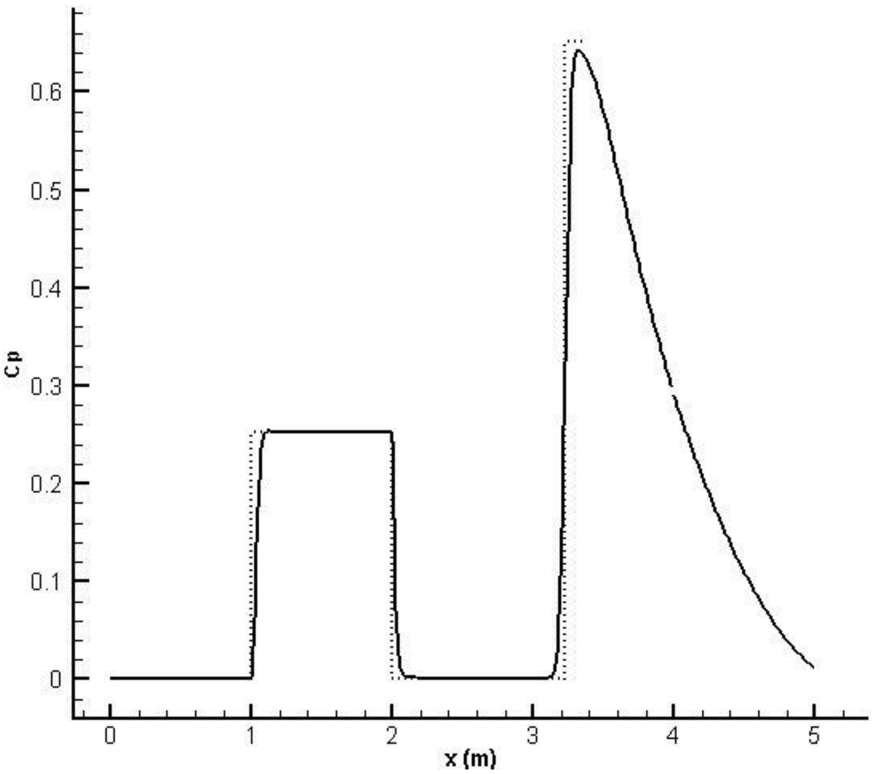

Fig. 5-9 Lower wall pressure coefficient distribution. (—) the present solver. (···) Analytical solution.

5-2.3 Test case 3: Spherical explosion (3D inviscid flow)

A three-dimensional spherical explosion test case is used to validate 3D Euler equation solver. The test case geometry is a cube of length 2.0m divided into two zones, as shown in fig. 5-10. The initial condition of the test case consists of two regions. The first region is the inside of a 0.4m radius sphere centred at (1m, 1m, 1m). The second region is the domain outside the sphere, as shown in fig. 5-10. The flow conditions at t=0.0 seconds for both regions are listed in table 5-3. The number of cells in the x, y, and z directions is 81x90x90 for zone 1 and 27x90x90 for zone 2. The numerical solution output is obtained at t=0.25 seconds using CFL=0.25. The results are compared against a reference radial solution described by Toro [1999] (the solid line) as shown in fig. 5-11 and 5-12. The figures show that the solution has a good agreement with the reference radial solution and contains the following basic characteristics:

- At x=0.2m and 1.8m, a spherical shock wave moves away from the centre of the sphere, (1,1,1).
- At x=0.39m and 1.61m a spherical contact surface discontinuity moves away from the centre of the sphere.
- Between $0.54 \leq x \leq 0.88$ and $1.12 \leq x \leq 1.46$, a spherical rarefaction wave moves toward the centre of the sphere.

Figures 5-13 to 5-15 show the density, pressure, and internal energy distributions on plane z=1.0m at t=0.25sec. The pressure is continuous across the contact surface discontinuity and the scheme preserves the monotonicity in the solution across all the step-like changes in flow state of this test case (shocks, expansions, contact surface discontinuity).

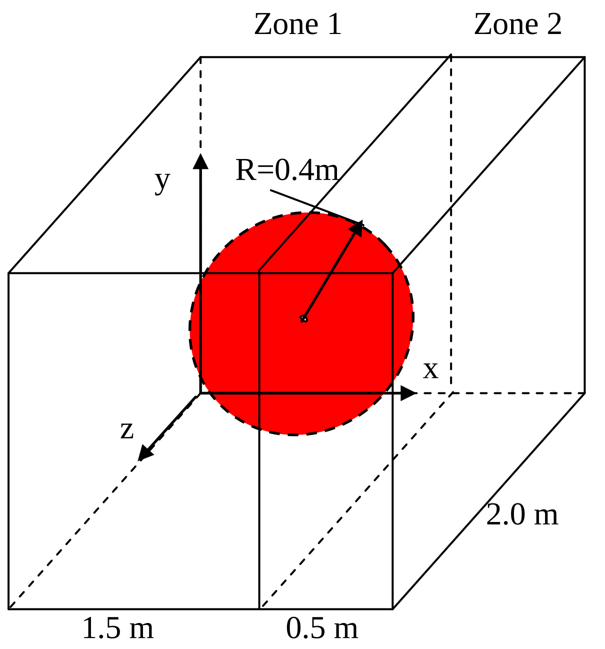

Fig. 5-10 Diagrammatic sketch for the spherical explosion test case geometry.

The flow state	Inside the sphere	Outside the sphere
ρ (kg/m^3)	1	0.125
U (m/s)	0.0	0.0
V (m/s)	0.0	0.0
W (m/s)	0.0	0.0
p (Pa)	1.0	0.1

Table 5-3. Fluid state inside and outside the sphere at t=0.0 seconds.

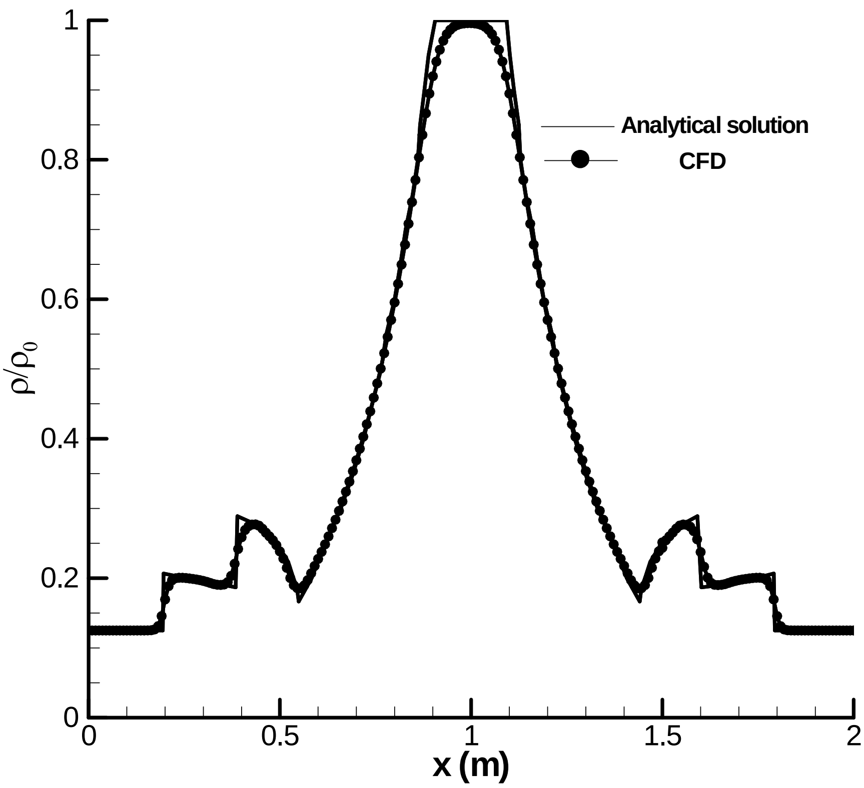

Fig. 5-11 Non-dimensional density distribution along x axis at y =1.0m, and z =1.0m at t=0.25 seconds. Density normalized by the state inside the sphere at t=0.0 seconds.

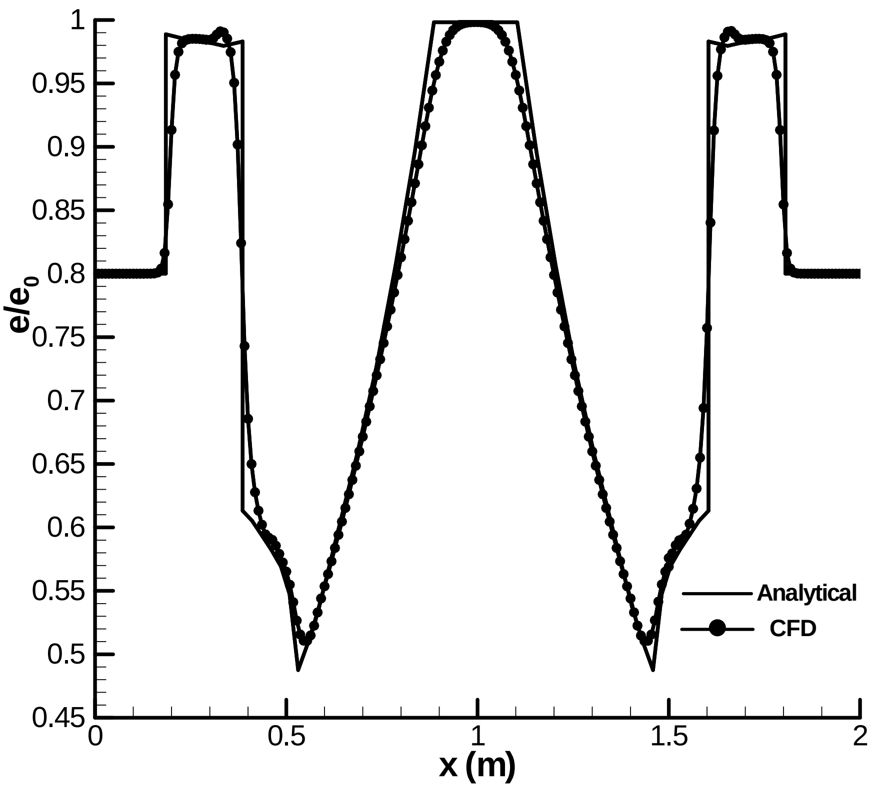

Fig. 5-12 Non-dimensional internal energy distribution along x axis at y =1.0m, and z =1.0m at t=0.25 seconds. Internal energy normalized by the state inside the sphere at t=0.0 seconds.

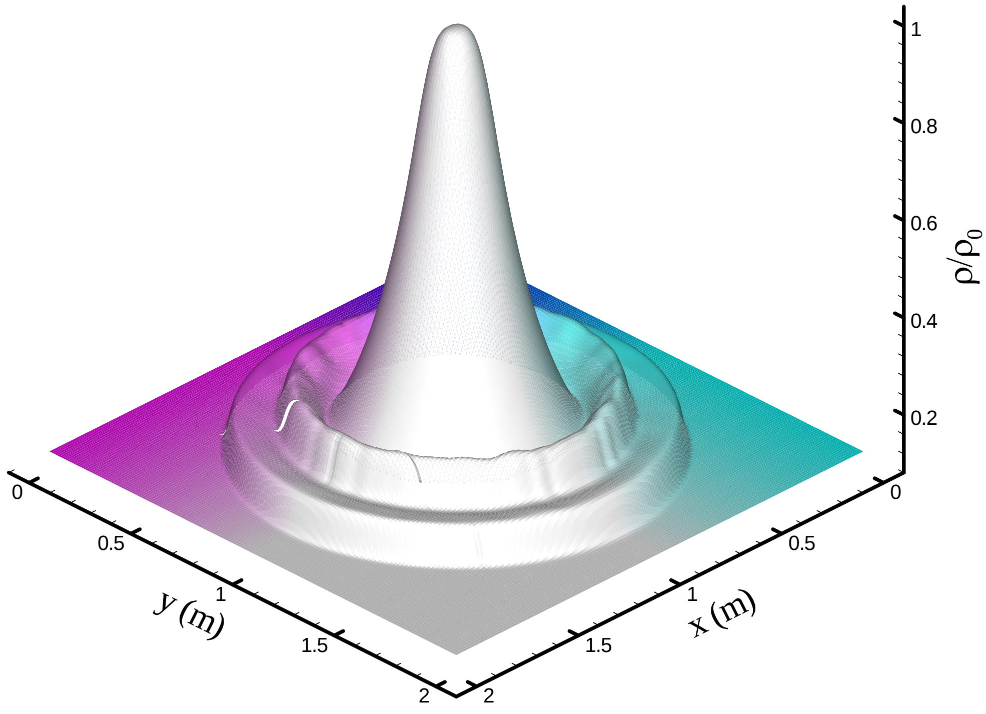

Fig. 5-13 Normalized density distribution at plane z=1.0m and t=0.25 seconds.

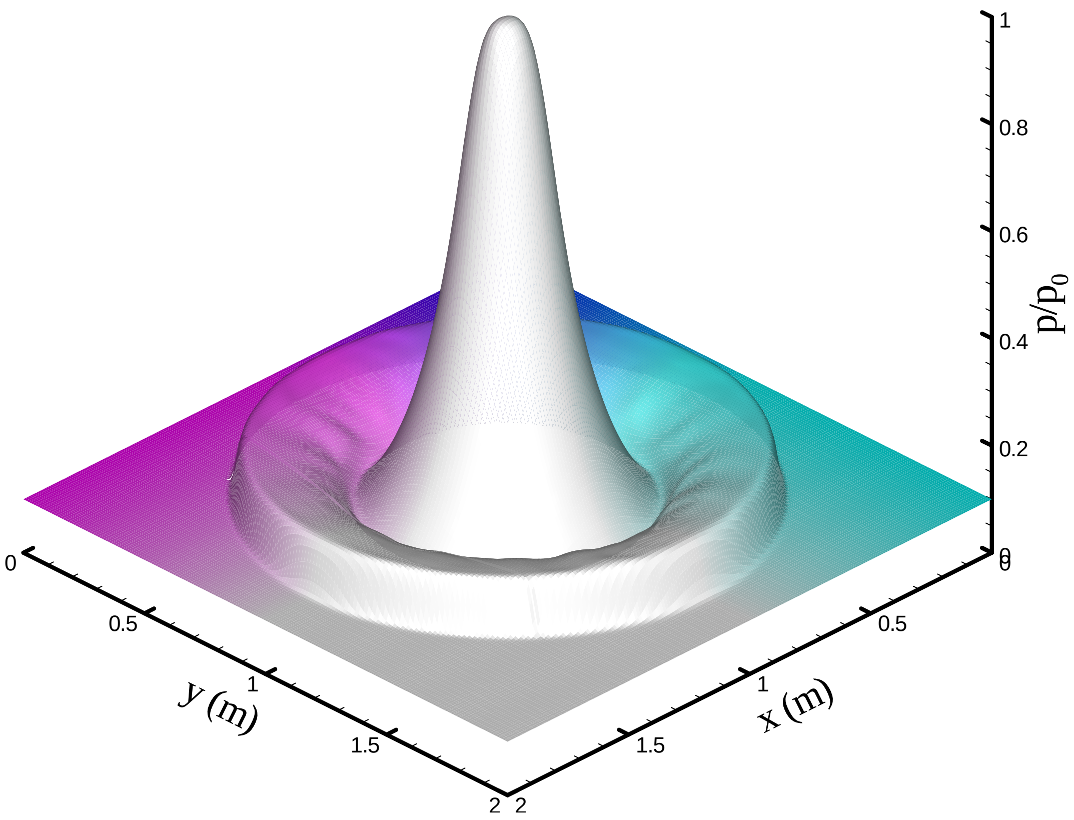

Fig. 5-14 Normalized pressure distribution at plane z=1.0m and t=0.25 seconds.

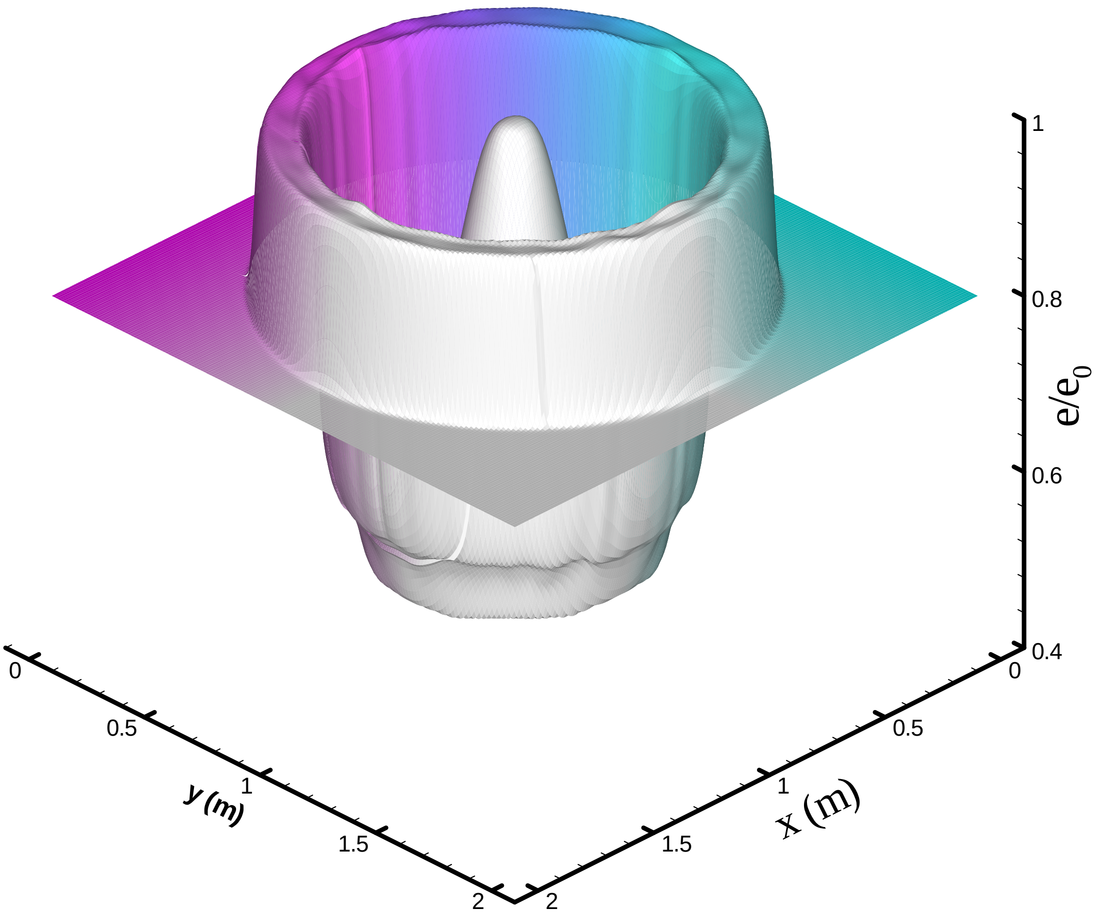

Fig. 5-15 Normalized internal energy distribution at plane z=1.0m and t=0.25 seconds.

5-2.4 Test case 4: Wing-body junction flow (3D viscous flow)

5-2.4 .1 Objective

A three-dimensional turbulent wing-body junction flow is selected as the fourth test case to validate the 3-D CFD scheme, using the hybrid RANS/LES turbulence model. The reasons of selecting this case study are:

- A three-dimensional complex flow occurs near the wing-body junction, where the flow exhibits large streamwise vortical structures that affect the wall boundary layers. Therefore, this flow contains many phenomena that resemble those at the hub and tip of a turbine stage, such as horseshoe vortex and other vortices located upstream and downstream of the wing body junction. A horseshoe vortex is present in the separation region at the front of the leading edge of the wing.
- A three-dimensional pressure driven turbulent boundary layer, created by a wing-body junction flow, was experimentally studied by Devenport and Simpson [1990]. The measurements include the mean velocity and all Reynolds stresses at several *(x, z)* stations. Detailed experimental data are available in the ERCOFTAC database (Devenport and Simpson [1990] and Fleming et al. [1993]) under case number 8.

The available experimental and theoretical data offer a good opportunity to test the 3D hybrid RANS/LES method on a flow that exhibits a number of similarities with a cascade passage flow, which is the target test case of this PhD work.

5-2.4 .2 Introduction

The three-dimensional flow separation that generates a horseshoe vortex is a common occurrence in many practical aerodynamic and hydrodynamic flows. This sort of flow can occur when the turbulent boundary layer approaches an obstacle mounted on to a surface. This process is encountered in several engineering applications, such as the wing-body junction in aeroplanes, blade-hub configurations in turbomachinery, electronic components-board assemblies in cooling processes, rudder and keel-ship junctions, and river–bridge flows. The undesirable characteristics associated with the vortical flow, such as loss in aerodynamic performance, river bed erosion, vibration and noise generation, attracted the attention of the aerodynamic community towards this problem. Therefore, the horseshoe vortex at these junctions has been intensively studied both numerically (Parneix et al. [1998], Apsley and Leschziner [2001], Jones and Clark [2005], Paciorri et al. [2005], Paik et al. [2007], Fu et al. [2007]) and experimentally (Devenport and Simpson [1990], Ölçmen and Simpson[1995,2006], Fleming et al. [1993]).

The fundamental character of this flow has been studied on suitably simplified geometries using wings, cubes, and cylinders fastened to the wall surface. A detailed review of the experimental work carried out on these geometries is given by Simpson [2001]. The review describes how the interaction between the pressure gradients around the obstacle and the approach turbulent boundary layer generates a three-dimensional separation with a horseshoe vortex. This vortical structure is stretched and warped around the appendage, forming an opened necklace shape, as shown schematically in figure 5-16. The LDV measurements by Devenport and Simpson [1990] showed that the flow around the wing leading edge undergoes non-periodic low frequency velocity fluctuations, leading to a bimodal statistical distribution in LDV measurements. The frequency associated with this unsteadiness is much lower than the frequency of the coherent structure (in the outer layer of the approaching boundary layer) so that its effect on the turbulence structure is small, as suggested by Parneix et al. [1998]. While the resulting bimodality of the velocity probability density function around the leading edge seems to affect turbulent quantities, which is a feature that cannot be captured by a conventional two-equation RANS model, its effect on the mean flow parameters is small, Parneix et al. [1998].

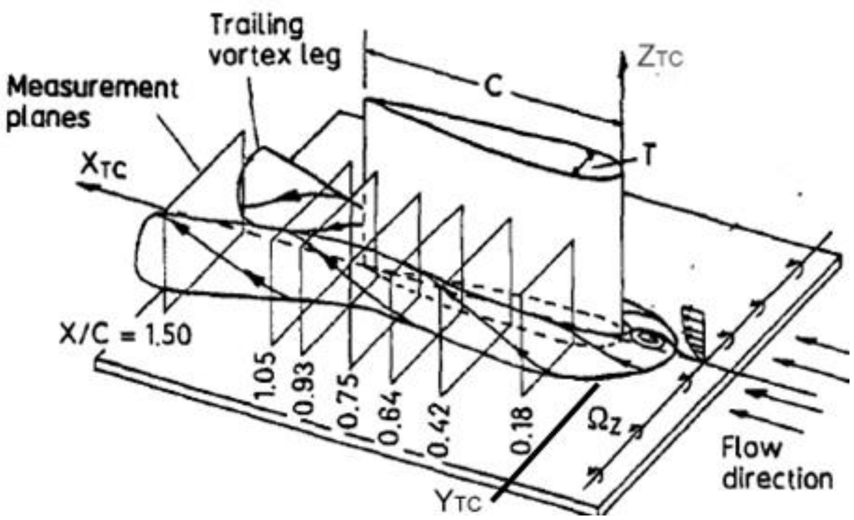

Fig. 5-16 Sketch of the horseshoe vortex around a wing-body junction, Fleming et al. [1993].

Several simulations studied a 3:2 semi-elliptical nose joined with a NACA 0020 tail at the maximum thickness, known as the Rood wing, mounted normally on a flat plate with zero angle of attack, (Parneix et al. [1998], Apsley and Leschziner [2001], Jones and Clark [2005], Paciorri et al. [2005], Paik et al. [2007], Fu et al. [2007]). Parneix et al. [1998] modelled the velocity components and the turbulent kinetic energy upstream of the Rood wing at many locations near the separation line of the horseshoe vortex in the necklace region. They used the V2F turbulence model that extends the standard k-ε model by incorporating both near-wall turbulence anisotropy and non-local pressure-strain effects, while retaining the linear eddy viscosity assumption. From the comparison with the experimental results, they showed that the V2F simulation is able to predict the separation location as well as the intensity of the back-flow at the wing upstream symmetry plane more accurately than the standard k-ε model.

A collaborative university-industry study of a wing-body junction flow is summarized by Apsley and Leschziner [2007]. In this study, twelve turbulence closure models are used and classified into three classes as follow: five linear (or isotropic) eddy-viscosity models (different types of $k-\varepsilon$, $k-\omega$, and $k-g$ models), three non-linear (or anisotropic) eddy-viscosity models (all based on the $k-\varepsilon$ transport equations), and four differential stress (second-moment closure) models. The study compared the output from the different turbulence models with the experimental data, focussing on the structure of the horseshoe vortex and its effects on the forward flow. This study showed that Reynolds stress models offered the most favourable predictive advantages over the other models tested, especially in terms of the far-field structure of the horseshoe vortex, although no model achieved close agreement with the experimental data in respect of both mean flow and turbulent quantities.

Another study, made by Jones and Clark [2005], simulated this flow using the realizable $k-\varepsilon$ model, the Reynolds stress model, the V2F model, the Spalart-Allmaras model and the $k-\omega$ model, running the commercial computational fluid dynamic package Fluent. They judged the performance of the turbulence models by comparing the mean velocity components upstream of the wing-body junction as well as the pressure distribution along the wing surface at some selected locations. They concluded that, while none of the models tested were able to simulate accurately the correct behaviour of the mean kinetic energy as a function of position, all the turbulence models display similar acceptable levels of accuracy except the realizable $k-\varepsilon$. Also, they confirmed the finding of Parneix et al. [1998] that the V2F model gives the closest agreement with the experimental data among the five RANS models tested.

Paciorri et al. [2005] numerically simulated the wing-body junction using structured and unstructured RANS codes with the one-equation Spalart-Allmaras and the two-equation $k-\varepsilon$ eddy viscosity models. This study carefully assesses the mesh dependence of the predictions by evaluating the grid convergence index as well as the validation of the implemented turbulence models.

Paik et al. [2007] followed the Detached-Eddy-Simulation (DES) approach, using the Spalart-Allmaras turbulence model for the RANS turbulence closure, to study the bimodality of the velocity probability density function around the horseshoe vortex in a wing-body junction. They stated that there is a discrepancy between simulation and measurements in predicting the coordinates of the horseshoe vortex core. They ascribed this discrepancy to the use of the Spalart-Allmaras turbulence model and to the steady inflow conditions. In spite of the poorly predicted vortex core location, the results show the DES approach as a powerful simulation tool for modelling this highly complex turbulent flow.

Fu et al. [2007] modelled by DES a wing body junction flow with the more complex RANS closure of the $k-\omega$ and the $k-\omega-SST$ models. They controlled the turbulence scale of the Strelets DES method by using Menter's function (F_2) to delay the switching from RANS to LES. They showed that the results from this method deliver the primary horseshoe vortex and agree well with the measurements.

In this work, the hybrid RANS/LES model of section 4-7 is used in an unconventional way. Specifically, it is applied to predict a complex three-dimensional steady flow. The Yoshizawa one-equation model is used to account for the effects of the flow unsteadiness on the time-mean flow away from the walls, while large-scale vortical structures around the Rood wing are resolved. The results indicate that this unconventional application of this hybrid turbulence closure gives predictions with a level of detail similar to the ones obtained using full Reynolds stress models or second order moment closures. The simpler algorithm of the Yoshizawa model compared to a full Reynolds stress RANS closure makes this computation more computationally affordable. This makes this unconventional application of the hybrid model of interest to the computational fluid dynamic community engaged in industrial design, where affordable predictions of the time-mean flow are sought around complex geometries.

5-2.4.3 Test-case geometry and boundary conditions

The model consists of a flat plate upon which the Rood wing is fixed, as shown in fig. 5-16. The wing maximum thickness T = 0.0717 m, the chord-to-thickness ratio (C/T) is 4.254, and the inflow u_0 gives a Reynolds number based on the wing thickness of 115000.

The inflow boundary conditions are imposed along the curved surface using the experimental data from the ERCOFTAC database. The subsonic outflow boundary condition with zero streamwise pressure gradients is applied at x/T=10. The boundary condition at y/T=18.24 is assumed to be far-field. At y/T=0 and z/T=3, the symmetry boundary conditions are applied. For all walls, the no-slip boundary condition is used.

Numerical mesh stretching is used near physical walls in the flow domain to capture the near-wall flow features. The wall-normal distance of the centre of the first cell closest to the wall is less than 0.00047 T and is designed to give a $y^+ < 0.5$, where y^+ is the cell centre height normalized by the friction velocity and kinematic viscosity. The number of cells in the x, y, and z directions are 168, 76, and 76 respectively. The mesh contains one million cells approximately. This test case is symmetric along the x-axis, so the structured mesh covers only half of the physical domain. A FORTRAN program was written to generate the C-type grid around the wing, shown in Fig. 5-17 (a). This is then extruded along the wingspan to obtain the three-dimensional computational mesh shown in Fig. 5-17 (b). The grid, boundary condition, and initial solution file are written in the CGNS format. The comparisons with the available experimental data are mainly done at the three planes shown in fig. 5-18. The inflow free-stream velocity u_0 is used to normalize the predicted velocity components.

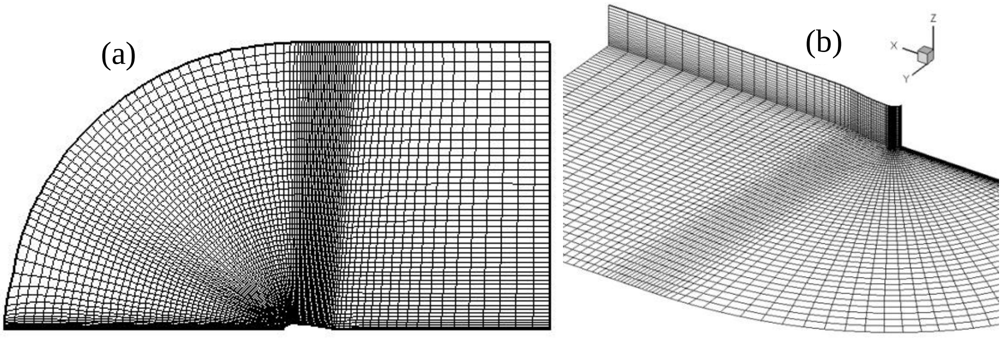

Fig. 5-17 Structured computational mesh: (a) plan view (b) diametric view. For clarity, one every two mesh points in x, y and z directions is plotted.

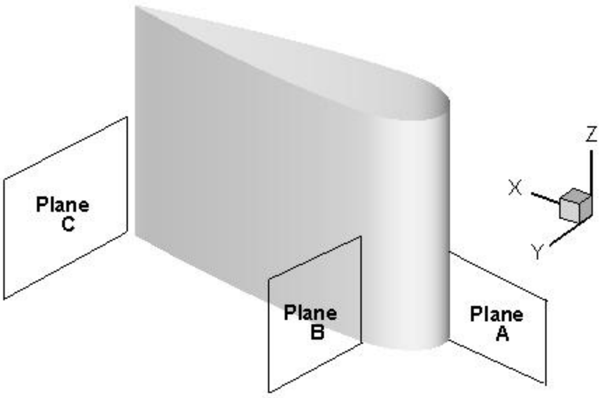

Fig. 5-18 The upstream symmetry plane A at x/T=0, the maximum wing thickness plane B at x/T=0.18 and the just downstream the trailing edge plane C at x/C=1.05.

To show the role of the blending function eqn. 4-103, fig. 5-19 shows the iso-level plot of the blending function Γ in the symmetry plane upstream the wing body junction leading edge, labelled as plane A in fig.5-18. Figure 5-19 shows the RANS dominant region near the flat plate and the wing appendage walls by red and the LES dominant region away from the walls by blue.

To examine the grid sensitivity of the simulation, a second coarser grid is generated by reducing the number of grid cells by factor of 2/3 along the three curvilinear directions. The height of the centre of the first cell closet to the wall is kept within the viscous sublayer ($y^+ < 1.5$). Figure 5-20 shows that the sensitivity of the pressure distribution along the wing to this grid density change is negligible. In fig. 5-21, the normalized velocity components u/u_0 and w/u_0 in x and z exhibit a small sensitivity to the grid density near the wing nose. The predictions presented in the results section are obtained from the fine mesh.

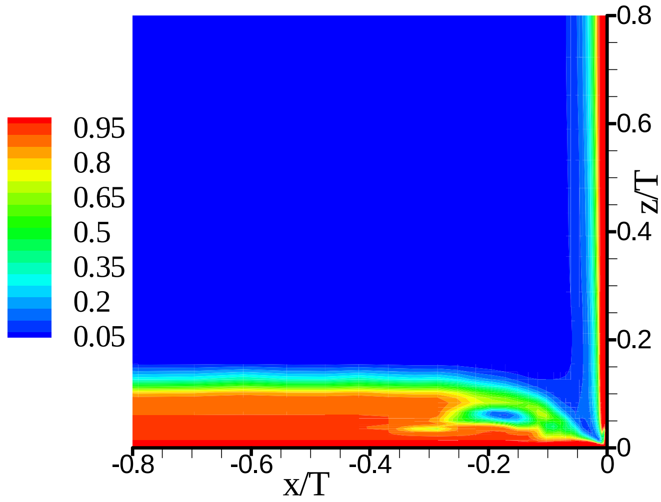

Fig. 5-19 Iso-levels of the blending function at the symmetry plane A.

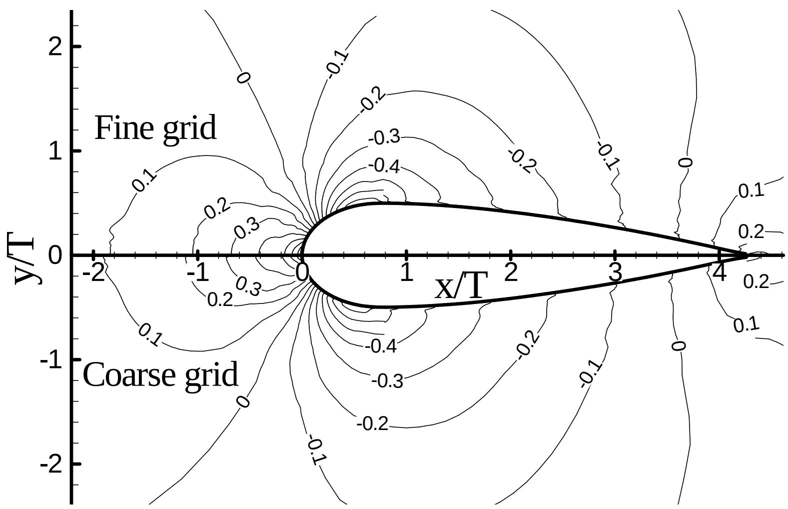

Fig. 5-20 Contours of static pressure coefficient Cp for the fine and coarse grids.

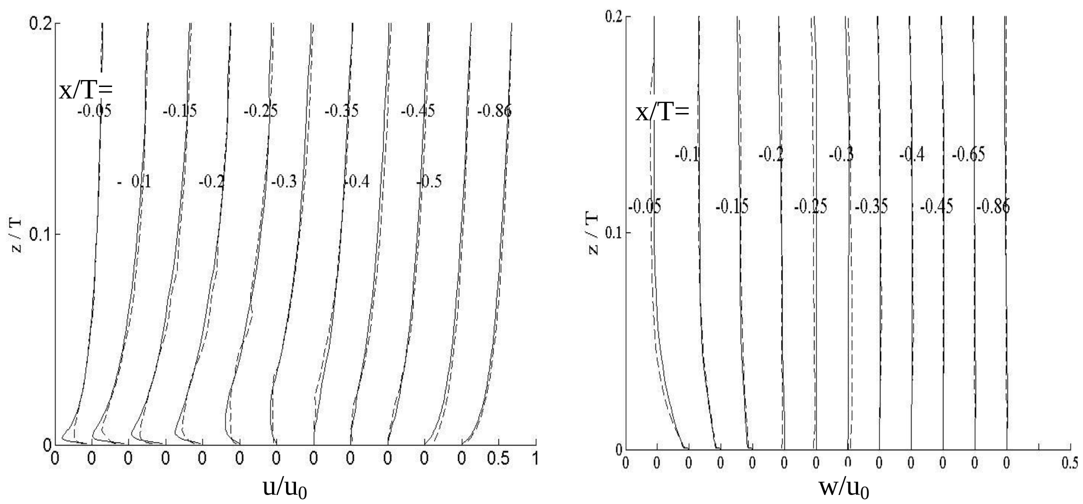

Fig. 5-21 Streamwise and flow-normal velocity profiles for the coarse grid (----) and the fine grid (—) at the symmetry plane A.

5-2.4.4 Results and discussion

Symmetry plane upstream of the wing leading edge

One of the most important aspects in this flow simulation is to predict the horseshoe vortex around the wing-body junction sketched in fig. 5-16. To this end, the simulation needs to locate correctly the vortex core in the upstream symmetry plane, plane A in fig. 5-18. In general, RANS simulations with either linear or nonlinear eddy viscosity models are not able to capture the location and the shape of this vortex as well as the increase of the turbulent kinetic energy in the vicinity of the junction, Paik et al. [2007]. Figure 5-22 shows the horseshoe vortex core and velocity vectors on the symmetry plane compared to the corresponding experimental plot. The vortex has an elliptical shape with a clockwise direction of rotation.

The measurements of Devenport and Simpson [1990] show that the locations of the separation point upstream of the wing nose and the vortex core are at X/T= -0.35 and -0.2 respectively. In figure 5-22 (a), the location of the separation point and the centre of the vortex are captured slightly upstream from the experimental location, figure 5-22 (b), by approximately 5% and 8% respectively. This earlier separation is due to the use of the k-ω-SST model as the RANS component in the hybrid RANS/LES simulation. It is known that the k-ω-SST model is more sensitive to adverse pressure gradient in boundary layer flows, Menter [1992]. The discrepancy in the prediction of the separation point is also found in previous DES results by Paik et al. [2007] and Fu et al. [2007] and in predictions from different turbulence closure models by Parneix et al. [1998], Apsley and Leschziner [2001], and Jones and Clark [2005]. The 5% discrepancy in the current prediction indicates that DES is arguably an affordable technique that gives engineering accurate results in a rather complex flow. The streamlines of fig. 5-22 (a) show a kink located upstream of the separation point. The streamline through this wall-attached layer is bent into a hook shape, indicating an upwell in the predicted velocity field. The same feature is visible in fig. 5-22 (b) starting from x/T= -0.48 and terminating just downstream of the separation point at x/T= -0.33. Paik et al. [2007] stated that this kink is formed due to the vorticity tail that originates from the vortex core and stretches upstream parallel to the flat plate.

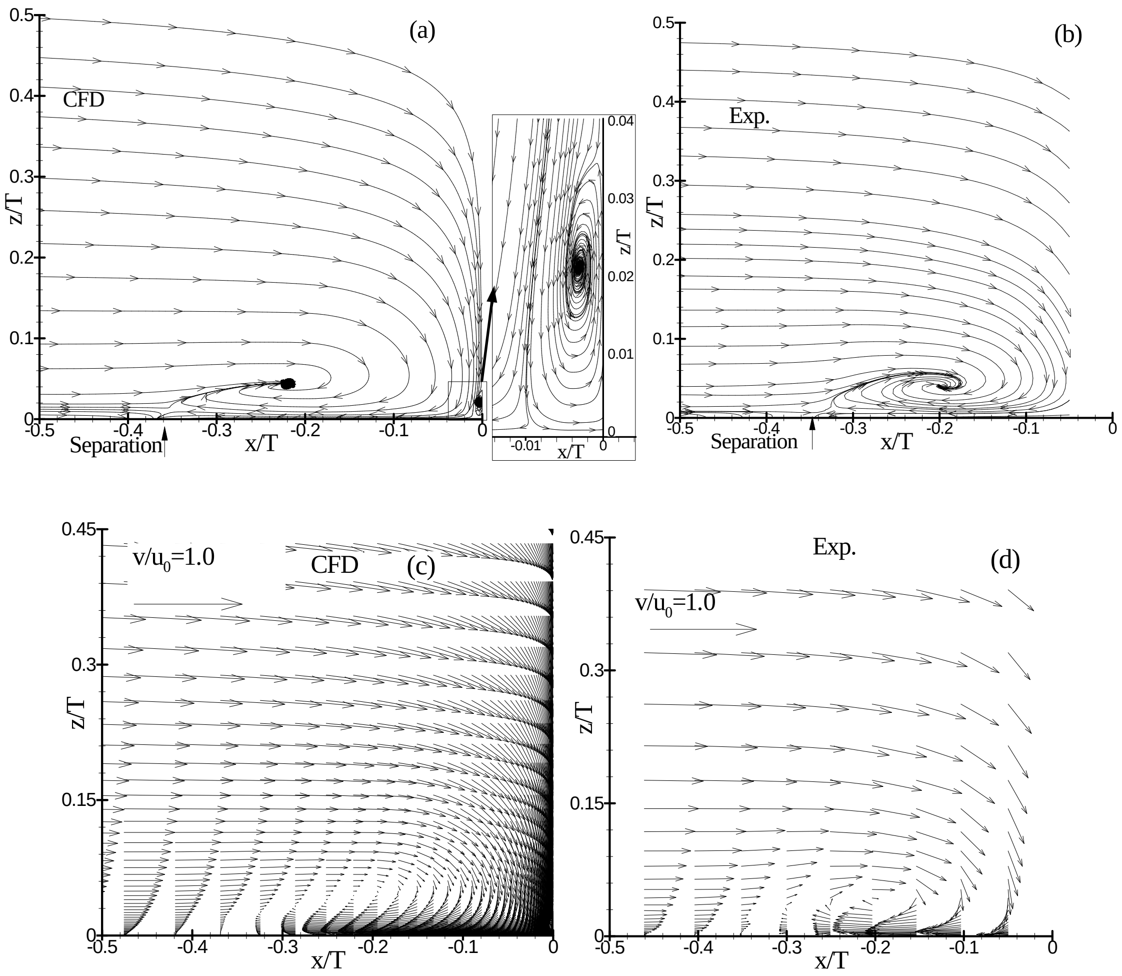

Fig. 5-22 Upstream symmetry plane vortex and velocity vectors.

In addition to the primary vortex, the simulation showed another secondary vortex close to the junction between the wing leading edge and the flat plate. Although the secondary vortex is not clearly captured by Devenport and Simpson [1990] through their oil flow visualizations, they commented that there is a small region of secondary separation in the corner between the wall and the wing.

Figure 5-23 shows the CFD contour lines of the velocity components (u/u_0, w/u_0) compared to the experimental contours. Figure 5-23 shows a good quantitative and qualitative agreement between simulation and experiment. The most noticeable difference between the computed contour lines and the experimental measurements of the streamwise velocity lies between the separation point and the core of the horseshoe vortex near the wall, where indicated by the dashed line in Fig. 5-23 (b). This difference may be attributed to the calculation of the turbulent eddy viscosity using a sensitive blending function along the separating boundary layer upstream the horseshoe vortex. Specifically, as the flow separates from the flat plate at x/T= -0.35, the upwell develops under an adverse pressure gradient that promotes the production of turbulent kinetic energy in the DES model.

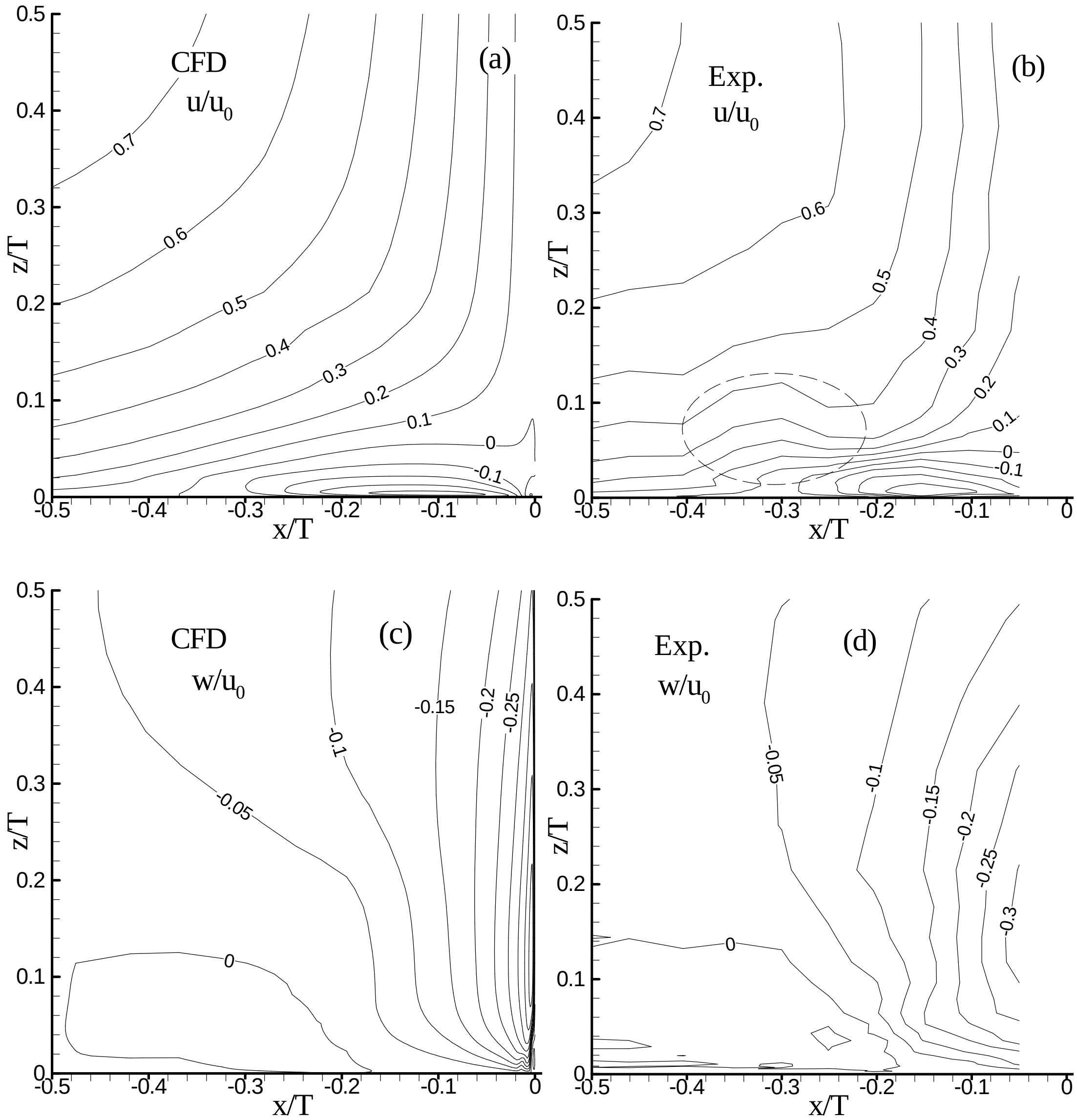

Fig. 5-23 Streamwise and flow-normal velocity distributions in the symmetry plane A.

The turbulent kinetic energy contours at the symmetry plane A of fig. 5-18 are shown in fig. 5-24. The computed turbulent kinetic energy contours are compared against the experimental data. While RANS simulations fail to capture the increase in the turbulent kinetic energy near the wing junction, Paik et al. [2007], the hybrid RANS/LES captured this increase qualitatively, as shown in fig. 5-24. While the DES model has improved the agreement with the measurements, there are still noticeable differences. The mean velocity in the DES is modelled by the k-ω-SST RANS technique. This model is unable to reproduce the local turbulence anisotropy, leading to an underestimate in the predicted turbulent kinetic energy. Also, streamline curvature generates extra strain rates that significantly affect the turbulent stress production. This effect may be modelled in further DES applications by modifying the *k*-ω-SST model by introducing the rotation and curvature sensitization by Hellsten [1998].

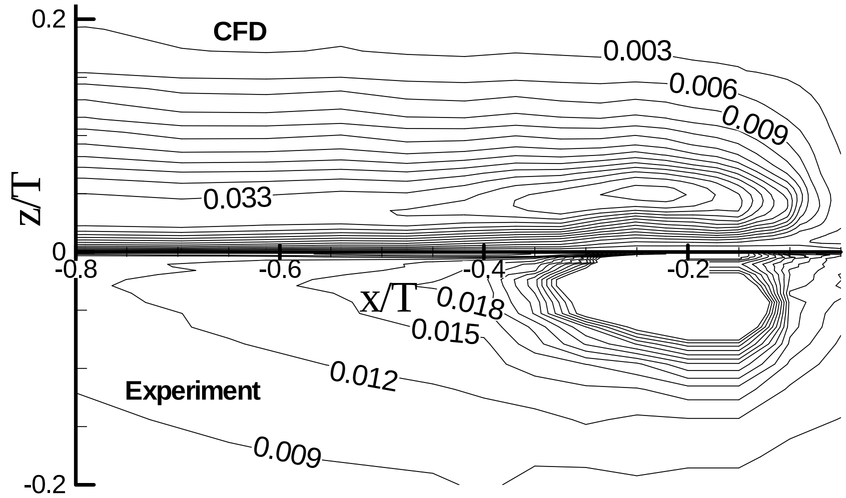

Fig. 5-24 Turbulent kinetic energy distribution in the upstream symmetry plane A, $\Delta k = 0.003u_0^2$.

The wing root flow

The computed contours of the time averaged pressure coefficient Cp on the bottom wall (z/T=0.0) at the wing junction are plotted and compared with the experimental values in fig. 5-25.

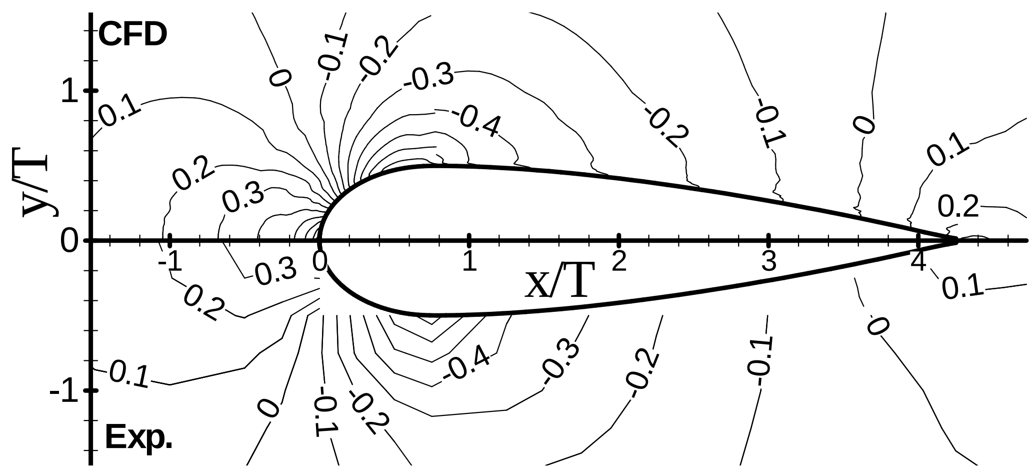

Fig. 5-25 Static pressure coefficient distribution about the wing at z/T=0.

Figure 5-25 shows that the predicted static pressure distribution is in good agreement with the measured data. The pressure rise on approach to the leading edge stagnation point at (x/T, y/T) = (0, 0) is reproduced well by the CFD and the same level contours are pretty close to one another on the y/T=0 symmetry plane. The location and magnitude of the pressure minimum on the wing surface are also close. This shows that the simulation gives a good agreement of the mainly two-dimensional pressure field generated by the wing, aside from secondary flow effects. In general, the pressure along the wing is weakly dependent on the turbulence model, as reported by Apsley and Leschziner [2001], and is not greatly affected by the horseshoe vortex, as pointed out by Paciorri et al. [2005]. The pressure coefficient distribution along the wing surface is tested at two other locations above the flat plate, at z/T=0.133 and 1.726. The plots of the pressure coefficient at these locations are shown in fig. 5-26. At z/T=0.133 the numerical results are in a good quantitative and qualitative agreement with the experimental data while at z/T=1.726 the numerical values are underestimated. This difference at z/T=1.726 may be partly attributed to the difference between the top boundary condition used in experiment and that in the simulation. While there is a gap between the top of the wing and the tunnel ceiling wall, the simulation used a slip wall as a slide fence at the wing tip.

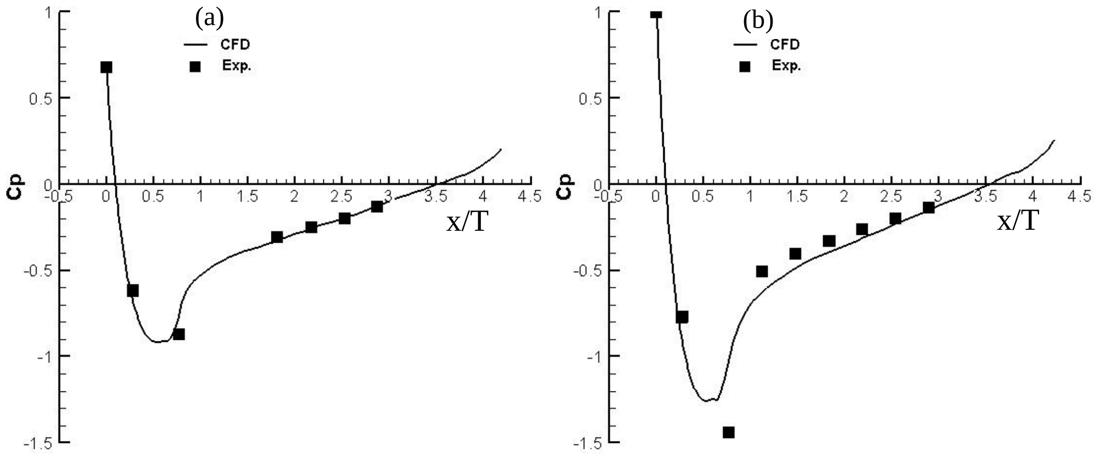

Fig. 5-26 Static pressure coefficient distribution at (a) z/T=0.133, (b) z/T=1.726.

Figure 5-27 shows the predicted streamlines over the flat plate at the wing root compared with the oil flow visualization performed by Ölçmen and Simpson [1995]. The flow over the flat plate, which is the body of the wing-body junction geometry, features a three-dimensional separation. Figure 5-27 shows the stagnation saddle point at the plane of symmetry and the separation line which emanates from this point and wraps around the wing. The separation line around the wing represents the path of the horseshoe vortex. A good agreement is noticed between the simulation results and the experimental flow visualization.

Figure 5-28 shows the predicted surface streamlines both on the flat plate and on the wing surface from roughly a three-quarters view angle. This figure also includes the surface streamlines on the symmetry plane A, as defined in fig. 5-18. The streamlines over the wing surface indicate that, away from the wing root, the flow remains attached from the leading edge to about 85% chord. Downstream of 80% chord, the flow separates from the wing surface, forming the near vertical separation line at about 85% chord, as shown in fig 5-23. Close to the wing root, the flow becomes more three-dimensional and this separation streamline spirals into a vortex. This vortex drives a small recirculation on the flat plate between 90% chord and the trailing edge. The oil flow visualization of figure 5-27 shows a single gray line departing form the wing surface at 80% chord. This line is evidence of the predicted trailing edge corner recirculation, which is a feature previously identified by Parneix et al [1998]. By combining surface streamlines on the flat plate and on the wing surface, the present study has added to the state of art by showing the wing surface vortex that drives the secondary recirculation near the trailing edge observed in experiment.

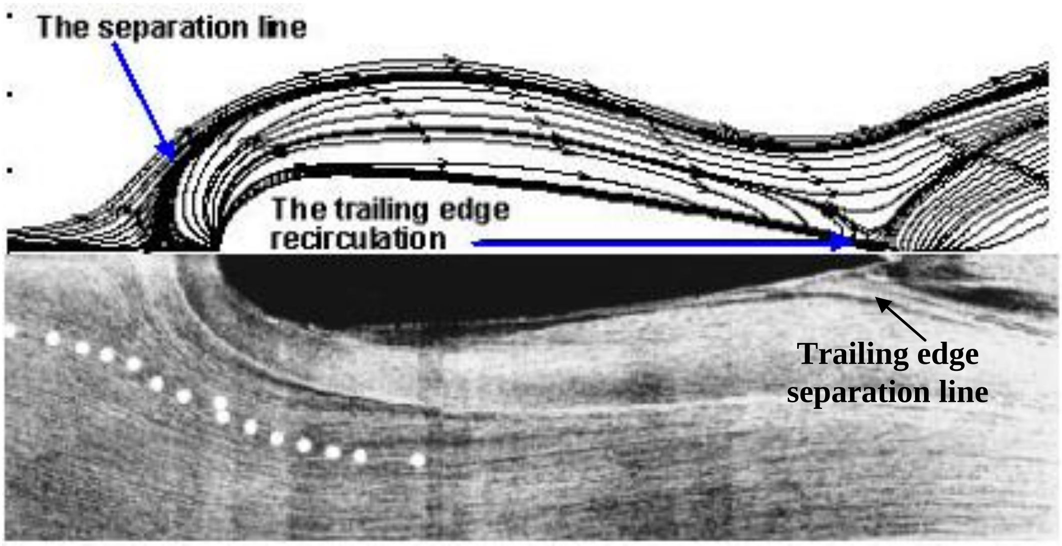

Fig. 5-27 Predicted streamlines against the oil flow visualization

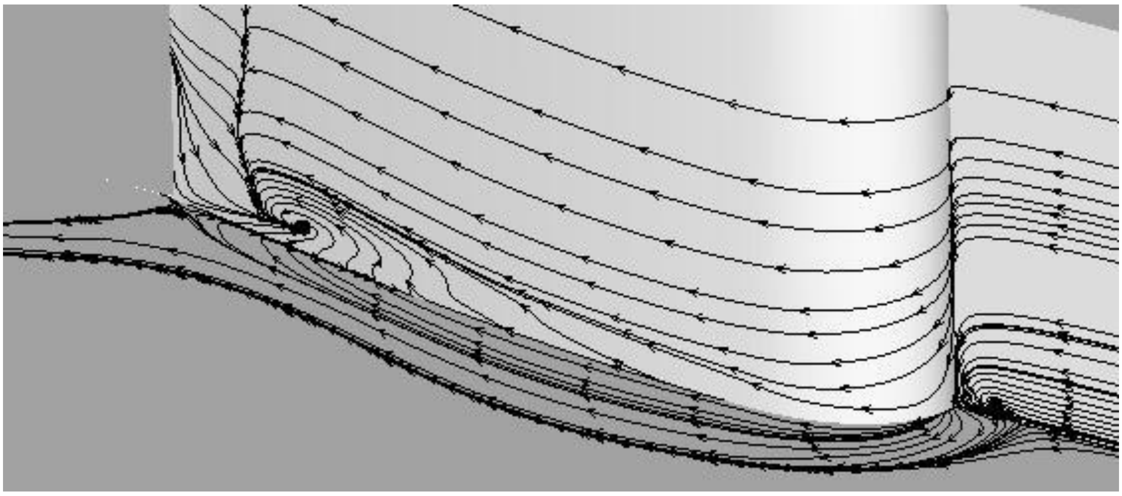

Fig. 5-28 The circulation and trailing edge vortex.

Figure 5-29 shows the contour plot of the velocity components at the maximum wing thickness compared to the experimental data. The computed streamwise velocity component (u/u_0) matches reasonably well with the experimental data even near the wall and along the wing span. Away from the wing surface, the streamwise velocity is weakly affected by the potential pressure field of the wing and asymptotes to the velocity distribution of a two-dimensional boundary layer. Specifically, the u velocity is very low close to the flat plate, at $z/T=0$, and increases monotonically in the positive z/T direction. Approaching the wing surface, which is located at $y/T=0.5$, the u velocity increases due to the wing thickness effect that induces a maximum velocity close to the location of maximum wing thickness. This shows as the location of minimum surface pressure in fig. 5-25. The streamwise velocity close to the wing surface is highest away from the flat plate, where it is less affected by the skin friction along this surface. A close inspection of figure 5-29 (a) shows densely packed u contours close to the wing surface, at $y/T=0.5$. These are due to the growing boundary layer on the wing surface. This boundary layer grows under a favourable pressure gradient from the wing leading edge to plane (B), leading to a thin boundary layer. This effect is not captured by fig. 5-29 (b), probably due to the limitation in the experiment in measuring the flow velocity close to the wall. This is a common occurrence in LDV data that is affected by surface reflection of the laser beams on the solid walls.

The contours of the pitchwise velocity component v in fig. 5-29 (c) are in reasonable agreement with the experimental contours in fig. 5-29 (d), except for a small difference to the side of the wing surface. The v contours show a horizontally elongated region of relatively high pitchwise velocity above the flat plate at z/T=0.025. This area of increased pitchwise velocity is induced by the horseshoe vortex above the flat plate. Specifically, the anti-clockwise circulation induced by the horseshoe vortex drives the pitchwise motion of fluid below the vortex core along the flat plate and away from the wing. The proximity of the flat plate increases the magnitude of the pitchwise velocity induced by the vortex that adds to the pitchwise velocity induced by the wing thickness effect. The near-wall peak is due to a mechanism similar to that of a wing in ground effect, in which the packing of the streamlines due to the non-permeable wall is equivalent to having an image vortex below the wall, driving the pitchwise flow. The CFD predictions of fig. 5-28 (c) show that the area of relatively high v is detached from the flat plate surface and the near-surface pitchwise velocity rapidly decreases to zero at the surface, thus satisfying the non-slip boundary condition at the wall of v=0. This near-wall decay is not shown in the experiment where it was not possible to measure the velocity in close proximity to the wall. Therefore the current CFD predictions are a good complement to the measurements, displaying understandable flow physics in one region where measurements are difficult to obtain and contributing towards obtaining a full picture of the wing-body junction flow.

Figures 5-29(e) and 5-29(f) show the predicted and the experimental flow-normal velocity on the flat plate. The spanwise velocity shows a similar trend to that of the pitchwise velocity, in that an area of greater spanwise velocity magnitude is shown close to the wing surface. The extent of this area is smaller compared to that of figures 5-29(c) and 5-29(d). The reason for the lower spanwise velocity magnitude close to the wing as compared to the pitchwise velocity maximum above the flat plate is that the horseshoe vortex core is farther away from the wing than from the flat plate on plane (B). The agreement between the experiment and computation on plane B in flow-normal velocity is coarser than the one for the other two velocity components, which probably results from the spanwise velocity being the smallest of the three components, hence suffering from a proportionally greater uncertainty in the measurements, Paciorri et al. [2005].

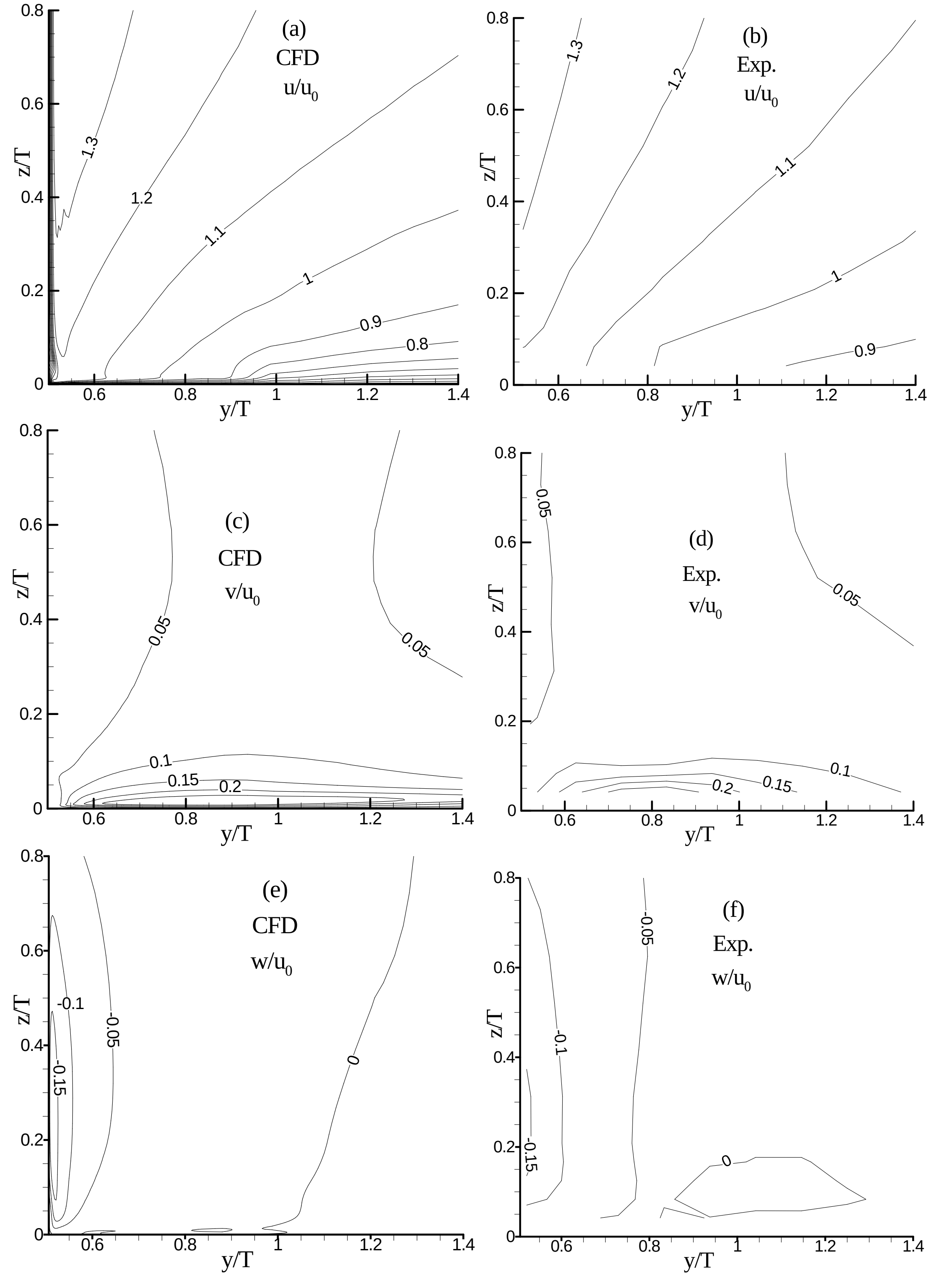

Fig.5-29 Contours of normalized velocity components at the wing maximum thickness, plane B.

Downstream of the trailing edge

The development of the vortical flow downstream of the trailing edge and in the wake is as important as the flow at the symmetry plane. Figure 5-30 shows contour plots of the predicted normalized velocity components just downstream of the trailing edge, x/C=1.05 compared to the experimental data. The location of this plane is sketched in fig. 5-18 as plane C. Figure 5-30 shows that the simulation gives a fair agreement with the experimental data. The simulation captured the growth of the thin shear layer separating from the wing trailing edge. This is shown by the streamwise velocity contours packed on the left of fig. 5-30(a), along the y/T=0 axis. Above the flat plate wall, which in fig. 5-30 coincides with the z/T=0 axis, the streamwise velocity contours are spread further apart to each other than normal to the y/T=0 axis, marking the presence of the thicker boundary layer on the flat plate as compared to the separating shear layer at the wing trailing edge. The presence of the horseshoe vortex is shown by the S shaping of streamwise velocity contour levels $u/u_0= 0.7$ and $u/u_0= 0.8$. The anti-clockwise horseshoe vortex generates an upwash-downwash pair that convects high-speed free-stream flow into the boundary layer on the downwash side and rises lower speed flow away from the wall on the upwash side. This displaces the streamlines at $y/T < 0.7$ towards the z/T=0 floor and rises the streamlines at $y/T > 0.8$ away from the z/T=0 floor in figures 5-29(a) and 5-29(b). The effect of the anti-clockwise vortex is also visible in the flow-normal velocity and spanwise contours of figures 5-30(c, d) and 5-30(e, f). The near-horizontal contours of fig. 5-29(c) above z/T=0 are replaced by a near-wall local maximum at $y/T \approx 0.6$ in figures 5-30(c) and 5-30(d), with the contour lines bending towards the wall at $y/T > 0.6$. This pattern can be explained by the presence of a streamwise vortex in the boundary layer that creates upwash and downwash regions near the wall, leading the near-wall flow-normal velocity contours shown in figures 5-30(c) and 5-30(d). The quantitative comparison of the velocity cross-flow components is difficult because they have small values and consequently the accompanied uncertainties of their measured values become significant, as stated by Paciorri et al. [2005].

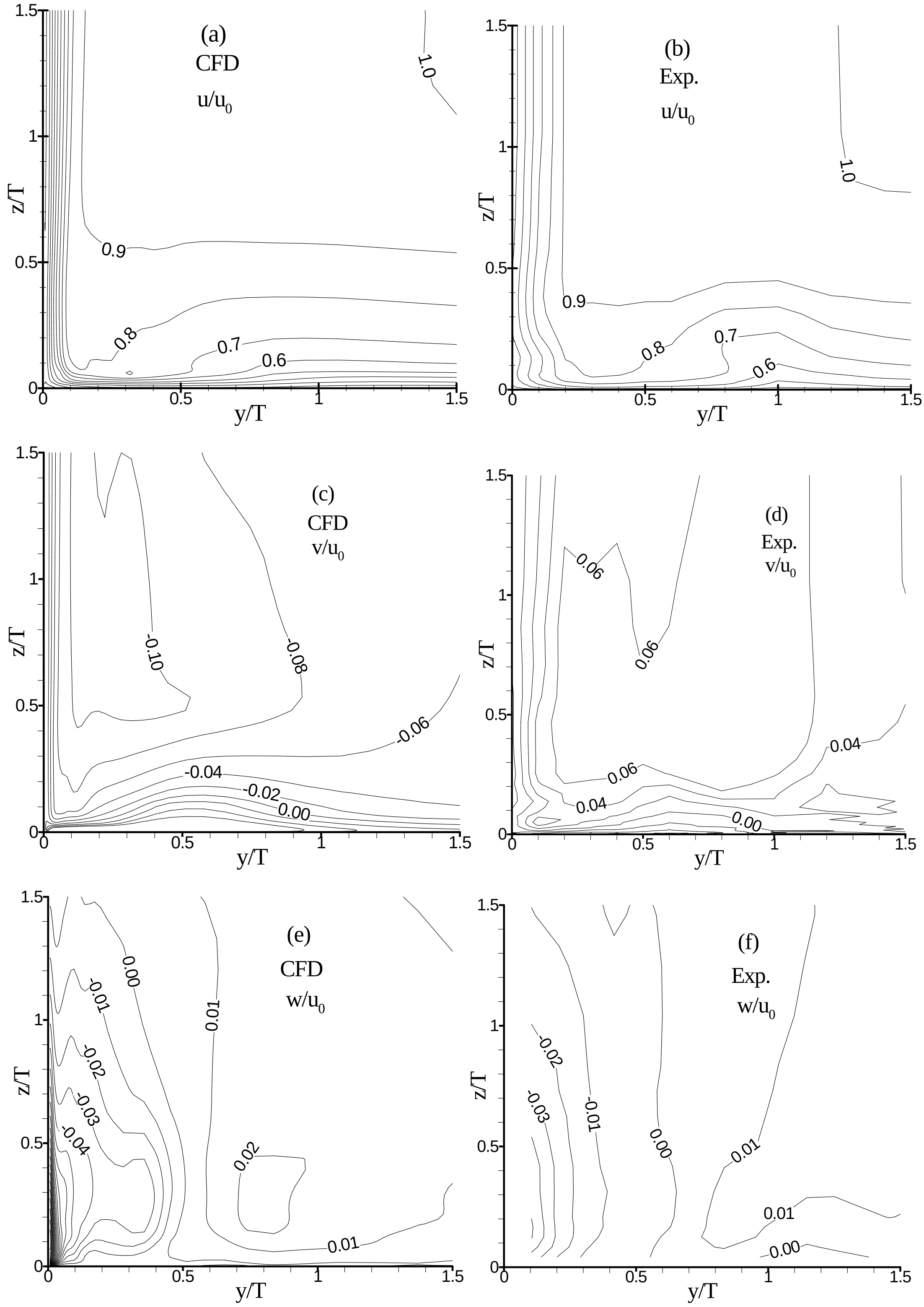

Fig. 5-30 Contours of normalized velocity components at the wing trailing edge, plane C.

Figure 5-31 shows the velocity vector field further downstream from the trailing edge, at x/T=6.38. Since there is no comparative experimental data in the

ERCOFTAC database at this location, the simulation results are compared with the numerical predictions by Apsley and Leschziner [2001] obtained by using the Reynolds stress model of Jakirlić and Hanjalić [1995]. Figure 5-31 shows that the hybrid RANS/LES method predicts the vortical flow with approximately the same core centre position of the transverse vortex motion with respect to the predictions of Apsley and Leschziner [2001].

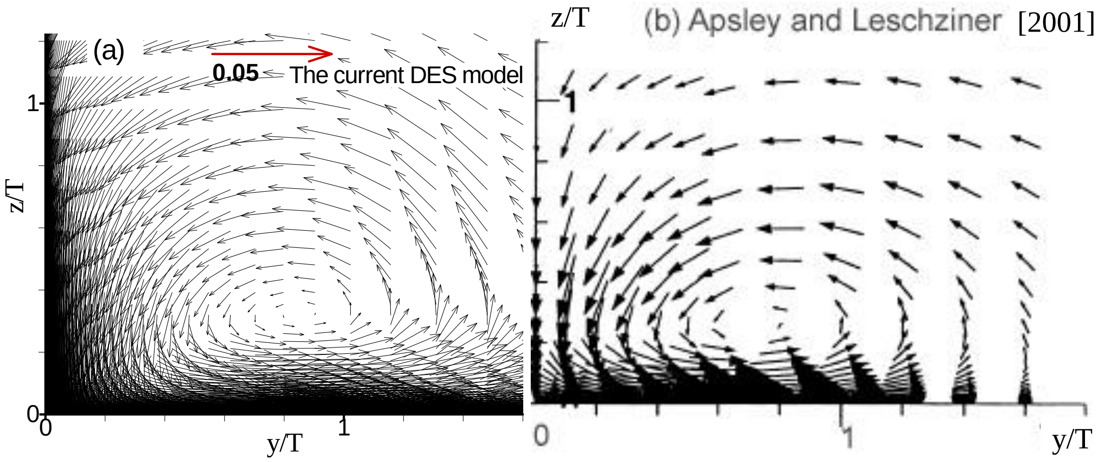

Fig. 5-31 Cross flow velocity vectors showing the horseshoe vortex at x/T=6.38.

An overall view for the vortical flow downstream the wing is shown in fig. 5-32. This figure shows the development of the horseshoe vortex and the lift up of its core in the wake region.

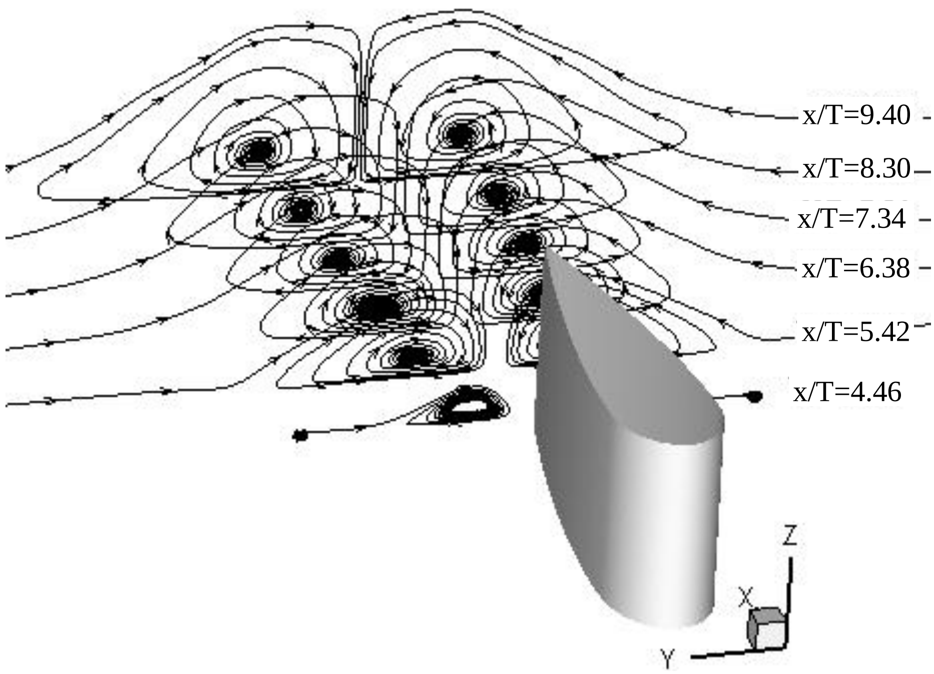

Fig. 5-32 The horseshoe vortex development downstream of the trailing edge.

5-2.4.5 Conclusion

In the present study, the numerical simulation of the turbulent flow past the wing-body junction has been performed using a hybrid RANS/LES turbulence closure approach. The switching between RANS and LES turbulence closure is done automatically and smoothly using a blending function. The blending function behaves similarly to the Menter function F_1, giving a RANS closure dominant region near the wall over a range of streamwise velocity profiles. Comparisons between the computed flow field and the experimental data from the ERCOFTAC database are presented. The results show that the hybrid RANS/LES turbulence closure is able to capture salient characteristics of this complex flow with reasonable accuracy. The simulation captured the upwind vortex, the 3-D stagnation saddle point, the separation line at the symmetry plane, the trailing edge recirculating flow, as well as the development of the horseshoe vortex downstream of the trailing edge.

The main finding in this simulation is the ability of the hybrid RANS/LES turbulence closure to capture the small vortices which to some degree are not captured clearly by the flow visualization techniques. The hybrid RANS/LES turbulence closure is able to capture the small secondary vortex in the front of the appendage junction with the flat plate and the trailing edge vortex. Also at the trailing edge, the simulation shows the surface streamlines spiralling near the junction with the flat plate, the separation line and the recirculation associated with the secondary flow pattern. Downstream of the trailing edge, the simulation shows that the vortex core is close to the wall and the spanwise spacing between the horseshoe vortex legs increases in the downstream direction, Fleming et al. [1993].

The location of the vortex core is predicted slightly upstream of the experimental position. This difference could be reduced by using an adjustable blending function to better control the extent of the region where the k-ω-SST model is active. The other factor which can be altered is the equivalent Smagorinsky constant used to calculate both the eddy viscosity constant and the destruction constant in the transport equation of the specific turbulent kinetic energy. The k-ω-SST model can be modified by introducing the rotation and curvature sensitization made by Hellsten [1998] that may improve the predicted location of the separation point. Still, the results show that the hybrid RANS/LES turbulence closure is a powerful tool for the simulation of complex three-dimensional flows.

The numerical predictions in this work clarify interesting aspects of the secondary flow physics in a Rood wing-body junction and helped to achieve a better interpretation the available experimental data. This work also shows how a hybrid RANS/LES turbulence closure can be used in a non-conventional way to predict complex three-dimensional flow with important steady vortex structures. The lower computational cost of the hybrid approach compared to a full Reynolds stress model makes this technique attractive for industrial design computational fluid dynamics, provided supportive validation elements are available alongside the CFD predictions to keep this unconventional use of the LES turbulence closure in check against real flow data.

5-3 Rotating frame of reference test cases.

5-3.1 Test case 5: Turbulent flow in a rotating square duct (3D flow)

5-3.1 .1 Objective

A three-dimensional turbulent flow in a rotating square duct is selected as the fifth test case to validate the 3-D CFD scheme in a rotating frame of reference. A reference simulation is also performed at the same inflow conditions in a stationary square duct. The reasons for selecting the non-rotating and rotating square duct cases are:

- They have a specific flow structure containing a weak secondary flow, which is a challenge for the CFD solvers. Specifically, the maximum secondary velocity is 2-3% of the mean stream velocity for the stationary duct, as stated by Pallares and Davidson [2000], and less than 10% for the rotating duct up to $Ro = 0.77$, as stated by Mårtensson et al. [2005].
- Both duct test cases contain both kinds of Prandtl secondary flows.
    - The first kind is generated by inviscid effects like the secondary flow due to Coriolis force in the rotating duct case.
    - The second kind is generated by Reynolds stresses like the secondary flow near the corner of the stationary duct.
- The stationary duct simulation is used as a cross-validation for the fixed frame of reference scheme with $\boldsymbol{\omega} = 0.0$ and it is also used as initial solution for the rotating test case at $\boldsymbol{\omega} \neq 0.0$.

5-3.1 .2 Introduction

The flow in a rectangular rotating duct features in many of engineering applications, such as cooling within turbine blades and the flow through radial compressor impellers. The simulation of this flow gives a close view for the Coriolis effects on the rotating flow mean values and the turbulent kinetic energy intensities. The available literature documents extensive research on the flow structure in a rotating duct, using Direct Numerical Simulation (DNS) by Mårtensson et al [2005] and Gavrilakis [1992], Large Eddy Simulation (LES) by Pallares and Davidson [2000, 2001,2002] and Qin and Pletcher [2006] and Reynolds Averaged Navier-Stokes (RANS) by Belhoucine et al [2004].

Mårtensson et al [2005] modelled the flow in a rotating duct using DNS at different rotational speeds. They stated that the secondary flow magnitude increases linearly with the rotational speed and the thin boundary layer attached to the horizontal surface is responsible for the higher streamwise pressure drop in rotating systems compared to non-rotating systems.

Pallares and Davidson [2000, 2002] studied the fully developed turbulent flow and heat transfer in a stationary and rotating duct using LES with a one-equation dynamic subgrid scale model. They assessed the influence of the Coriolis force on the spatial distributions of the average velocity fields and Reynolds stresses.

Another LES study, carried out by Qin and Pletcher [2006], investigated the turbulent heat transfer in a rotating square duct. They studied the effects of the Coriolis force and the rotational buoyancy on the mean flow structure, turbulent intensities and heat transfer performance.

Belhoucine et al. [2004] used an explicit algebraic Reynolds stress model to simulate the incompressible turbulent flow in a rotating square duct. A two-equation $k-\varepsilon$ model was used by Dutta et al [1996] to predict the heat transfer in a smooth rotating square duct at different Reynolds, Grashof numbers.

In the present study, a hybrid RANS/LES technique is used to simulate the flow in a square duct. The simulation has been carried out for a non-rotating and a rotating duct to validate the flow solver in a rotating frame of reference.

5-3.1.3 Test-case geometry and boundary conditions

The computational domain is shown in fig. 5-33, in which the components of the Coriolis acceleration are indicated by the arrows. The rotation vector $\boldsymbol{\omega}=(0,0,\omega_z)$ is oriented along the positive z axis as shown in fig.5-33. In the present study, the rotation number Ro varies in the range of 0.0 to 0.176 where, the Ro is given by:

$$Ro=\frac{\omega_z h}{u_0} \qquad (5-1)$$

where h is the side length of the duct square cross-section and u_o is the inflow bulk velocity and related to the mass flow rate $\dot{m}$ as

$$u_0=\frac{\dot{m}}{\rho A}=\frac{\int \rho u dA}{\rho A} \qquad (5-2)$$

and $A=h^2$.

The computational grid size for all cases is 66x63x63 in $x, y,$ and z respectively. The grid is stretched toward the duct walls using a hyperbolic tangent function as shown in fig. 5-34. The centre of the first cell closest to the wall is designed to have $y^+ < 5$, where y^+ is the cell centre height normalized by the friction velocity, u_τ, and kinematic viscosity, v.

The non-slip boundary condition is applied at the walls surrounding the duct flow. A translational periodic boundary condition is applied along the x direction. As the static pressure decreases in the streamwise direction, an imposed streamwise pressure gradient $\frac{dp}{dx}$ along the x direction is applied. The static pressure difference between the inflow and the outflow is calculated as follows, Rokni et al. [1998]:

$$\Delta p = \frac{dp}{dx}\mathrm{L} = f\frac{\mathrm{L}}{D_h}\frac{\rho u_o^2}{2} \qquad (5-3)$$

where f is the Darcy friction factor and D_h is the hydraulic diameter. The friction factor f is calculated using the Petukhov equation $f = \big(0.790\ ln\ Re_{D_h} -$ $1.64 - 2$ which is valid for $3000 \leq Re \leq 5 \times 106$.

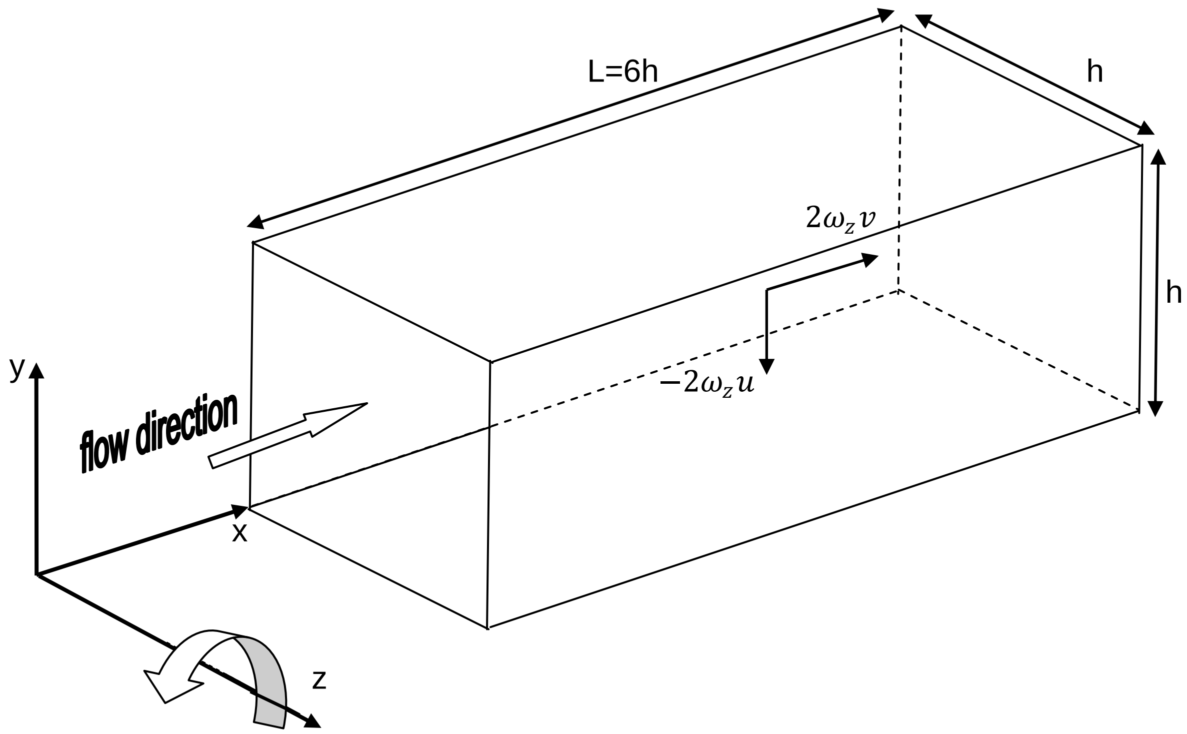

Fig. 5-33 3D schematic drawing for a rotating straight square duct (not to scale).

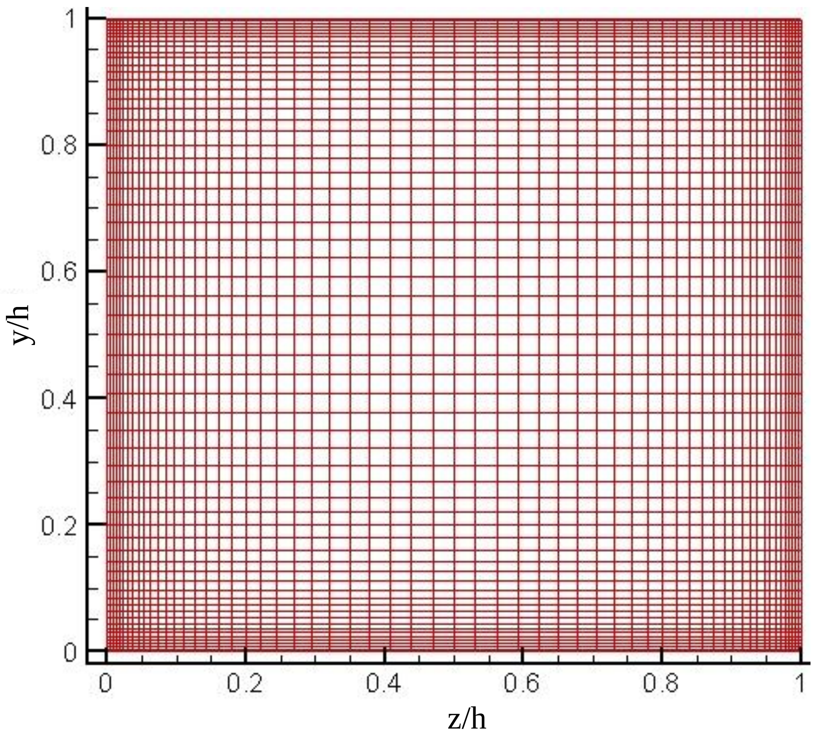

Fig. 5-34 The stretched grid using a hyperbolic tangent function.

5-3.1.4 Results and discussion

The turbulent flow in a non-rotating square duct (Ro$=$ 0.0) is simulated because it has a unique flow structure, to be used as the starting flow condition for the rotating duct case, and to confirm that the code recovers the results from the fixed frame of reference scheme when $\boldsymbol{\omega} = 0.0$.

Figures 5-35 (a) and (b) show the contour plot of the mean streamwise velocity and the vector field of the cross-stream components (v, w) compared to the LES results of Pallares and Davidson [2002]. Figure 5-35(c) shows the details of the near-wall secondary flow structure in the non-rotating duct cross-section. The secondary flow consists of eight counter-rotating vortices divided into four pairs located in the four quadrants of the duct cross-section. Each pair of vortices is symmetric about the corner bisector and convects the high momentum fluid from the duct core to the corner region along the corner bisector.

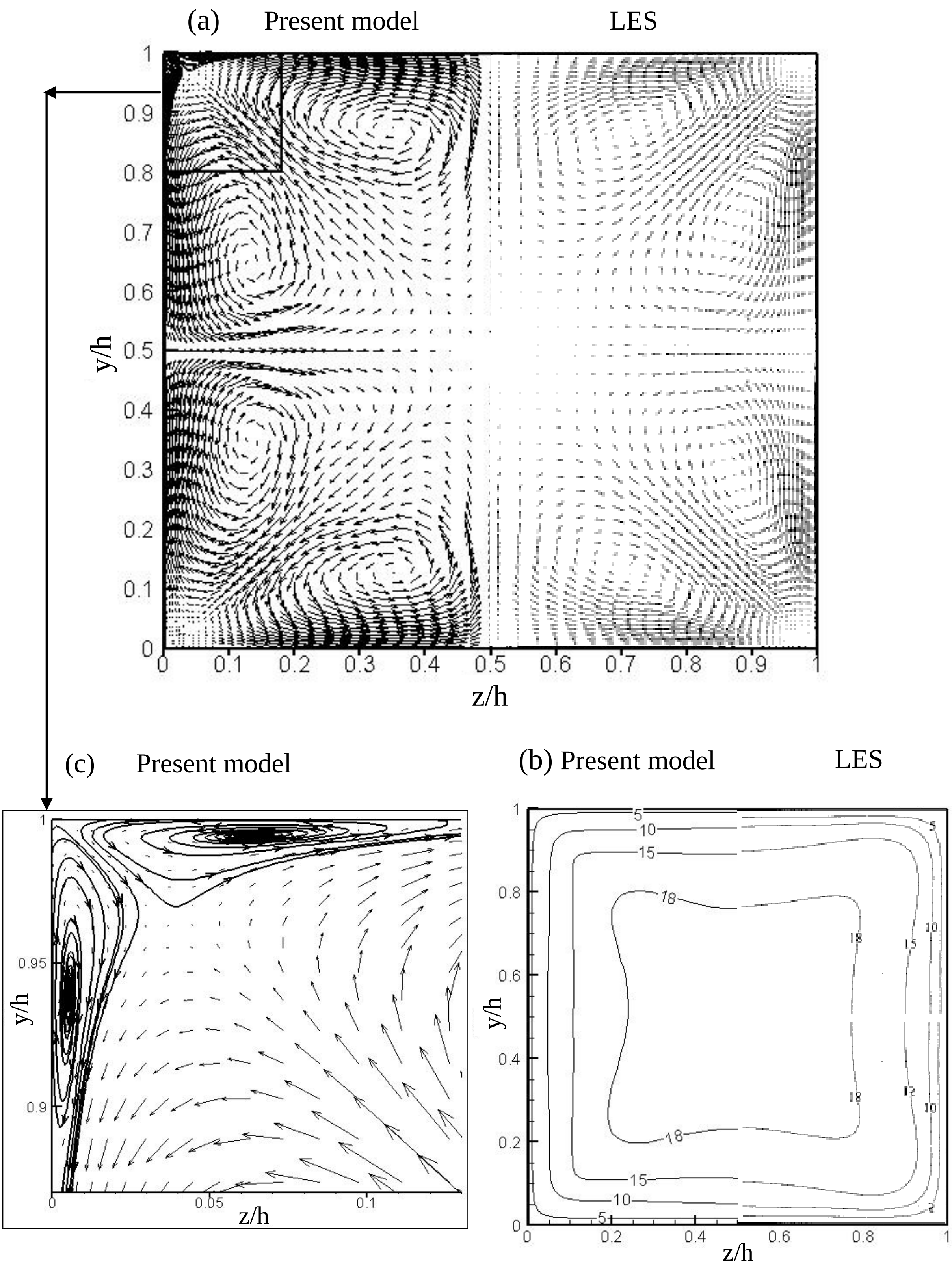

Fig. 5-35 (a,c) The velocity filed of the secondary flow in a stationary duct, (b) The mean streamwise velocity contour normalized by the friction velocity compared to LES results of Pallares and Davidson [2002].

In addition to the primary pair of vortices in each quadrant, the simulation captured another secondary pair of vortices close to the corner and symmetry along the corner bisector, shown in fig. 5-35(c). According to DNS work by Huser and Biringen [1993], this small pair of secondary vortices in each corner is generated because the area region close to the corner is suppressed by the reduced mean shear along the corner bisector, in addition to the ejection of the low momentum fluid from the walls. The direction of rotation of the small pair of vortices determines the direction of rotation of the big pair of vortices as reported by Huser and Biringen [1993]. In the present study, the DES model reproduced the characteristic flow pattern associated with the counter-rotating corner vortices, but the bulging contour of the axial velocity is not captured as in the DNS results. This difference can be attributed to the fact that this turbulence driven secondary flow is relatively weak, with only a few percent of the mean axial velocity (a maximum of 2% -3% u_0), as reported by Pallares and Davidson [2000].

The rotating duct simulations are carried out at five rotational speed numbers which are $Ro = 0.00999, 0.026, 0.041, 0.088, \text{and } 0.176$. The instantaneous fully developed velocity and pressure fields of the non-rotating duct are used as the initial condition for the $Ro = 0.00999$ test case. The predicted flow field of the rotating duct at different rotation numbers Ro shown in fig. 5-36 is completely different from the flow pattern of the stationary duct. Figures 5-36(a) to 5-36(d) show the contour of the streamwise velocity and the cross-stream vectors for $Ro = 0.026, 0.041, 0.088, \text{and } 0.176$ respectively. These figures show only one half of the flow fields since the flow fields are symmetric about $z/h = 0.5$. For qualitative comparison, the other half in these figures represents the LES simulation of Qin and Pletcher [2006] (a and d) and Pallares and Davidson [2000] (b and c) at the corresponding rotation number. As shown in fig. 5-36 for the rotating duct, the secondary flow is dominant by two counter rotating vortical cells. These two vertical cells arise due to a rotational induced pressure gradient in the positive y direction set up to balance the Coriolis force component $-2\omega_z u$. This Coriolis force component causes a secondary flow directed to negative y direction and convects low momentum fluid from the suction side (stable side) at $y/h = 1.0$ to the pressure side (unstable side) $y/h = 0.0$. The vertical Coriolis force component near the side walls $(z/h = 0.0,1.0)$ is smaller than that at the channel centre due to the reduced streamwise velocity near the walls; therefore the flow is moved in the direction of the positive y axis. This force-momentum balance among the induced rotational pressure gradient, the viscous forces, and the vertical Coriolis component generates the dominant vortical cell. These figures show four distinct boundary layers, two Ekman layers at side walls ($z/h = 0.0, 1.0$), and two Stewartson layers on the stabilized suction side at $y/h = 1$ and on the unstabilized pressure side at $y/h = 0$. The Ekman layer is created in the rotating fluid near the solid boundary where the viscous forces play an important role in the force-momentum balance between the pressure gradient in the y direction and the vertical component of Coriolis force.

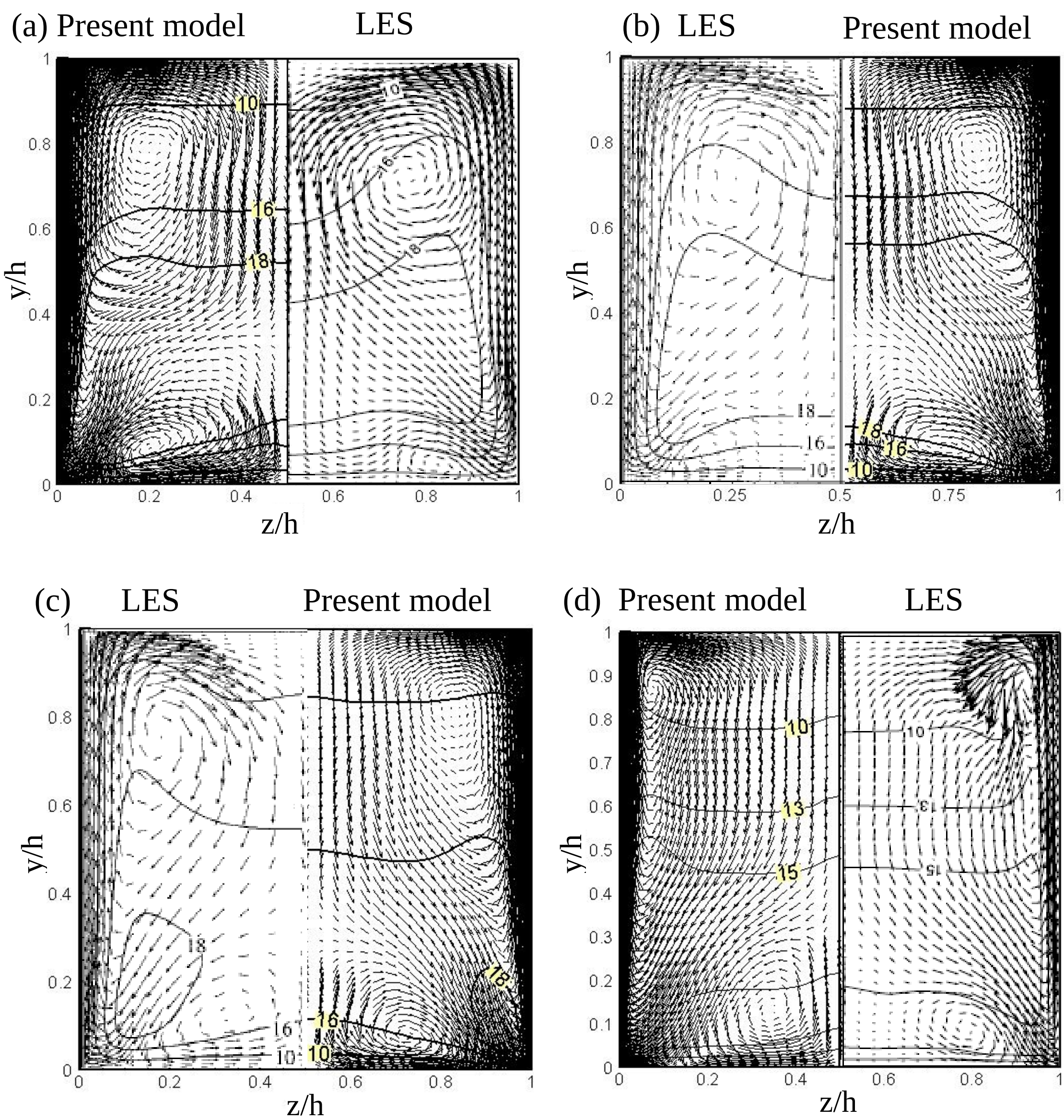

Fig. 5-36 The contours of the streamwise mean velocity normalized by the friction velocity along with the velocity vector field of the secondary flow for (a) $Ro = 0.026$ (b) $Ro = 0.041$ (c) $Ro = 0.088$ (d) $Ro = 0.176$.

The convection of axial momentum by the secondary flow shown by the vector maps of fig.5-36 (a - d) shifts the location of the maximum axial velocity towards the unstable wall at $y/h = 0.0$. The Stewartson layer at the stable wall (suction side) convects the fluid from Ekman layer towards the core of the duct while at the unstable wall (pressure side) at $y/h = 0.0$ a small vortical cell is formed due to the turbulence level enhancement by rotational body forces. These small cells recirculate part of the fluid sliding towards the bottom wall bisectors. The centres of the large vortical cells are located near the stable top wall below the top bisector, while the centres of the small ones are located near the unstable bottom wall below the bottom bisector. For the tested range of the rotation numbers, as the rotation speed increases, the size of the small cells increase. Also, the centres of the large cells move towards the top corners as the rotation number increases.

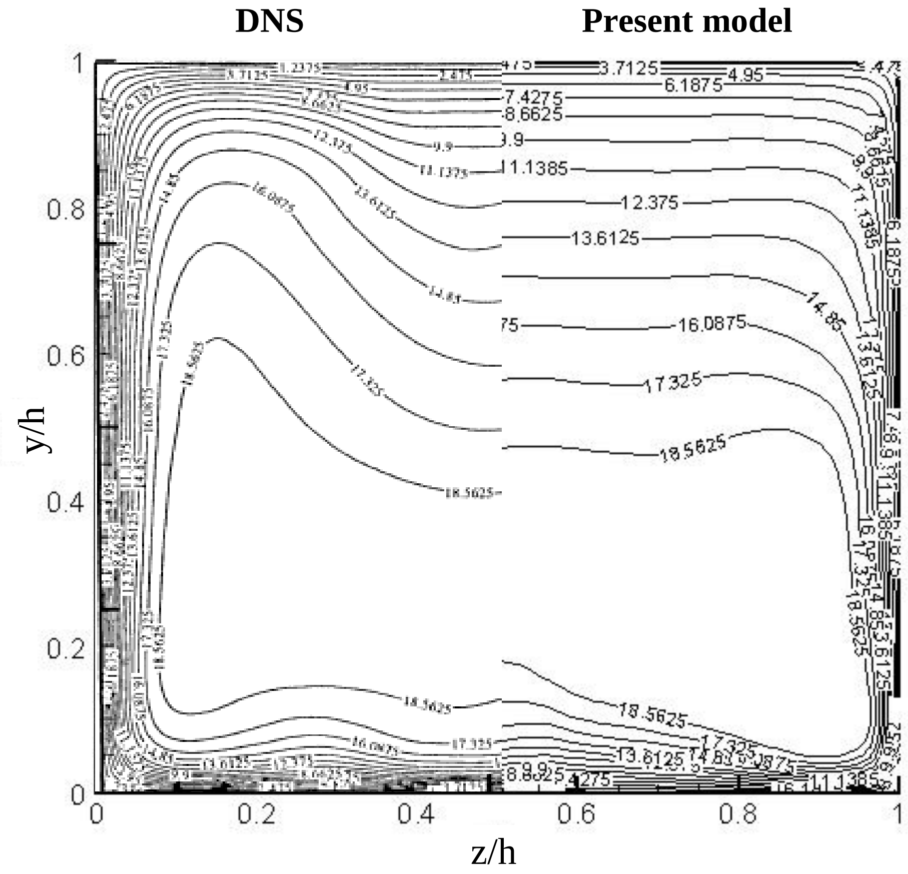

Fig. 5-37 Normalized mean axial velocity contours for $Ro = 0.026$ compared with the DNS results by Gavrilakis [1992].

Figure 5-37 shows the normalized axial velocity contours compared to the DNS results by Gavrilakis [1992]. Figure 5-37 shows that the simulation model reasonably reproduces the three boundary layers and the significant shifts of the peak value of the normalized mean axial velocity towards the pressure side of the duct. The axial velocity is normalized using the friction velocity $u_\tau = \sqrt{\tau_w/\rho}$ where τ_w is the perimeter-averaged wall shear stress. Figures 5-38(a) to 5-38(d) show the normalized axial velocity profiles at the symmetry plane, $z/h = 0.5$, compared to the available DNS and LES results for $Ro = 0.00999, 0.026, 0.088,$ and 0.176. These figures show an asymmetric velocity profile, which is due to the rotation effect. The peak values of the normalized velocity, $u^+ = u/u_\tau$, are shifted towards the unstable wall side (the pressure side) at $y/h = 0.0$ and the extent of this shift depends on the rotation numbers. At the low rotation number $Ro = 0.00999$, the action of the rotation body forces is low so the velocity profile has a near-parabolic shape, typical of a fully developed channel flow in a non-rotating duct, as shown in fig. 5-38(a). As Ro increases, the profile becomes progressively more skewed towards $y/h = 0.0$.

(a) for $Ro = 0.00999$

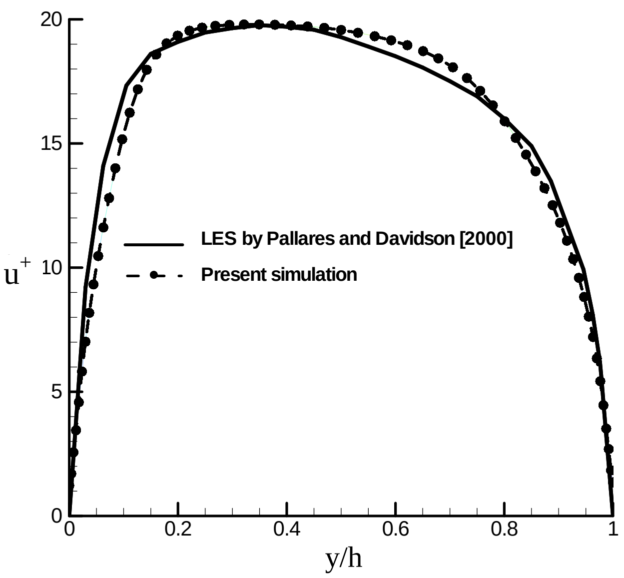

(b) for $Ro = 0.026$

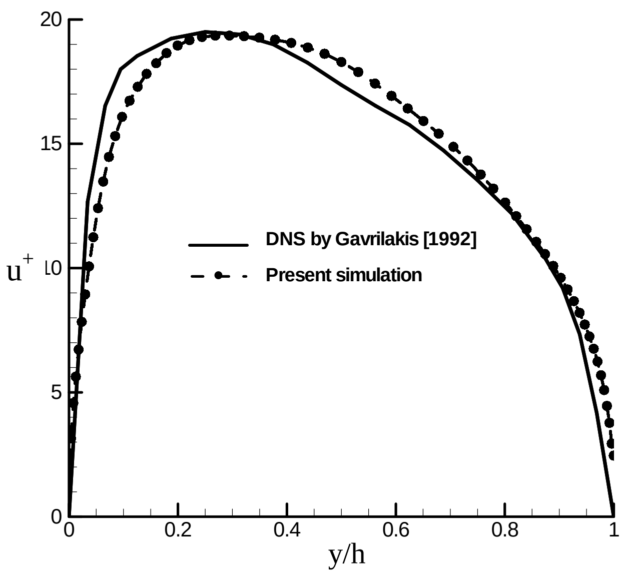

(c) for $Ro = 0.088$ (d) for $Ro = 0.0176$

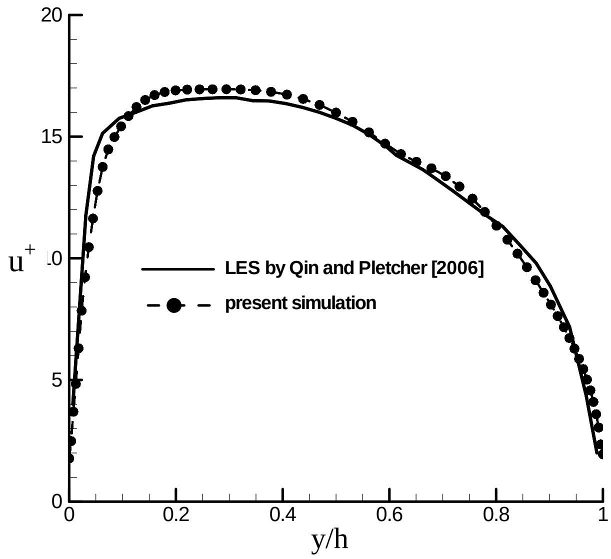

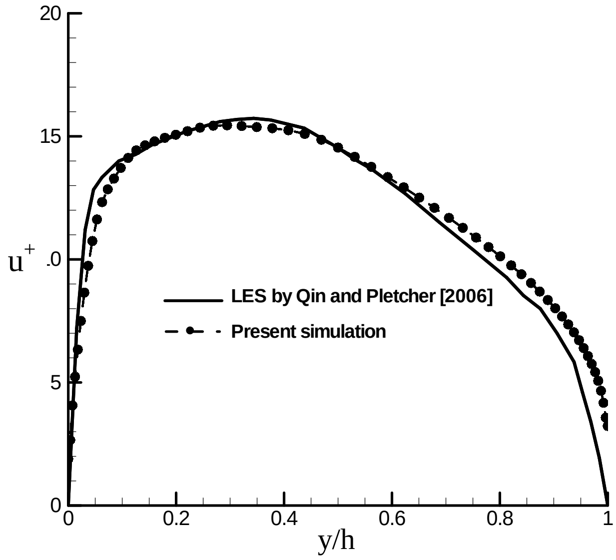

Fig. 5-38 Normalized mean axial velocity profile along the symmetry plane, $z/h = 0.5$.

Figures 5-38(a) to 5-38(d) show a quite good agreement between the present simulation and the available DNS and LES results. The comparison shows a small shift in the location of the predicted maximum velocity, u^{+}, between the present simulation and the DNS and LES results, and this shift decreases as the rotation number increases. This is probably due to the simulations being able to render better the inertia forces dominated field at the higher Ro compared to the lower Ro fields, where the fine balance between the viscous and inertia forces is more important in determining the flow pattern. The normalized mean axial velocity profile along the bisector starting from $\left(\frac{y}{h}, \frac{z}{h}\right) = (0,0)$ is shown in fig. 5-39. The profile is compared with the DNS results of Gavrilakis [1992]. The present simulation shows an acceptable agreement with the reference DNS simulation and the discrepancy between the predictions can be attributed to the effect of the anisotropic Reynolds stresses near the corner, which is not captured by the linear eddy viscosity model in the RANS, and to the higher grid density used in the DNS compared to that of the current RANS model.

The other effect of rotation is the interaction of the Coriolis force with the mean shear producing the stabilization and the destabilization of the flow near the top wall $y/h = 1$ and the bottom wall $y/h = 0$ respectively. The definition of the stabilization and destabilization is related to the respective increase and the decrease of the turbulence level near the suction ($y/h = 1.0$) and pressure ($y/h = 0.0$) sides. This redistribution of the turbulence level is clearly shown in fig. 5-40 that compares the distribution of the turbulent kinetic energy normalized by ${u_o}^2$ for the stationary duct, fig. 5-40(a), and the rotating duct at $Ro = 0.026$, fig. 5-40(b), and at $Ro = 0.0176$, fig. 5-40(c). Figure 5-40 shows that, as the rotation number increases, the turbulence level reduced on the stable wall at $y/h = 1.0$ and increased on the unstable wall at $y/h = 0.0$ but with a thinner area. In case of a sufficiently high rotation number, this change in turbulent kinetic energy can lead to complete suppression of the turbulence on the stable side and to flow relaminarization, as stated by Pallares and Davidson [2000].

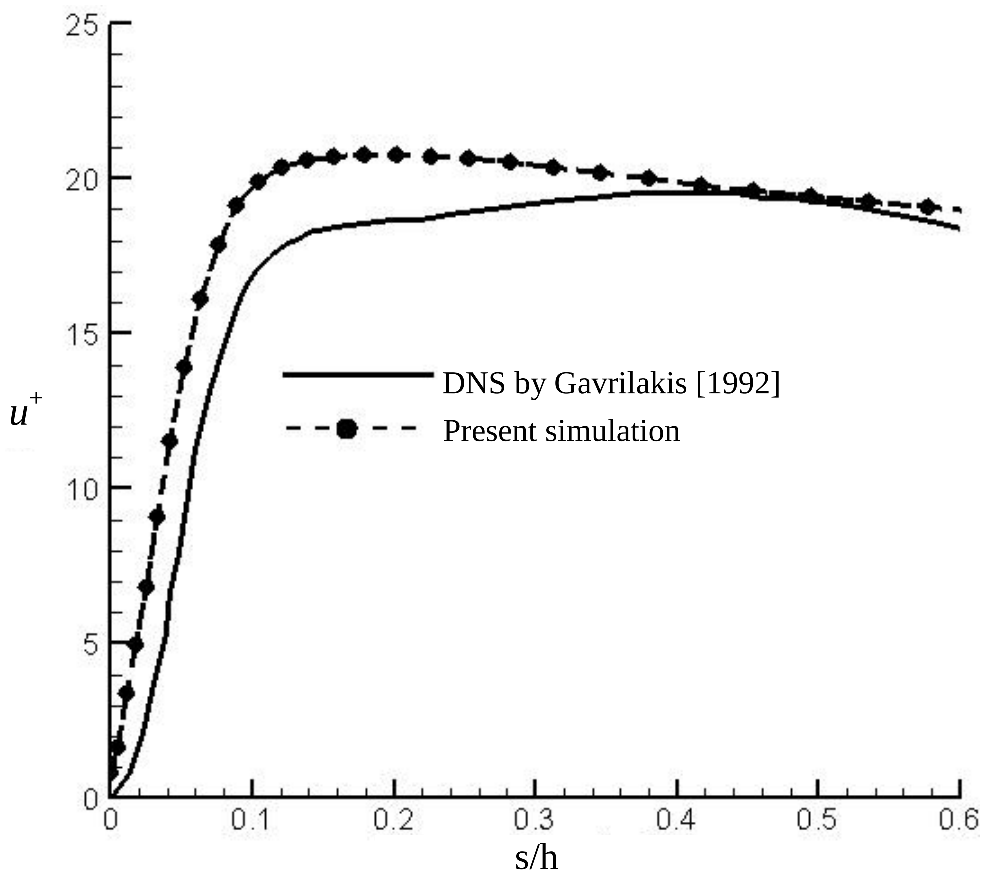

Fig. 5-39 Normalized mean axial velocity profile along the corner bisector at $Ro = 0.026$ and s is the distance along the bisector from $\left(\frac{y}{h}, \frac{z}{h}\right) = (0,0)$.

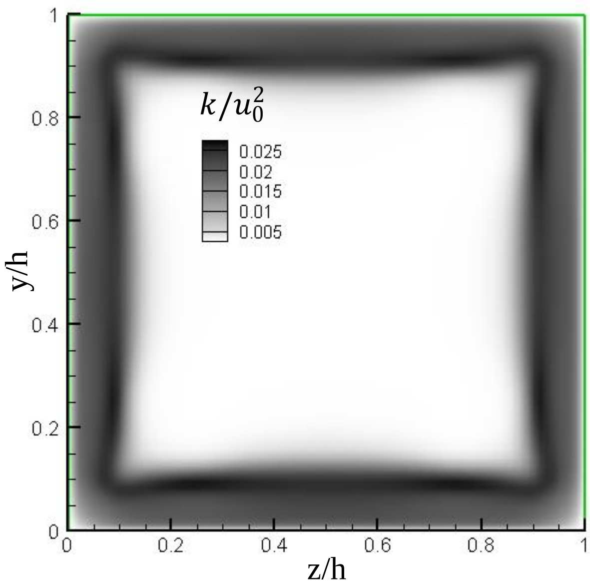

(a) $Ro = 0.0$

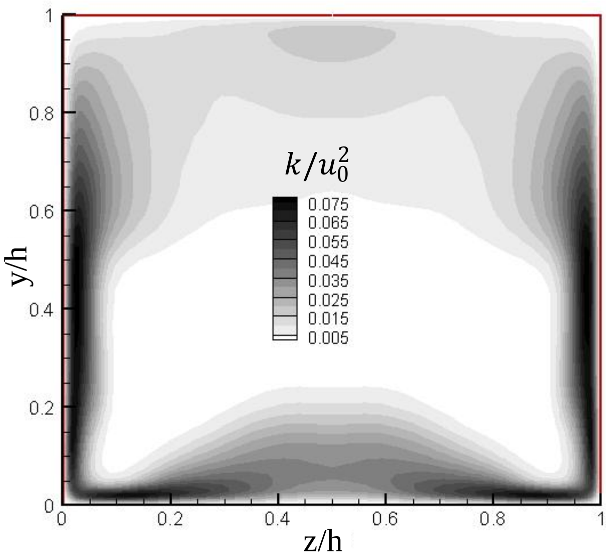

(b) $Ro = 0.026$

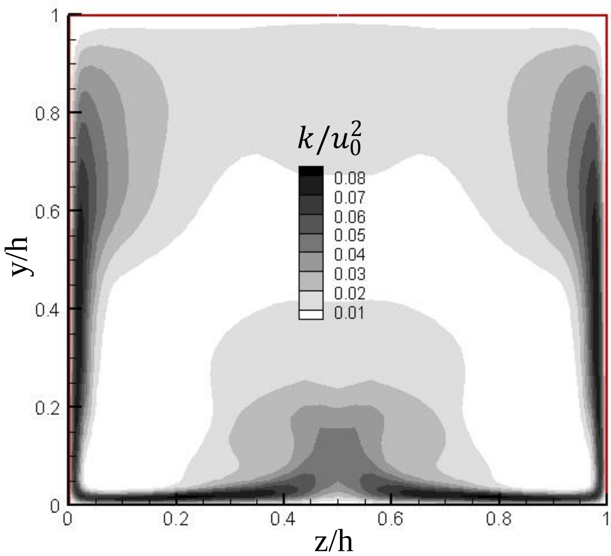

(c) $Ro = 0.176$

Fig. 5-40 Turbulent kinetic energy iso-levels normalized by the ${u_0}^2$

5-3.1.5 Conclusion

Stationary and rotating duct flows have been studied by a hybrid RANS/LES method. The stationary duct simulation captured the main flow pattern of eight counter rotating cells and the secondary flow of two small counter rotating cells near each corner, which is reported in DNS work by Gavrilakis [1992]. The axial velocity predictions show a good agreement with the LES of Pallares and Davidson [2000, 2002]. The only difference in the contour shape is near each corner, where the secondary flow is weak and the case study is sensitive to the near-wall anisotropy of the Reynolds stresses.

The rotating duct model reproduces the two main features of the interaction of the Coriolis force with the mean shear. The first is the formation of the two large counter-rotating cells that convect the low momentum fluid from the stable side (suction side) to the unstable side (pressure side) of the duct, passing through its central region. Two small vortices located on the unstable side convect the high momentum fluid towards the stable side. The second aspect is the redistribution of the turbulent kinetic energy that increases the turbulence levels on the unstable side and the opposite occurs on the stable side, compared to the stationary duct. The comparison of the axial velocity profiles with the available results from DNS and LES shows a good agreement for different values of the rotation number Ro. This study has verified the ability of the in-house hybrid RANS/LES method to predict three-dimensional turbulent flows in a rotating frame of reference.

5-3.2 Test case 6: Unshrouded axial turbine rotor cascade (3D flow)

5-3.2.1 Objective

The final validation test case is the flow simulation in an unshrouded axial flow turbine rotor. The rotor belongs to a subsonic $1\frac{1}{2}$ axial flow turbine stage. The reasons of selecting this test case are:

- The turbine rotor geometry and the turbine non-dimensional numbers are similar to the shrouded turbine rotor of chapter 6, which is the main target of this study.
- Detailed measurements are available that represent a good opportunity to validate the code against a flow structure that is similar to the one of the shrouded rotor of chapter 6, for which only numerical data is available for comparison.

5-3.2 .2 Introduction

Three-dimensional steady flow simulations are required by turbomachinery designers to study the physical flow phenomena in turbine stage, to optimize the stage performance. Many experimental measurements and numerical simulations have been performed in a laboratory $1\frac{1}{2}$ subsonic axial flow turbine stage to give a better understanding of the flow field structure. Steady flow calculations using an isolated rotor blade row and the complete $1\frac{1}{2}$ stage turbine were performed by Emunds et al. [1999]. They showed that the mean flow parameters downstream of the isolated turbine rotor are predicted reasonably well compared with the full turbine results. Detailed experimental measurements have been carried out by Zeschky and Gallus [1993] followed by both steady and unsteady simulations by Gallus et al. [1995]. Steady and unsteady flow calculations have been performed on this turbine by Yao et al. [2000, 2001].

5-3.2 .3 Test-case geometry and boundary conditions

The model rotor blade uses the modified VKI profile, as stated by Zeschky and Gallus [1993]. The rotor blades are untwisted. The rotor main parameters are shown in table 5-4. The computational domain covers one blade passage and the mesh sizes are: $133 \times 60 \times 53$ for the rotor blade passage and $81 \times 15 \times 9$ for the tip gap.

The total number of nodes is 433875. The computational grid for the rotor blade passage is shown in fig. 5-41.

Aspect ratio (height/chord)	0.917
Pitch (mid-span)	41.8 mm
Rotational speed	3500 rpm
Hub diameter	490 mm
Tip diameter	600 mm
Blade number	41
Tip clearance	0.4 mm

Table 5-4. The design data for the modified VKI turbine rotor, Zeschky and Gallus [1993].

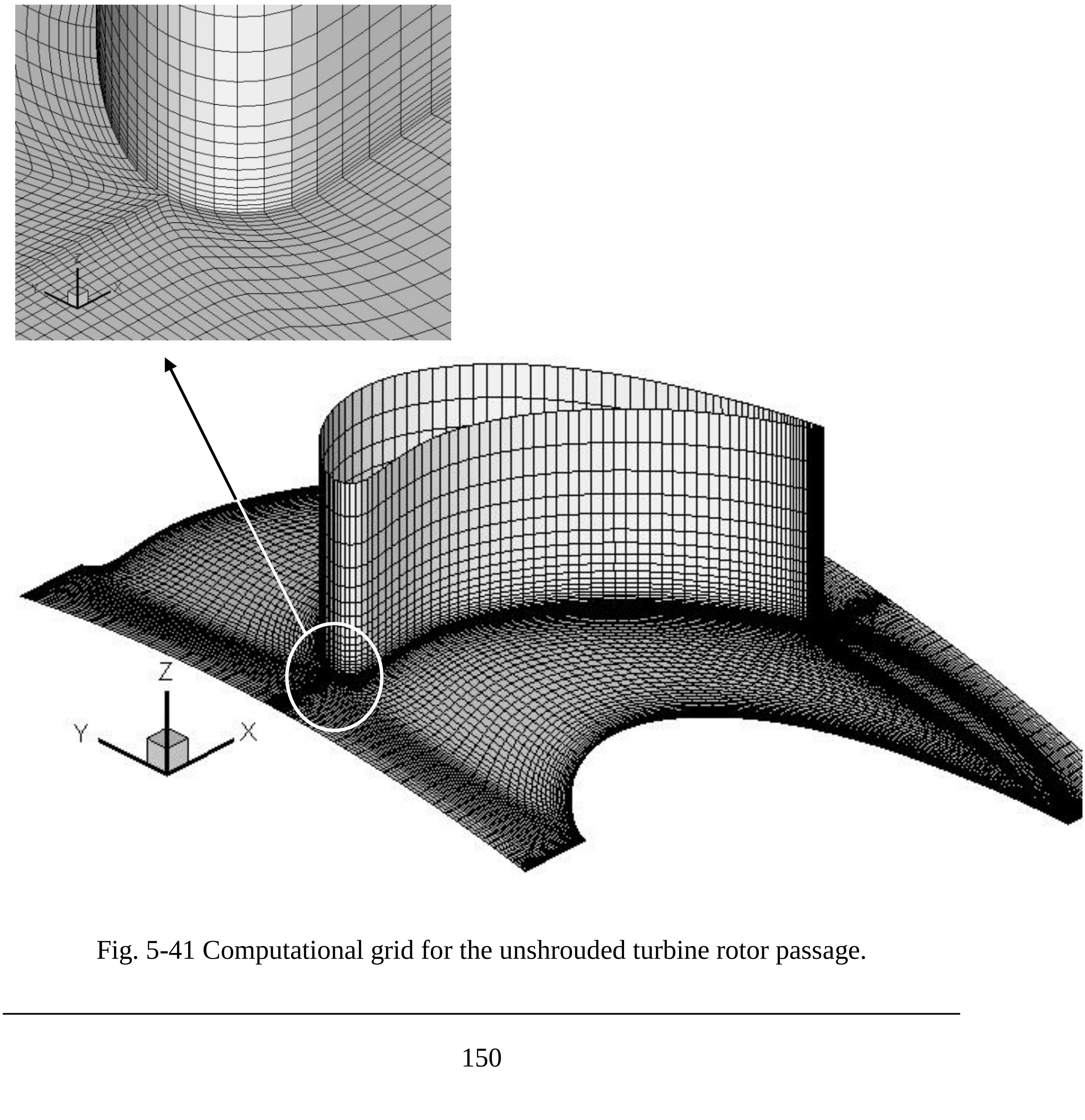

Fig. 5-41 Computational grid for the unshrouded turbine rotor passage.

The subsonic inlet boundary condition is applied at passage inlet by knowing the stagnation pressure, stagnation temperature, and the inflow angle distribution from the upstream stator cascade (mixing plane). The mixing plane flow state from a $1\frac{1}{2}$ stage simulation by Ince [2008] was used as inflow condition. At the passage outlet, the subsonic outlet boundary condition is applied using the pitchwise averaged static pressure profile from the $1\frac{1}{2}$ stage simulation of Ince [2008]. For the repeated fluid surfaces, the rotational periodic boundary condition of section 4-10.8 is used. The no-slip boundary condition of section 4-10.5 is applied at all walls, taking into account whether the wall is rotating or fixed with respect to the blades.

5-3.2.4 Results and discussion

The normalized time-averaged surface static pressure distribution is shown in fig. 5-42. Figure 5-42 shows the surface pressure distribution at five spanwise locations ranging from near the rotor hub to near the blade tip. The comparison between the calculated surface static pressure and the measured values shows a good agreement at all radial locations. The agreement between the calculated and the measured pressure confirms that the steady numerical solver is able to predict the time-averaged blade loading with adequate engineering accuracy when appropriate boundary conditions are applied. These surface pressure distributions are important for the turbomachinery designer to evaluate the steady aerodynamic forces on the blade. The pressure distribution on the suction side shows that the flow on the suction side is exposed to a high acceleration in a narrow region close to the leading edge near the hub while it is exposed to a gradual acceleration up to 60% of the chord from the mid-span to the blade tip. Over the reminder of the suction surface, the flow decelerates with deceleration ranging from low to significant at radial locations ranging from hub to tip respectively. The radial location has a lower effect on the flow over the pressure side than over the suction side. The influence of the radial location on the pressure side flow is more observable near and after 50% chord, where the flow accelerates towards the trailing edge.

Figure 5-43 shows the static pressure contours on the endwall above the rotor normalized by the inlet total pressure. Figure 5-43 compares the static pressure distribution on the endwall of the current CFD calculation with the CFD results by Gallus et al. [1995] and with the experimental results by Zeschky and Gallus [1993]. The comparison shows overall a good agreement between the present results and both

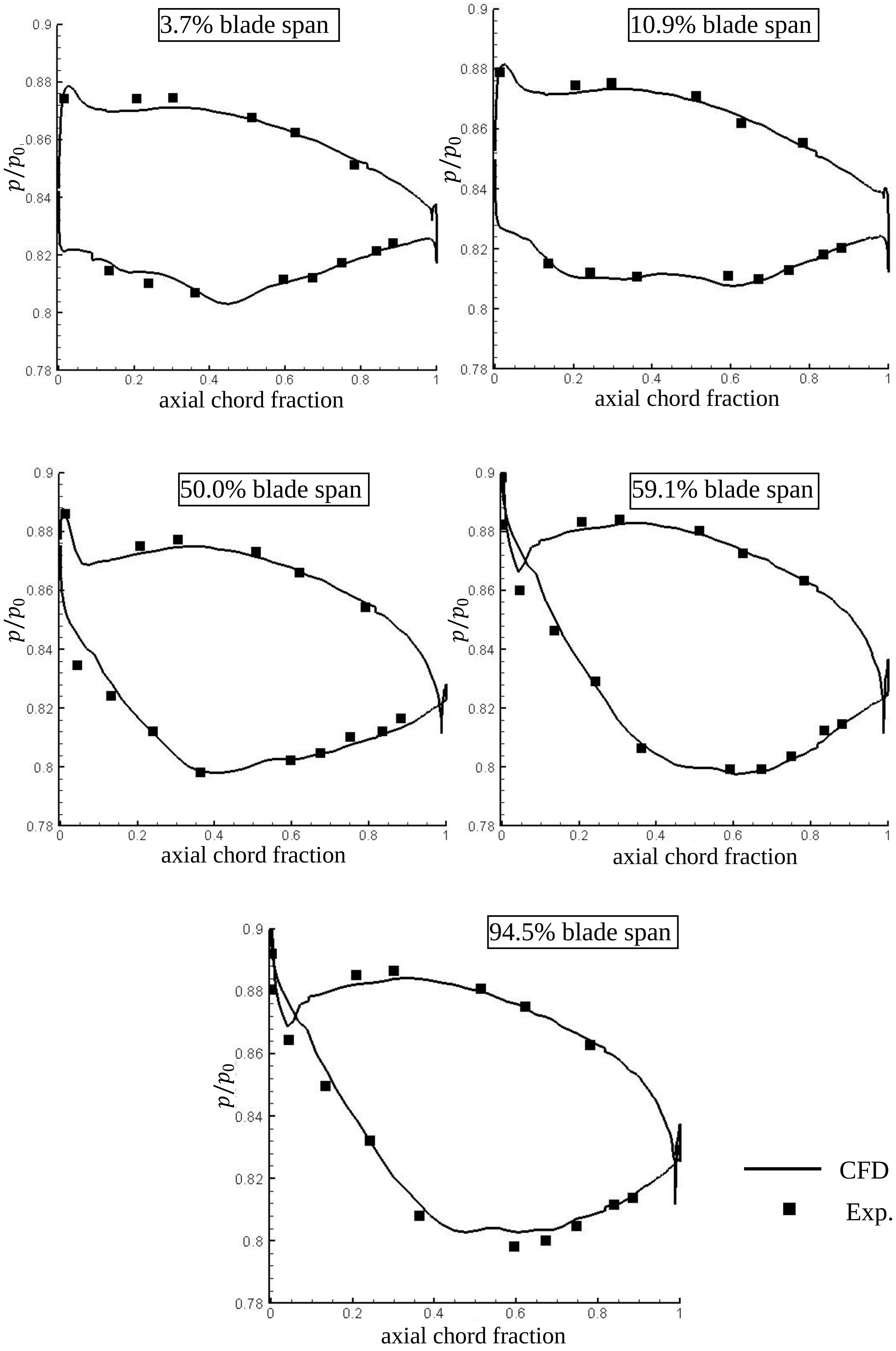

Fig.5-42 Blade surface static pressure distribution normalized by the total inlet pressure p_0.

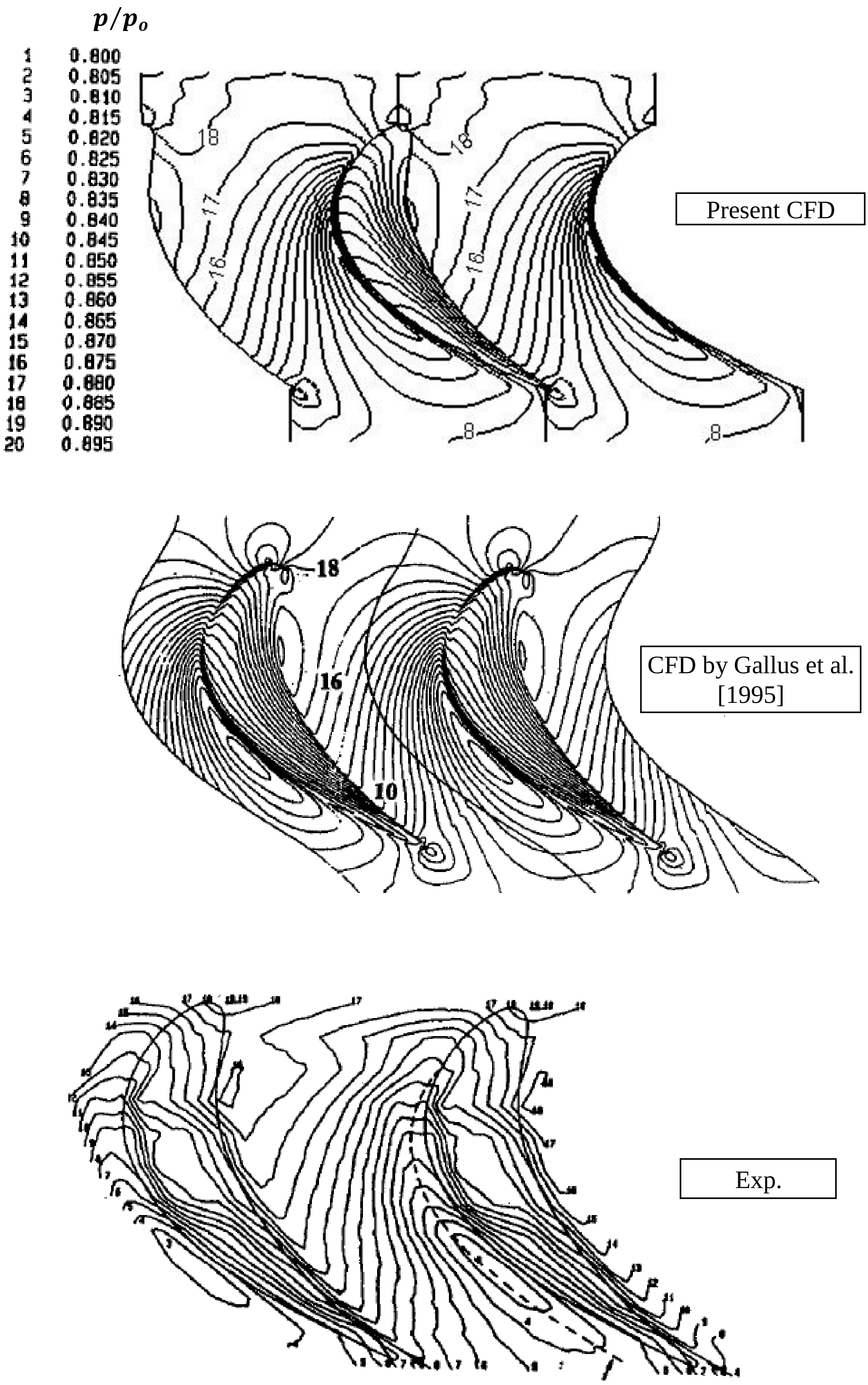

Fig. 5-43 Static pressure field at the rotor casing normalized by the total inlet pressure p_0.

the previous CFD and experimental results. The present model reproduces very well the location of the stagnation point at the leading edge, where the flow approaches the blade tip clearance with approximately zero incidence angle, as reported by Zeschky and Gallus [1993]. The simulation shows a good prediction for the axial location of the minimum pressure along the suction side, but the pitchwise location of this static pressure minimum, which represents the footprint of the tip clearance vortex on the rotor casing, is predicted by both CFD outputs closer to the suction side than in the experimental plot. Cross-flow over the blade tip is indicated by the close spacing between the constant pressure lines over the blade tip starting downstream of 50% axial chord and extending to the trailing edge. The presence of this cross-flow is confirmed by plotting the predicted velocity vector field over the blade tip, shown in fig. 5-44(a). Arrows show only the flow direction and not the magnitude due to the large flow acceleration towards the profile trailing edge. The velocity vector field was not measured in experiment due to the difficulty of using a velocity measurement device, such as a five-hole probe, in the small clearance between the blade tip and the casing. The CFD data is therefore a good complement to the pressure measurements. The velocity vector map of figure 5-44 (a) shows the emergence of a tip leakage cross-flow downstream of 50% axial chord due to the 0.4 mm clearance gap between the rotating blade tip and the stationary casing. This cross-flow induces a tip leakage vortex on the blade tip suction side downstream of 50% axial chord. Three-dimensional view of this tip leakage vortex is presented in fig. 5-44 (b) by plotting the local streak lines. Figure 5-44 (b) shows the formation of the tip leakage vortex with compact core, close to the suction side. The small core size is due to tight clearance fit between the blade tip and the casing.

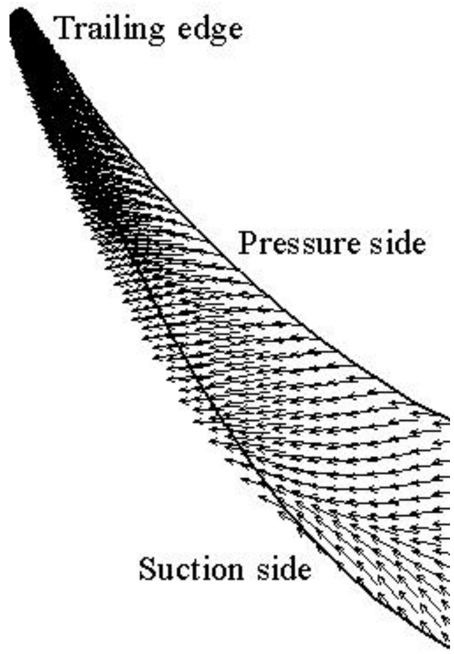

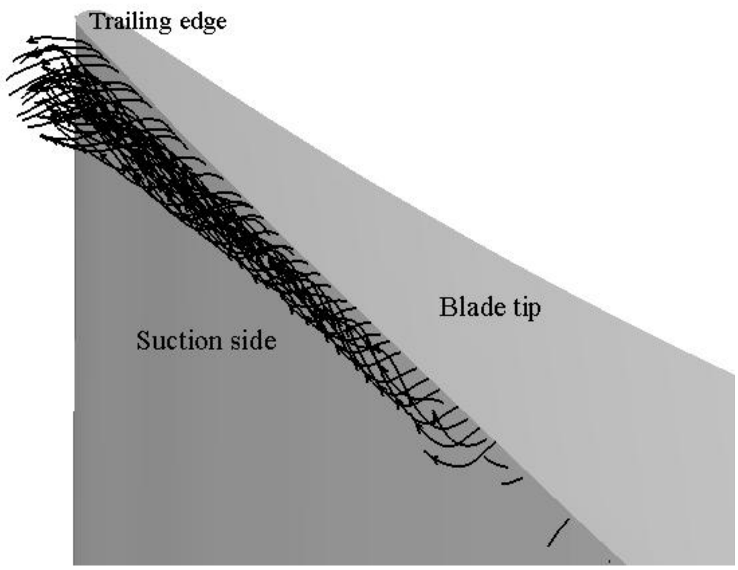

Fig. 5-44 (a) Velocity vector field above the rotor blade tip.
(b) Streaklines showing the tip leakage vortex near the, rotor blade suction side.

The averaged circumferential absolute flow velocity, c_2 across the blade span is given in fig. 5-45 at the rotor outlet. The rotor exit absolute velocity is compared to the measurements using hot-wire and pneumatic probes by Zeschky and Gallus [1993]. The predicted velocity distribution fits in between the two experimental results below 60% of the blade span. The predicted velocity distribution agrees well with the hot-wire probe measurements, especially below 25% of the blade span, where the passage vortex is dominant. This means that the present model is able to reproduce the effect of the passage vortex on the pitch-averaged absolute velocity distribution close to the hub at the rotor exit. Above 60% of the blade span, the discrepancy between the calculated flow velocity and the measurements increases with the blade span. There is also a noticeable discrepancy between the experimental measurements by the hot-wire technique (unsteady technique) and the measurements by pneumatic probe (steady-state technique). This difference between the two measuring techniques is more observable in the regions where the flow is more unsteady, as reported by Zeschky and Gallus [1993]. This is below 20% of the blade span, where the passage vortex develops and above 60% span, where the upstream vane tip passage vortex, the rotor tip vortex, and the rotor trailing edge vortex develop. The more likely reasons for the difference between the predictions and measurements in fig. 5-45 are the use of the steady inlet boundary condition in the computation, which smears the upstream vane tip passage vortex. Even so, the trend of the radial distribution of the pitchwise averaged absolute velocity at the rotor outlet is reasonably well predicted.

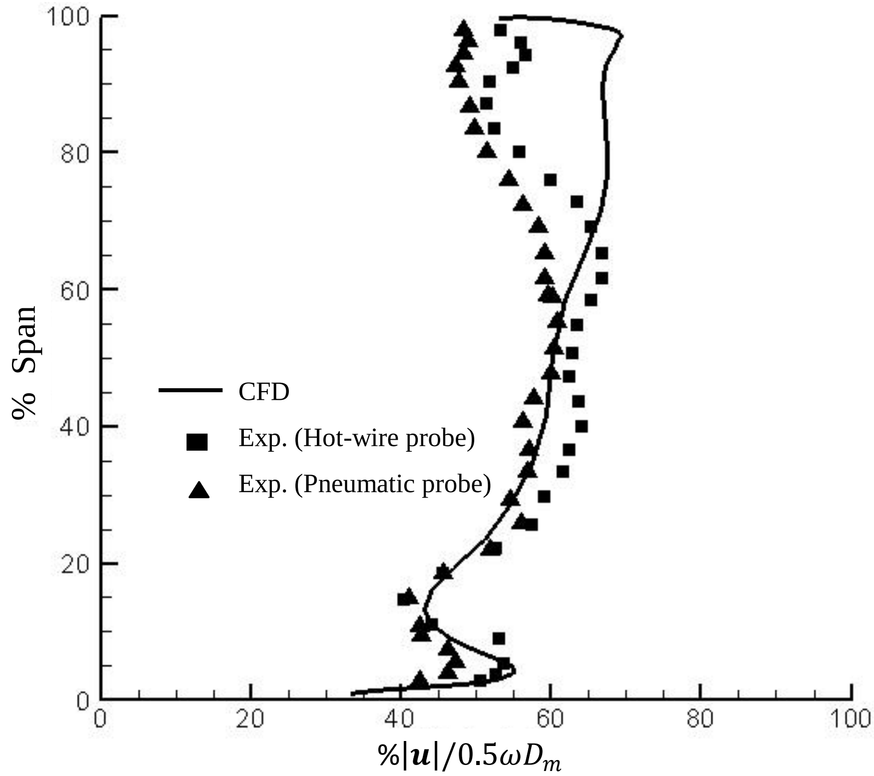

Fig. 5-45 Radial distribution of the circumferential averaged absolute velocity at rotor exit, normalized by the blade mean diameter velocity.

The computed and the measured pitch-averaged absolute total temperature and pressure at the rotor outlet are compared in Fig. 5-46 (a) and (b) respectively. The absolute total temperature and pressure are normalized by the corresponding reference values at the stage inlet. Figure 5-46 (a) shows an appreciable agreement between the computed and measured absolute pitch-averaged total temperature along the blade span, with the CFD overestimating T_0 by up to 0.5 ^{o}C. The comparison of the absolute total pressure in fig. 5-46 (b) points to an overestimation of p_0/p_{0i} along the blade span, despite that the radial trend is reproduced reasonably well. This overestimation of the absolute total pressure can be attributed to two reasons. The first reason, as suggested by Volmar et al. [1998] is that the measurements were taken over different tests inside the $1\frac{1}{2}$ turbine stage at slightly different values of mass flow rate and inlet total pressure. The second reason is that the CFD simulation is performed at a slightly higher value of mass flow rate, as shown in the flow velocity distribution in fig. 5-45. Figure 5-46 (b) shows that the flow solver captures the pressure peak at 8% span and the pressure drop at 15% span, recorded in the experiment, where the hub passage vortex effect is dominant, as stated by Yao et al. [2001].

The radial distribution of the pitch-averaged absolute flow angle at the rotor exit is shown in fig. 5-47, where it is compared with the measured values in Emunds et al. [1999]. Figure 5-47 shows a good agreement with the experimental data, particularly over the range 0% to 60% span. The measured profile of the absolute flow angle at the rotor exit is a measure of the strength of the secondary flow upstream of it and the consistency of the computed flow angle spanwise distribution with the measured one for producing engineering accurate predictions, indicates that the present simulation is able to capture the secondary flow to a satisfactory degree. The predicted secondary flow is visualized by plotting the limiting streamlines on the suction surface of the rotor blade. These streamlines are the footprint of the horseshoe vortex, the passage vortex and the tip leakage vortex. The limiting streamlines of the present simulation are compared with the ones from the simulation Yao et al. [2001] in fig. 5-48. The limiting streamlines from the present computation seem to be quite similar to the ones from the simulation by Yao et al. [2001], where two different flow solvers were used.

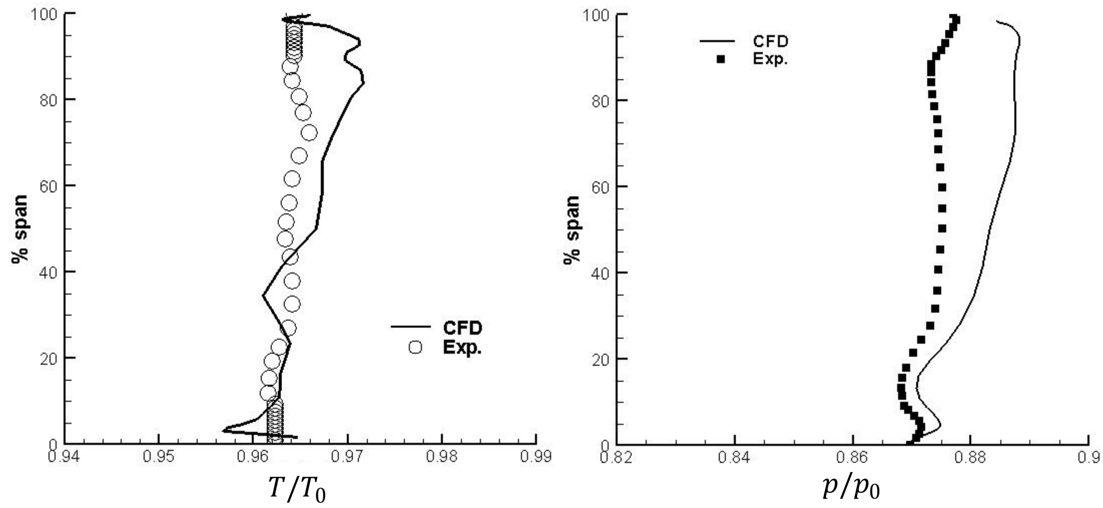

Fig. 5-46 (a) Absolute total temperature at the rotor exit normalized by the total inlet temperature T_0.
(b) Absolute total pressure at the rotor exit normalized by the total inlet pressure p_0.

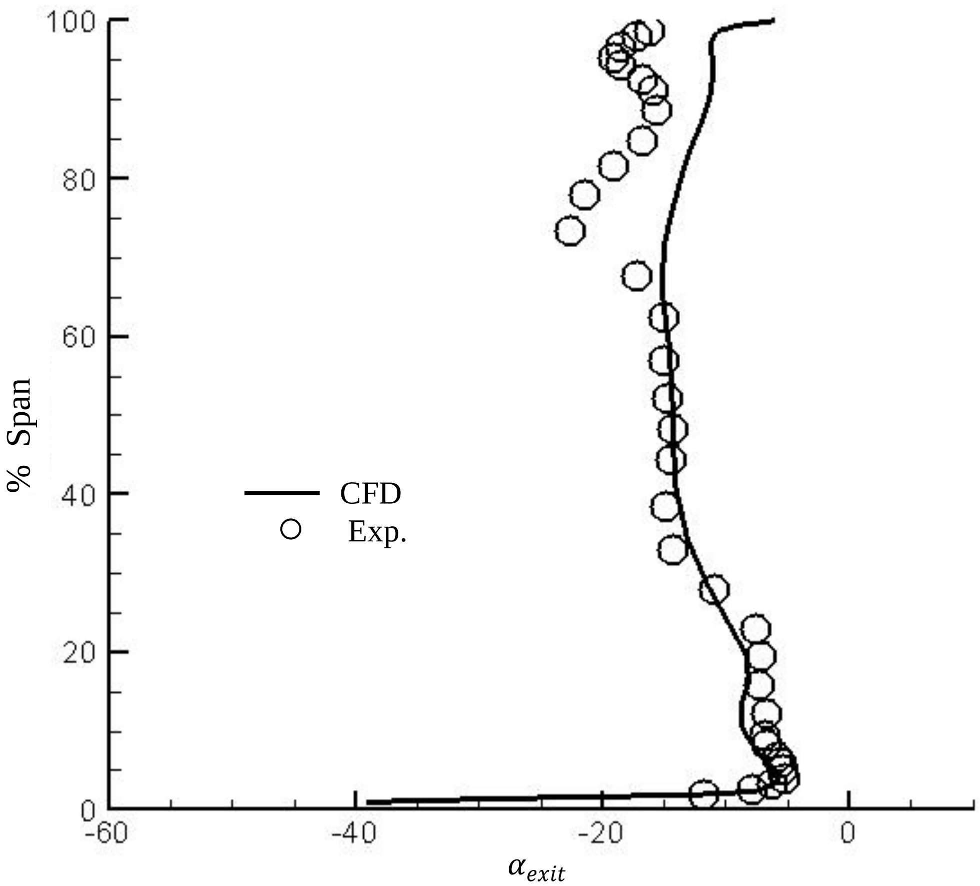

Fig. 5-47 Pitchwise averaged absolute flow angle at rotor exit.

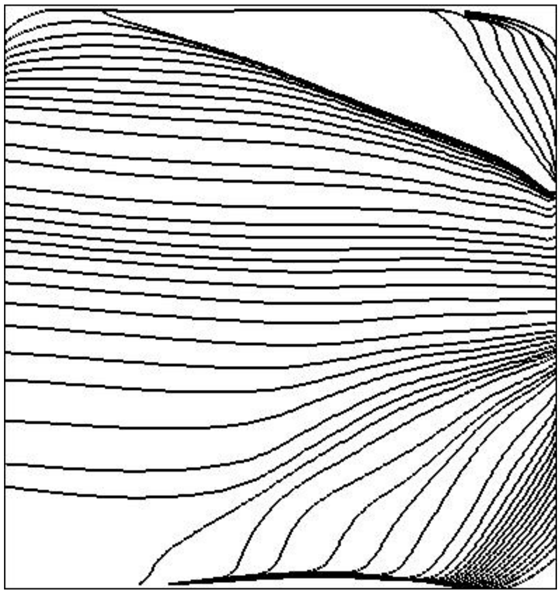

(a) The present solver

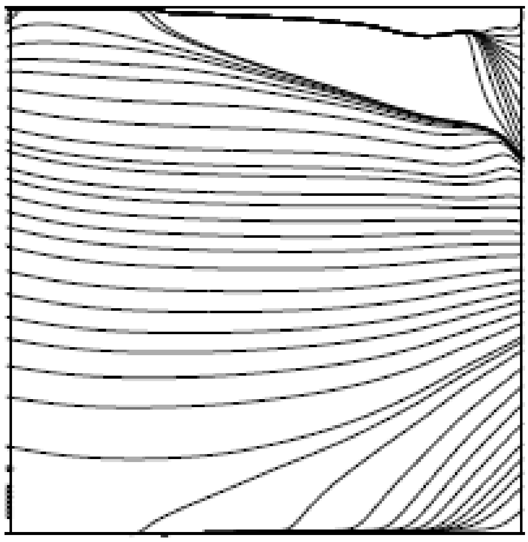

(b) Yao et al. [2000] using the TFLO solver

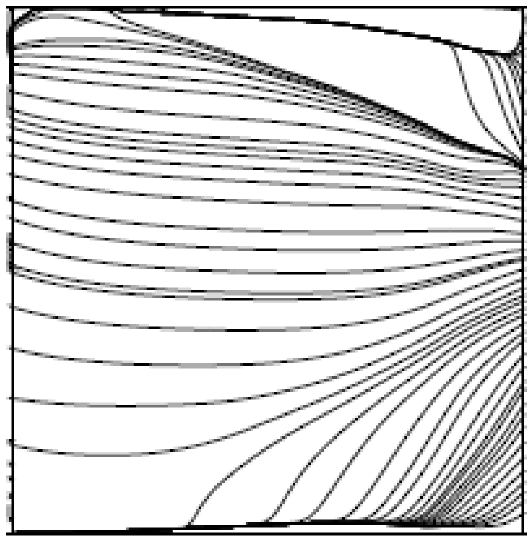

(c) Yao et al. [2000] using the 3DFLOW Solver

Fig. 5-48 Limiting streamlines predicted on the rotor suction surface.

5-3.2.5 Conclusion

Three-dimensional steady flow predictions have been obtained of an isolated unshrouded rotor from a $1\frac{1}{2}$ stage axial flow turbine, in the rotational frame of reference of the rotor. The flow solver reproduces the main flow characteristics such as:

- The blade surface static pressure distribution along the blade span shows a good agreement with the experimental data.
- The cross flow over the blade tip from the pressure side to suction side explains the surface pressure distribution measured at the casing, complementing this experimental data.
- The tip leakage flow vortex with a small core size, determined by the small clearance between the rotor blade tip and the casing
- The radial distribution of the pitchwise averaged flow velocity, absolute total temperature, absolute total pressure, and absolute flow angle, showing a reasonable agreement with experiment, especially below 60% of the blade span. The coarse agreement with measurements above 60% span can be attributed to the use of the steady inlet boundary condition, which smears the upstream stator secondary flow. However, the predicted trends agree well with experiment along the whole span.
- The footprint of the horseshoe vortex, the passage vortex, and the tip leakage vortex represented in the limiting streamlines on the rotor suction surface. The comparison of these streamlines with the ones by Yao et al. [2000] shows consistent results.

Chapter 6

CFD simulation of tip leakage flow in a shrouded axial turbine rotor

Increasing the turbine isentropic efficiency has received a great deal of attention over the years leading to current turbine designs reaching up to 93% efficiency. These improvements have been achieved by the use of three-dimensional turbine blade profiles and advanced manufacturing technology. For further improvements, a better understanding of the flow structure and of the associated loss generation is required, to reduce the stage loss and control the secondary flow effects on the downstream components. By considering the loss generation sources of a shrouded turbine stage, the tip leakage loss represents one of the most important sources of loss generation. For instance, it contributes 16.2 % and 27.6% of the stage loss for gap clearance values of 0.3% and 1% of the blade span respectively, as reported by Pfau [2003]. These tip leakage losses are related to the decrease of mass flow rate in the working section of the turbine stage, the aerodynamic and windage loss inside labyrinth seal, and the mixing between the leakage jet flow and the main working passage flow. In addition to these quantified losses, there are some effects that cause further losses downstream of the leakage jet injection point, such as the induced incidence angle and increased flow unsteadiness.

The present part of the study aims to assess the impact of the labyrinth seal leakage flow on the loss generation and on the flow field of a shrouded turbine rotor. The study focuses on:

- The flow field structure at the labyrinth seal inlet and exit cavity
- The labyrinth seal performance variation with geometrical parameters
- The interaction of the leakage flow jet with the rotor main flow

6-1 Test-cases geometry and boundary conditions

To meet the above objectives, an isolated shrouded rotor is modelled by CFD. The rotor belongs to a subsonic $1\frac{1}{2}$ axial flow turbine stage. The rotor blade is untwisted and uses a modified VKI profile, Gallus et al. [1995]. The rotor blade statistics are listed in table 6-1. The gap between the rotor shroud and the casing is occupied by a look-through type labyrinth seal. The labyrinth seal consists of the inlet cavity, a number of fins evenly spaced normal to the blade shroud, and the exit cavity. The number of the simulated cases is seven. The simulated cases can be classified into three groups as follows:

- 3 cases with a different number of fins.
- 3 cases with a different clearance between the rotor shroud and the labyrinth fin.
- 3 cases with a different angle of the leakage jet injection into the main passage flow. This angle represents the tangent at the exit cavity interface with the main flow passage.

The number of cases is seven because one case is common among all 3 groups. In addition to these cases, a reference case with zero clearance and a clean endwall is simulated for purpose of comparison. This case is determined by closing the inlet and exit cavities. A summary of the geometrical parameters of the simulated cases is given in table 6-2. Figure 6-1 shows a sketch of the labyrinth seal arrangement components and its position over the shrouded rotor. Figure 6-2 shows sketches of geometries with variations in the number of fins and in the injection angle at the cavity exit. The computational domain consists of the rotor flow passage and the labyrinth through flow. The rotor computational domain contains 6 blocks. The mesh sizes for the rotor passage blocks are $133 \times 45 \times 45$ grid points in axial, pitchwise, and spanwise directions respectively. The number of blocks for the labyrinth seal computational domain depends on the number of fins ranging, from 6 blocks for 2 fins to 10 blocks for 4 fins. The total number of grid points for both domains is approximately 460500 when using two fins and 600000 when using 4 fins. A structured H mesh is used. Figure 6-3 (a) shows the mesh at the rotor blade passage with the over-shroud labyrinth seal and at the blade hub. The mesh through the labyrinth seal across the meridonal plane is shown in fig. 6-3 (b).

The main limitation of the single blade row simulation is the need to apply inlet and outlet boundary conditions, as stated by Rosic et al. [2006]. This limitation is overcome by getting the inlet and exit boundary flow states respectively after and before the mixing planes from the simulation of the whole $1\frac{1}{2}$ turbine stage using an industrial code Ince [2008]. This data is combined with the subsonic inlet and exit boundary conditions developed by Chima [1998] based on Giles' non-reflecting boundary characteristics. These characteristics allow the boundary conditions to be applied close to the turbine blades without any significant loss of accuracy as reported by Giles [1990]. These characteristics enabled the CFD community to simulate multistage turbomachinery by simulating successive blade rows from inlet to exit, as pointed out by Chima [1998]. Also, Chima stated that these boundary conditions can be used close to the blade row without forcing the flow to be axisymmetric.

For the pitchwise boundaries, shown in fig. 6-3 (a), a rotational periodic boundary condition is used. The no-slip boundary condition is applied at all walls taking into account whether the wall is rotating or fixed.

Aspect ratio (height/chord)	0.917
Pitch (mid-span)	41.8 mm
Rotational speed	3500 rpm
Hub diameter	490 mm
Tip diameter	600 mm
Blade number	41
Reynolds number based on the chord	4.9×10^5

Table 6-1. Design data for the turbine rotor.

Case No.	No of fins	Gap clearance/blade height	Leakage jet injection angle (deg.)	Comments
0	N/A	N/A	N/A	Removed labyrinth seal and its inlet and exit cavities
1	2	0.01	90	The common test case
2	3	0.01	90	Group 1
3	4	0.01	90	Group 1
4	2	0.005	90	Group 2
5	2	0.015	90	Group 2
6	2	0.01	30	Group 3
7	2	0.01	60	Group 3

Table 6-2 Geometrical parameters of the modelled labyrinth seals.

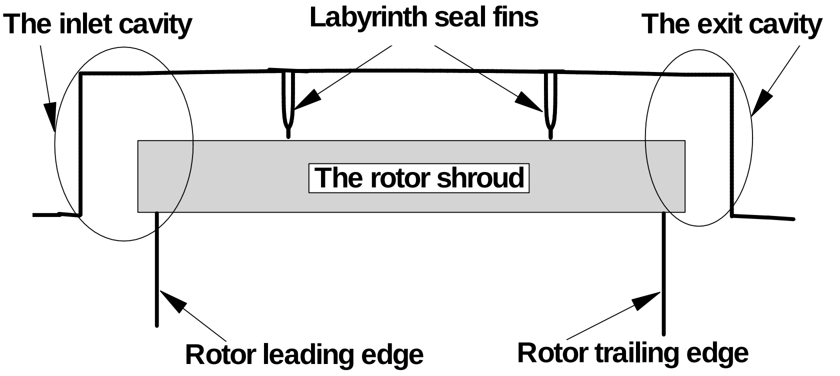

Fig.6-1 Schematic of a look-through type labyrinth seal.

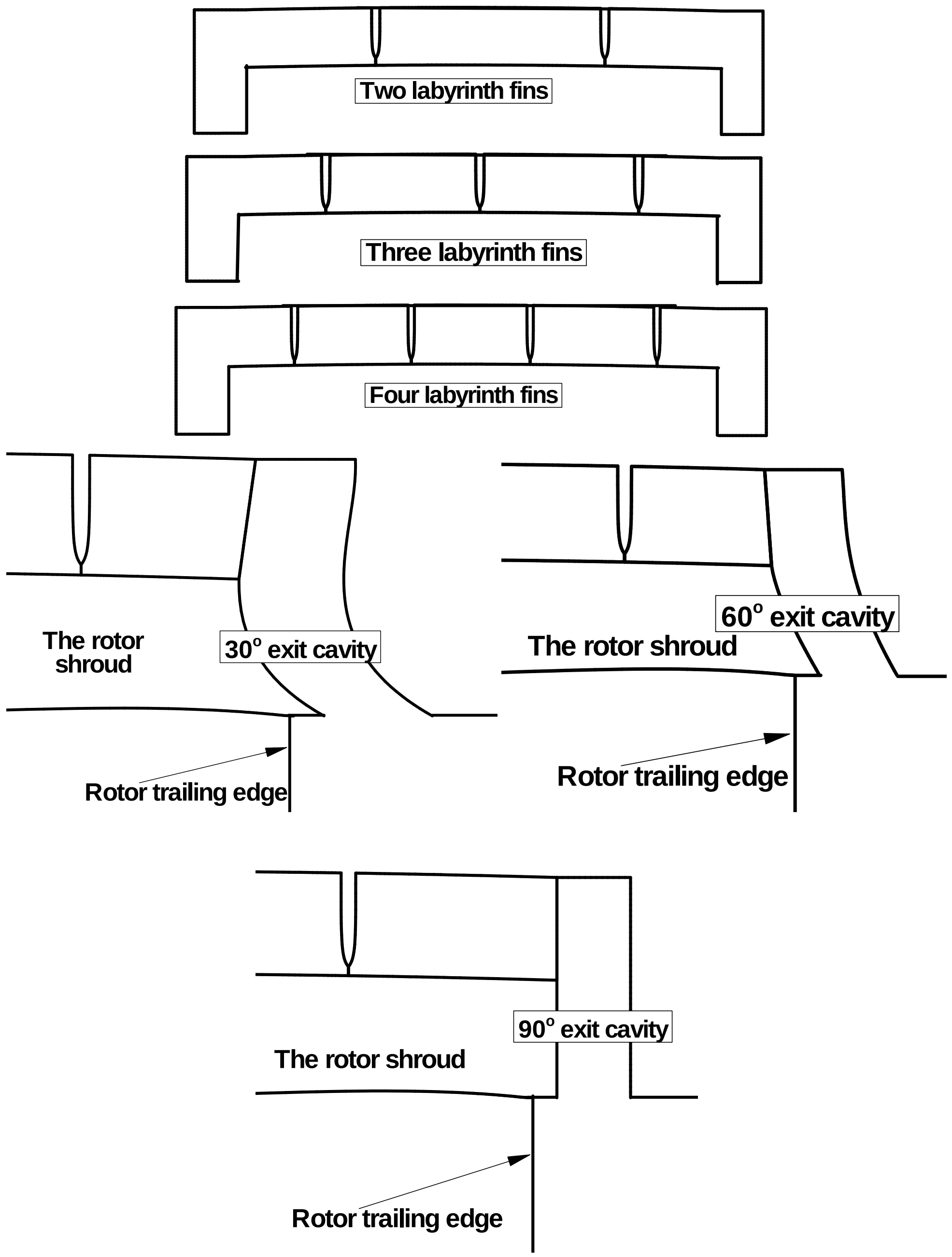

Fig. 6-2 Different number of fins and exit cavity angles for the shrouded rotor.

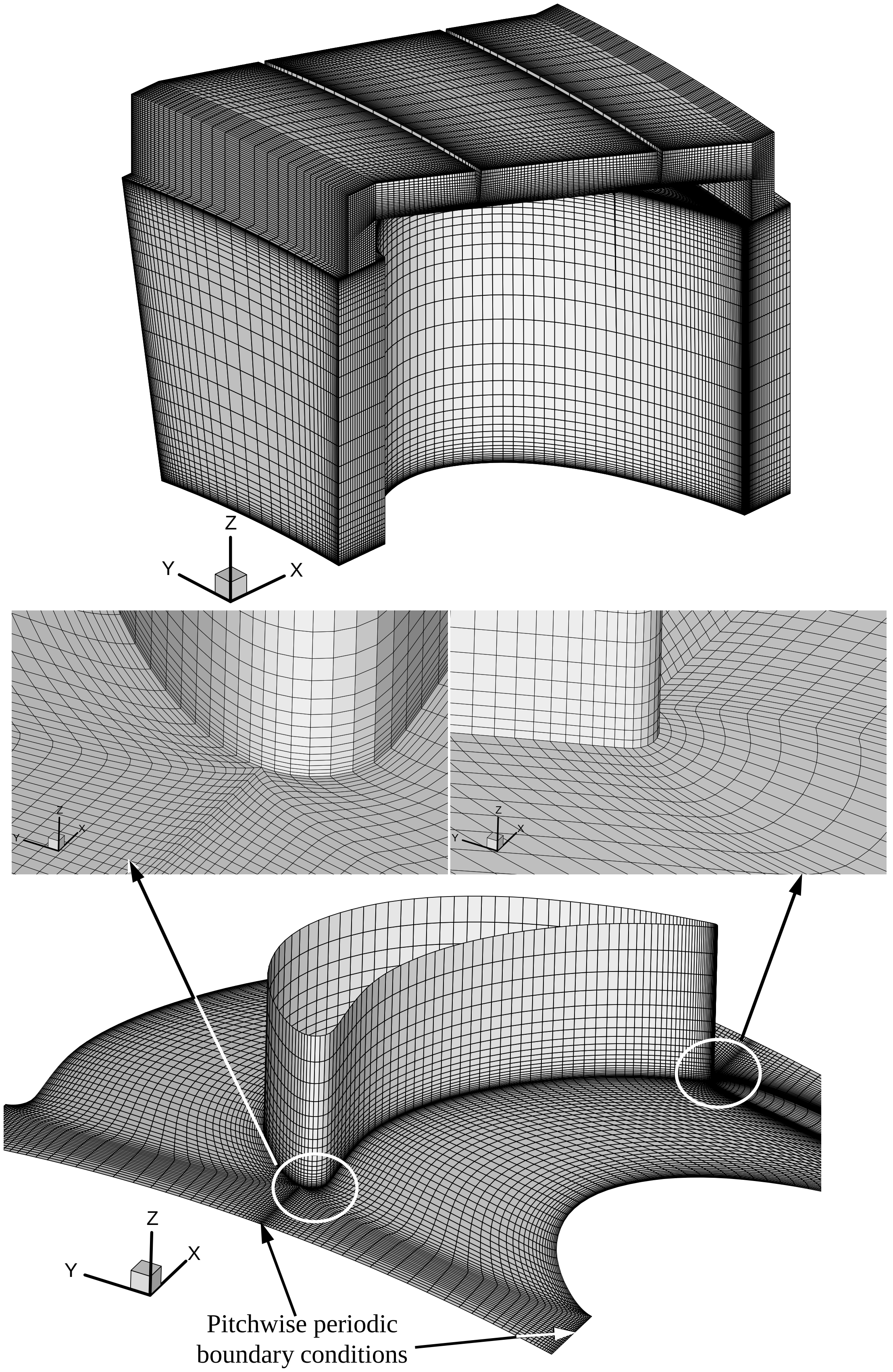

Fig. 6-3 (a) Structured H grid for the shrouded rotor.

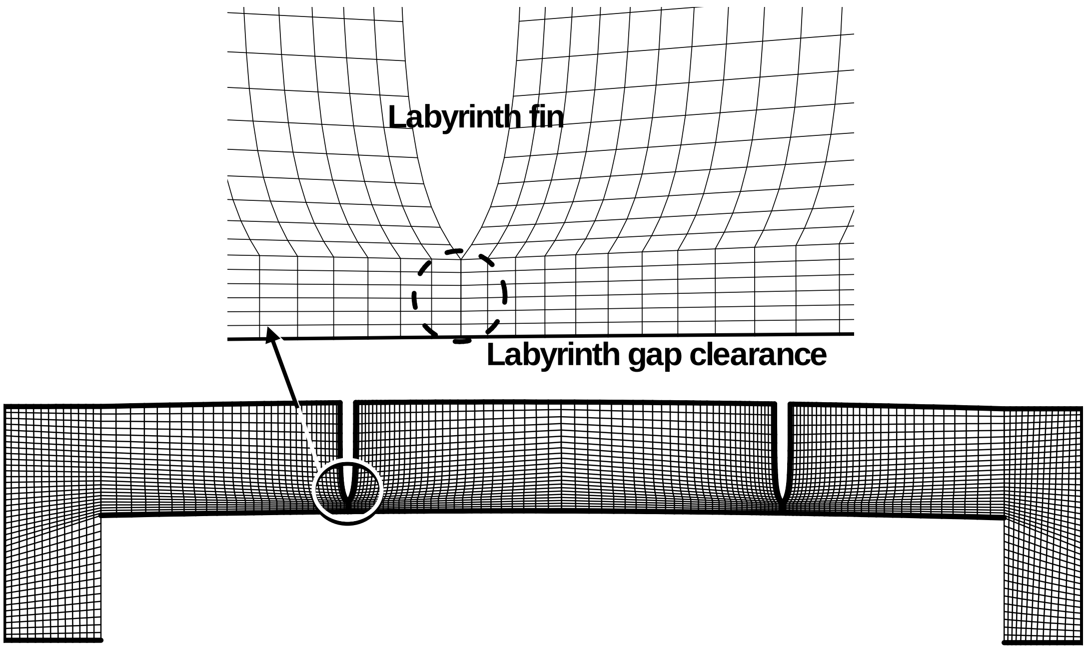

Fig. 6-3 (b) Structured grid for the labyrinth seal computational domain.

6-2 Turbine rotor performance

6-2.1 Mean flow field

In chapter 5, the in-house code was shown to perform well over a hierarchy of test cases that collectively include the same flow features of a rotor cascade. To further improve the confidence in the numerical predictions, the shrouded rotor cascade predictions of the common test case are compared against CFD results from a reference code, Ince [2008]. Figure 6-4 shows the static pressure distribution along the blade surface at the hub, the mid-span, and the tip respectively. The comparison with the CFD results of the reference code shows a good agreement along the blade span. This agreement in the blade surface pressure distribution indicates that the selected inflow, outflow, and periodic boundary conditions are appropriate for modelling a rotor cascade, in agreement with Gallus et al. [1995]. In fig. 6-4, the blade surface pressure distribution is in the shape of a closed loop. The top part shows the surface pressure on the pressure side of the blade, which is the convex surface. The bottom part of the loop shows the surface pressure distribution on the suction side of the blade, which is the concave surface. The static pressure distribution near the hub shows a shift of the stagnation point toward the pressure side, due to the relatively high positive incidence angle. Downstream of the stagnation point, the static pressure on the pressure side nearly remains unchanged up to 0.4 of the axial chord. Then the flow is accelerated along the reminder of the blade pressure surface. On the suction side, the pressure distribution indicates that the flow is strongly accelerated near the leading edge, followed by a weak to moderate deceleration towards the trailing edge. The static pressure distribution at the blade mid-span and the blade tip shows that the flow on the suction side has been accelerated approximately up to the middle of the axial chord then decelerated in the direction of the trailing edge. The blade to blade static pressure and relative Mach number contours at the mid-span are compared with the CFD results from the reference code in fig. 6-5. The static pressure and the relative Mach number contours show a good agreement with the CFD results from the reference code. The relative Mach number contours captured clearly the suction surface boundary layer growth and the wake behind the blade trailing edge. The entropy generated at both locations will be shown later in the turbine secondary flow subsection.

The pitchwise averaged normalized relative total pressure, normalized relative total temperature, non-dimensional absolute total pressure, relative flow angle, and absolute flow angle at the rotor exit are plotted against the span fraction and compared with the reference code results in figs. 6-6 to 6-10. The figures show a quite good agreement between the present results and the reference code results. The distribution of the non-dimensional relative total pressure in fig. 6-6 displays some important flow features, such as the reduction in p_{0r}/p_{ori} below 0.2 span, where the hub passage vortex is present. The effect of the hub passage vortex extends up to 0.4 span by it lifting the endwall flow up the rotor suction surface. The non-dimensional relative total pressure distribution also shows the presence of the leakage vortex near the blade tip by reproducing a considerable drop in the non-dimensional relative total pressure in its core. The effect of the hub passage vortex is captured clearly in the plot of the absolute total pressure in fig. 6-7. The peak at about 0.08 span and the drop at about 0.15 span are predicted by both simulations. Since the output of the mixing plane used as an inlet boundary condition maintains the radial variation of the upstream row, the signature of the upstream vane passage vortex in addition to the rotor trailing edge vortex can be seen in figs. 6-6 and 6-7 in the range 0.6 to 0.8 of the blade span. A good agreement between the present relative total temperature at the rotor exit and the output from the reference CFD code can be observed in fig. 6-8.

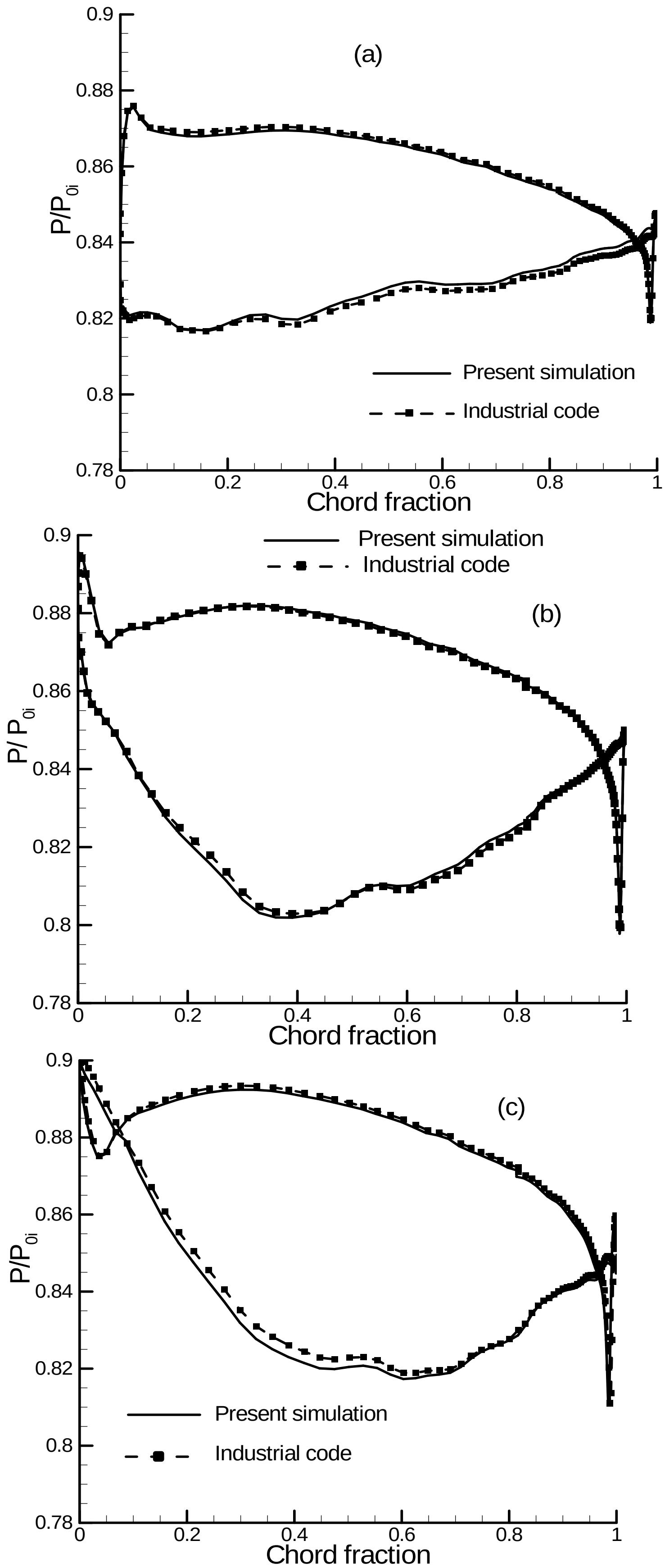

Fig. 6-4 The pressure distribution on the blade surface at (a) hub, (b) mid-span, and (c) tip.

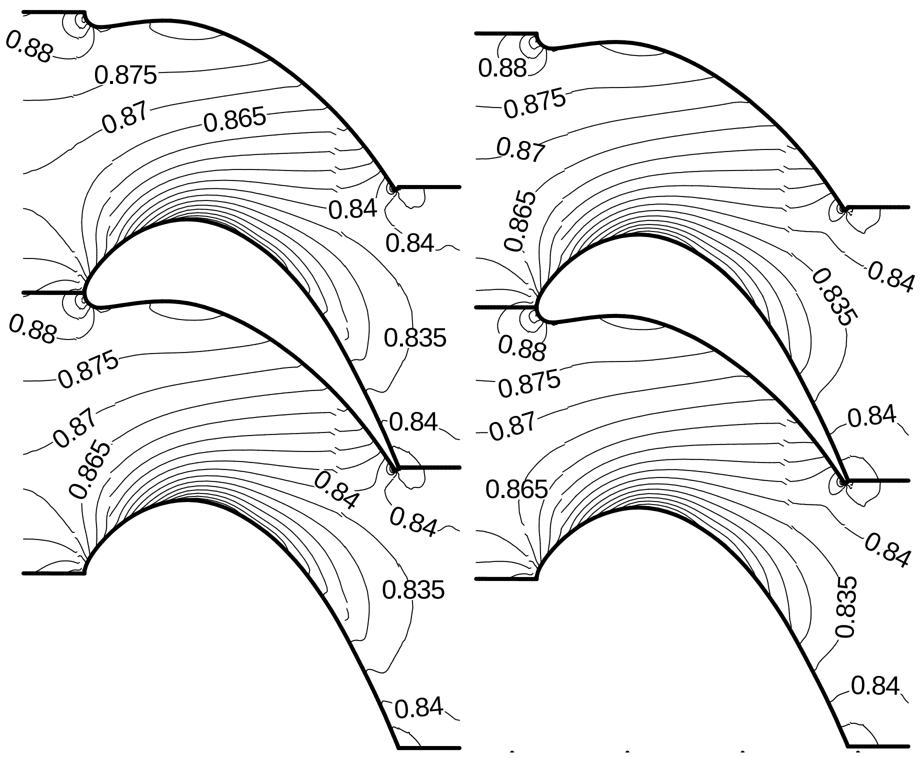

The present solver Industrial CFD code

a) static pressure contours.

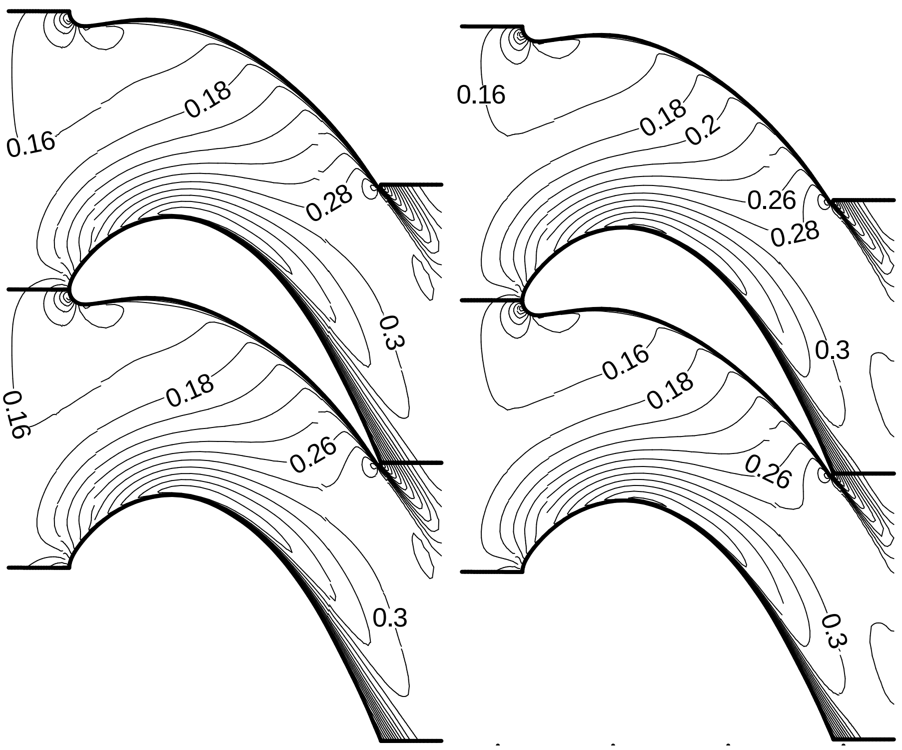

The present solver Industrial CFD code

b) relative Mach number contours.

Fig. 6-5 Static pressure and Mach number contours at the blade mid-span.

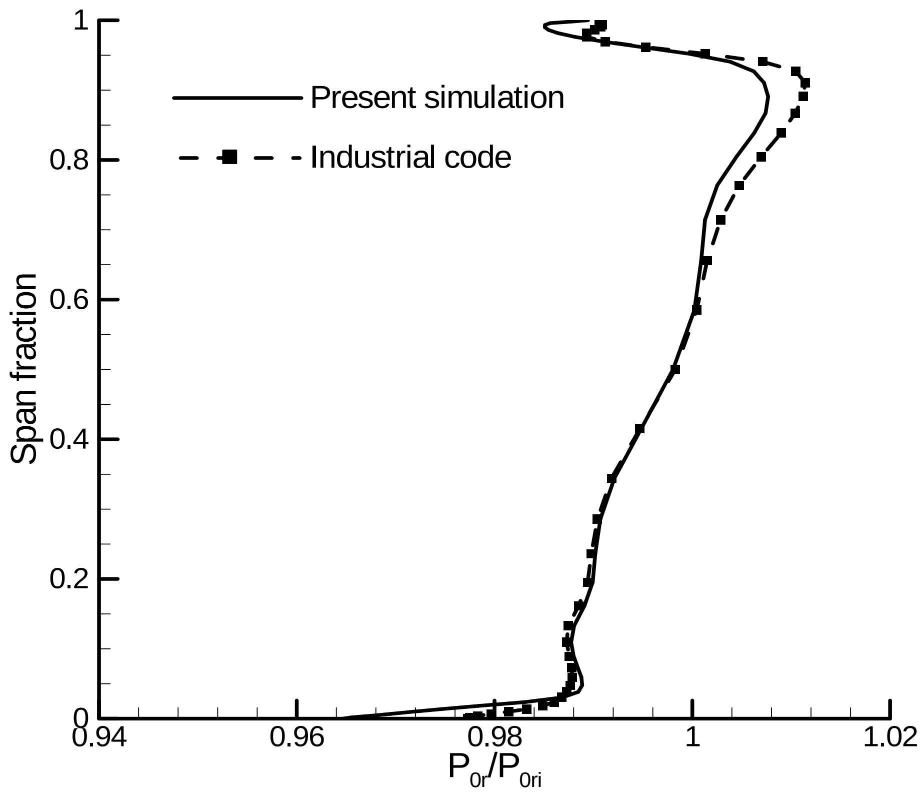

Fig. 6-6 Relative total pressure at rotor exit, normalized by the inlet relative total pressure p_{0ri}.

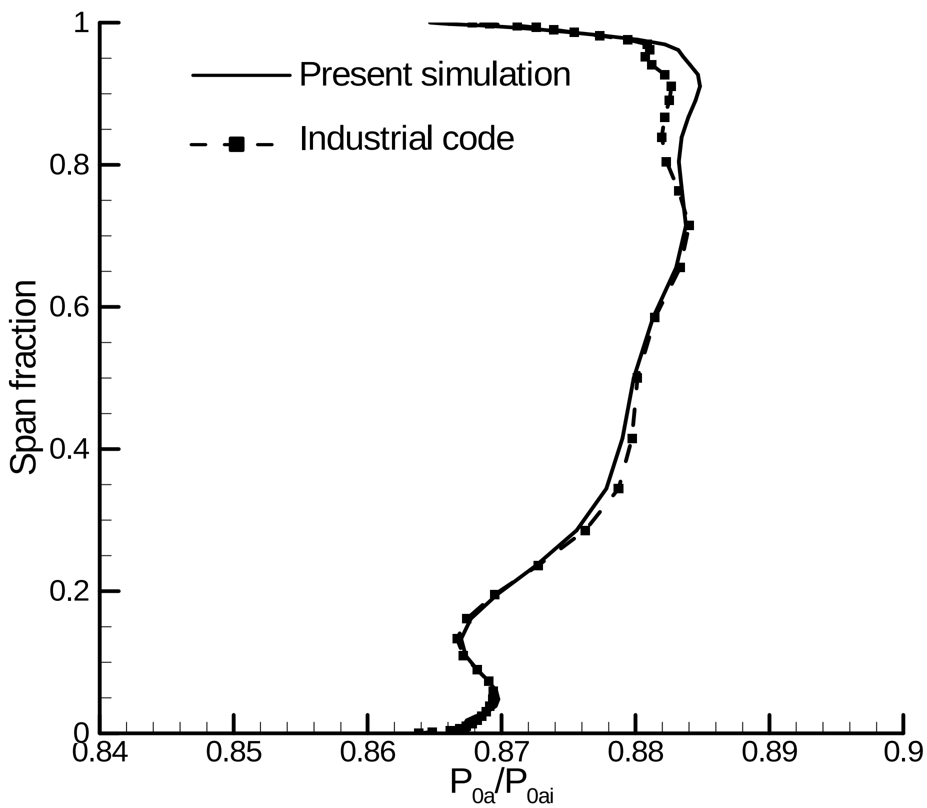

Fig. 6-7 Absolute total pressure at rotor exit, normalized by the inlet relative total pressure p_{0ai}.

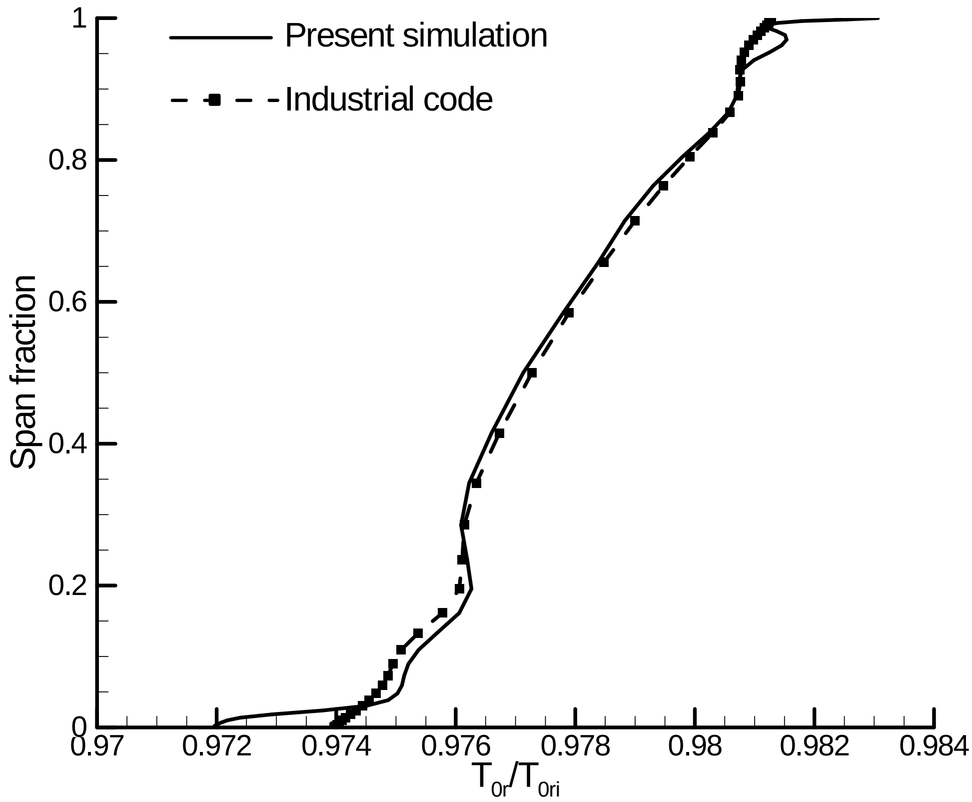

Fig. 6-8 Relative total temperature at rotor exit.

The distribution of the calculated pitchwise averaged absolute flow angle along the span is plotted and compared with the output results from the reference code in fig. 6-9. The comparison shows an overall good agreement between the present and reference code results. The profile of the absolute flow angle indicates that secondary flows affect the flow direction downstream of the rotor trailing edge. Each change in the flow angle spanwise direction represents the effect of a specific secondary flow feature as follows: below 0.2 span, the rotor hub passage vortex, from 0.2 to 0.4 span the upstream vane hub passage vortex, from 0.6 to 0.8 span the trailing edge vortex and the vane casing passage vortex, and near the tip, the leakage vortex.

The predicted profile of the pitchwise averaged relative flow angle along the span is compared with the reference CFD results in fig. 6-10. Once again, a general good agreement between both results is obtained. The rotor secondary flow overturns the main passage flow near the endwall, increasing the relative flow angle, as shown in fig. 6-10. This is followed by the main passage flow underturning towards the mid-span. Between 0.6 and 0.8 span, a little underturning is followed by overturning, as shown in fig. 6-10, which is due to the trailing edge vortex and the vane casing passage vortex interaction. The effect of the leakage jet results in flow underturning near the case. This underturning due to the leakage effects is captured by the present solver.

The comparison with the reference code is very encouraging, since a quantitative and qualitative agreement has been achieved for all the main flow parameters of figures 6-6 to 6-10. The in-house code shows the ability to deliver results that are very similar to those obtained by the other calibrated codes.

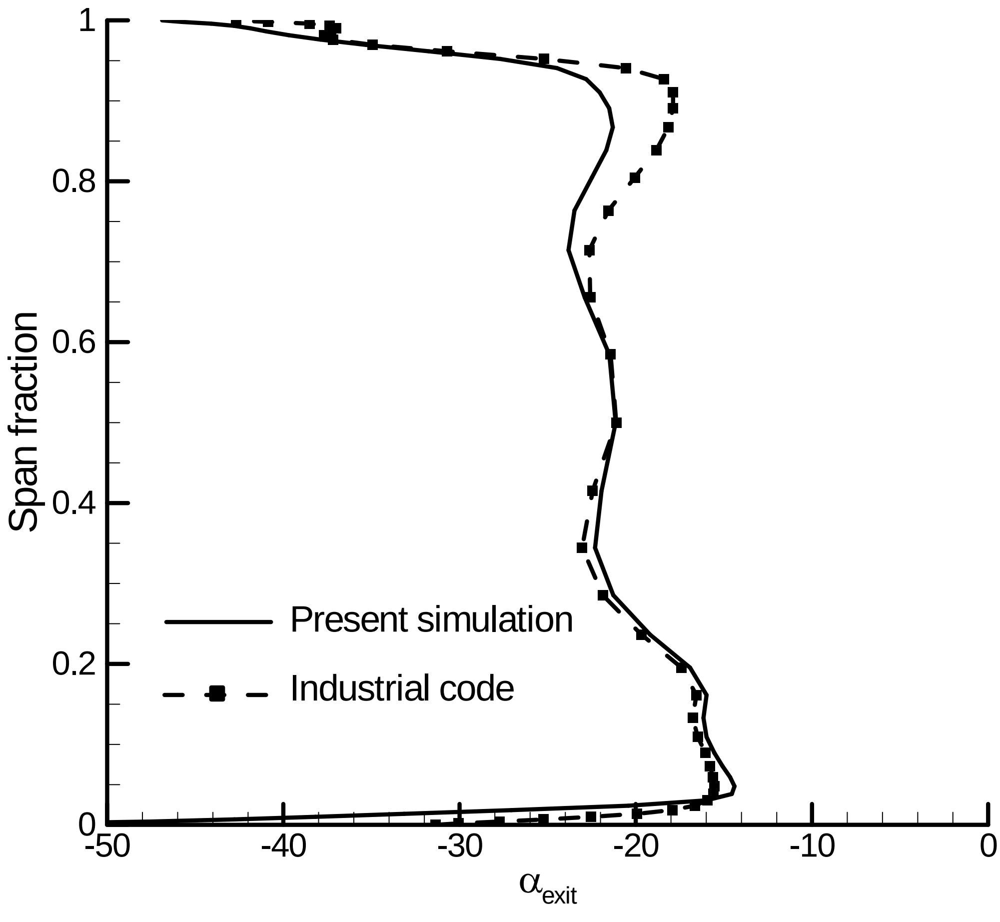

Fig. 6-9 Absolute flow angle at rotor exit.

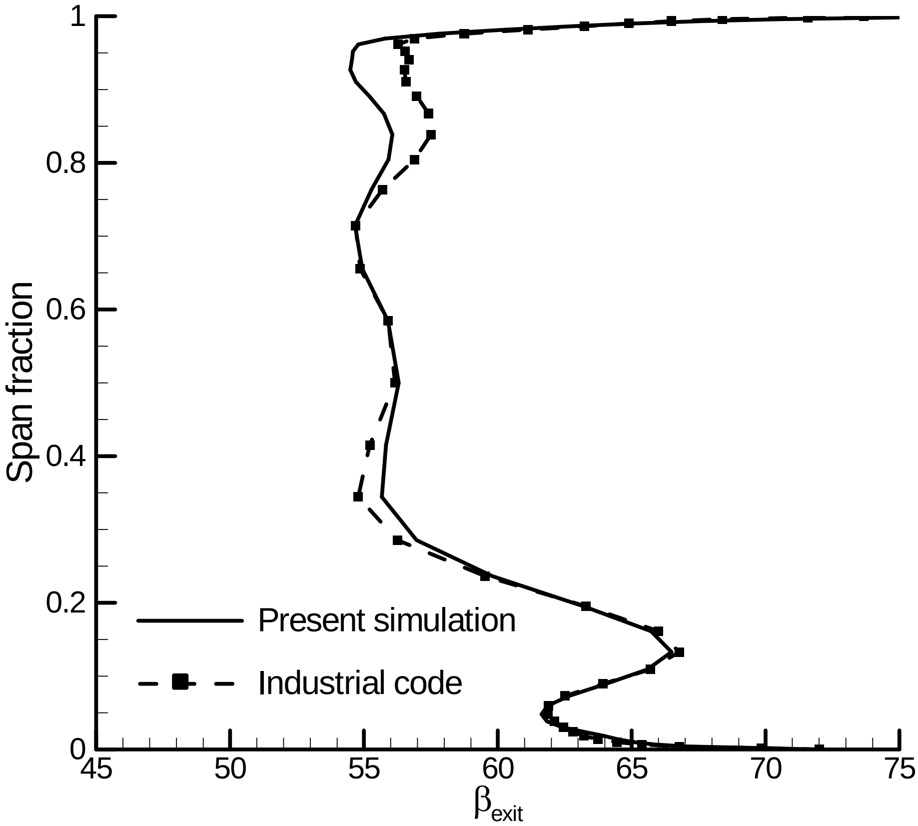

Fig. 6-10 Relative flow angle at rotor exit.

6-2.2 Secondary flow field

The rotor blade passage is occupied by highly unsteady secondary flows due to the high turning angle over the rotor blades. In the low aspect ratio blades, the losses generated due to these secondary flows may reach roughly half the total loss across the blade row, Gregory-Smith and Cleak [1992]. At the hub, the inlet end-wall boundary layer separates at the saddle point upstream of the rotor blade, due to the streamwise pressure gradient generated by the presence of the rotor blade. The end-wall boundary layer rolls up, forming the leading edge vortex shown in fig.6-11. The vortical structure formed at the leading edge is stretched around the rotor blade, forming a horseshoe vortex. One of the two legs of the horseshoe vortex is named pressure side leg and the other is named suction side leg, as labeled in fig. 6-12. The whole stream surface starts to slowly rotate behind the leading edge forming, what is known as the passage vortex. The pressure side leg travels through the passage between two adjacent blades following a smooth curve. The pressure side leg merges with the passage vortex, as suggested by Sieverding [1985] since they have the same

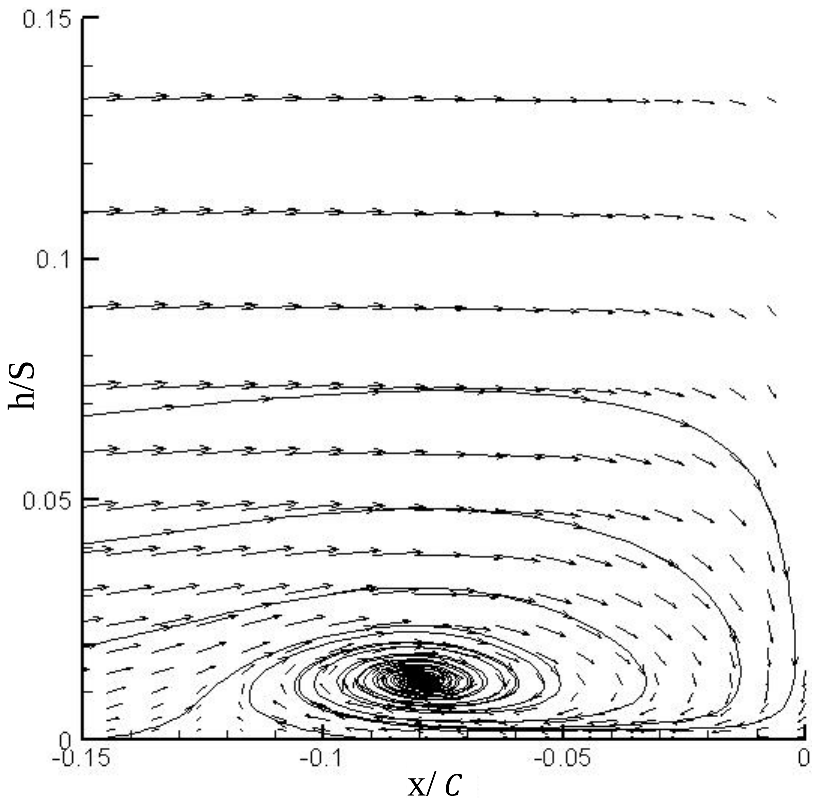

Fig. 6-11 The leading edge vortex (the core of the horseshoe vortex).

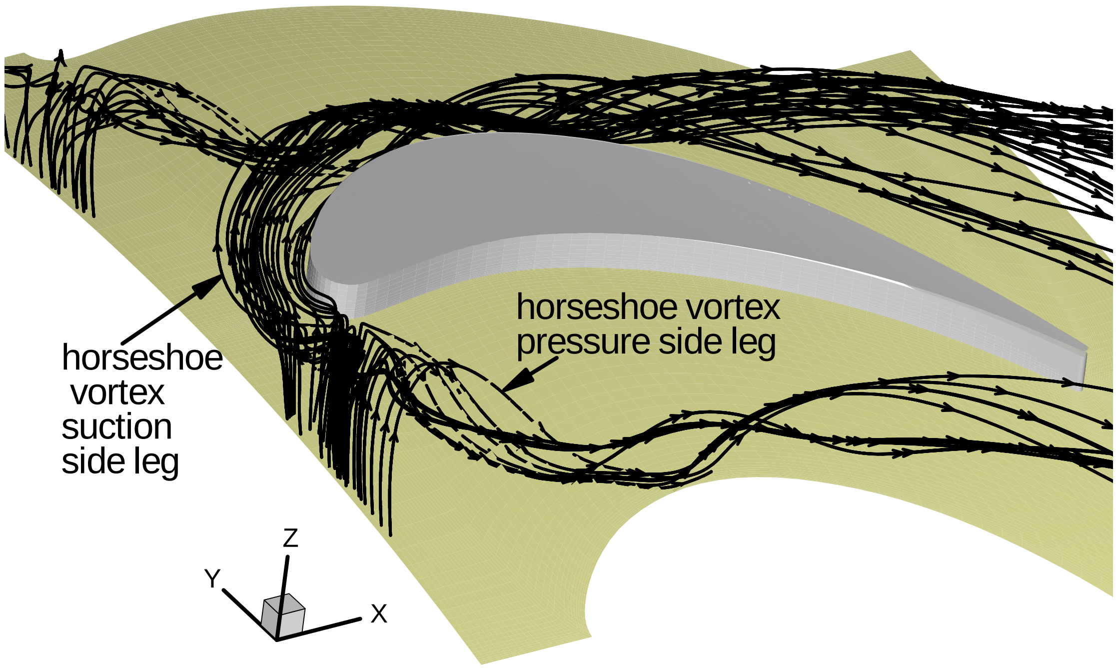

Fig. 6-12 The horseshoe vortex legs.

sense of rotation and their cores align. The suction side leg remains close to the suction side and warps itself around the passage vortex, like a planet rotates around the sun, Langston [2000]. The warping of the suction side leg around the stronger passage vortex induces the formation of a new vortex. In its way downstream, the suction side leg loses its intensity and gradually dissipates in the last part of the decelerating portion of the axial chord. The passage vortex is subjected to the blade to blade pressure gradient and it is washed across the endwall towards the suction surface. It grows and merges with the pressure side horseshoe vortex leg and is fully developed at 0.55 of axial chord, which is still upstream the passage throat. It concentrates the low energy fluid in a loss core on the suction side. The passage vortex is one of the main sources of loss due to its size and intensity, particularly at the rotor exit. Figure 6-13 shows the velocity vector field in a plane normal to the streamwise direction at 0.55 of the axial chord. Figure 6-13 shows the secondary flows of the fully developed passage vortex, the new induced vortex, the rotor secondary flow, and the upper passage vortex. There are also two vortices, counter rotating with respect to the passage vortices, at the hub and tip, known as the corner vortices. These two vortices are located in the corner formed by the endwall and the blade suction side surface. These have a small size, therefore they are difficult to visualize experimentally but evidence of their existence can be obtained by visualizing the endwall limiting streamlines, as reviewed by Sieverding [1985]. The present simulation captured the upper wall corner vortex clearly, while the lower corner vortex is squeezed between the suction side and the dominant hub passage vortex, as shown in fig. 6-14 at 0.99 of the axial chord.

The trailing edge vortex near the blade endwall junction is shown in fig. 6-15. The trailing edge vortex arises due to the pressure gradient over the trailing edge. The trailing edge vortex has an opposite direction of rotation to the hub passage vortex. The footprint of most secondary flows can be presented by plotting the limiting streamlines on the endwall as shown in fig. 6-16. This figure shows the development of the saddle point near the leading edge of the rotor blades. The saddle point is formed by the intersection of the separation lines (S_s, S_p) and the streamline to the blade leading edge stagnation point (reattachment line R). This pattern matches schematic by Langston [1977], shown to the right of the CFD predictions. Four distinct regions are generated due to this intersection. The horseshoe vortex pressure

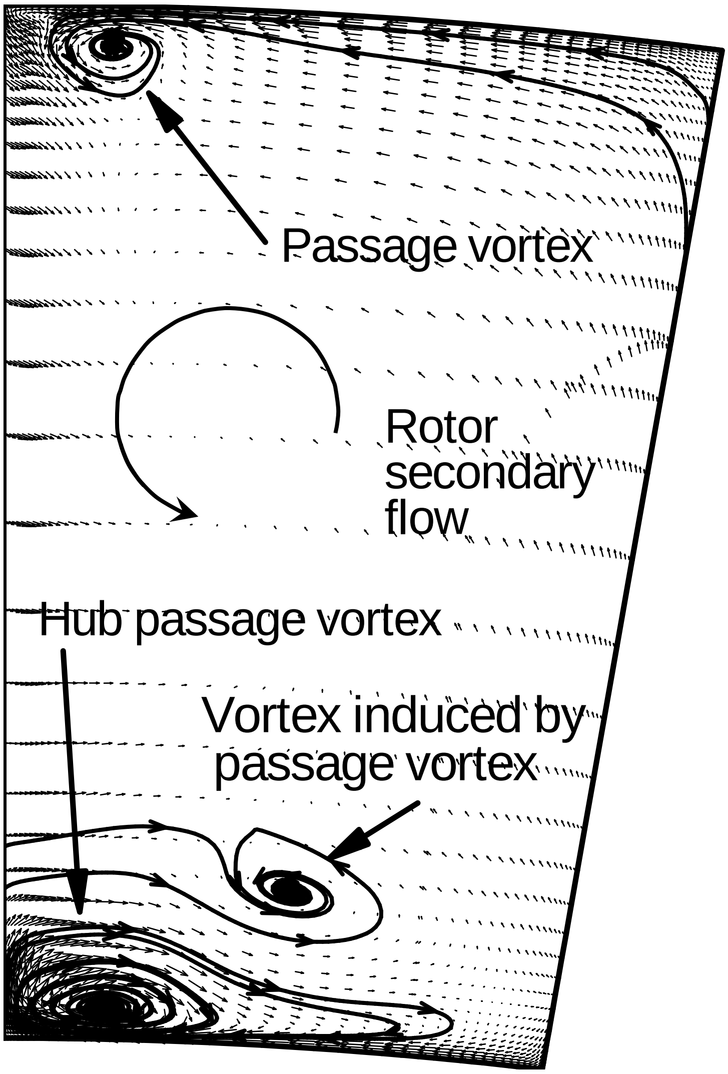

Fig. 6-13 The secondary flows in the plane normal to the axial direction at x/c_{ax}=0.55.

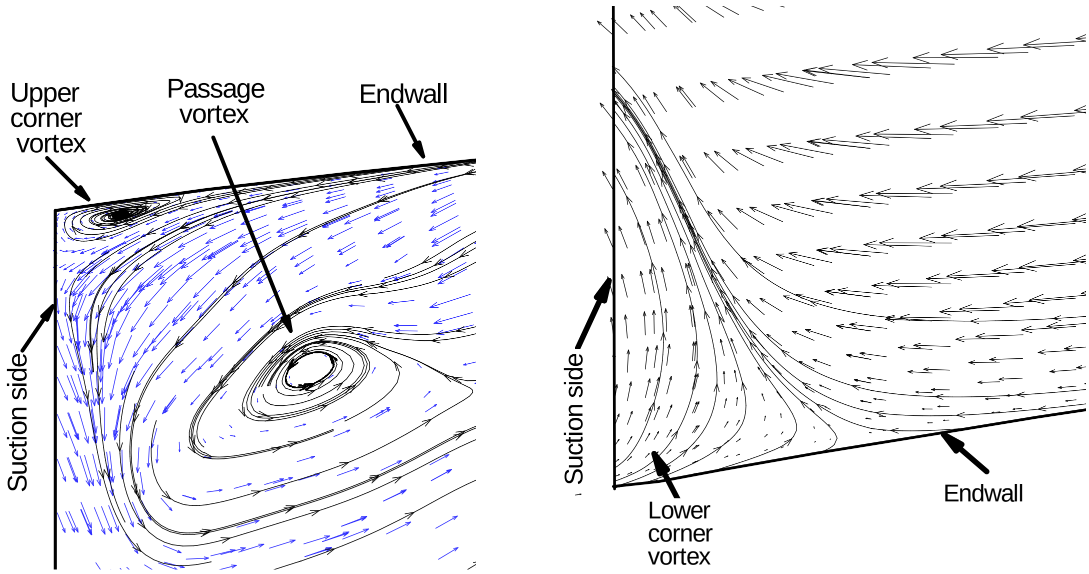

Fig. 6-14 Streamlines showing the corner vortices between the suction side and the endwall at x/c_{ax}=0.99.

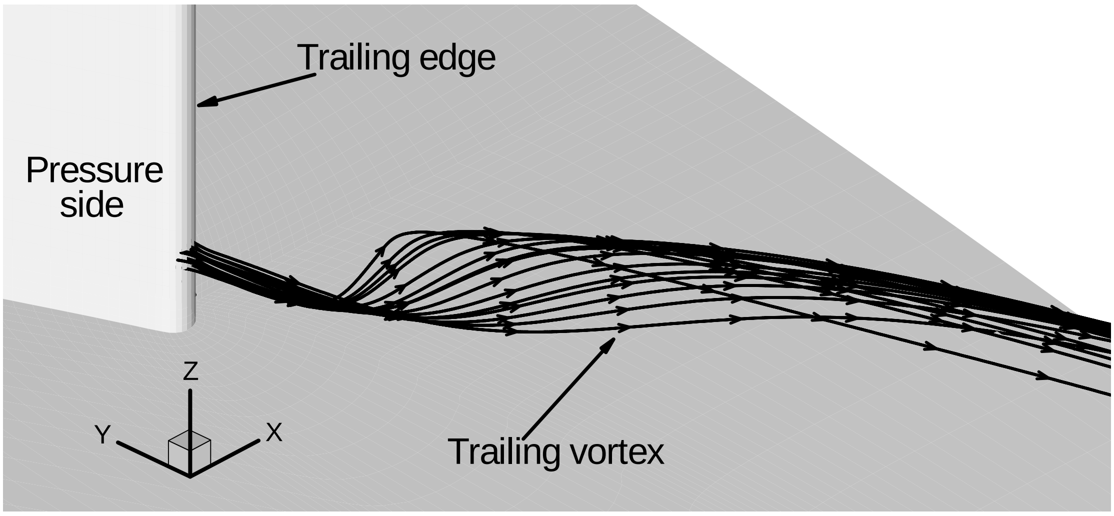

Fig. 6-15 Near-surface streamlines showing the trailing edge vortex.

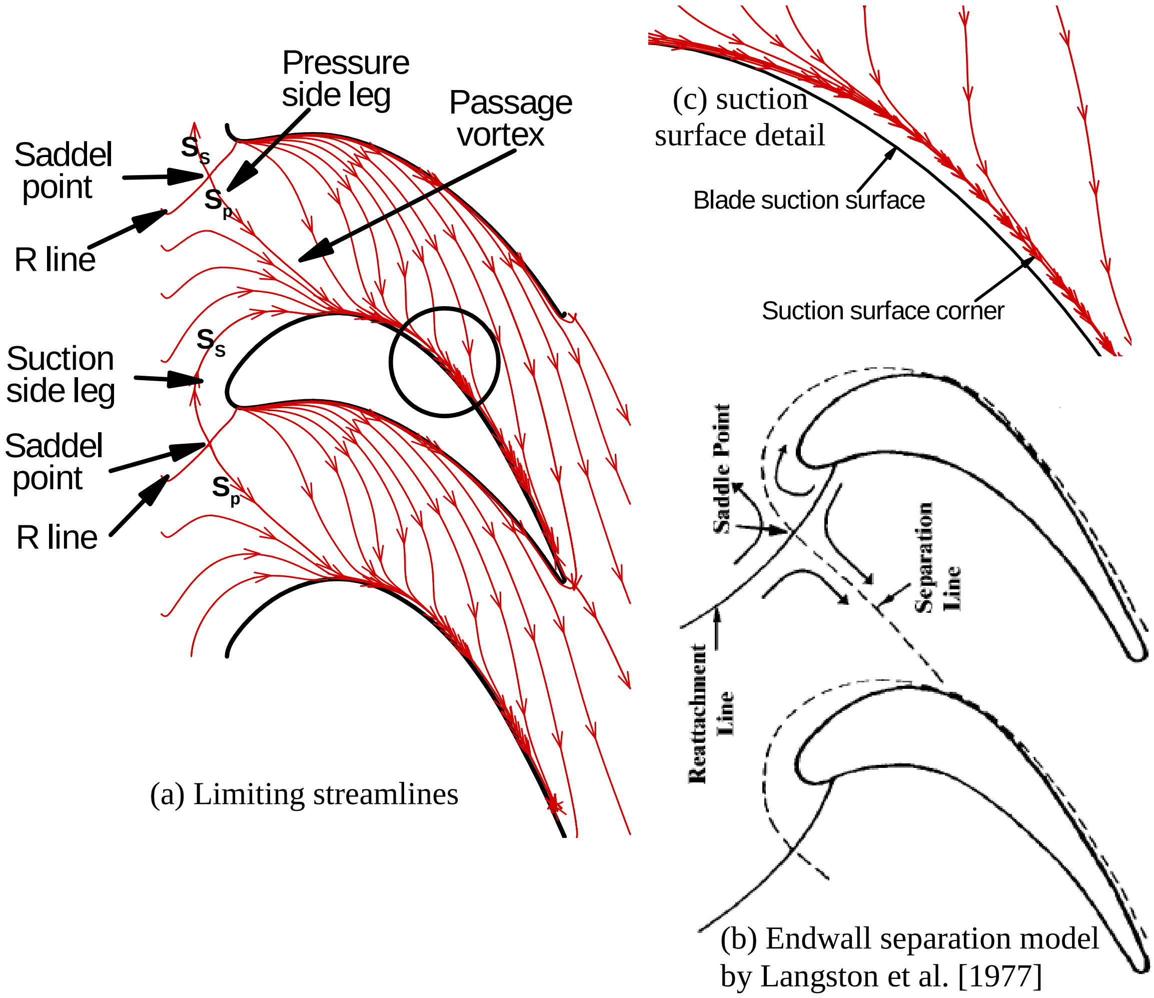

Fig. 6-16 Endwall flow.

and suction legs are started from the saddle point and advance behind the separation lines S_p and S_s respectively. The passage vortex starts behind the leading edge and moves across the passage from the pressure side to the suction side, merging with the pressure leg of the horse shoe vortex. Figure 6-16 shows the detail of the suction surface corner on an enlargement at the top right. The suction surface corner is the corner of the blade suction surface with the endwall. The surface, shown in the detail of fig. 6-16 (c), starts upstream of the lift-off line of the horseshoe vortex, where indicated by a circle in fig. 6-16 (a). This region is mainly occupied by the corner vortex which has an opposite sense of rotation to the passage vortex.

The secondary flows described in this section affect the axial turbine by

- Changing the flow angle, which results in a reduction in the stage work output.
- Introducing a spanwise variation in the incidence angle and increasing the flow nonuniformity, which results in a reduction in work output from subsequent blade rows.
- Generating a considerable amount of loss, which may reach approximately 50% of the total turbine stage loss.
- Increasing the flow tendency to separate, which has a substantial effect on the performance of the turbomachine.
- Affecting the heat transfer and cooling process of the turbomachine.

Due to the adverse effects of the secondary flow, the next section presents predictions of the generation of loss and turbulence in the rotor, which are accompanied by the development of the secondary flow within the rotor passage and downstream of the rotor exit.

6-2.3 The loss generation within and downstream the rotor passage

Entropy can be generated due to heat transfer or due to an irreversible process. Since most turbomachines can be considered mostly adiabatic, then the generation of the entropy is an indicator of irreversible process that causes stage loss. So, the convenient parameter to measure the stage loss is entropy, Denton [1993]. Denton stated that entropy represents the accurate measure for the loss in an unsteady flow. An attractive feature of entropy is that its value is independent of the frame of reference, unlike other parameters such as stagnation pressure, stagnation enthalpy, and kinetic energy. Entropy is a convected quantity and all the entropy generated within the flow field is conservatively convected through the blade passage and passed through the exit boundary of the computational domain. This entropy outflow represents the blade row loss. Entropy is not a measurable quantity but it is evaluated using other measurable quantities, such as pressure and temperature. The entropy increment can be calculated for a perfect gas using Eqn. 3-23 or Eqn. 3-24. The entropy rise through the blade row can be written as, Chaluvadi [2000]

$$\Delta s = R\, ln\left[\frac{p_{0r1}}{p_{or2}}\left(\frac{T_{or2}}{T_{or1}}\right)^{\frac{\gamma}{\gamma-1}}\right] \qquad (6-1)$$

where $p_{or1}, T_{or1}, p_{or2},$ and T_{or2} are the mass averaged relative stagnation pressure and temperature at inlet and exit respectively and R and γ are the specific gas constant and the ratio of the specific heats. Chaluvadi stated that, for an adiabatic turbomachine and assuming there is no change in the radius of rotation between state 1 and 2, Eqn. 6-1 can be simplified as

$$e^{(-\Delta s/R)} = \frac{p_{0r1}}{p_{or2}} \qquad (6-2)$$

The function $e^{(-\Delta s/R)}$ is known as the entropy function. The areas where the entropy function approaches unity are the low loss production regions, while the low entropy function areas represent the regions rich in losses. This function represents a good marker for the flow field for identifying the loss generation. Another good marker for identifying areas of loss generation is the turbulence intensity, which defined as

$$\mathrm{Tu} = \frac{k}{u_{ref}^2} \qquad (6-3)$$

where k is the turbulent kinetic energy and u_{ref} is the velocity at the rotor exit.

Figure 6-17 shows the locations of the quasi-orthogonal planes where the loss generation is monitored along the axial chord. There are six planes at 20, 50, 75, 90, 101, and 120 percent of the axial chord. The planes are numbered from left to right, with a plane name made up of plane, its number, and its location with respect to the axial chord stated between brackets, for instance plane1 (20%).

Figures 6-18 and 6-19 show respectively the development of the secondary flow and the associated entropy generation and turbulence intensity levels at the 6 axial planes of fig. 6-17. The passage vortex formed behind the leading edge due to the effect of the pitchwise pressure gradient on the inlet boundary layer cannot be distinguished from the pressure side leg of the horseshoe vortex, as shown by the entropy function iso-levels on plane 1 (20%). This observation agrees with the experimental work by Harrison [1990]. The stretching core of the vortex near the end-wall may indicate that the pressure side of the horseshoe vortex merges with the passage vortex and becomes part of the passage vortex, as suggested by Langston et al [1977]. Further downstream, the passage vortex is fully developed and washed up toward the suction side. As the passage vortex reaches plane 2 (50%), it has become stronger, as shown in fig. 6-13, and the lower / upper passage vortices roll up / down the low energy fluids onto the suction side. The low energy fluids coming from both passage vortices meet in a thin loss layer on the suction side. The thickness of this layer rapidly increases downstream, as shown in planes 3 (75%) and 4 (90%). At plane 5 (101%), the core loss of the rotor trailing edge wake is captured. Near the rotor exit at plane 6 (120%), a leakage vortex forms near the endwall, due to the injection of the leakage jet into the main passage flow. The loss core of the passage vortex becomes more visible on plane 6 (120%) because it contains not only the inlet boundary layer fluid but also part from the wake fluid. The passage vortex core loss is further enhanced by the leakage jet. The centre of the passage vortex slightly shifts towards the blade mid-span from plane 1 (20%) to plane 4 (90%), while it is considerably increasing downstream of plane 4 (90%). The turbulence intensity shows similar flow structure to the one identified in the entropy function iso-levels, as shown in fig 6-19. Each loss core has a corresponding iso-located high turbulence intensity core which contains the loss-generating turbulence. The entropy function iso-levels at the rotor blade mid-span in blade to blade passage are given in fig. 6-20. they show the two regions of high entropy production. The two regions are the suction surface boundary layer and the blade trailing edge wake mixing with mainstream flow. To summarize the loss generation along the blade axial chord at the mid-span, the mass averaged stagnation pressure loss at the mid-span is given in fig. 6-21. The stagnation pressure loss coefficient is given by

$$Cpt = \frac{p_{ori} - p_{or}}{p_{ori} - p_e} \qquad (6-4)$$

The distribution of the stagnation pressure loss coefficient shows different growth rates from the leading edge to the rotor exit. The loss coefficient grows steadily up to 90% of the axial chord, then it grows rapidly up to the location of the leakage jet injection where it reaches a maximum due to leakage jet mixing with the main passage flow. These two different growth rates have also been observed in experiments by Langston et al. [1977] and Gregory-Smith and Graves [1983] using their rotor cascades where there was no leakage jet. The rapid growth of the loss coefficient from plane 4 (90%) up to upstream the leakage jet injection point is due to the losses generated by the endwall that are swept out by the passage vortex, in addition to the mixing caused by the secondary flows. The physics of the leakage jet and its effects on the performance of the rotor will be further discussed in the later sections.

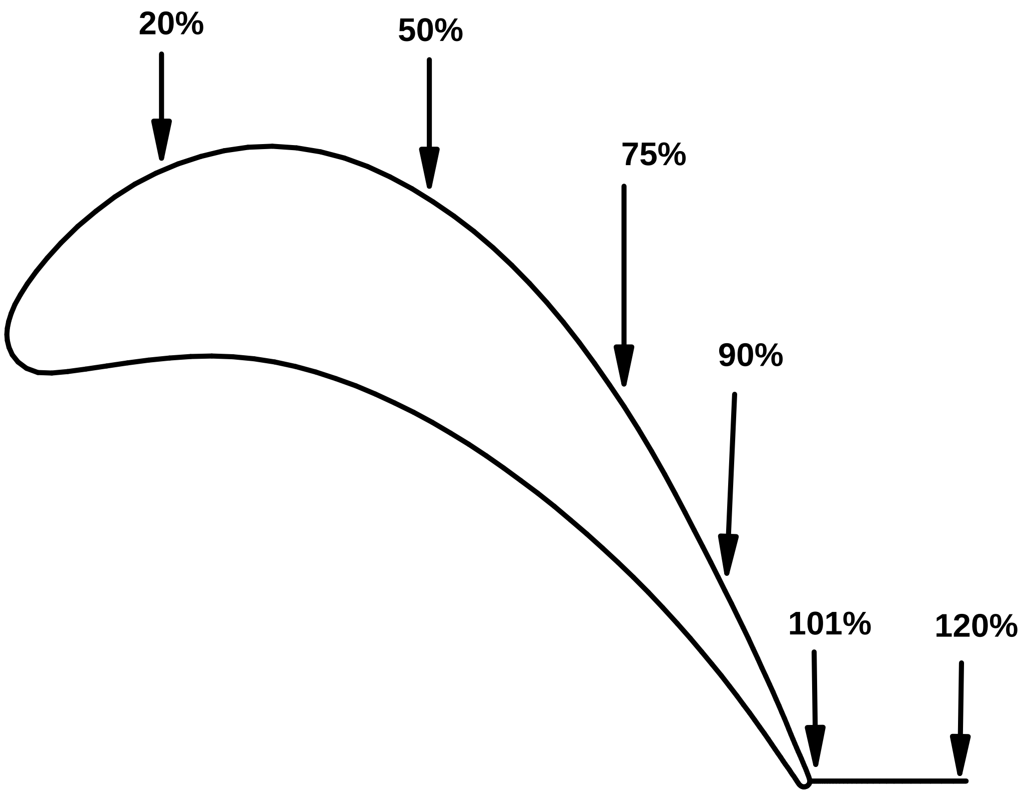

Fig. 6-17 Location of the quasi-orthogonal planes used to plot the flow characteristics.

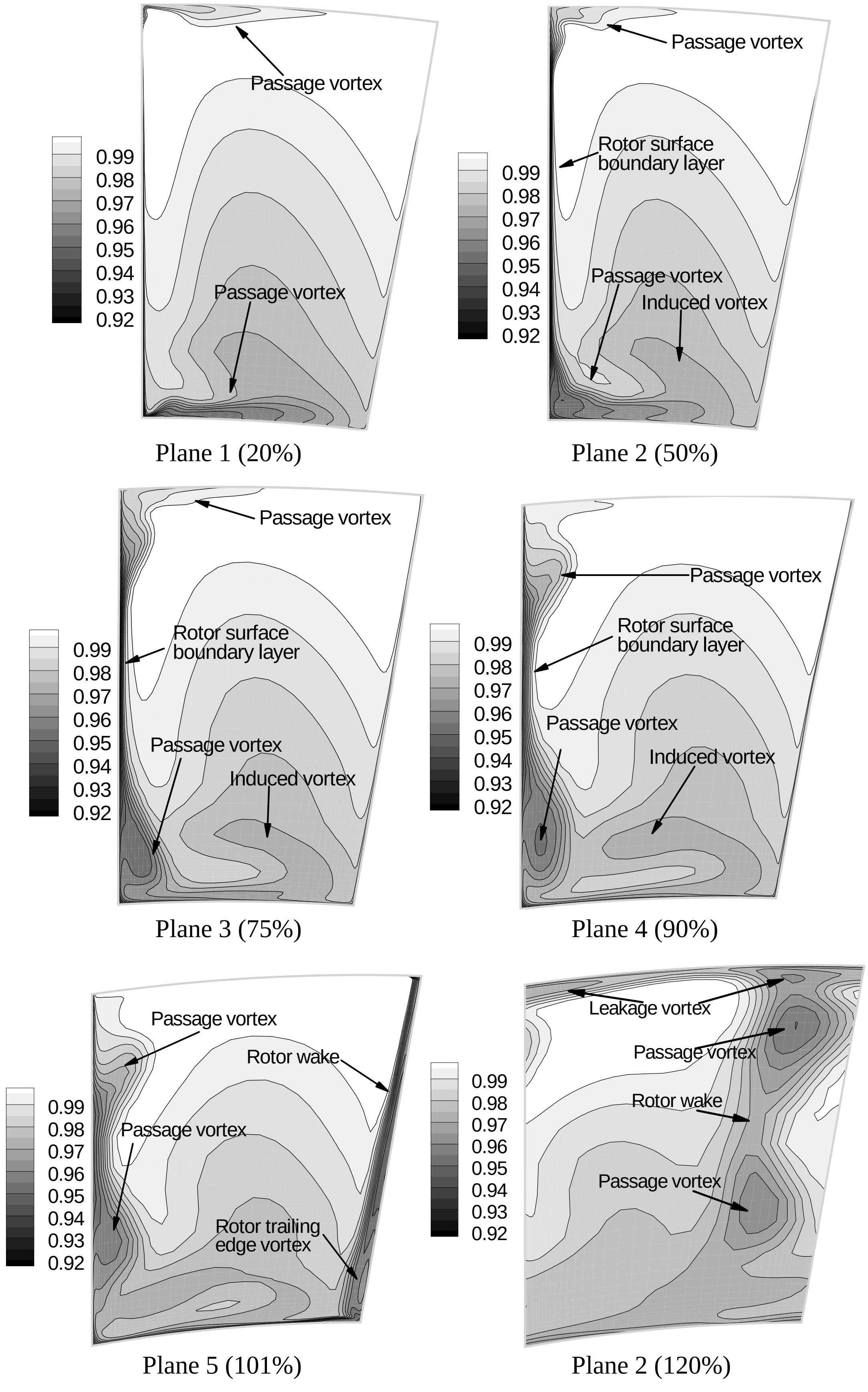

Fig. 6-18 Entropy function iso-levels within and downstream the rotor blade to blade passage.

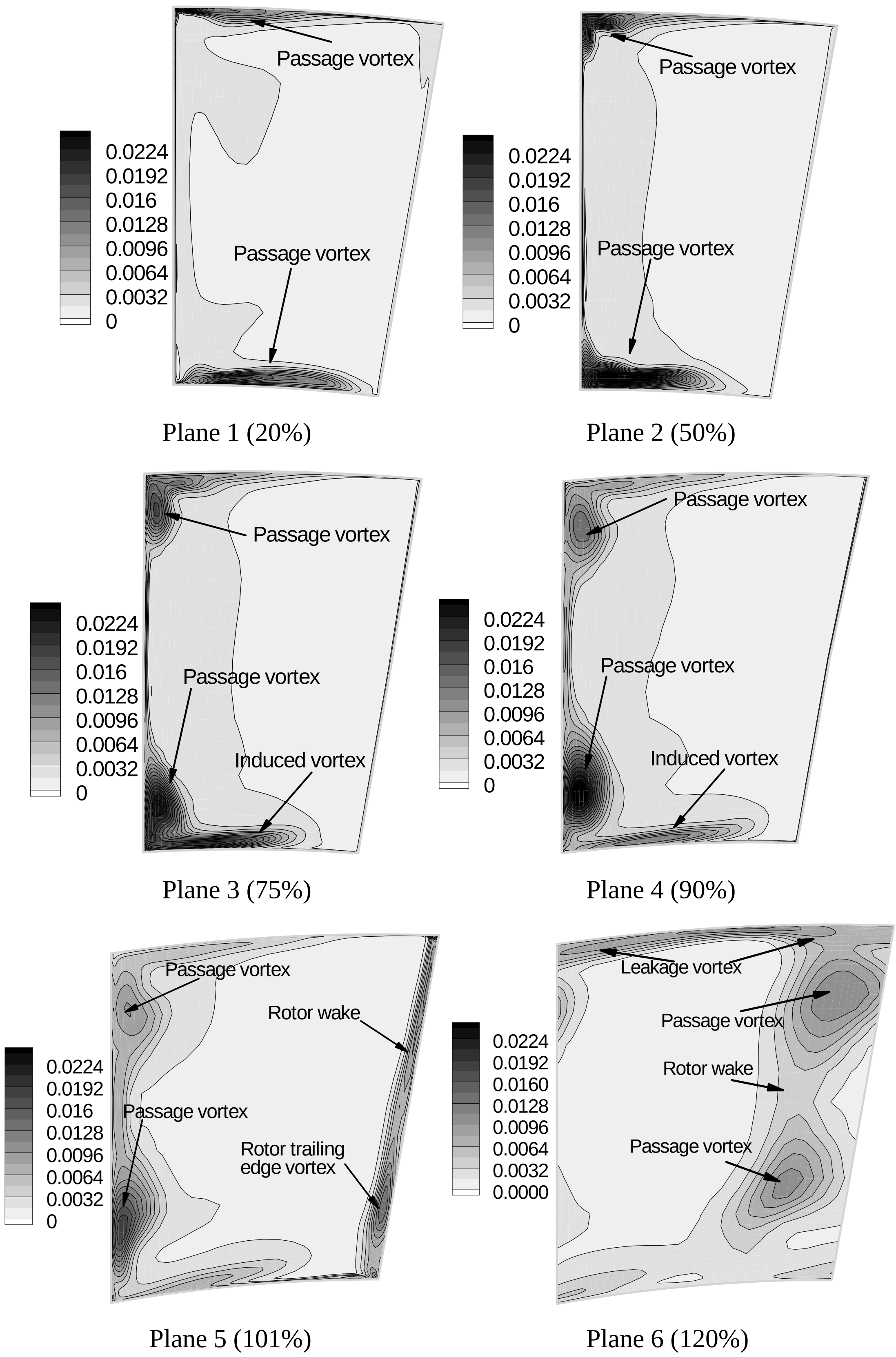

Fig. 6-19 Turbulent intensity iso-levels within and downstream the rotor blade to blade passage.

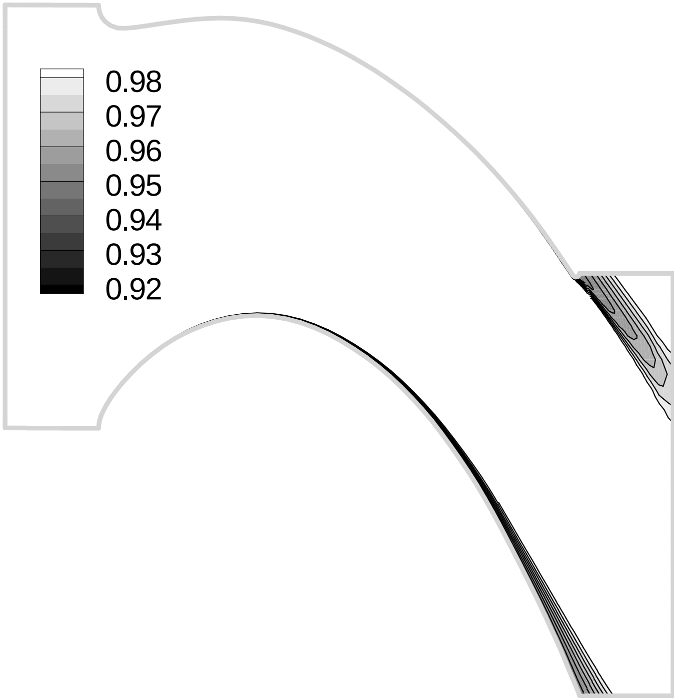

Fig. 6-20 Entropy function contours at the mid span in the rotor blade to blade passage.

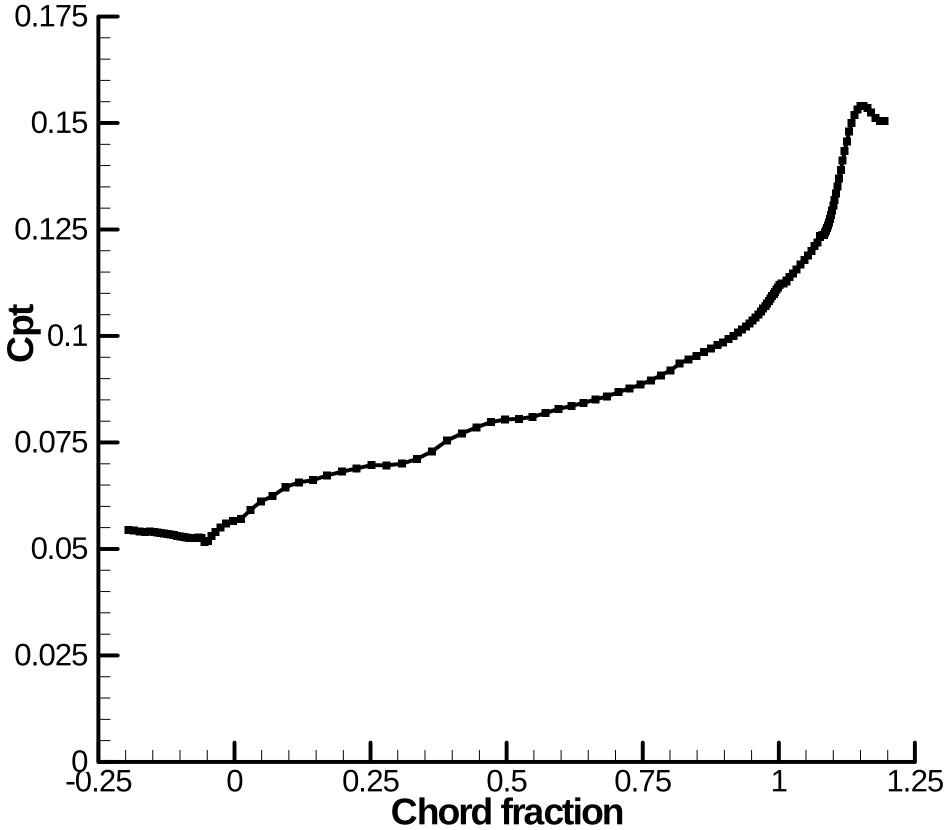

Fig. 6-21 Growth of the mass averaged stagnation pressure loss coefficient through the turbine rotor.

6-3 Labyrinth seal flow structure

6-3.1 Inlet cavity flow

A labyrinth seal is commonly used in the low aspect ratio high pressure turbines to minimize the leakage flow through the unavoidable gap between the rotor shroud and the turbine casing. A labyrinth seal is made up of an inlet cavity, a small number of fins, and an exit cavity. In this section, the inlet cavity flow characteristics are investigated. This study considers specifically the impact of the number of fins, the clearance between the labyrinth fin and the rotor shroud, and the injection angle of the leakage jet at exit from labyrinth seal.

Three test cases having 2 fins, 3 fins, and 4 fins are modelled to study the effect of the number of fins on the inlet cavity flow. The fins are evenly distributed along the rotor shroud. A two-dimensional schematic of the inlet cavity geometry is given in fig. 6-22. This sketch shows the interface plane between the inlet cavity and the main flow passage, plane (A) in fig. 6-22, in addition to the radial plane at the cavity middle, plane (B) in fig. 6-22. Figure 6-23 shows the mean velocity vector field through the labyrinth inlet cavity, the iso-levels of the radial velocity component, and selected streamlines. At the entry of the cavity, part of the casing boundary layer is sucked into the cavity inlet through plane (A), due to the pressure gradient across the seal. The amount of the leakage flow passing through the labyrinth seal depends on the flow resistance of the labyrinth seal for a given pressure drop across the rotor blade row. Therefore, as the number of fins increases, the flow resistance increases and consequently the leakage flow decreases. The iso-levels of the radial velocity component at the cavity inlet plane (A) are given in fig. 6-24 (a) while fig. 6-24(b) shows the distribution of the pitchwise averaged radial velocity component along the mid radial plane (B) at the cavity inlet. In figure 6-24, 1.0 span corresponds to the shroud inner surface, while 1.27 span corresponds to the casing inner surface. The dashed contour lines represent the negative radial velocity i.e. the reverse flow. The pitchwise averaged radial velocity shows higher positive value of radial velocity in the region at the cavity inlet (1.0 span fraction) for the 2 fins case than 3 fins and 4 fins cases, for instance the $\boldsymbol{u_r = 0}$ contour with two fins stretches towards the inlet cavity leading edge than with the 3fins. This means that more leakage flow gets into the cavity as the number of fins decreases. The radial velocity profile inside the cavity indicates a maximum positive value at 1.23 span and maximum negative value at 1.06 span. The results indicate that the bulk of the cavity inflow clusters alongside the rotor shroud, at an axial location in front of the blade leading edge junction near the blade pressure side and decays towards the blade suction side, where there is a strong reverse flow. This distribution of positive contours of the radial velocity component shows the pumping effect of the adverse pressure gradient of the rotor leading edge, while reverse flow occurs at the centre of the rotor passage. A large portion of the leakage fluid flow sucked trough the labyrinth seal transports a positive axial momentum, causing flow separation at the shroud leading edge. The size of the flow separation vortex increases as the distance between the shroud leading edge and the first fin increases, increasing the cavity inflow radial velocity. This distance is specified according to the rotor shroud axial length and the distribution of the labyrinth seal fins along it.

Another part of the leakage flow is redirected upstream, forming a counter clockwise recirculation, as shown in fig. 6-23 (a-d). The vortex axis is in the direction of the blade pitch. This counter clockwise vortex induces a negative radial velocity peak followed by a positive radial velocity peak observed in fig. 6-24 (b). Specifically, the vortex convects the high radial momentum flow flowing alongside the shroud at x=1.0 in the x=0.5 plane at 1.23 span generating the radial velocity maximum in fig. 6-24 (b). The vortex then convects low radial momentum flow from alongside the casing at x=0.0 in the x=0.5 plane at 1.06 span, generating the radial velocity minimum in fig. 6-24 (b). The intensity of the counter clockwise vortex increases slightly as the number of fins increases and the vortex centre displaces radially outwards towards the casing, as indicated by the negative peaks of the radial velocity component shown in fig. 6-24 (b). Figures 6-23 (a-c) show that the inflow from the main passage to the labyrinth seal leading edge cavity produces two large flow recirculations. The first is the upstream flow recirculation at the inlet cavity, as indicted by the arrow in figs. 6-23 (a-c), and the second is due to the flow separation at the shroud edge. This pattern agrees with the flow schematic by pfau [2003], based on extensive experimental work.

Figure 6.25 (a) shows the iso-levels of the absolute tangential velocity component at plane (A), fig. 6-22. Figure 6.25 (b) shows the profile of the mass-averaged absolute tangential velocity component at plane (B), fig. 6-22. The profile data is continuous across the interface plane (A) between the main passage and the cavity. In fig. 6-25 (b) a discontinuity is shown in the profile that is spurious. This is due to a limitation of the graphics package that resamples from cell centred to vertex centred coordinates. Both figures show that the number of fins has not any major impact on the tangential velocity of the inlet cavity flow. Figure 6.25 (a) shows that the reverse flow through plane (A) has a low tangential velocity, as it would be expected, given that this reverse flow flows adjacent to the non-rotating casing wall. The viscous dissipation in the boundary layer on the stationary wall reduces the tangential velocity of the grazing flow. The iso-levels of the stagnation pressure loss coefficient at the plane (A) and the distribution of the pitchwise averaged stagnation pressure loss at plane (B) are given in figures 6.26 (a) and (b) respectively. The stagnation pressure loss coefficient contours are slightly affected by the number of fins. They show a higher loss for the case of low number of fins in the reverse fluid flow area. The pitchwise averaged results indicate a higher stagnation pressure loss inside the cavity than at the cavity inlet plane (A). A strong radial increase in the stagnation pressure loss coefficient starts from 0.92 span towards the blade tip and continues inside the cavity until the core of the recirculating flow at 1.07 span approximately. This steep positive gradient indicates the amount of loss introduced due to the interaction of the reverse leakage flow with the main passage flow. This reverse flow not only increases the loss near the rotor tip but also introduces a negative incidence angle due to its low tangential velocity shown in fig. 6-25 (a). This negative incidence angle reduces the work generated by the flow near the rotor tip. The iso-levels of the axial velocity on plane (A) and the pitchwise averaged axial velocity on plane (B) are given in fig 6-27 (a) and (b) respectively. Figure 6-27 (a) shows a stagnation line at the shroud leading edge and an essentially zero axial velocity line at the casing. Above plane (A), as the number of fins increases the axial velocity through the labyrinth seal leading edge cavity decreases, as shown in fig. 6-27 (b). Figures 6-27 (a) and (b) also show that the variation of the number of fins has very little or no effect on the distribution of the axial flow through the labyrinth seal leading edge cavity.

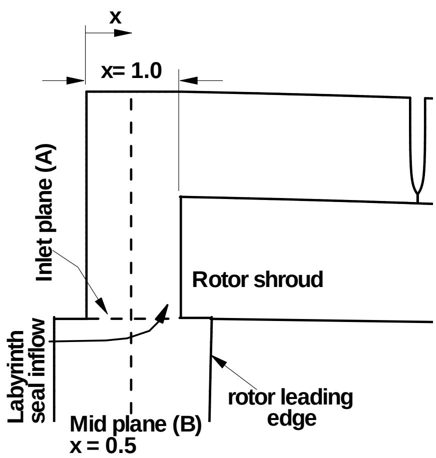

Fig. 6-22 Schematic of the labyrinth seal inlet cavity, x=1.0 is the normalized axial clearance of the rotor shroud.

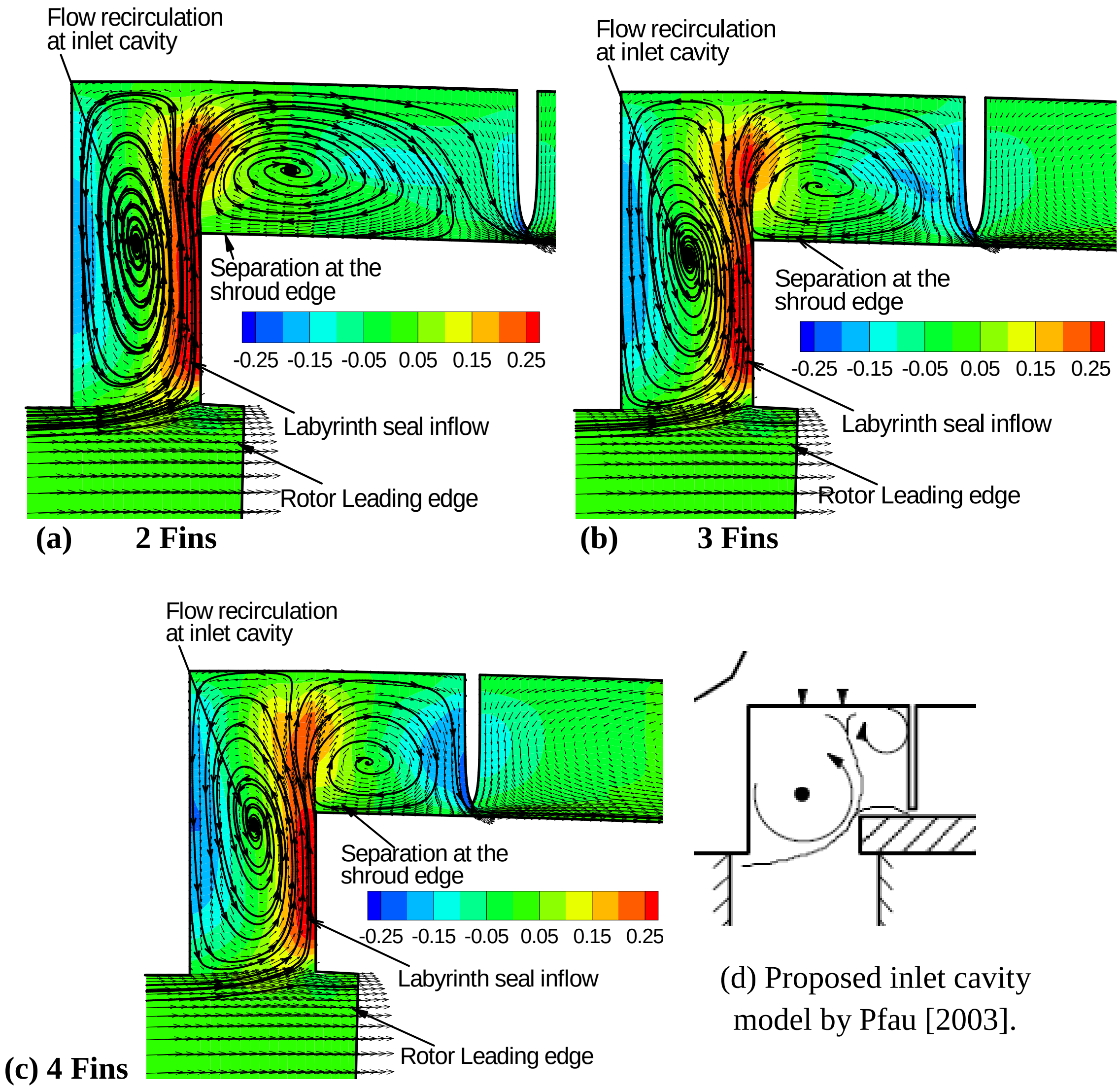

Fig. 6-23 Labyrinth seal inlet cavity pitchwise averaged velocity vectors at varying number of fins.

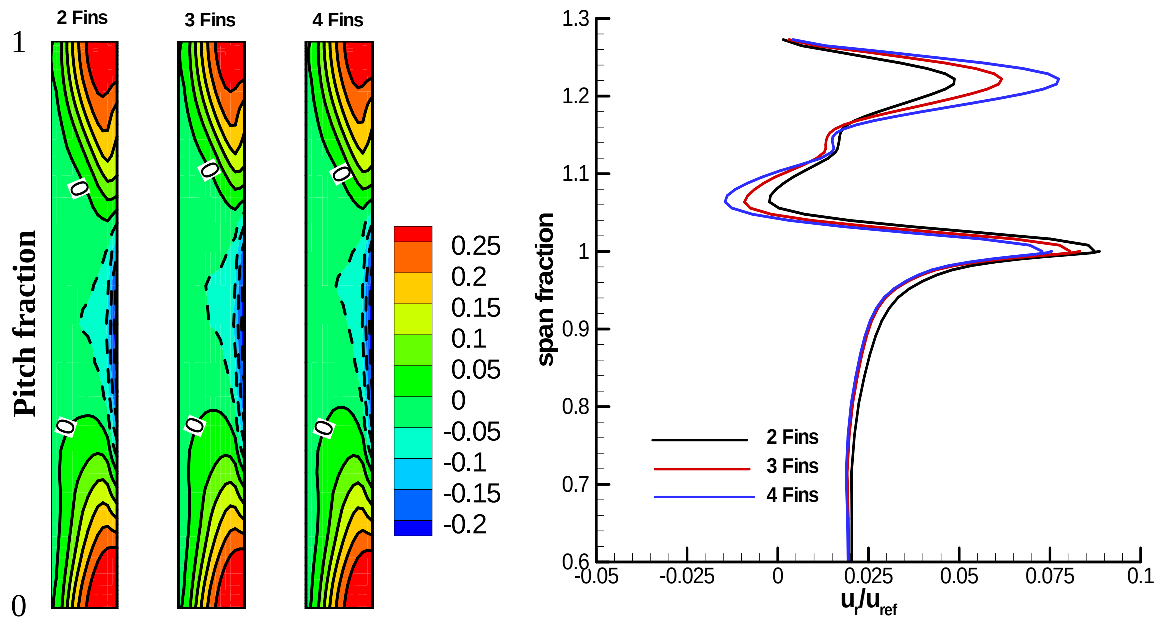

Fig. 6-24 (a) Radial velocity iso-levels at plane (A)

(b) The pitchwise averaged radial velocity profile at plane (B).

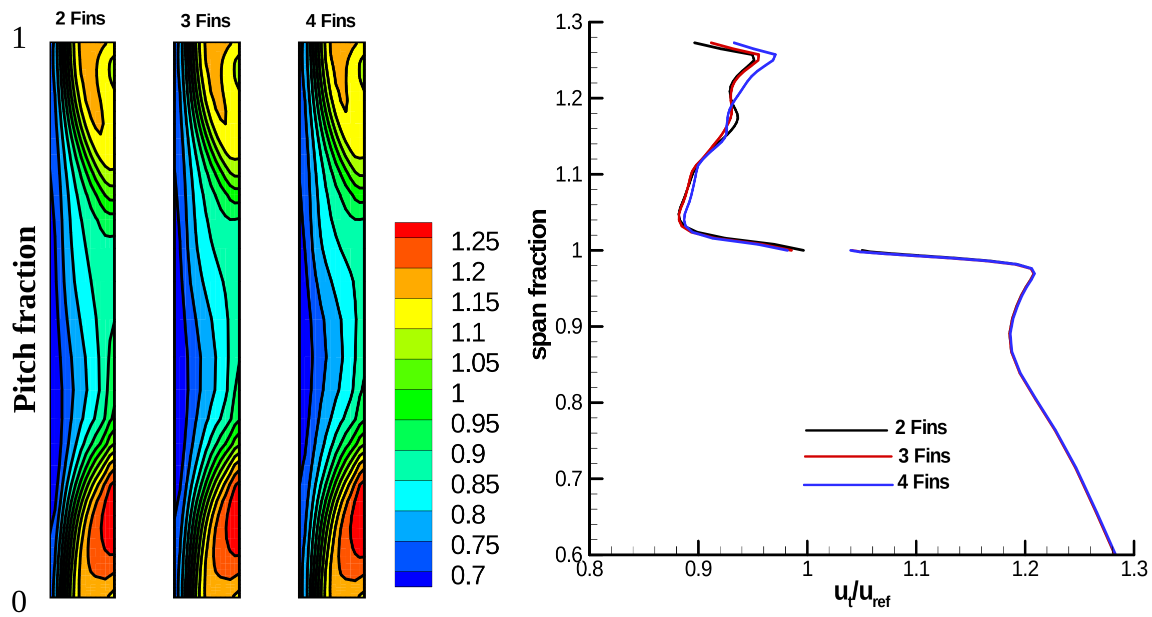

Fig. 6-25 (a) Tangential velocity iso-levels at plane (A)

(b) The pitchwise averaged tangential velocity profile at plane (B).

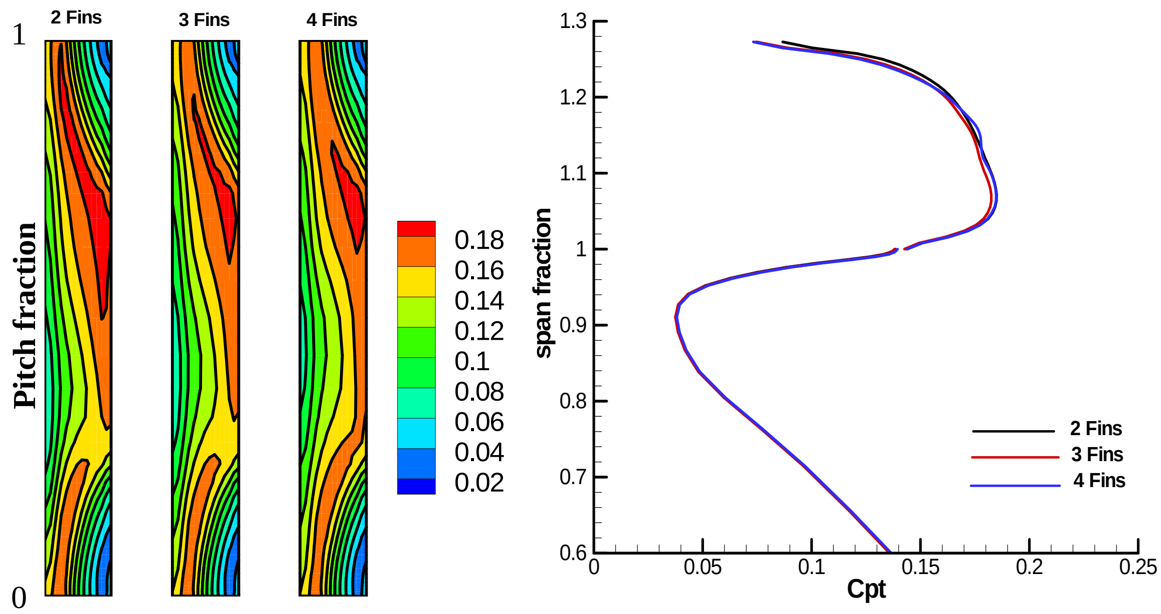

Fig. 6-26 (a) Stagnation pressure loss coefficient iso-levels at plane (A).
(b) The pitchwise averaged stagnation pressure loss coefficient profile at plane (B).

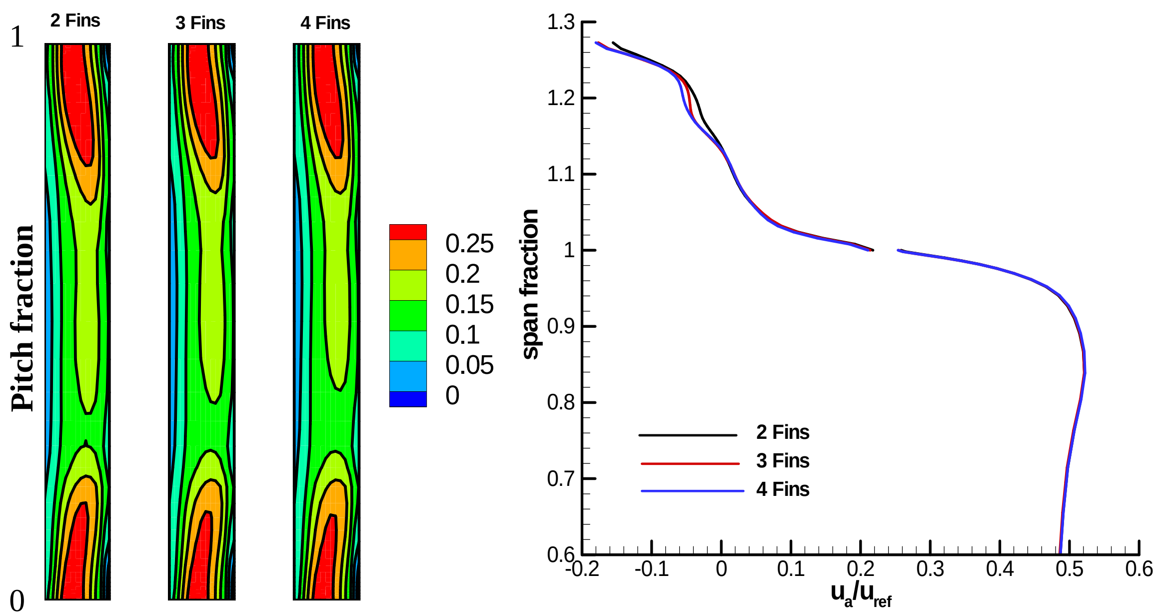

Fig. 6-27 (a) Axial velocity iso-levels at plane (A)
(b) The pitchwise averaged axial velocity profile at plane (B).

The second parameter that is investigated by CFD modelling is the gap clearance ratio. Three cases are modelled, with variable gap clearance ratio of 0.5%, 1.0%, and 1.5% respectively. The labyrinth seal of the three cases has 2 fins with a 90^{o} exit cavity. Figures 6-28 (a), (b), and (c) show the same overall vortical flow structure as in fig. 6-23. The colour iso-maps of the relative helicity $\boldsymbol{H_r}$ appears in the background of fig. 6-28, where $\boldsymbol{H_r}$ is defined as

$$\boldsymbol{H_r} = \frac{\boldsymbol{H}}{\|\boldsymbol{u_r}\|\|\boldsymbol{\omega}\|} \qquad (\mathbf{6-5})$$

where $\boldsymbol{H} = \boldsymbol{u_r} \cdot \boldsymbol{\omega}$ is the helicity, $\boldsymbol{u_r}$ is the relative velocity vector and $\boldsymbol{\omega} = \boldsymbol{\nabla} \times \boldsymbol{u_r}$ is the relative vorticity vector. The helicity represents the rate of transport of the secondary flow, Anker et al. [2005]. The helicity and relative helicity are chosen as vortical flow structure markers. The helicity has the advantage over the vorticity of identifying the concentrated vortices and their separation and reattachment locations more clearly, as its value vanishes near the no-slip walls because the velocity vector and the vorticity vector are orthogonal in the sheared layers, as stated by Anker et al. [2005]. A positive relative helicity region marks the upstream counter-clockwise vortex while a negative relative helicity region marks the clockwise vortex from the flow separation at the shroud leading edge. The centre of the downstream vortex lifts up as the gap clearance increases, due to the increase of the radial momentum of the leakage jet at inlet. The intensity of the flow separation decreases as the gap clearance increases, as indicated by the reduction in the relative helicity levels in fig. 6-28 (b) and (c). The convected secondary flow downstream of the inlet cavity, which is shown by the circled area in fig. 6-28 (a) to (c), decreases as the clearance gap increases. This effect will be discussed later, when addressing the interaction of the leakage flow with the main passage flow. Figures 6-29 (a) and (b) show respectively the iso-levels of the normalized radial velocity at the cavity inlet plane (A) and the pitchwise averaged normalized radial velocity at plane (B). The effect of the gap clearance on the leakage mass flow rate can be observed through the iso-levels of the radial velocity at plane (A). Negative radial velocity contours are represented by dashed lines in fig. 6-29 (a) to mark the reverse flow area. The contours show that, as the clearance gap increases the reverse leakage flow towards the main passage decreases, decreasing the secondary flow convected towards the rotor inlet passage. The pitchwise averaged radial velocity distribution shows a higher radial velocity at 1.0 span as the gap clearance increases, therefore more leakage flow rate passes into the labyrinth inlet cavity with a larger gap clearance. The pitchwise averaged radial velocity distribution inside the cavity confirms the presence of the recirculating flow by a minimum radial velocity value at 1.08 span followed by a maximum at 1.22 span. The iso-levels of the normalized tangential velocity at plane (A) are given in fig. 6-30 (a). The pitchwise averaged normalized tangential velocity profile at plane (B) is given in fig. 6-30 (b). Once again, contour lines in fig. 6-30 (a) indicate that the reverse leakage flow has a low tangential velocity which causes underturning of the flow close to the shroud tip, which in turn reduces the generated specific work at this radial location. The profile of the pitchwise averaged tangential velocity at plane (B) shows an underturning followed by an overturning at radial positions 0.87 and 0.97 respectively, due to the stator radial flow characteristics that are preserved and convected through the radial distribution of the inlet boundary condition. Specifically, the stator radial flow has a dip in the tangential velocity profile due to the mixed-out stator tip passage vortices. Inside the cavity, the bigger clearance gap case, $\boldsymbol{\tau = 1.5}\%$ span, has the smallest tangential velocity. The iso-levels of the normalized axial velocity component at the cavity inlet plane (A) and the profile of the pitchwise averaged axial velocity along the radial plane (B) are given in fig. 6-31 (a) and (b) respectively. The pitchwise averaged axial velocity distribution of fig 6-31 (b) shows an increase in the axial velocity near the shroud tip (1.0 span) as the clearance gap increases. The iso-levels at plane (A) of fig. 6-31 (b) confirm this increase in axial velocity as the clearance gap increases. This increase in axial velocity indicates a reduction in the boundary layer thickness at the blade tip. This reduction of the boundary layer thickness due to the removal of the slowly moving layer through the labyrinth seal has an appreciable effect on enhancing the secondary flow development within the rotor passage, as will be seen later. Due to the larger net leakage flow rate at larger gap clearance ratios, the positive axial velocity inside the inlet cavity increases as the gap clearance ratio increases between 1.0 span up to 1.18 span as shown in fig. 6-31 (b). The effect of the gap clearance ratio on the stagnation pressure loss coefficient is shown in figs. 6-32 (a) and (b). Figure 6-32 (b) shows that the stagnation pressure loss inside the cavity increases as the gap clearance increases at all radial locations in plane (B). An increment in the stagnation pressure loss coefficient can be seen between 0.92 span and 1.0 of span, due to the interaction between the cavity flow and the main passage flow. The reverse leakage flow area shown by the dashed contour lines in fig. 6-29 (a) has a high stagnation pressure loss, as shown in fig. 6-32 (a) which increases as the gap clearance ratio increases.

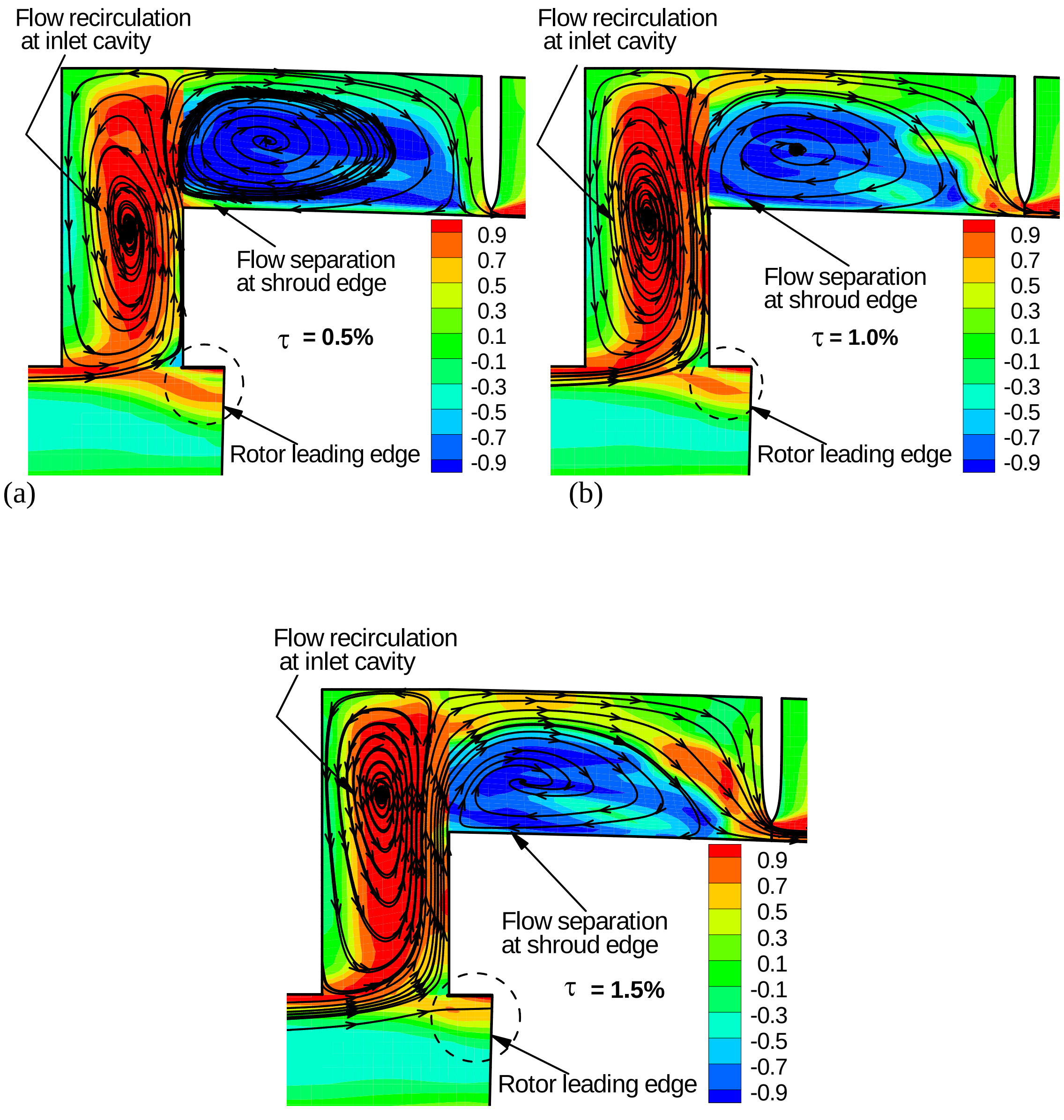

(c)

Fig. 6-28 Selected streamlines through the labyrinth seal inlet cavity and relative helicity iso-levels in the background, at varying gap clearance ratios.

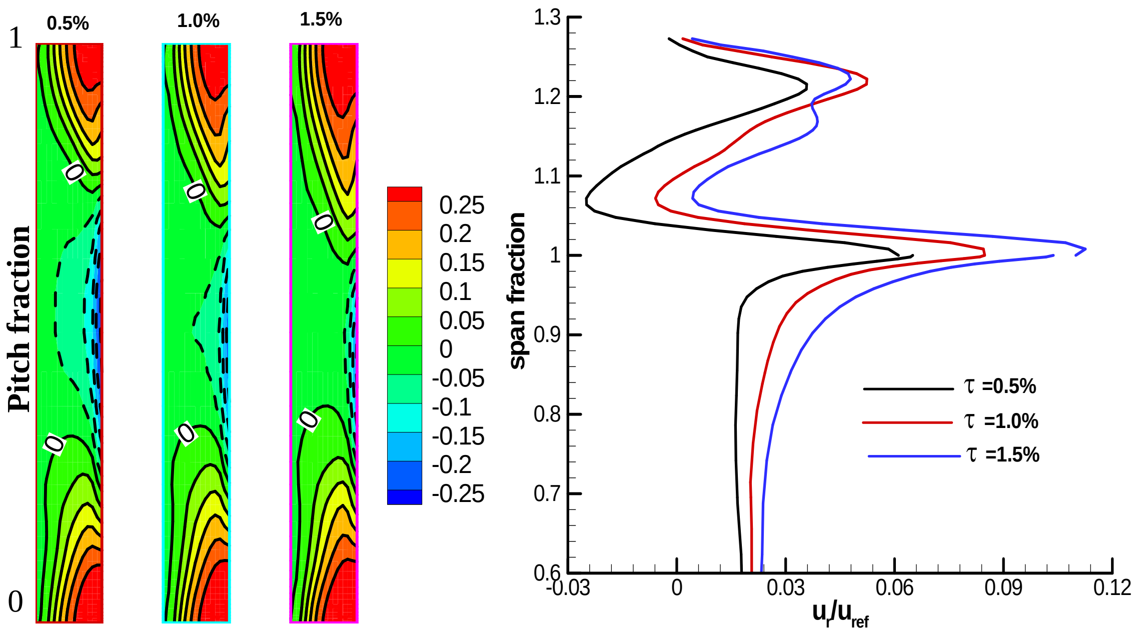

Fig. 6-29 (a) Radial velocity iso-levels at plane (A)

(b) Pitchwise averaged radial velocity profile at plane (B).

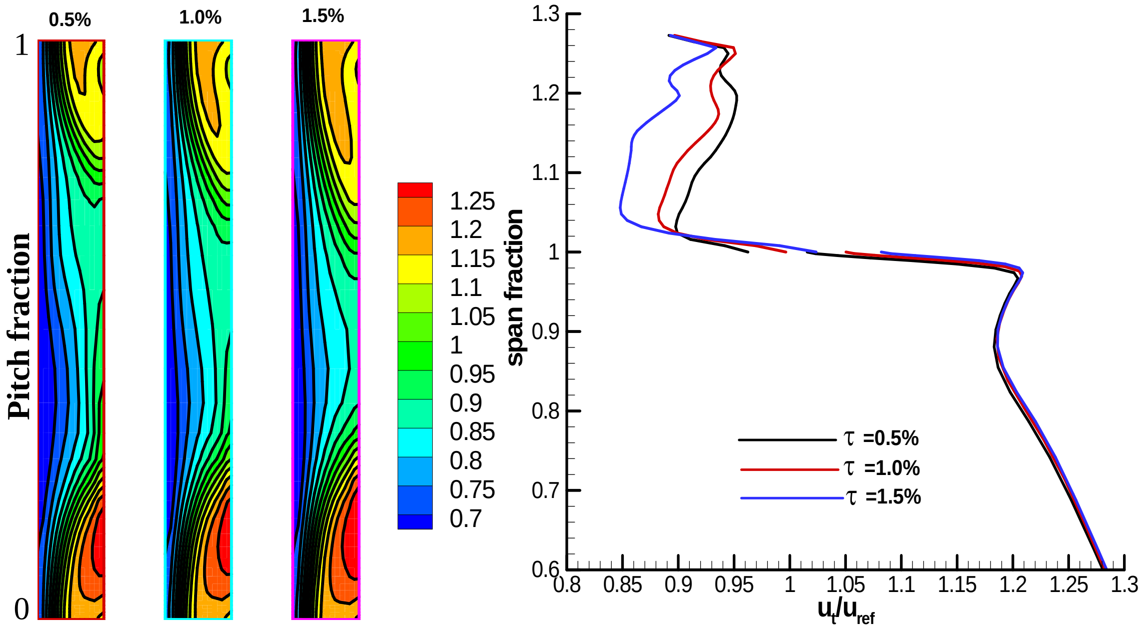

Fig. 6-30 (a) Tangential velocity iso-levels at plane (A)

(b) Pitchwise averaged tangential velocity profile at plane (B).

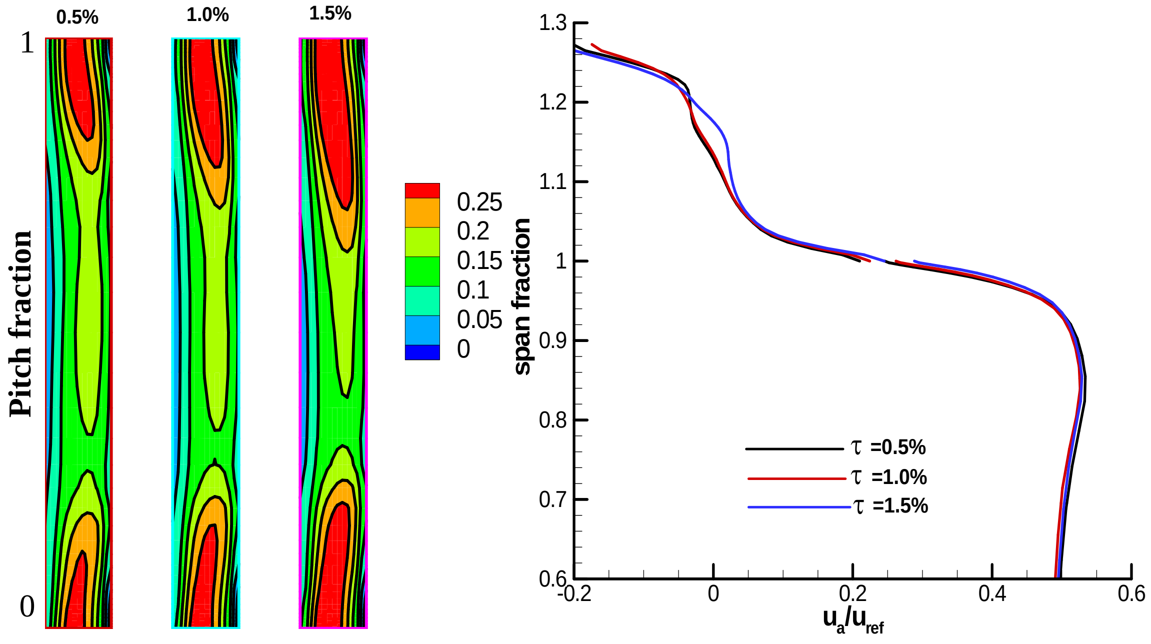

Fig. 6-31 (a) Axial velocity contours at plane (A)

(b) Pitchwise averaged axial velocity profile at plane (B).

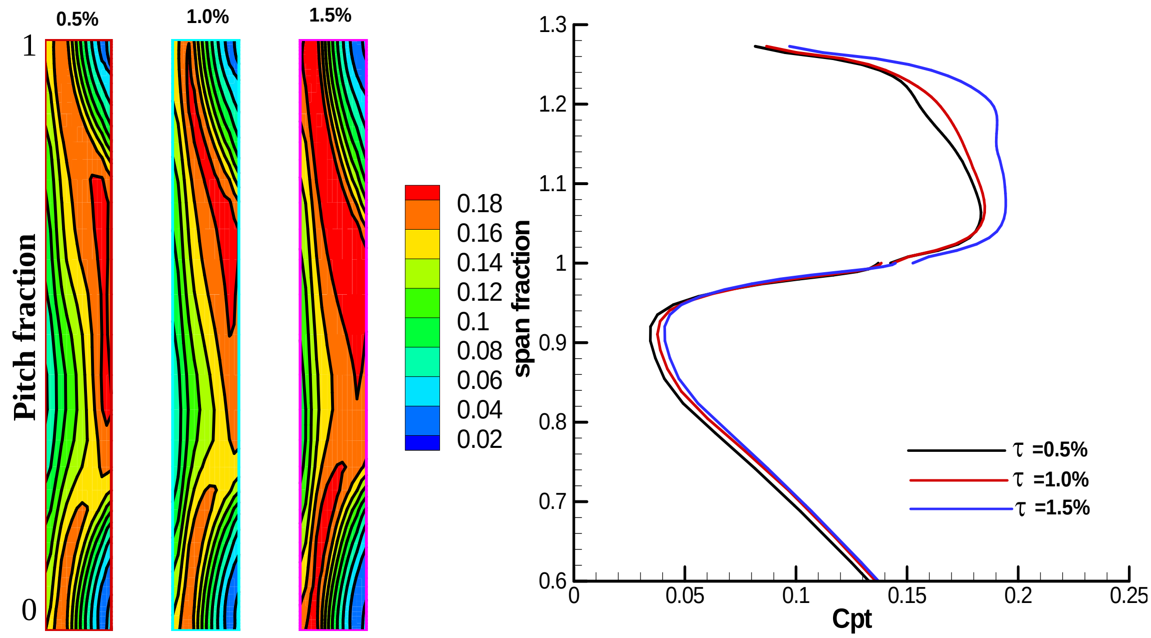

Fig. 6-32 (a) Stagnation pressure loss coefficient at plane (A)

(b) Pitchwise averaged stagnation pressure loss coefficient profile at plane (B).

The impact of using 30°, 60°, and 90° injection angles at the exit of the labyrinth seal on the upstream inlet cavity flow is investigated. Figures 6-33 (a), (b), (c), and (d) respectively show the normalized pitchwise averaged radial, axial, and tangential velocity distributions and the stagnation pressure loss coefficient profile at the radial plane (B). These profiles show that using different exit angles has no significant impact on the pitchwise averaged flow parameters at the labyrinth seal cavity inlet. The flow features and the vortical structures are the same as the 90° injection angle of fig. 6-28 (b).

It is concluded that the gap clearance ratio has the major impact on the labyrinth seal inlet cavity flow. The second parameter affecting the inlet cavity flow is the number of fins. Finally, the exit flow angle at the labyrinth exit cavity has no significant effect on the inlet cavity flow.

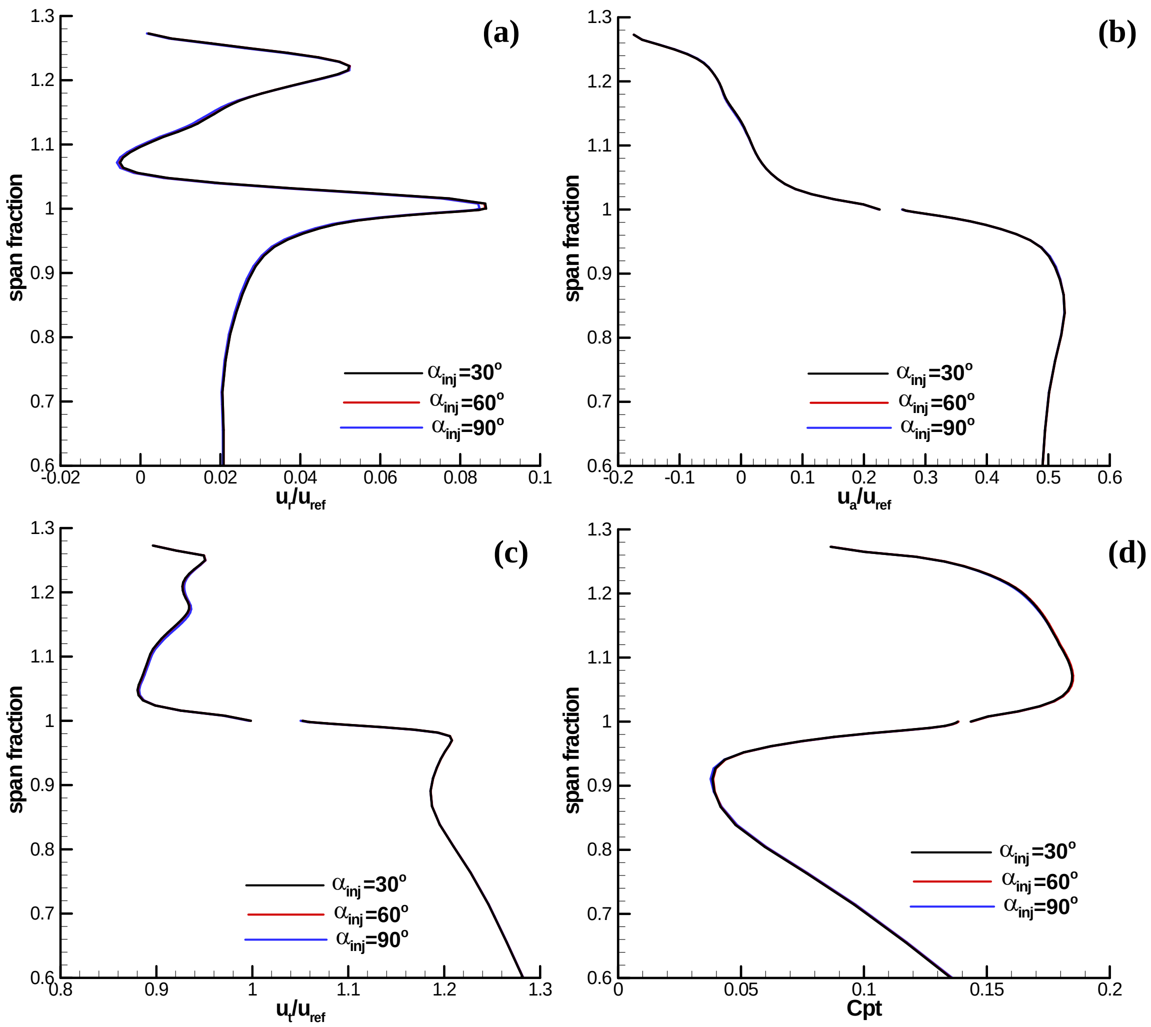

Fig. 6-32 Averaged flow states at plane (B) (a) the radial velocity (b) the axial velocity (c) the tangential velocity (d) the stagnation pressure loss coefficient

6-3.2 Exit cavity flow

The leakage jet leaving the labyrinth exit cavity and entering the main flow passage causes many sources of loss such as the irreversible mixing with the main flow, amplification of the secondary losses, flow separation on the endwall casing, and variation of the outflow incidence angle that affects the downstream blade row. The exit cavity losses are not constant and vary with the labyrinth seal geometry and the exit cavity design, as stated by Rosic et al. [2007b]. This makes the understanding of the exit cavity flow important to control these types of loss. In this part of the present study, the effect of the number of fins, the gap clearance, and the exit leakage jet angle on the exit flow structure are studied. The fins are evenly distributed along the rotor shroud. Therefore, the number of fins affects the strength of the leakage jet and the position of the last fin affects the leakage jet pressure recovery before it mixes with the cavity flow. The pressure distribution along the labyrinth seal will be addressed in the following subsection.

Figure 6-33 shows selected streamlines and the iso-levels of radial velocity at the rear of the labyrinth seal. The streamlines show the vortical flow structure downstream of the last fin and at the cavity exit near the pressure side. The main passage flow has a higher pressure near the blade pressure side trailing edge that forces it to enter the exit cavity of the labyrinth seal. Part of this inflow generates an entrance vortex at the lower shroud trailing edge, due to the change in its direction. The reminder mixes with the leakage jet and reinforces the shroud trailing edge vortex. The leakage jet leaves the exit cavity with a high radial velocity that generates a separation vortex at the intersection downstream between the casing endwall and the exit cavity. This vortical flow structure at the cavity exit is in agreement with the CFD results by Rosic et al. [2007b], as shown in fig. 6-33. The size of the vortices in the current predictions is different since different blade passage and labyrinth geometries are used. The trailing edge inflow that feeds the cavity vortex decreases and finally vanishes as the cavity vortex progresses towards the suction side. At this point, the entrained flow re-enters the main passage with the leakage jet, as shown in fig. 6-34. Figure 6-34 shows the development of the vortical structure near the suction side for 2 fins simulation only since this flow pattern is repeated in all test cases.

The radial velocity iso-levels and the velocity vector map at the labyrinth seal exit cavity are presented in fig. 6-34. Selected stream lines show the evolution of the vortical structures in fig. 6-34. This evolution shows a good agreement with the CFD results by Rosic et al. [2007b]. Further details of the rear cavity flow are shown on the interface plane (A) at the cavity exit and on the radial plane (B) at the middle of the exit cavity, sketched in fig. 6-35. The iso-levels of the normalized radial velocity at plane (A) and the pitchwise averaged normalized radial velocity distribution along plane (B) are presented in fig. 6-36 for different numbers of fins. The solid line contours in fig. 6-36 (a) represent the positive radial velocity i.e. the inflow from the main passage into the exit cavity, while the dashed line contours represent the leakage jet leaving the exit cavity. The results indicate that the leakage jet stick to the casing wall with a high radial velocity except near the suction region where the size of the cavity vortex blocks and redirects the leakage jet to enter the main passage near the shroud endwall, as shown in fig. 6-34. The reverse flow (positive radial velocity) in fig. 6-36 (a) occurs near the blade pressure side. It starts strongly and then decays towards the suction side, re-entering the main passage. The iso-levels of fig. 6-36 (a) show that the reverse flow increases as the number of fins increase making the leakage flow more non-uniform along the blade to blade passage. The net leakage fluid flow leaving the exit cavity decreases as the number of fins increases, as indicated by the reduction in the area bounded by the $\boldsymbol{u_r = 0.0}$ contour line on plane (A) in fig. 6-36 (a). The pitchwise averaged normalized radial velocity shown in fig 6-34 (b) reveals the complex flow nature of the flow in the rear labyrinth cavity through its non-monotonic trend. A strong normalized radial velocity gradient occurs between 0.95 and 1.0 span, due to the pressure difference between the exit cavity and the main passage. The leakage flow induces a negative radial velocity on the mainstream near the exit cavity, which increases as the number of fins decreases.

The normalized axial velocity iso-levels at plane (A) and the pitchwise averaged normalized axial velocity profile along plane (B) are given in fig 6-37 (a) and (b) respectively. The maximum axial velocity inside the cavity represents the leakage flow centre velocity downstream of the last fin to shroud clearance gap. An axial velocity gradient starts close to the cavity exit plane towards the main stream, driven by viscous stresses in the re-entering flow, as shown in fig. 6-37 (b) between 0.94 span and 1.04

span. The cavity vortex blockage, which increases as the number of fins increases, introduces a higher axial velocity by redirecting the flow near the cavity exit.

Figures 6-38 (a) and (b) show the normalized absolute tangential velocity iso-levels and the pitchwise averaged normalized absolute tangential velocity on planes (A) and (B) respectively. As the number of fins increases, the position of the last fin becomes nearer to the shroud trailing edge and this position reduces the distance of contact between the leakage jet and the shroud, which in turn reduces the tangential absolute velocity component. This effect is shown clearly in fig. 6-38 (b), where the tangential velocity inside the cavity decreases as the number of fins increases. The reduction in the tangential velocity means a reduction in the windage loss and a reduction in the negative incidence angle introduced by mixing the leakage jet with the main stream. This gives spanwise more uniform out flow that benefits the downstream blade row. The stagnation pressure loss coefficient iso-levels at plane (A) and the pitchwise averaged stagnation pressure loss coefficient profile at plane (B) are presented in fig. 6-39 (a) and (b) respectively. The profile of the stagnation pressure loss coefficient inside the cavity reflects the reduction in the windage loss, as the stagnation pressure loss coefficient reduces as the number of fins increases. The increment in pressure loss coefficient between 0.95 span and 1.0 span can be attributed to the mixing out of the leakage jet and the main passage flow.

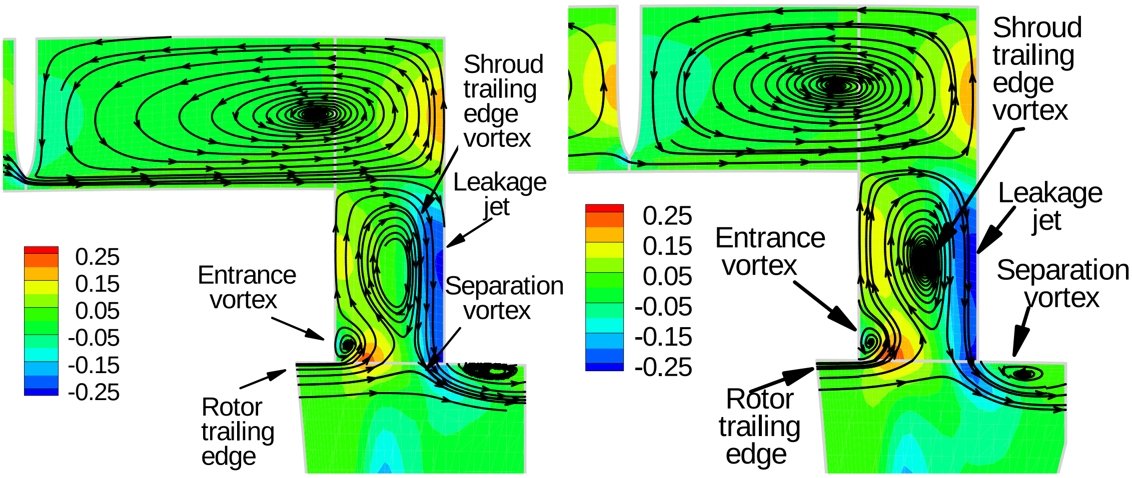

(a) 2 Fins (b) 3 Fins

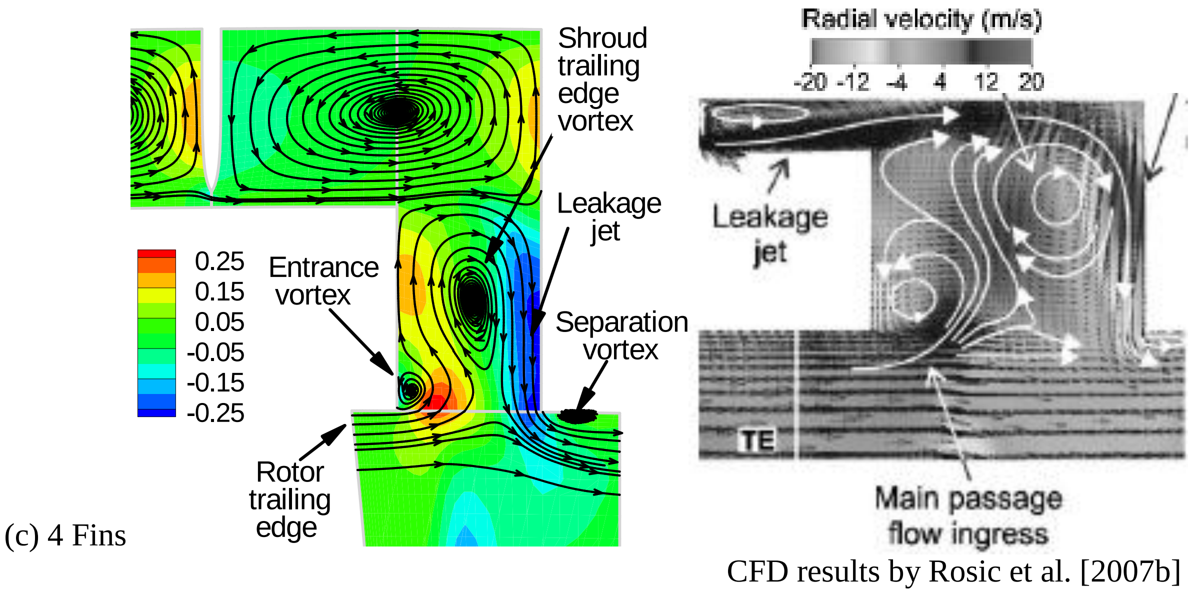

Fig. 6-33 Selected streamlines at the exit cavity with radial velocity iso-levels.

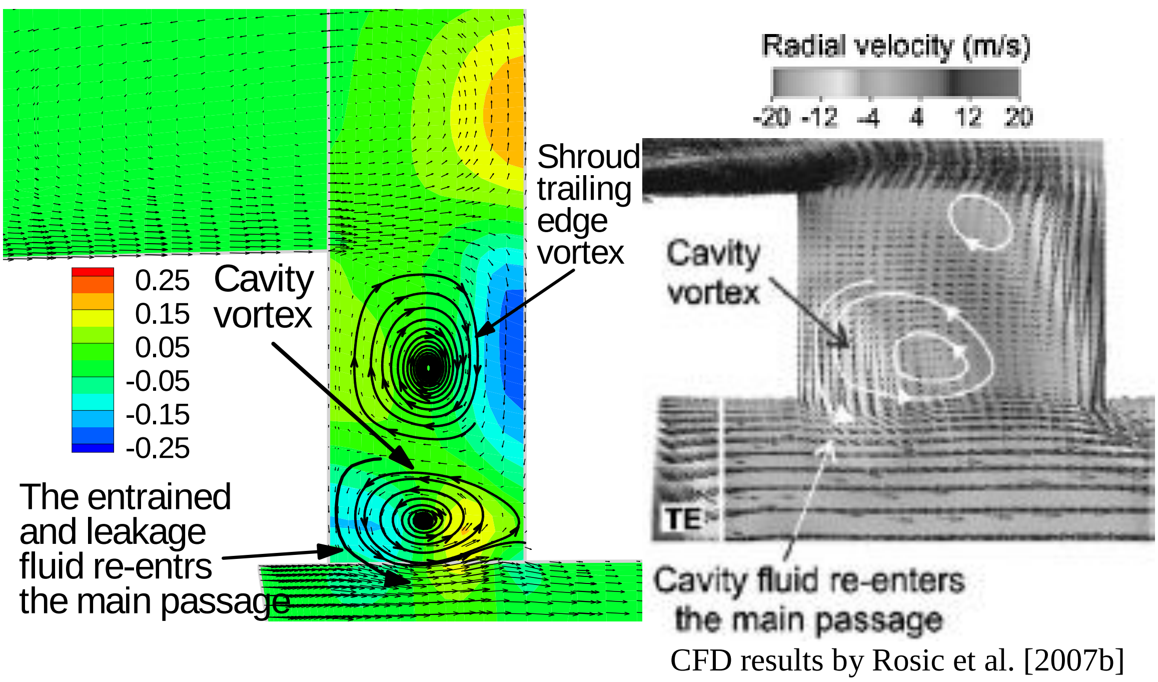

Fig. 6-34 the cavity vortex near the suction side with radial velocity iso-levels.

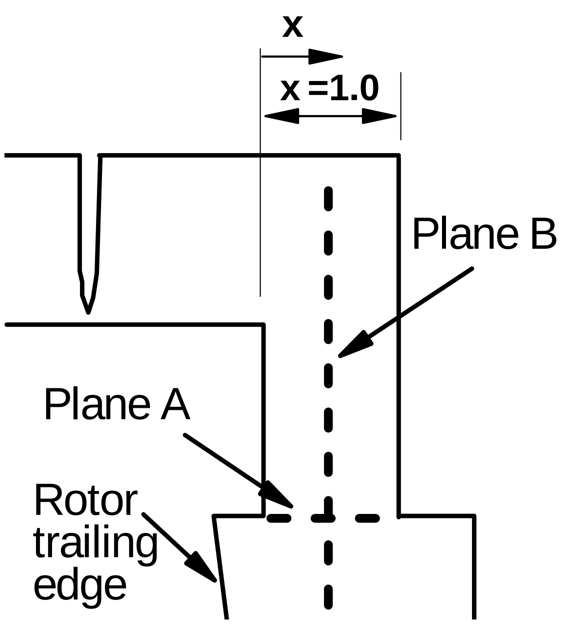

Fig. 6-35 the planes of investigation at the labyrinth seal exit cavity.

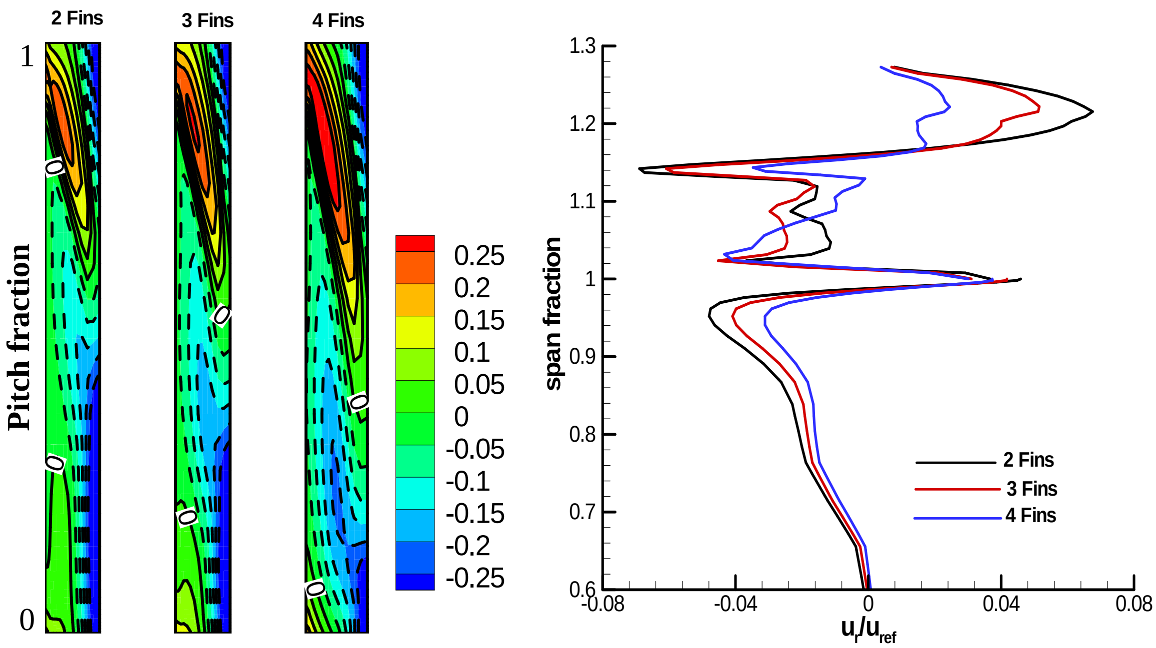

Fig. 6-36 (a) Radial velocity contours at plane (A),

(b) Pitchwise averaged radial velocity profile at plane (B).

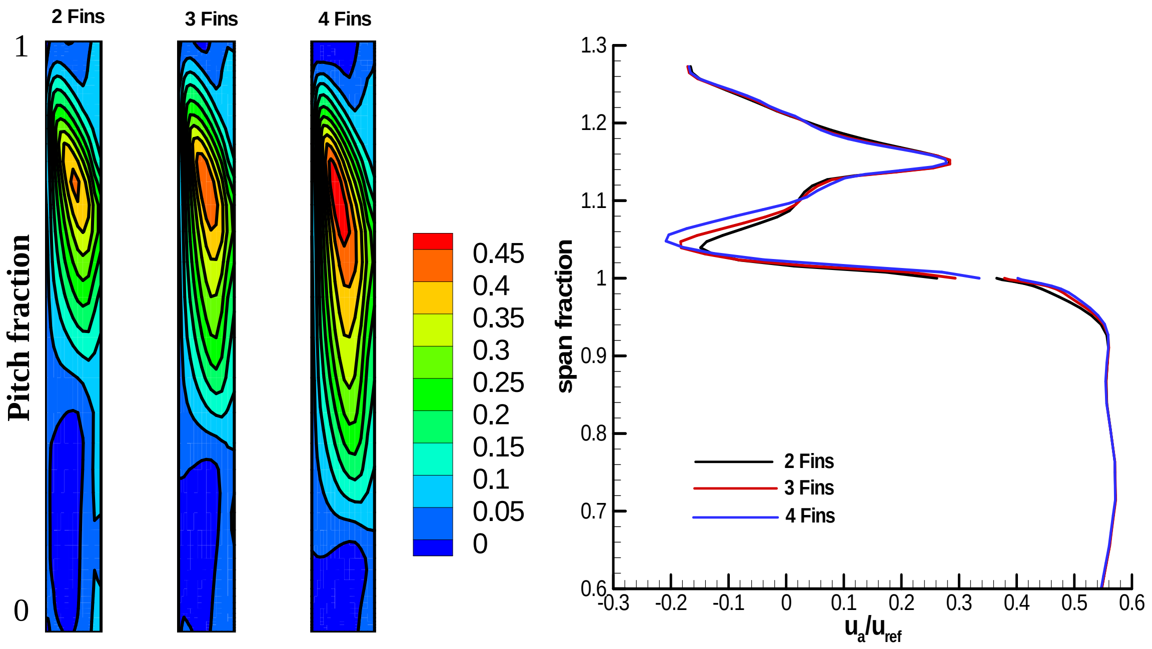

Fig. 6-37 (a) Axial velocity contours at plane (A),

(b) Pitchwise averaged axial velocity profile at plane (B).

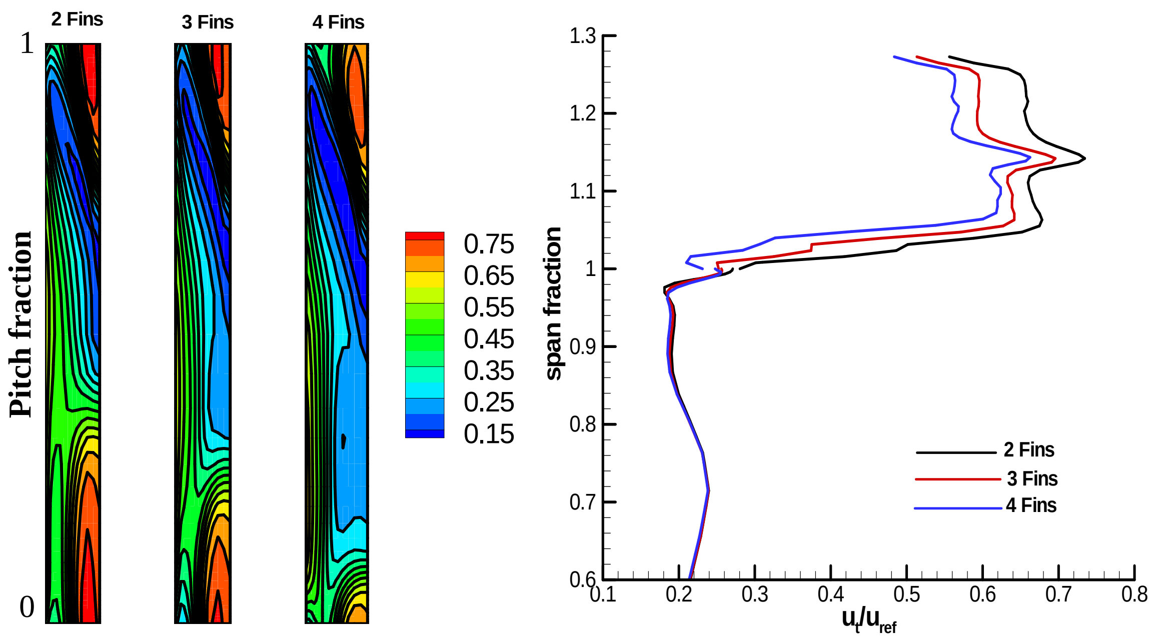

Fig. 6-38 (a) Tangential velocity contours at plane (A),

(b) Pitchwise averaged tangential velocity profile at plane (B).

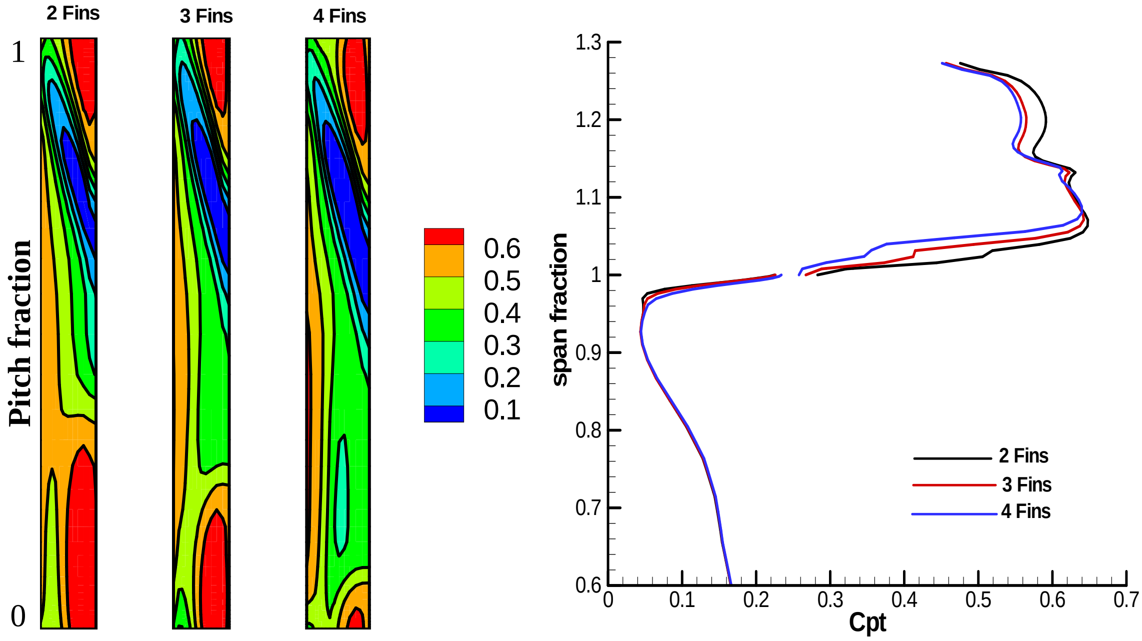

Fig. 6-39 (a) Stagnation pressure loss coefficient at plane (A),

(b) Pitchwise averaged stagnation pressure loss coefficient profile at plane (B).

The main geometrical parameter affecting the quantity of the leakage jet is the gap clearance, which throttles the leakage flow through the labyrinth seal. The effects of this parameter on the exit flow field structure are investigated. Figures 6-40 (a), (b), and (c) streamline plots show the vortical flow within the exit cavity area and downstream of it. In the background of the figures, the relative helicity is presented to show the effect of gap clearance on the intensity of the vortices. The predicted vortical structure within the cavity consists of the shroud trailing edge vortex and the entrance vortex. The shroud trailing edge vortex is due to leakage jet that separates from the shroud trailing edge, forming an injection stream running along the casing with negative radial velocity and the radially positive counter flow from the blade exit plane into the cavity, along the shroud trailing edge. The entrance vortex is due to the abrupt change in the direction of the counter flow around the shroud trailing edge at 1.0 span. Both vortices are affected by the clearance gap in opposite ways, as the helicity contours reveal. The shroud trailing edge vortex depends mainly on the leakage jet, so its intensity increases as the gap clearance increases, which means that a higher leakage flow passes through the labyrinth seal at a larger gap clearance. On the other hand, the intensity of the entrance vortex depends on the ingested mainstream fluid that reduces as the gap clearance increases. Downstream the exit cavity, a separation vortex is formed in the main passage just downstream of the leakage jet injection point. This separation vortex reduces in size as the gap clearance decreases but the tendency of the flow to swirl is still approximately unchanged as indicated by the positive helicity iso-levels.

The iso-levels of the normalized radial velocity at plane (A) and the pitchwise averaged radial velocity profile at plane (B) are given in figs. 6-41 (a) and (b) respectively. The iso-level plot shows that, as the gap clearance increases, the leakage mass flow rate increases and the inflow from the main passage into the exit cavity decreases. The iso-levels of fig. 6-41 (a) indicate that the strong leakage jet that across with a large gap clearance ratio attaches to the casing wall at the exit plane, while the weak jet that across with a small gap clearance ratio spreads over a wider area. This reduces the flow separation at the casing and exit cavity intersection, as shown in fig. 6-40 (c). The imprint of the complex flow structure within the exit cavity appears in the pitchwise averaged normalized radial velocity distribution of fig. 6-41 (b). The negative pitchwise averaged normalized radial velocity near the top of the rotor shroud at 1.14 span, increases as the gap clearance increases, which indicates that more leakage flow is passed through the labyrinth seal. At $\tau = 1.0\%$ and 1.5%, the leakage jet sticks to the casing wall so the average value of the radial velocity at the mid section x=0.5 is positive at 1.0 span. At $\tau = 0.5\%$, the spreading of the leakage jet over the exit plane lets the average value of the radial velocity at the mid section x=0.5 to be negative at 1.0 span. Below 1.0 span, the main passage stream displays a negative pitch averaged normalized radial velocity in fig. 6-41, due to mixing with leakage jet and the pitch averaged normalized radial velocity increases as the gap clearance increases.

The normalized axial velocity iso-levels at the exit cavity plane (A) and the pitchwise averaged normalized axial velocity at the plane (B) are shown in fig. 6-42(a) and (b) respectively. From the iso-levels plot, it is shown that the leakage flow gives a positive axial velocity from the boundary layer flow in the main passage. Specifically, this normalized axial velocity increases as the gap clearance decreases and this confirms that the development of the cavity vortex is fed by the inflow from the main passage near the pressure side at the trailing edge. This cavity vortex is responsible for redirecting the leakage jet plus the entrained inflow to mix with the main passage flow further upstream at small gap clearance ratio, as shown in fig. 6-40. The smallest gap clearance entrains axial momentum from the passage into the cavity and reinjects flow with a higher axial momentum and lower radial velocity, reducing the downstream separation that thickens the boundary layer near the end wall, with respect to the $\tau = 1.0\%$ and 1.5% cases. This effect is also shown in fig. 6-42 (b) near 1.0 span, where the pitch averaged normalized axial velocity distribution becomes more uniform for the smallest gap clearance. The velocity profile of the leakage jet downstream of the last fin is represented in fig. 6-42 (b) between 1.14 span and 1.27 span. The maximum axial velocity in the leakage jet profile increases as the gap clearance increases and the profile gets thicker.

The normalized tangential velocity of the leakage jet at the interface plane (A) and the distribution of the pitchwise averaged normalized tangential velocity at plane (B) are plotted in fig. 6-43 (a) and (b) respectively. These results indicate that the tangential velocity of the leakage jet within the exit cavity increase as the gap clearance increases. This increase in the tangential velocity means an increase in the corresponding windage loss. Also, the higher tangential velocity of the leakage jet introduces a higher negative incidence angle affecting the following stator blade row.

Figure 6-43 (a) and (b) show respectively the stagnation pressure loss coefficient across plane (A) and the pitchwise averaged stagnation pressure loss coefficient at plane (B). The stagnation pressure loss coefficient at the exit plane A increases as the gap clearance increases as indicated by the iso-level plot shown in fig 6-44 (a). The profile of the pitchwise averaged stagnation pressure loss coefficient in fig. 6-44 (b) shows an increase of stagnation pressure loss coefficient with the gap clearance ratio near the exit cavity, between 1.0 span and 1.10 span. Above this range, the differences in the stagnation pressure loss coefficient are small. The mixing of the leakage jet with the main passage flow generates a strong radial gradient of the stagnation pressure loss coefficient in the range of 0.95 to 1.0 of the span.

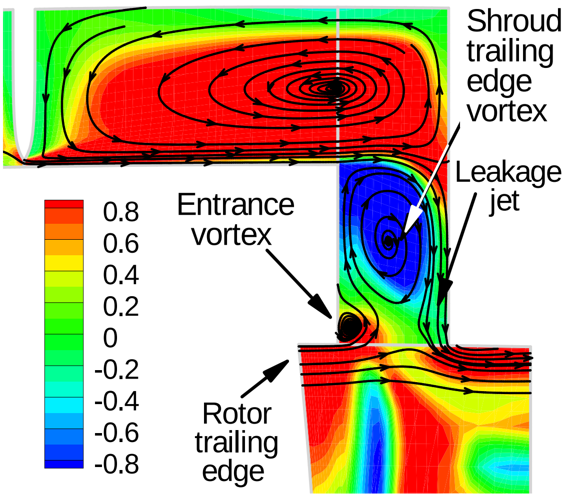

(a) τ =0.5%

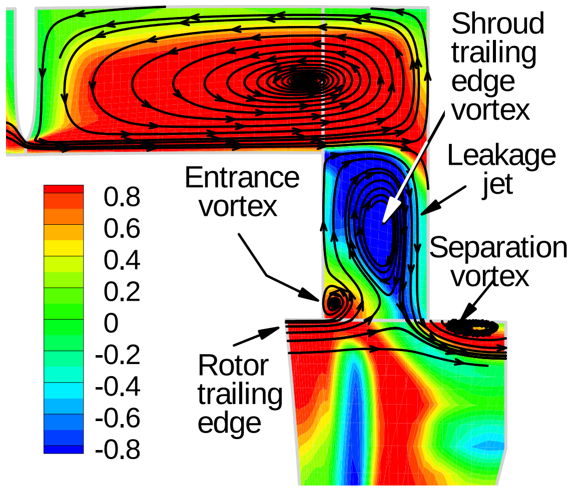

(b) τ =1.0%

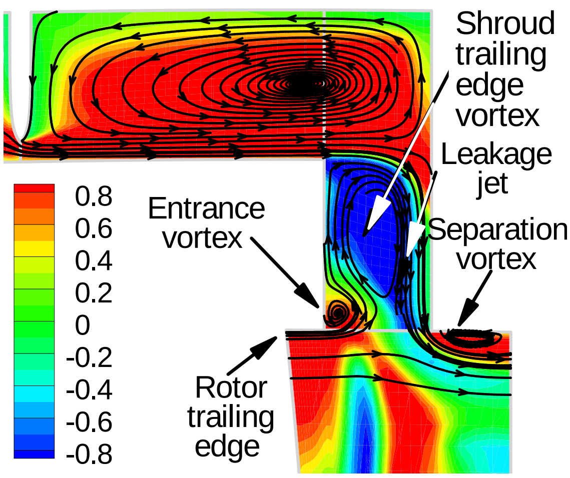

(c) τ =1.5%

Fig. 6-40 the exit cavity vortical flow with relative helicity iso-levels in the background at varying gap clearance ratios.

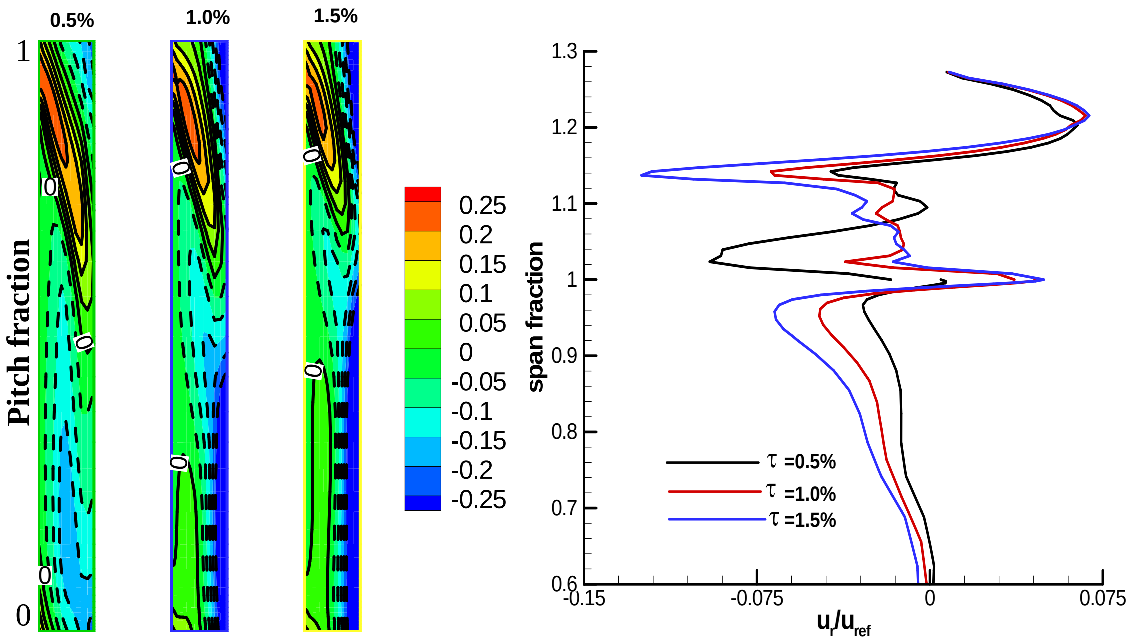

Fig. 6-41 (a) Radial velocity contours at plane (A),

(b) Pitchwise averaged radial velocity profile at plane (B).

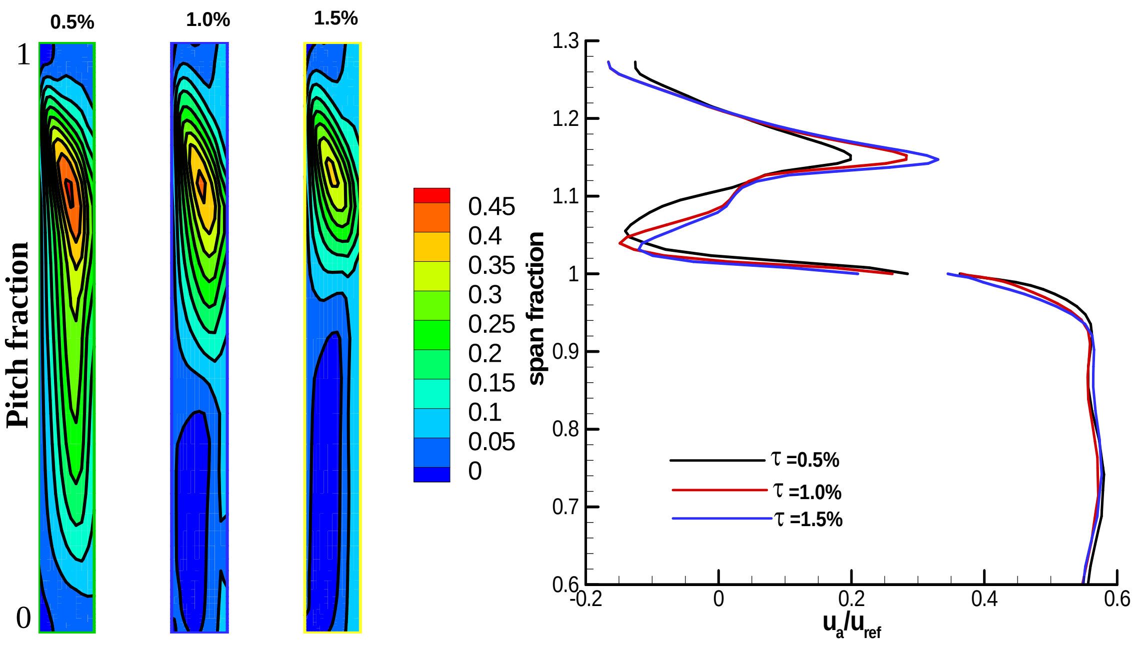

Fig. 6-42 (a) Axial velocity contours at plane (A),

(b) Pitchwise averaged axial velocity profile at plane (B).

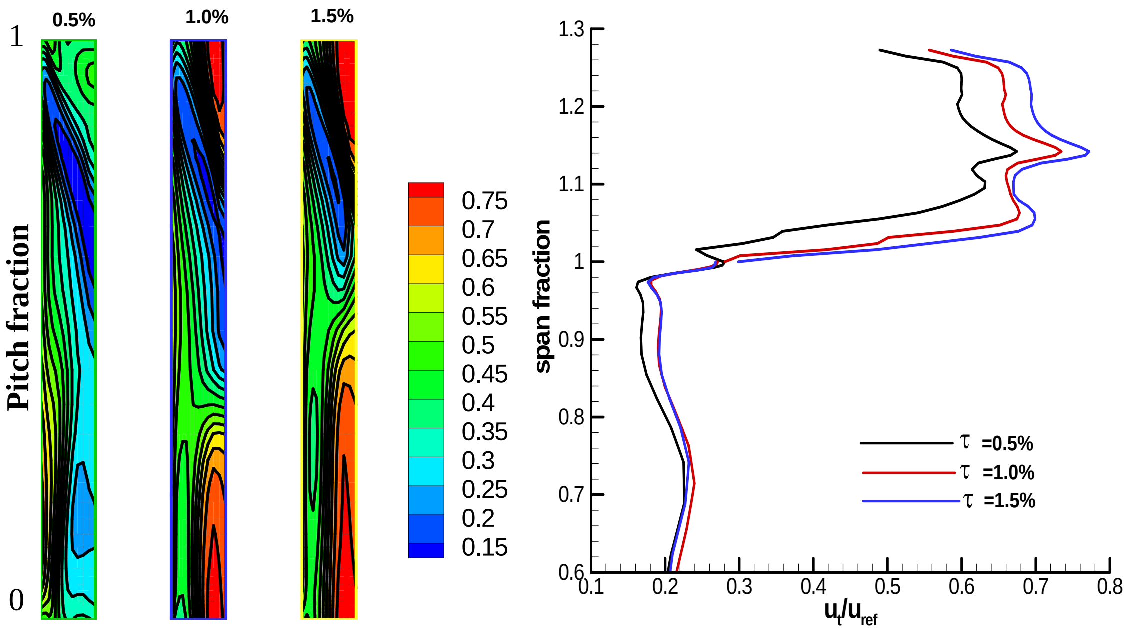

Fig. 6-43 (a) Tangential velocity contours at plane (A),

(b) Pitchwise averaged tangential velocity profile at plane (B).

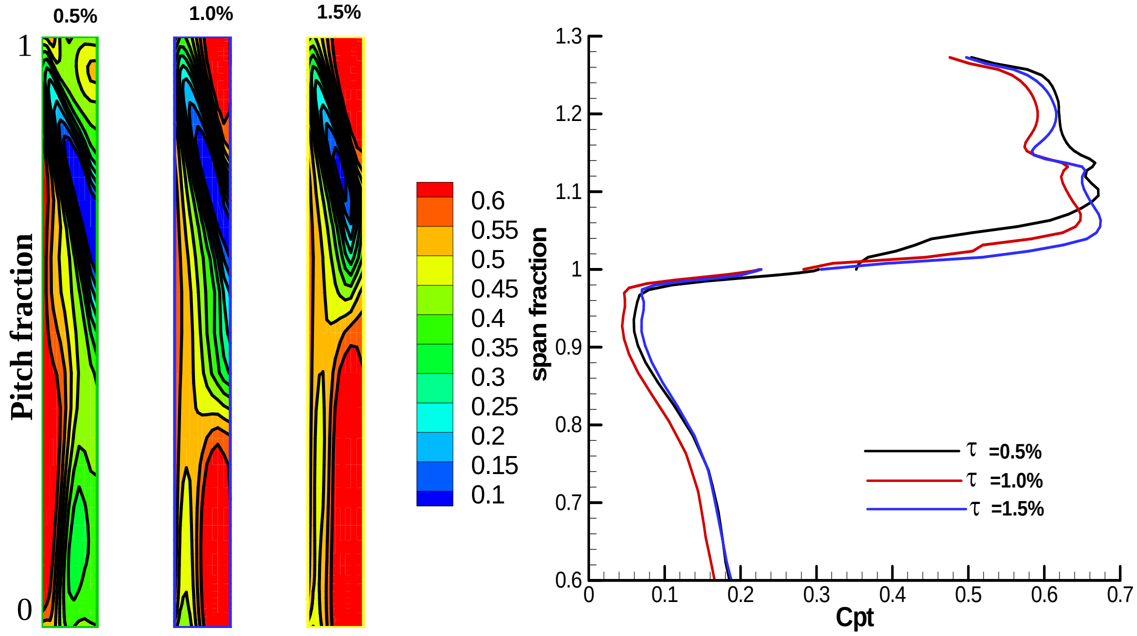

Fig. 6-44 (a) Stagnation pressure loss coefficient at plane (A),

(b) Pitchwise averaged stagnation pressure loss coefficient profile at plane (B).

The number of fins and the gap clearance mainly control the leakage jet mass flow rate, while the exit cavity angle affects mainly the leakage jet direction. The impact of the angle at which the leakage jet meets the mainstream is investigated using three casing wall angles 90^o, 60^o, and 30^o. Streamlines in fig. 6-45 show the predicted vortical flow at the cavity exit at the three cavity wall angles. The relative helicity iso-levels are shown in colour in the background of the figure. The results show that the separation downstream of the leakage jet mixing with the mainstream is eliminated by using 60^o and 30^o exit angles. By eliminating the downstream separation, this source of boundary layer thickening is removed. This effect can be monitored by observing the helicity contours in the circled area in fig. 6-45.

Figure 6-46 (a) shows the normalized radial velocity iso-levels at plane A for the three exit angles. The iso-level plot shows a lower radial velocity component at the exit plane (A) as the exit angle decreases. Also, the ingested main passage flow that feeds the cavity vortex is reduced by reducing the exit cavity angle, since the sharper shroud trailing edge angle increases the turning angle of the inflow which counteracts the inflow pressure gradient across pane (A). The leakage jet confinement area to the casing wall is alleviated and the leakage jet uses a larger part of plane A to exit.

The normalized axial velocity contours are presented in fig. 6-46 (b). The leakage jet from a lower exit angle casing wall has a higher axial velocity. This improves the boundary layer flow by increasing the axial momentum of this low momentum layer. The tangential velocity component of the leakage jet at the exit plane (A) decreases as the exit angle decreases, as shown in fig. 6-46 (c). The reduction in the tangential velocity leads to a reduction in windage loss and in the negative incidence angle introduced into the mainstream through the mixing process. This reduction in loss can be seen in fig. 6-46 (d), which presents the contour plot of the stagnation pressure loss coefficient at plane (A).

The exit flow investigation within the labyrinth cavity shows some benefits introduced by controlling both the leakage mass flow rate through the gap clearance and the number of fins, and the leakage jet direction, through the casing angle. The effects of these controlling parameters on the main passage flow downstream the mixing region will be investigated later.

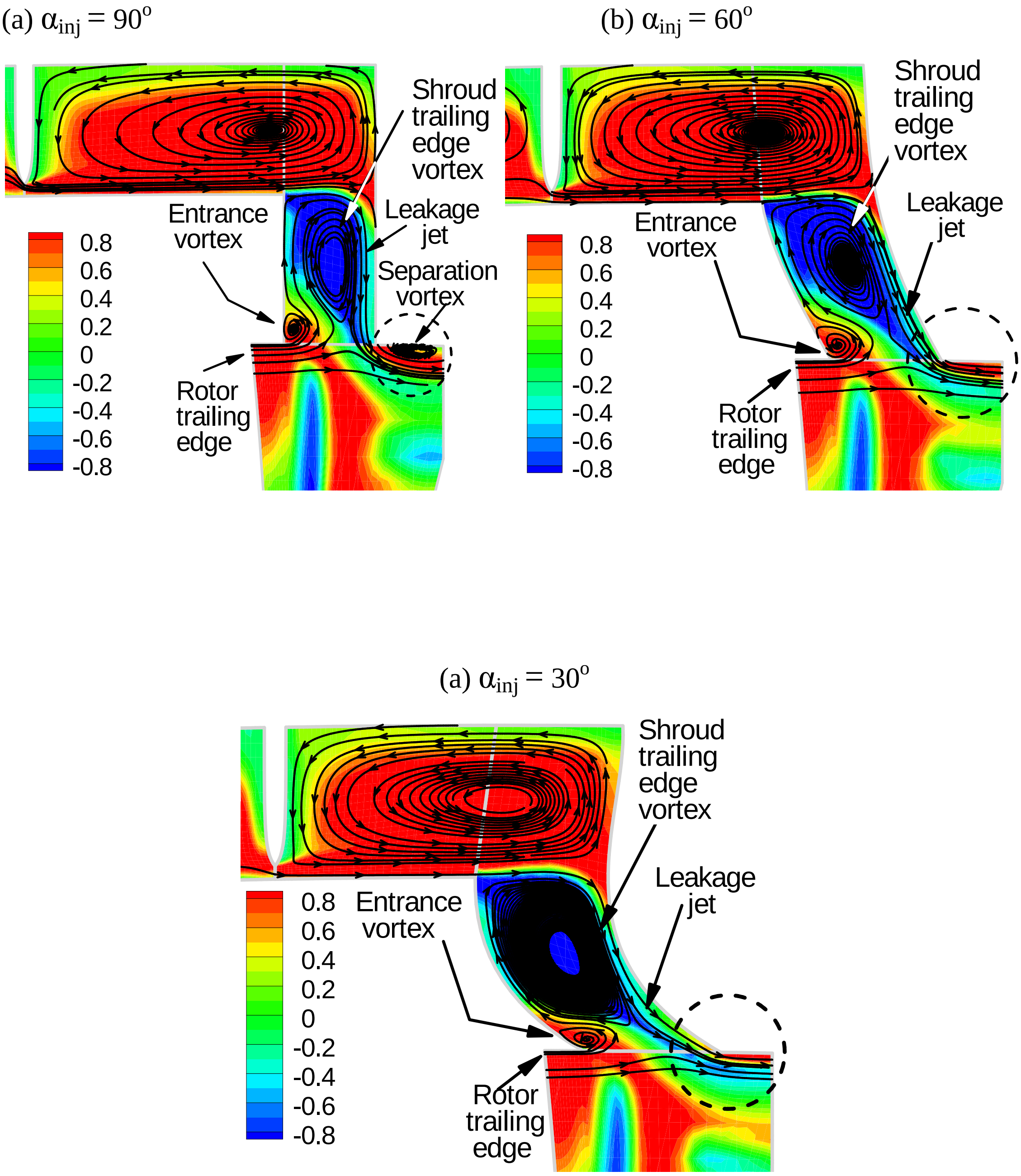

Fig. 6-45 the exit cavity vortical flow with relative helicity iso-levels in the background at varying casing injection angle.

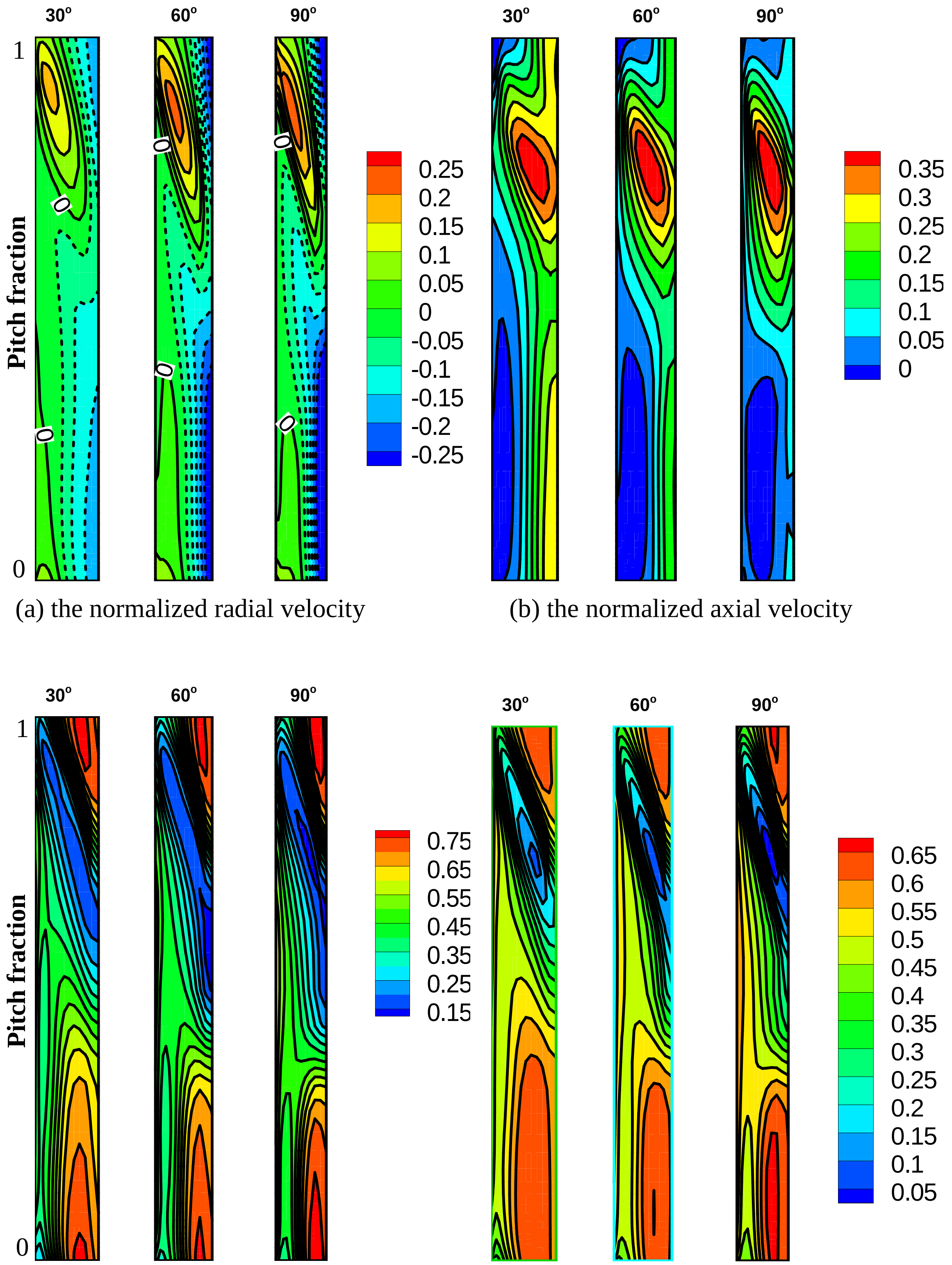

(a) the normalized radial velocity (b) the normalized axial velocity

(a) the normalized tangential velocity (b) the stagnation pressure loss coefficient

Fig. 6-46 Normalized flow states iso-levels at plane (A) at varying injection angle (a) the radial velocity (b) the axial velocity (c) the tangential velocity (d) the stagnation pressure loss coefficient.

6-3.3 The pressure distribution along the seal fins

The leakage mass flow rate is driven by the stage operating pressure ratio. The leakage mass flow rate increases as the operating pressure ratio increases. Therefore, the static pressure distribution through the labyrinth seal is important. Also, the pressure distribution is important for designers to calculate the turbine thrust. The mass averaged pressure drop through the labyrinth seal, $\mathrm{p} - \mathrm{p_e}$, is normalized by the pressure drop across the rotor to give the labyrinth seal static pressure coefficient Cp:

$$\mathrm{Cp} = \frac{\mathrm{p} - \mathrm{p_e}}{\mathrm{p_{0in}} - \mathrm{p_e}} \qquad (6-6)$$

where $\mathrm{p_{0in}}$ and $\mathrm{p_e}$ are the main passage rotor total inlet pressure and static exit pressure respectively. The flow through a constant area labyrinth seal is adiabatic with friction, i.e. follows the Fanno curve, provided that the contraction coefficient is constant. According to Egli [1935], the contraction coefficient can be assumed constant when Reynolds number based on the jet leakage velocity issuing from the throttling gap and the throttling gap clearance is above 10^3 and this condition is applicable for most steam turbines. The flow through the labyrinth seal undergoes a number of throttling processes equal to the number of fins. The static pressure coefficient distribution at the mid gap height for three different gap clearance ratios is shown in fig. 6-47. The static pressure coefficient distribution is plotted against the axial distance from the cavity inlet to the cavity exit, normalized by the labyrinth seal axial length. The signature flow at the shroud leading edge gives a peak pressure at x=0.09. This pressure peak is followed by minimum at x=0.16, approximately at the centre of the upstream separation vortex. It is observable that the lowest minimum at x=0.16 is obtained with the smallest clearance gap, $\tau = 0.5\%$ span, as the intensity of the flow separation increases with decreasing gap width, as stated in the discussion of fig 6-28. Downstream of x=0.16, the static pressure slightly increases before the flow approaches the first fin. This pressure recovery increases as the gap clearance increases, which is consistent with the experimental observation by Denton and Johnson [1976]. As the flow approaches the first fin, it accelerates, reducing its static pressure. Downstream of the fin, part of this acquired kinetic energy is converted into heat due to friction part is reconverted into potential energy, increasing local static pressure, and the rest enters the next fin throat. Just downstream of the first fin, where the leakage jet velocity is high, the static pressure appears to be constant or decrease due to the balance between the pressure recovery and the pressure loss, while further downstream the pressure recovery becomes dominant.

After the last fin passage, static pressure recovers from x=0.95, which is slightly after the trailing edge of the shroud, where x=0.93. This pressure rise above the static pressure immediately downstream of the last fin increases as the gap clearance height increases. This trend resembles the pressure rise after the throat of an orifice plate and is responsible for determining the leakage flow mass flow rate. The pressure drop across each fin is roughly equal. However, the testing of different gap clearance heights and consequently different leakage mass flow rates and momentum fluxes results in slight differences in the static pressure distribution through the labyrinth seal.

Figure 6-48 shows the effect of the leakage jet injection angle on the static pressure distribution through the labyrinth seal. The static pressure upstream of the first fin shows no significant variation with the injection angle which confirms that the injection angle has not significant impact on the inlet cavity flow characteristics. Downstream of the inlet cavity, some differences start to appear in the static pressure distribution between the test case with $\alpha_{inj} = 90^o$ and the test cases with $\alpha_{inj} = 30^o$, and 60^o in the cavity enclosed between the two fins. The main difference in static pressure occurs downstream the last fin. It is noticeable that the pressure recovery for $\alpha_{inj} = 30^o$ and $\alpha_{inj} = 60^o$ starts early but at a low rate with respect to $\alpha_{inj} = 90^o$. This is due to the contouring of the rotor shroud and of exit cavity brought about by the shallower injection angles. Also, the exit pressure at which the leakage flow meets the main passage flow at $\alpha_{inj} = 30^o$ seems to be less than for the $\alpha_{inj} = 90^o$ case, which leads to less mixing loss generation.

Figures 6-49 show the static pressure distribution along labyrinth seal containing 2, 3, and 4 fins. Due to the change in fin location among the three test cases, each case is plotted in a separate graph. As the number of fins increases above two, the pressure drop across the first fin is considerably higher than across the downstream fins. However, the rest of the pressure drop is equally distributed among the rest of fins. The shape of the pressure distribution between two consecutive fins changes from a straight line to a concave as the number of fins increases. This shape change suggests that the last seal should be placed near to the shroud trailing edge, to reduce the pressure recovery at the exit from the labyrinth seal and so reduce the

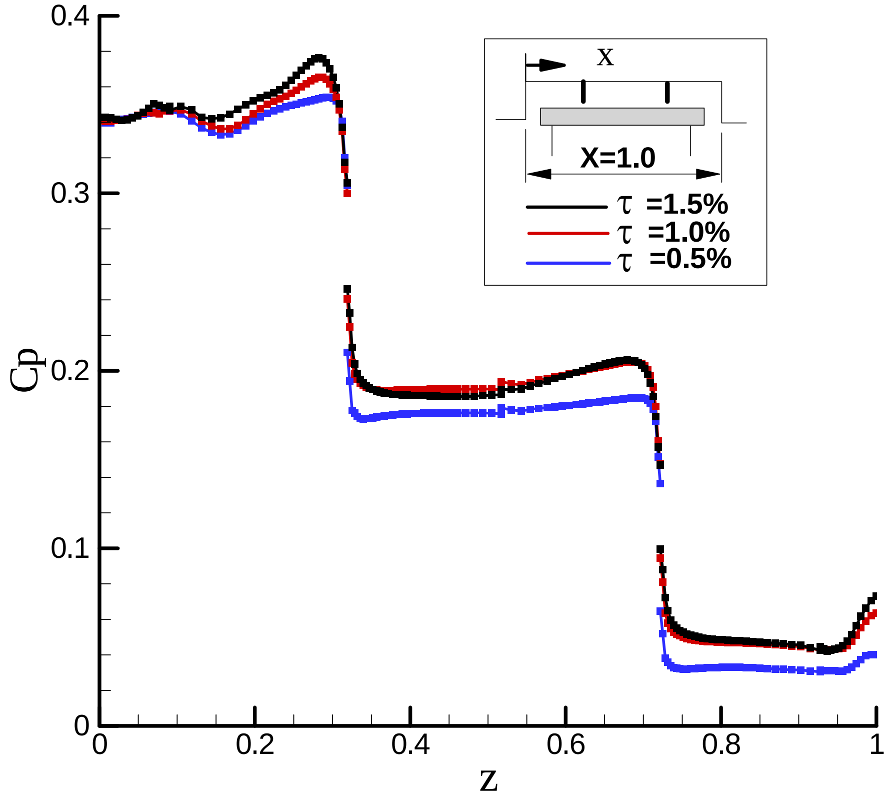

Fig. 6-47 the static pressure coefficient along the labyrinth seal at different gap clearance ratios.

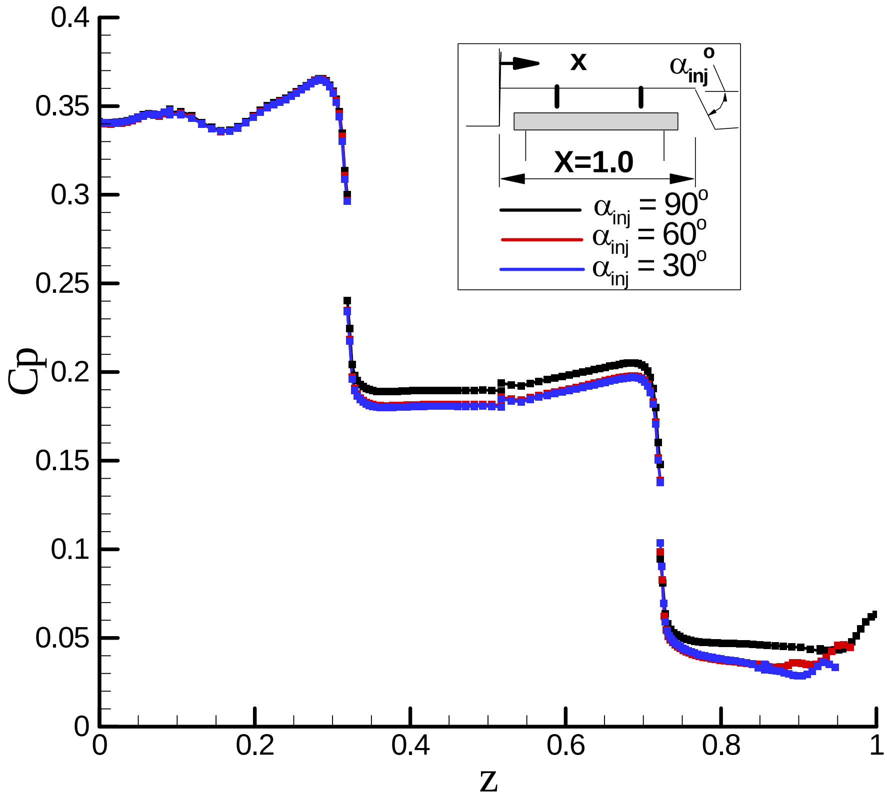

Fig. 6-48 the static pressure coefficient along the labyrinth seal atdifferent injection angles.

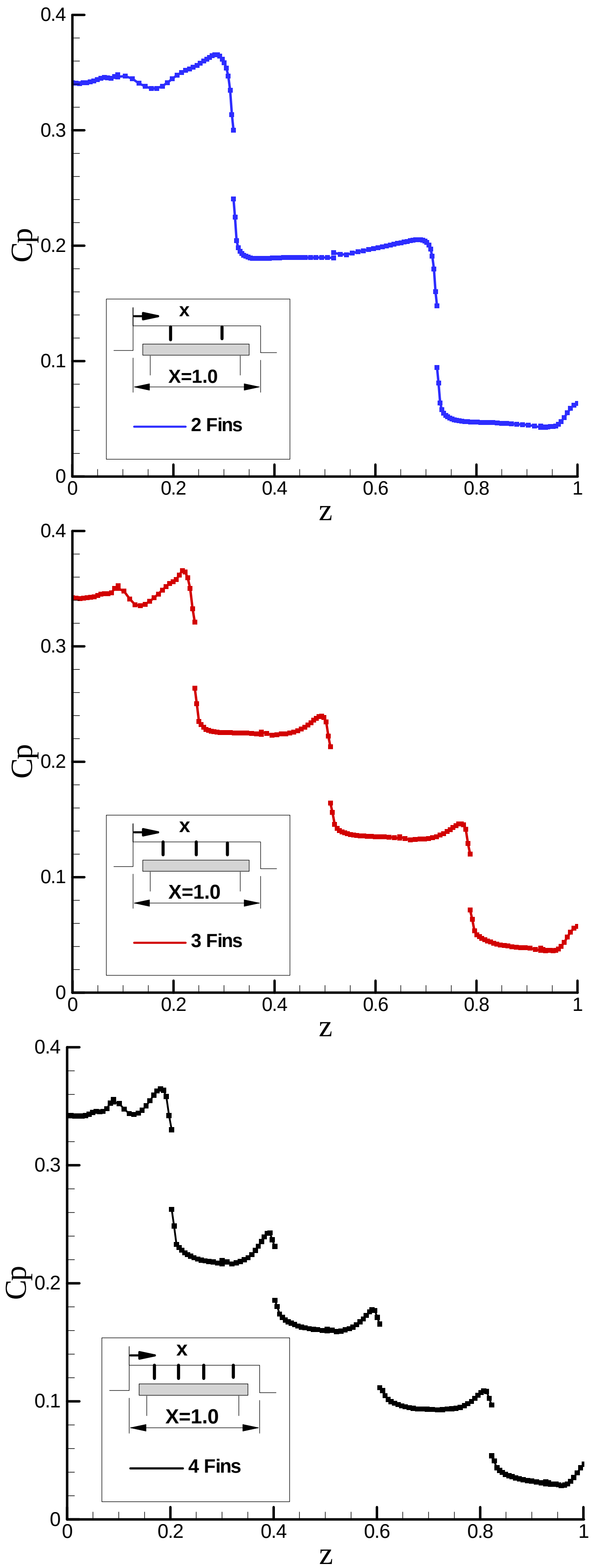

Fig. 6-49 the static pressure coefficient along the labyrinth seal at different number of fins.

mixing and windage losses. The short distance between two successive fins as the number of fins increases reduces the stagnation pressure loss across each fin which reduces the effectiveness of any further increasing in the number of fins.

6-4 The Labyrinth leakage flow evaluation compared with the analytical model

This section presents the evaluation of the mass leakage fraction for the modelled cases using CFD compared to the predictions output from the analytical model described in chapter 3. The mass leakage fraction of the modelled rotor is calculated by integrating over the exit cavity area to evaluate the leakage mass flow rate $\dot{m}_L$ and over the rotor exit area to evaluate the turbine mass flow rate $\dot{m}_m$. The analytical leakage mass flow rate is evaluated from Eqn. 3-13 in chapter 3. Figure 6-50 shows the mass leakage fraction $\frac{\dot{m}_L}{\dot{m}_m}$ against the gap clearance ratio τ. The results indicate that numerical and analytical models predict the same linear variation of the mass leakage fraction with the clearance gap. The CFD results show good agreement with the analytical model, with the gradient being slightly under-estimated. This difference in slope may be ascribed to the approximation in the integration of the cylindrical cavity exit area.

The variation of the mass leakage fraction with the number of fins at the flow coefficient $\phi = 0.52$ is shown in fig. 6-51. The addition of the third fin reduces the mass leakage flow by 18.0% while the addition of the fourth fin causes an 8.5% further reduction in the leakage mass flow. This result confirms that the effectiveness of reducing the leakage flow by increasing the number of fin decreases as the number of fin increases by more than three. The CFD results show a reasonable agreement with the analytical model.

The over shroud leakage flow contributes to the stage loss, due to the losses generated within the leakage flow itself and due to the mixing between the leakage jet and the main passage flow downstream the rotor. The loss generated within the mixing process is defined in terms of entropy increase. Figure 6-52 shows a control volume that is used to evaluate the entropy generation due to the mixing process. The control volume extends radially from 0.85 span to the edge of the exit cavity at 1.0 span. The effect of the leakage jet does not exceed 0.9 span in any of the modelled cases as will be shown later and from 0.9 to 0.85 there is no significant entropy change in the axial location just upstream and downstream of the mixing process. The rate of entropy change is calculated by applying the second law of thermodynamics.

$$\Delta\dot{S}_{mix} = \sum \dot{m}_e s_e - \sum \dot{m}_i s_i \qquad (6-6)$$

By substituting the entropy generation rate into Eqn. 3-26, the entropy mixing loss coefficient can be calculated. Figure 6-53 shows the entropy mixing loss coefficient against the gap clearance ratio compared with the results from the analytical model. The analytical results are obtained from Eqn. 3-26 in chapter 3. Both predictions indicate that, as the gap clearance ratio increases, the mixing loss increases. The CFD results are slightly higher than the analytical model. This difference can be attributed to the small contribution of other sources of losses within the selected control volume, such as the wake mixing loss that is not included in the analytical model. The variation of the entropy mixing loss coefficient with the injection angle is given in fig. 6-54. It is clear that reducing the injection angle leads to a considerable reduction in the entropy mixing loss coefficient. The entropy mixing loss coefficient is reduced by 18.50% when reducing the injection angle from 90^o to 60^o. A further 30^o reduction in injection angle leads to an additional reduction of 6.2%. This suggests that the reduction of the injection angle from 90^o to 0^o may lead to a 26.7% reduction in entropy mixing loss coefficient, which is consistent with the finding in chapter 3. The reduction in the mixing loss can be interpreted as increase in rotor static-to-static efficiency, as shown in fig. 6-55. This figure shows that the reduction of the injection angle from 90^o to 30^o leads to an increase in the rotor static-to-static efficiency of 0.2%. This increment appears to be sensible, since the mixing and negative incidence losses are estimated to reduce the stage efficiency by 0.4% as reported by Rosic and Denton [2008]. Still, controlling the leakage mass flow rate through the gap clearance ratio and the number of fins remains the most effective way to gain rotor efficiency. Figures 6-56 and 6-57 show respectively the effect of the gap clearance ratio and the number of fins on the rotor static-to-static efficiency. Figure 6-56 shows a linear relation between the rotor efficiency and the gap clearance ratio. Figure 6-57 shows that the rotor static-to-static efficiency increases non-linearly with the number of fins, confirming that increasing the number of fins improves the stage performance. However, due to the non-linear trend, the increment in the number of fins gives progressively diminishing return in the efficiency; consistently with the second conclusion of the analytical model in section 3-4. Figure 6-58 shows the rotor static-to-static efficiency against the mass leakage fraction. Figure 6-58 agrees with the classical shroud leakage theory, which states that the loss of efficiency associated with the leakage is directly proportional to the mass leakage fraction as reported by Rosic et al. [2007a]. The CFD results of figs. 5-50, 5-51, and 5-53 have shown a good agreement with the analytical model results applied to this rotor.

This section has discussed the effect of the labyrinth seal geometry on the rotor entropy generation, the leakage mass flow rate, and the rotor efficiency. The influence of the leakage flow on the secondary flow and flow angles of the main passage will be addressed in the following section.

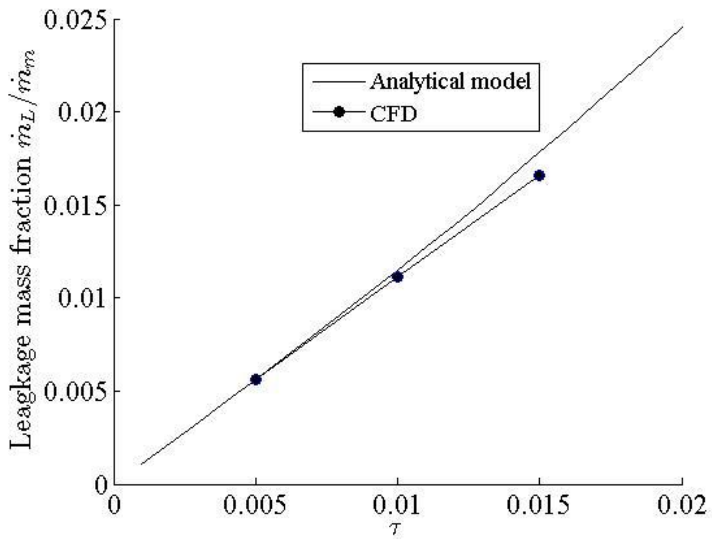

Fig. 6-50 Leakage mass flow fraction versus gap clearance ratio.

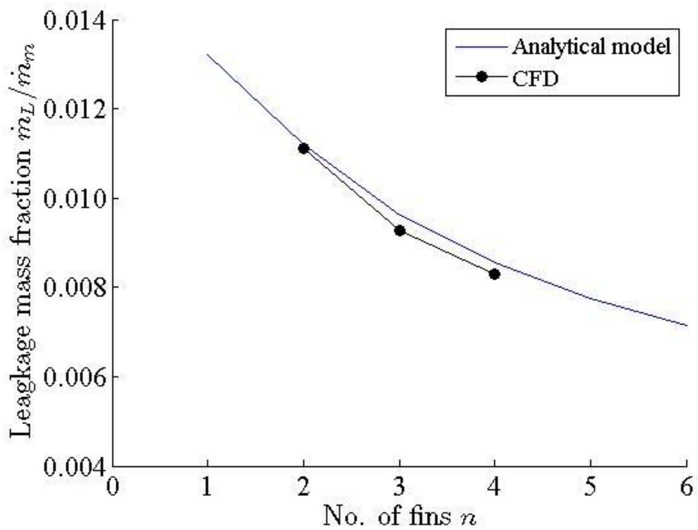

Fig. 6-51 Leakage mass fractions versus the number of labyrinth fins.

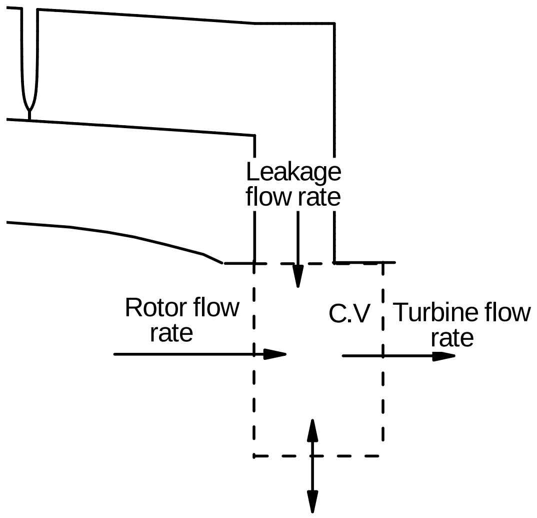

Fig. 6-52 The control volume to calculate the entropy generation due to the mixing process.

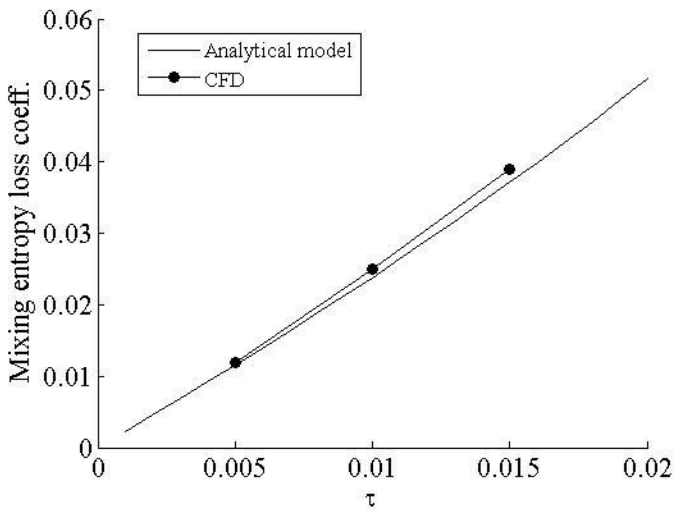

Fig. 6-53 The entropy mixing loss coefficient versus the gap clearance ratio.

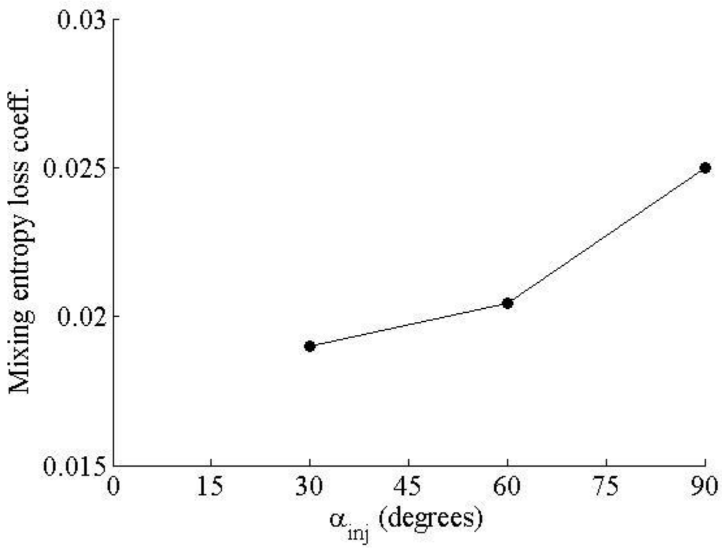

Fig. 6-54 the entropy mixing loss coefficient versus the injection angle.

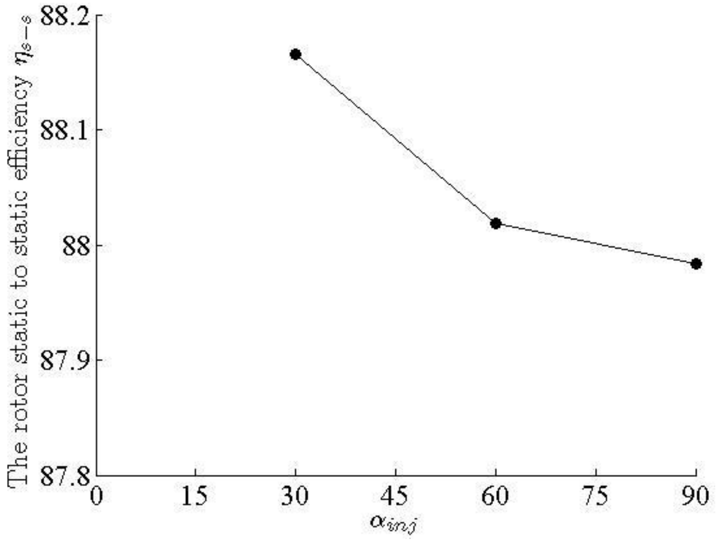

Fig. 6-55 the rotor static-to-static efficiency versus the injection angle.

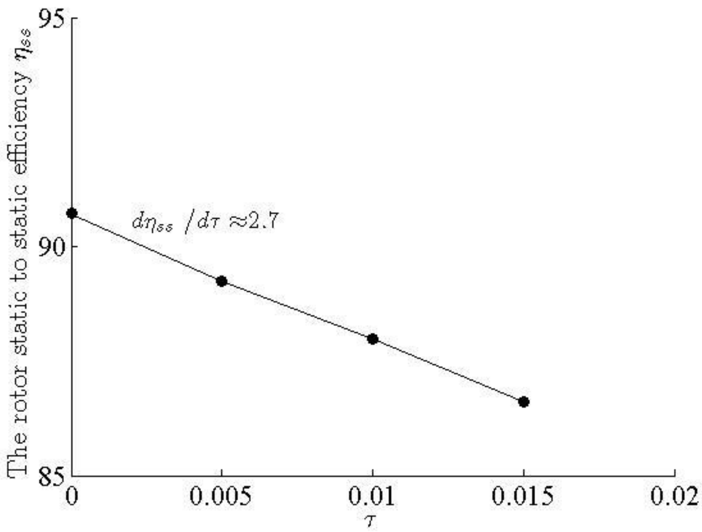

Fig. 6-56 the rotor static-to-static efficiency versus the gap clearance ratio.

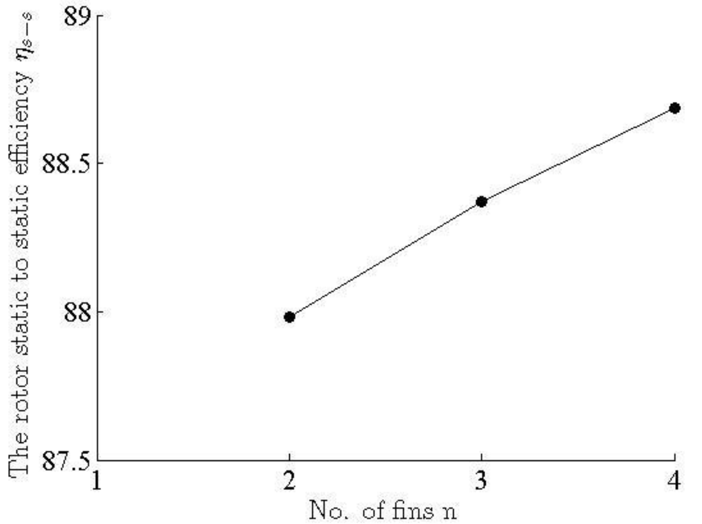

Fig. 6-57 the rotor static-to-static efficiency versus the number of labyrinth fins.

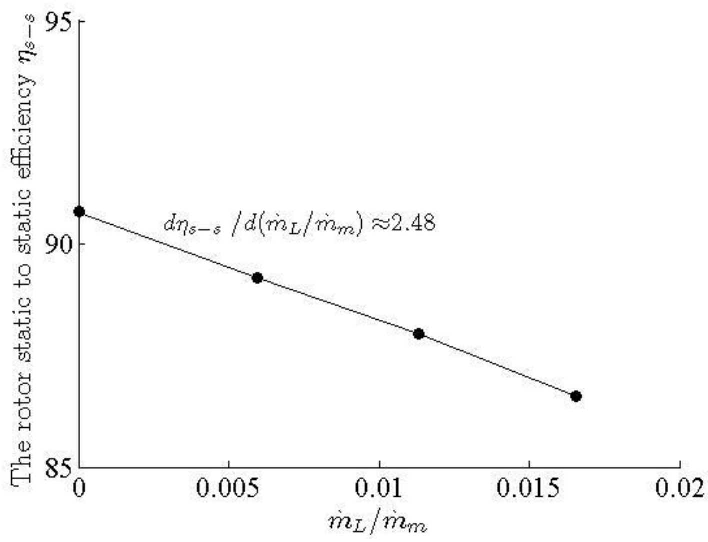

Fig. 6-58 the rotor static-to-static efficiency versus the leakage mass fraction.

6-5 The effects of the leakage flow on the turbine rotor flow

6-5.1 The effect on the rotor secondary flow

The leakage flow that enters the inlet labyrinth seal cavity has an appreciable effect on the secondary flow at the inlet to the rotor, as stated in the discussion of fig. 6-28 in section 6-3.1. The inlet leakage flow to the cavity radially removes the inlet boundary layer upstream of the rotor, which leads to a reduction in the secondary flow within the rotor passage. This effect is clearly shown in fig. 6-59. This figure shows the iso-levels of the helicity in a cascade plane at 50% of the axial chord. Helicity is plotted to identify secondary flows. Figures 6-59 (a-c) show the secondary flows at 0%, 0.5%, and 1.5% gap clearances respectively. Comparing figs. 6-59 (a-c) show that as the leakage flow increases, more boundary layer is removed from the main passage. This reduces the secondary flow within the rotor passage as shown by the reduction of helicity in figs 6-59 (a-c). In fact, as leakage mass flow rate increases, more slow moving boundary layer flow is removed from the blade tip inlet region and is bypassed through the labyrinth seal. This reduces the thickness of the boundary layer which affects the development of the upper passage vortex. Therefore, in the low gap clearance test case, the reduction in helicity iso-levels is not clearer as in the high gap clearance test case.

Figure 6-60 shows the stagnation pressure loss coefficient iso-levels downstream of the rotor at a quasi-normal plane located at 120% axial chord for 0% (no gap clearance), 0.5%, 1.0%, and 1.5% gap clearance. This figure shows three distinct areas of high loss for the reference test case (0% gap clearance ratio). Near the hub, a secondary flow loss associated with a large hub passage vortex can be seen occupying up to 40% of the span. Above this, the loss associated with the essential two-dimensional flow wake covers the following 30% percent of the blade span. Near the tip, a casing passage vortex develops close to the casing wall with its core at 83% of the span approximately.

Figure 6-60 shows that introducing a leakage flow mainly affects the casing passage vortex and the wake region. The passage vortex size increases as the gap clearance ratio increases, which increases the mass leakage fraction. This increase in the passage vortex size consequently reduces the area occupied by the wake flow. In addition to the casing passage vortex, a tip leakage vortex is introduced. This is shown in fig. 6-60 at $\tau = 1.0\%$ the appearance of a second local pressure coefficient maximum at the passage vortex core. The leakage vortex loss intensity increases as the mass leakage fraction increases. The high swirl component of the leakage jet (since it does no work) introduces a skew to the passage vortex shape. By increasing the leakage jet mass fraction, the passage vortex undergoes two opposite processes. Inside the rotor, its intensity reduces due to the removal of the boundary layer at the rotor inlet as shown in fig. 6-59. Downstream of the rotor, its intensity increases due to the separation introduced by the leakage jet at intersection between the cavity exit and intersection with the endwall casing, as shown in fig.6- 40. These two opposite processes can be observed at the biggest gap clearance ratio case $\tau = 1.5\%$ where the passage loss core is expected to have the highest level due to the interaction with a strong leakage jet but actually its core loss level is slightly lower than $\tau = 0.5\%$ and $\tau = 1.0\%$. The non-uniform leakage jet discharged from the cavity exit leads to a higher stagnation pressure loss near the suction side where most of leakage jet and the entrained flow re-enters the main passage.

The effect of the injection angle on the secondary flow at the rotor exit is shown by fig. 6- 61. These results indicate that controlling the radial velocity component of the leakage flow by reducing the angle of injection reduces the size of the passage vortex and its core level of loss. The redirection of the leakage jet that mixes with the mainstream reduces the separation at the cavity exit corner. The leakage jet axial velocity component adds momentum to the slowly moving fluid reducing the boundary layer thickness and consequently reducing the secondary flow levels. The main concern of this configuration is the still high leakage swirl component that increases the windage loss near the endwall.

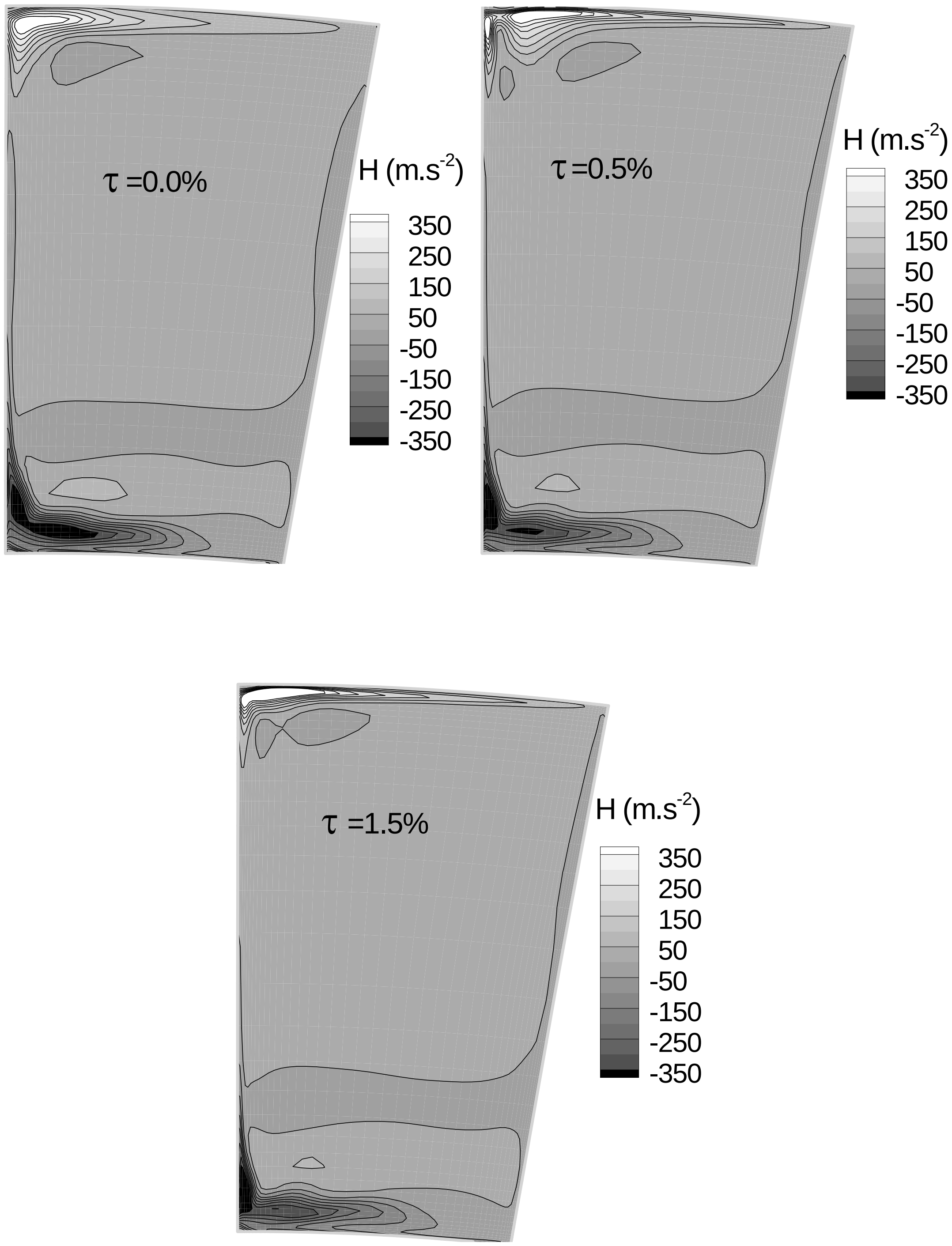

Fig. 6-59 Helicity iso-levels in a plane at 50% of the axial chord within the blade passage.

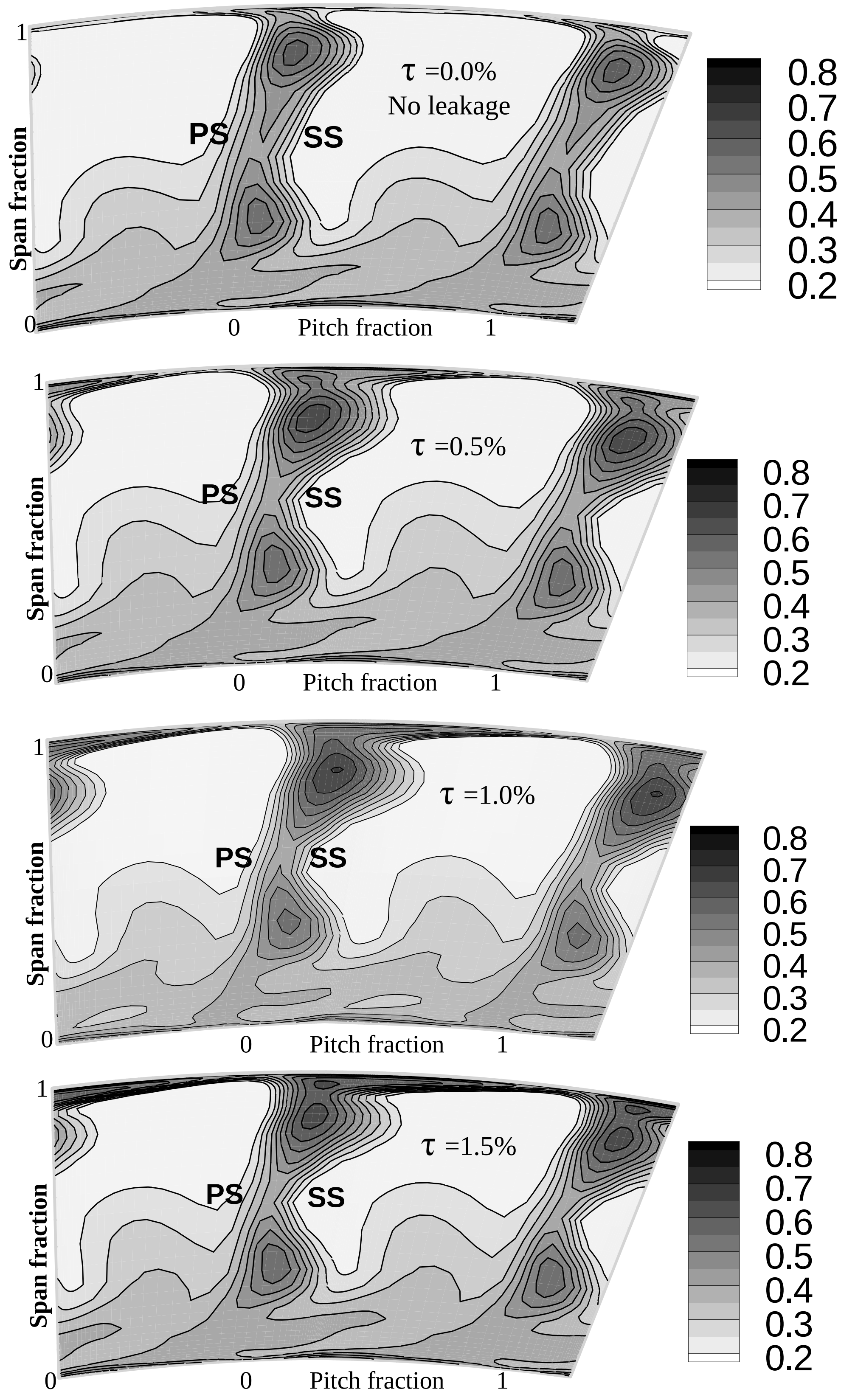

Fig. 6-60 the stagnation pressure loss iso-levels downstream of the rotor exit at 120% axial chord for different gap clearance ratio.

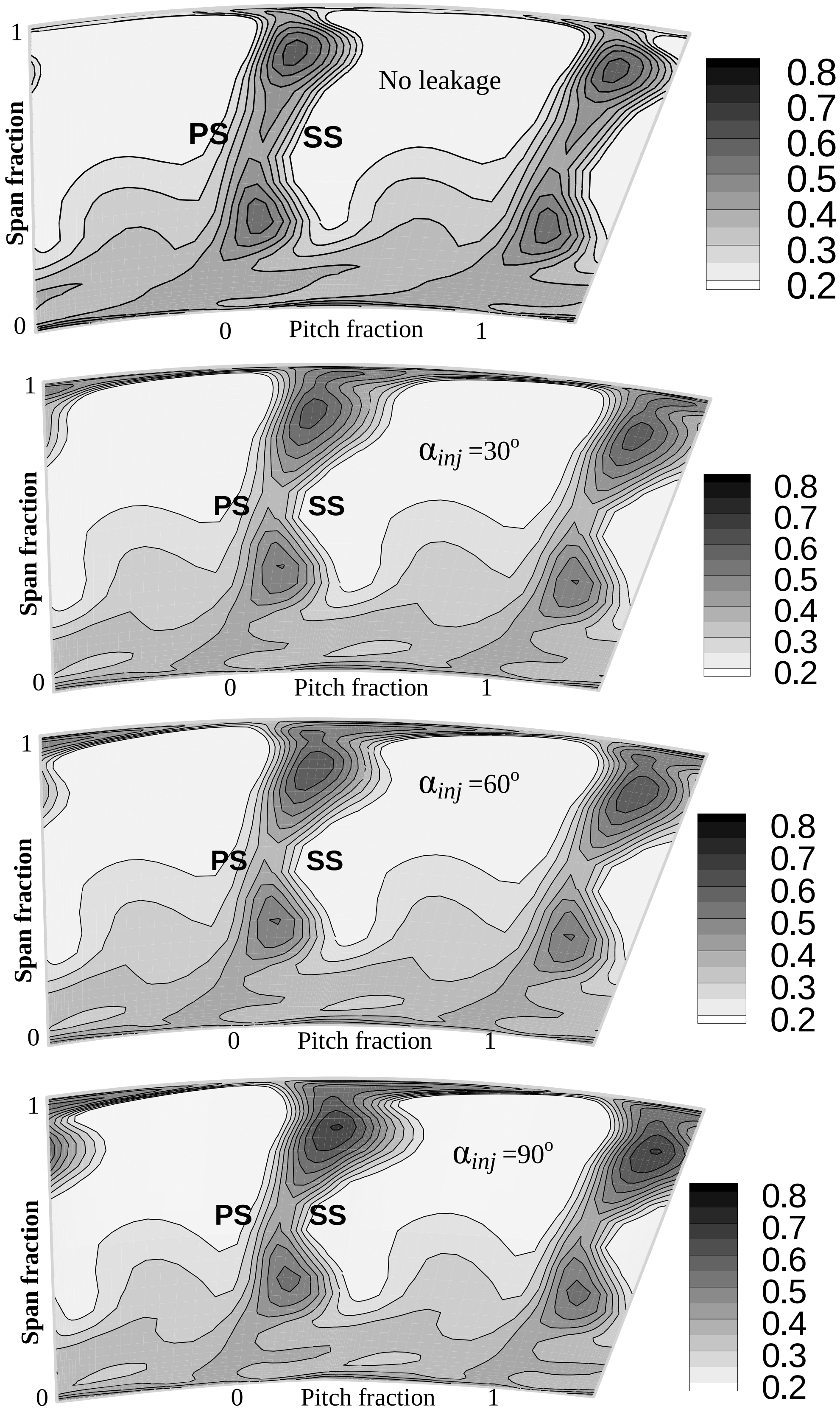

Fig. 6-61 the stagnation pressure loss iso-levels downstream of the rotor exit at 120% axial chord for different injection angle.

6-5.2 The effect on the rotor loss generation

Figures 6-62 and 6-63 show the penetration depth and the loss added by the mixing process of the leakage jet with the main stream at different gap clearance ratio (fig. 6-62) and injection angles (fig. 6-63). The entropy function is calculated using the mass averaged flow properties. The results of fig. 6-62 confirm that, as the clearance gap ratio increases, the leakage jet strength increases and consequently the penetration depth and levels of entropy generation increase. By increasing the gap clearance ratio form 0.5% to 1.5%, the area affected by mixing loss downstream of the cavity exit is doubled. The maximum level of loss downstream of the cavity is predicted at the exit cavity intersection with the endwall for the 1.0% and 1.5% cases. In the case of the lowest gap clearance ratio, $\tau = 0.5\%$, the levels of the entropy function inside the cavity show that the cavity fluid mixes out most of the leakage jet due to insufficient leakage flow to overcome the cavity dynamics, as reported by Rosic et al [2007]. This early mixing process dissipates the bundle structure of the jet and causes a significant reduction in the secondary flow downstream. On the other hand, the high leakage flow fraction of the $\tau = 1.0\%$ and $\tau = 1.5\%$ cases exits the cavity without suffering from any significant premixing, therefore it pushes the low momentum fluid radially downward causing a merging between the passage and leakage loss cores and consequently enhances the secondary flow.

Figure 6-63 shows that redirecting of the leakage jet flow reduces the jet penetration into the main passage and prevents the radial migration of the low momentum flow towards the centre of the main passage. This reduces the loss core and gives a more spanwise uniform out flow that benefits the downstream blade row performance and consequently the secondary flow downstream. Once again, the shallow leakage jet injection angle gives a higher windage loss generated by the swirl component higher near the endwall.

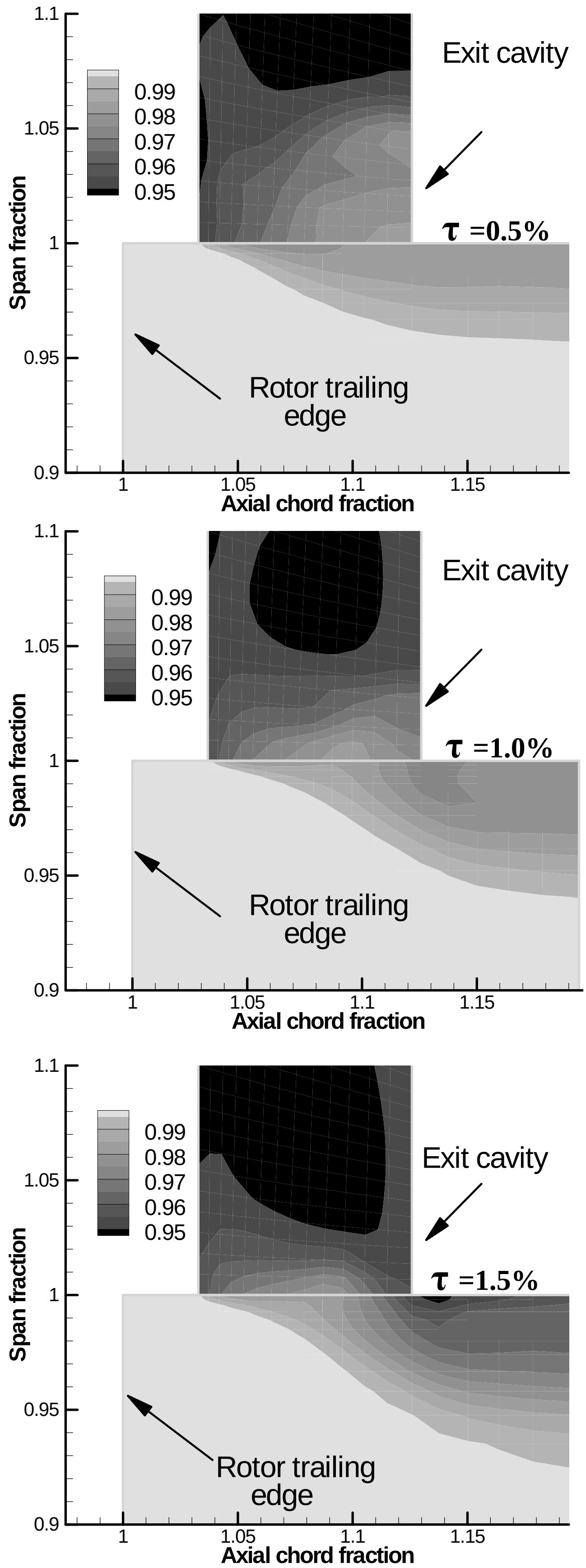

Fig. 6-62 the entropy function iso-levels in the mixing area at different gap clearance ratio.

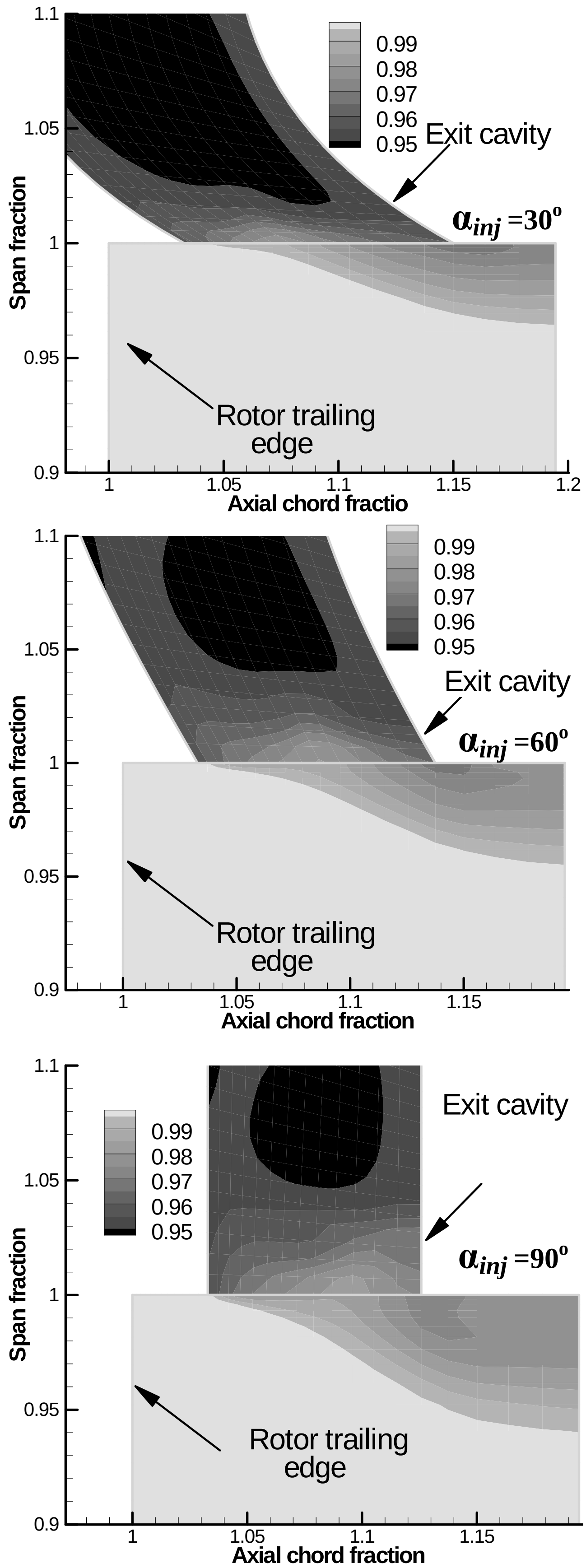

Fig. 6-63 the entropy function iso-levels in the mixing area at different injection angle.

Figures 6-64 to 6-66 quantify the reduction in the mixing loss due to using the leakage fraction controllers (i.e. the number of labyrinth fins and the gap clearance ratio) and radial velocity controller (i.e. the injection angle). These figures show the distribution of the mass averaged stagnation pressure loss coefficient just before the exit cavity and downstream of the mixing area. Figure 6-64 shows that increasing the number of fins decreases the mixing loss. This figure shows that the effectiveness of increasing the number of fins to reduce the leakage flow mixing loss decreases as the fin number increases. Figure 6-65 indicates that the mixing loss decreases as the gap clearance decreases. The gap clearance ratio can be reduced up to a certain limit specified by the mechanical constraints. The reduction in the injection angle reduces the mixing loss as shown in fig. 6-60. However, a local increase of stagnation loss coefficient occurs near the endwall, due to the swirl component of the leakage jet as its injection angle decreases.

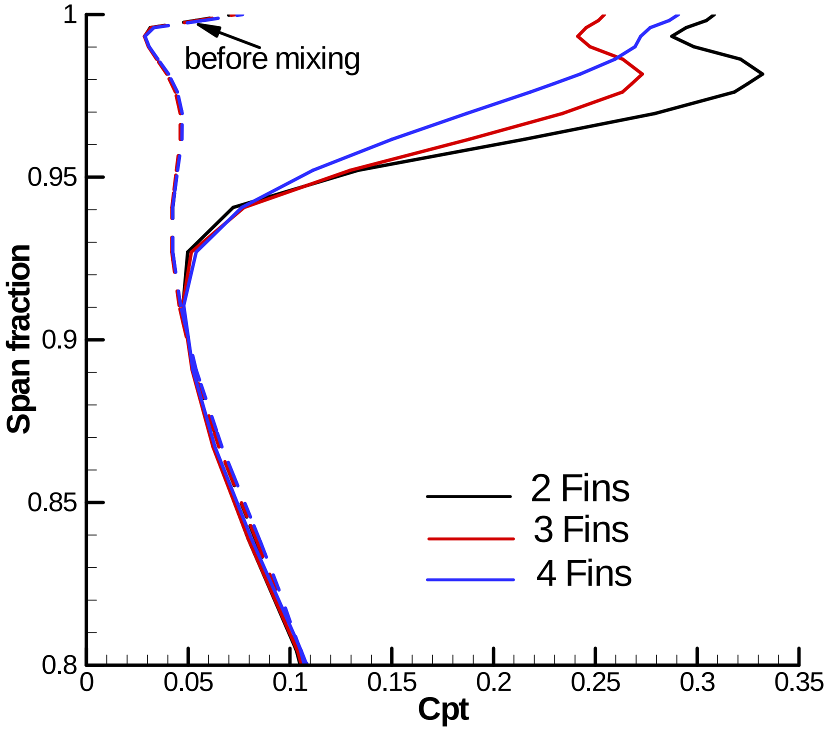

Fig. 6-64 The mass averaged stagnation pressure loss coefficient upstream (dashed lines) and downstream (solid lines) of the exit cavity for different number of fins.

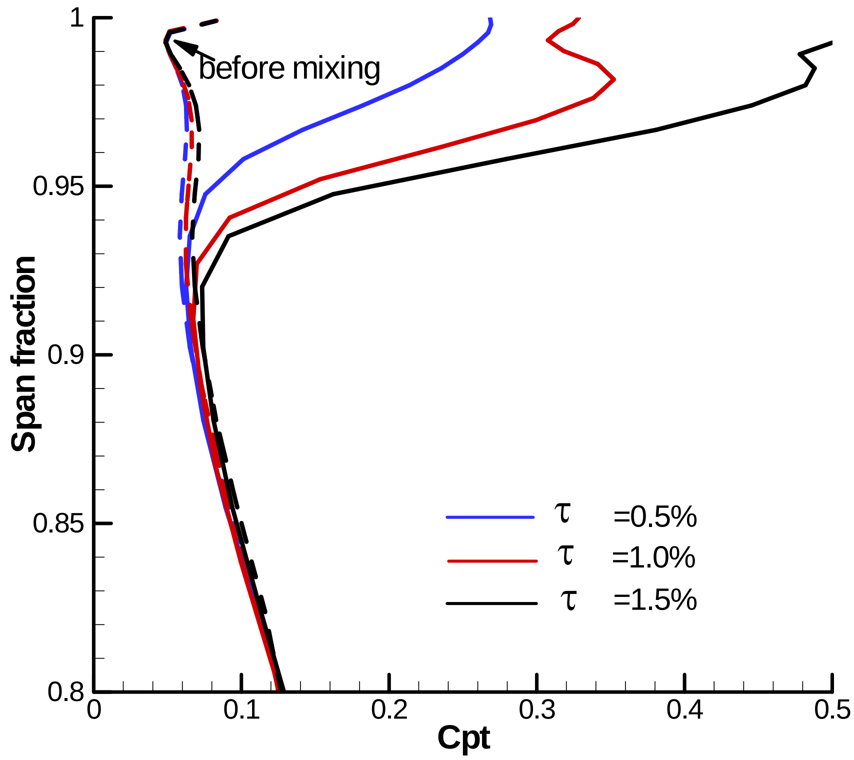

Fig. 6-65 The mass averaged stagnation pressure loss coefficient upstream (dashed lines) and downstream (solid lines) of the exit cavity for different gap clearance ratio.

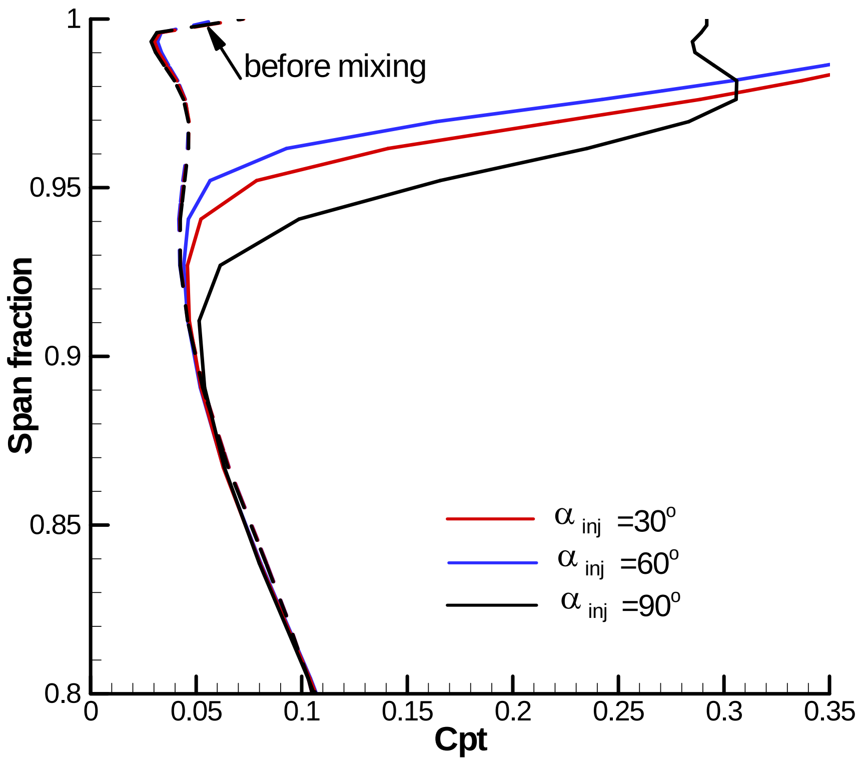

Fig. 6-66 The mass averaged stagnation pressure loss coefficient upstream (dashed lines) and downstream (solid lines) of the exit cavity for different injection angle.

6-5.3 The effect on the rotor flow angles

The leakage jet not only affects the main passage flow by generating losses and enhancing the secondary flow but also induces an incidence angle affecting the downstream blade row. The relative and absolute flow angles at the rotor exit are shown in figs. 6-67 and 6-68. The flow angle are pitchwise mass averaged at 120% axial chord. The flow angles are compared with the flow angles for the reference case with clean endwall. The results in figs. 6-67 and 6-68 indicate that the underturning caused by the leakage jet reduces as the gap clearance decreases and consequently the negative incidence angle decreases, which leads to decrement of the secondary flow loss in the downstream blade row. The effects of the injection angle on the relative and absolute flow angles at the rotor exit are given in figs. 6-69 and 6-70 respectively. These figures show that reducing the injection angle from 90^o to 30^o decreases the underturning in the top 10% of the span and the turning angle approaches the reference case. The decrease in negative incidence angle induced by the swirl component of the leakage flow can be confirmed by comparing the normalized absolute velocity at the rotor exit for the no leakage case, the maximum leakage fraction case, and the 30^o injection angle case. This comparison is given in fig. 6-71. This figure shows the absolute velocity iso-levels normalized by the mid-blade circumferential speed. In case of a large clearance gap, $\tau = 1.5\%$, the leakage mass fraction is high. This increases the absolute velocity near the endwall due to the leakage jet interaction with the main passage flow. This increase causes a high suction side negative incidence angle in the tip region of the subsequent blade row. In the case of using a 30^o injection angle, the absolute velocity iso-levels seem to be similar to the no leakage case, which indicates that a small incidence angle is induced by the leakage jet. Another benefit when using the 30^o injection angle is the reduction of the radial migration of the low momentum fluid by the leakage jet from the casing endwall towards the mid-span since the leakage flow penetrates less radially downwards near the suction side. This prevents the slow down of the wake flow occurred in 90^o test case. This slow flow on the suction side causes a flow blockage near the rotor tip region. Figure 6-72 shows the comparison of the relative velocity iso-levels at 0.95% of the span normalized by the mid-blade circumferential speed for the same three cases stated above. The no leakage flow iso-levels near the trailing edge suction side are clustered around the trailing edge and align approximately with the blade exit angle. The relative velocity iso-levels at $\tau = 1.5\%$, where a substantial leakage flow is injected from a 90° cavity, the suction side trailing edge contours spread towards the centre of the blade to blade passage. This confirms the presence of flow blockage near the trailing edge suction side. With the $\alpha_{inj} = 30^o$ shallower injection angle, the iso-levels re-cluster close to the trailing edge suction side, similarly to the no leakage results. This indicates that the 30° injection angle case removes the near-wall blockage that arises in the 90° exit cavity case.

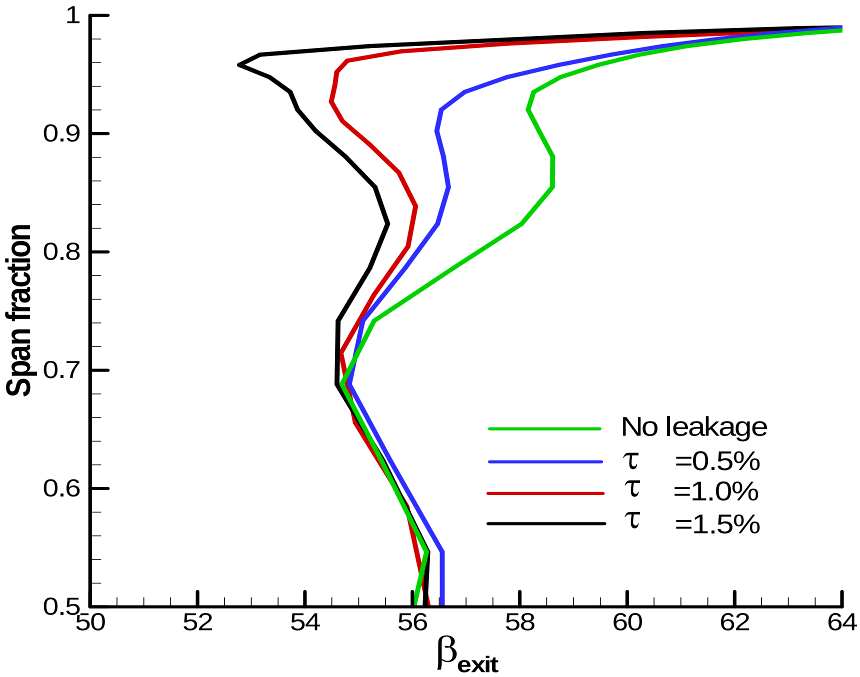

Fig. 6-67 the mass averaged relative flow angle at the rotor exit for different gap clearance ratios.

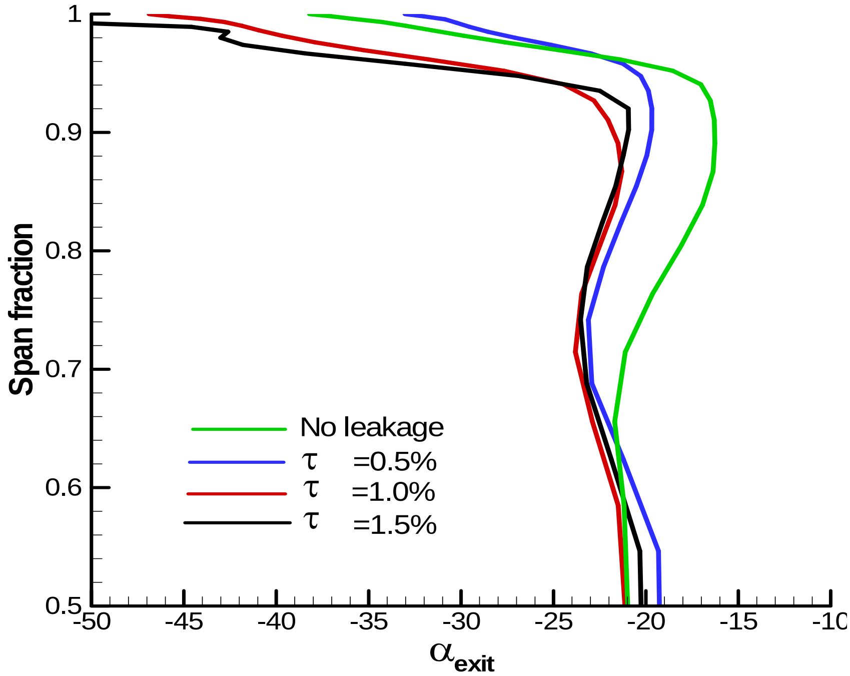

Fig. 6-68 the mass averaged absolute flow angle at the rotor exit for different gap clearance ratio.

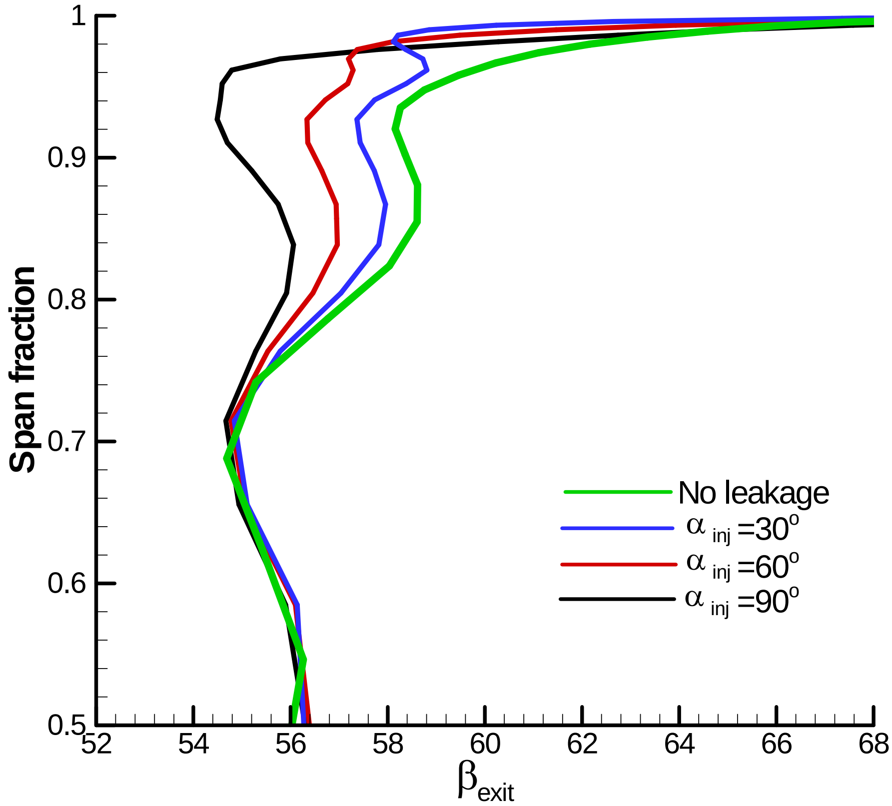

Fig. 6-69 the mass averaged relative flow angle at the rotor exit for different injection angles.

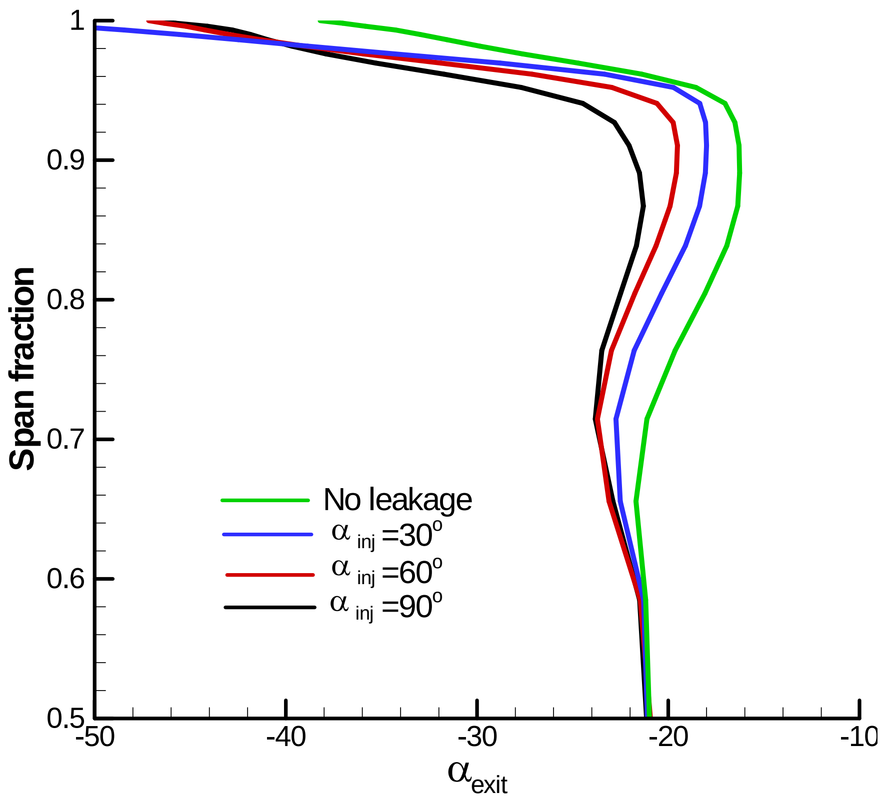

Fig. 6-70 the mass averaged absolute flow angle at the rotor exit for different injection angles.

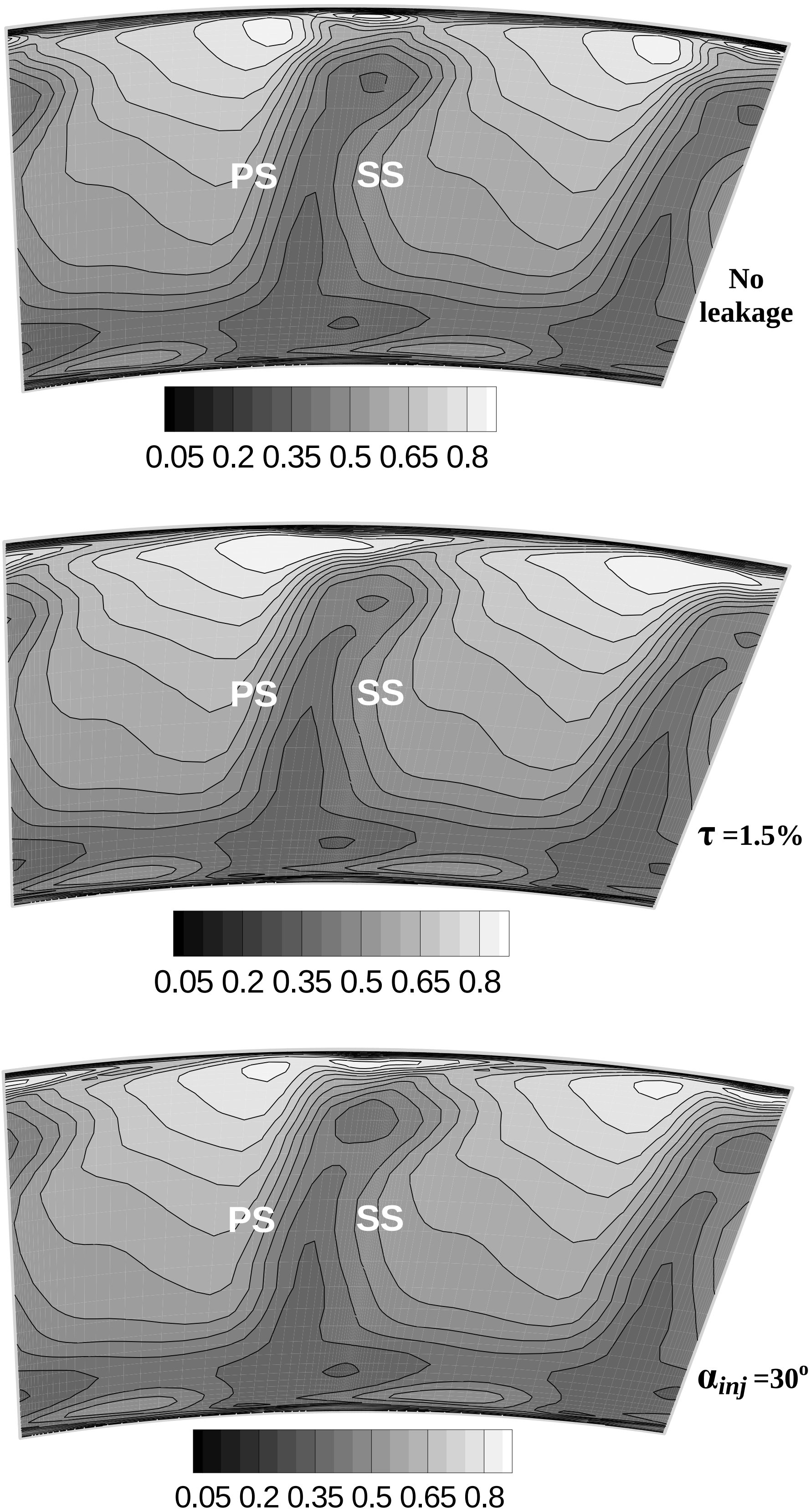

Fig. 6-71 Normalized absolute velocity contours, $|\boldsymbol{u}|/0.5\omega D_m$, at the rotor exit.

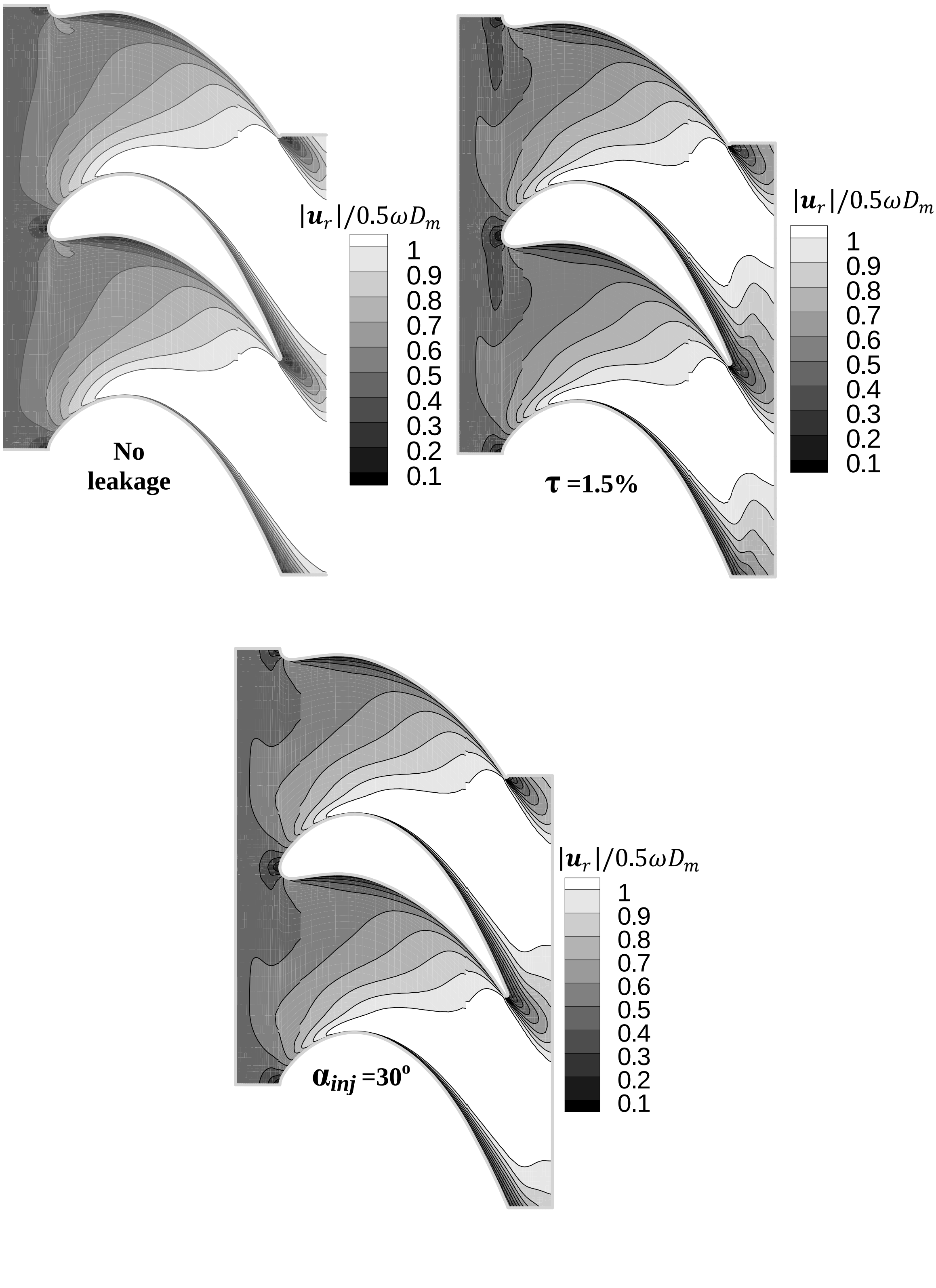

Fig. 6-72 Normalized relative velocity contours at 0.95% of the span.

Chapter 7

Conclusions

An analytical model of leakage flow loss over a shrouded turbine stage has been developed to predict the effect of some of the over shroud design parameters on stage performance.

An in-house three-dimensional turbomachinery CFD code was developed, validated, and used to predict the flow through a shrouded turbine rotor.

This work therefore met the main objectives stated in chapter 1.

Chapter 7 summarises the conclusions from the analytical model, the CFD flow solver validation, and the over-shroud leakage predictions and makes suggestions for further research.

7-1 The analytical model

Chapter 3 presented an analytical model that uses directly measurable flow quantities to predict the effects of over-shroud leakage on shrouded turbine stage performance. The model displays a good predictive ability for the mass leakage fraction and for the tip leakage and the mixing losses. The model resolves the negative incidence angle induced by mixing the leakage flow with the main stream and predicts the increment in the total mixing loss coefficient at increasing leakage jet injection angles. Modelling the injection angle effect on the stage performance by a simple parametrical approach is a new feature for the over-shroud leakage jet models documented in the open literature and contributes to the state of the art in this field. The second contribution comes from linking the mass leakage fraction through the labyrinth seal with the number of fins in an explicit way. The effects of the labyrinth seal geometry, such as the tip gap width and the number of seals, on the associated leakage losses as well as on the turbine stage performance are adequately represented. Overall, the present model exhibits a good qualitative and quantitative agreement with comparative benchmark data. It is concluded that

- Increasing the labyrinth through-flow resistance by increasing the number of fins leads to a decrement in the leakage flow and its adverse effects but the effectiveness of this reduction decreases as the number of fins increases by more than three.

- The mass leakage fraction and total mixing loss coefficient increase linearly as the sealing gap ratio increases.
- The negative incidence angle induced by the mixing process increases as the tip gap width increases.
- A conventional injection angle of 90^o increases the total mixing loss by about 28% compared to injecting parallel to the main passage flow.

7-2 The CFD flow solver validation

An in-house three-dimensional turbomachinery CFD code has been developed and validated to address the leakage flow through a shrouded turbine rotor. The flow solver underwent an extensive validation against inviscid and viscous test cases before it was applied to model a shrouded turbine rotor.

For the inviscid cases, the flow solver captured the compressible flow characteristics of these cases, such as rarefaction waves, shock waves, and expansion fans, predicting their location reasonably well compared to relevant analytical and numerical solutions.

For the viscous cases, the flow solver has been validated against one test case in a fixed frame of reference and two test cases in a rotating frame of reference. The first test case was a wing-body junction flow. The flow solver captured salient characteristics of this complex flow with reasonable accuracy and the prediction were in good agreement with the ERCOFTAC data base reference measurements. The second test case is the turbulent flow in a stationary and rotating square duct. In the stationary duct case, the flow solver captured the secondary duct flow of the second kind as denoted by Prandtl. In the rotating duct case, the Prandtl secondary flow of the first kind generated by the effect of the Coriolis force was reproduced. The square duct simulations have shown a good agreement with the available DNS and LES reference results. The third viscous test case is an unshrouded axial turbine rotor cascade. This was modelled at the same non-dimensional flow conditions as the shrouded turbine rotor, which is the main CFD test case of this study. The comparison with the experimental data has shown a reasonable agreement, concluding the validation of the in-house CFD code for 3D turbomachinery rotor studies.

The unshrouded axial turbine rotor cascade test case demonstrated the unconventional use of Detached Eddy Simulation (DES) to model a steady turbulent flow. Specifically, DES has been used as an advanced Reynolds Averaged Navier-Stokes (RANS) model, which is an unconventional and innovative use of DES, highlighting salient passage flow features.

7-3 The over-shroud leakage predictions

This part of the study simulated the leakage flow over a shrouded turbine stage, its interaction with the main passage flow, and the associated losses. Seven cases were modelled to study the effect of the number of fins, the clearance gap ratio, and the leakage jet injection angle on the flow. In addition to these cases, a reference case with zero mass leakage fraction and a clean end wall was simulated for comparison purposes. The following conclusions can be drawn from the analysis of the computational results:

The aerodynamic losses associated with the leakage flow are highly influenced by the geometrical parameters of the labyrinth seal. A positive linear trend between the mass leakage fraction and the gap clearance ratio is confirmed. Increasing the number of fins gives approximately the same decay rate in the mass leakage fraction as in the analytical model. The mixing loss coefficient varies linearly with the gap clearance and decreases considerably by reducing the leakage jet injection angle. The reduction of the leakage jet injection angle from 90^o to 30^o can increase the rotor efficiency by 0.2% and reduce the entropy mixing loss by 24.7%. To reduce the recovery pressure after the last throttling fin and consequently reduce the mass leakage fraction, the pressure distribution through the labyrinth seal suggests that the optimal location for the last fin is near the shroud trailing edge. This position of the last fin reduces also the windage loss caused by the swirl component, since the contact length between the leakage jet and the shroud is reduced. The details of the inlet and exit flow structure give an insight into the loss mechanisms and the leakage jet interaction with the main flow.

At low leakage mass fractions, the leakage jet gets almost mixed out inside the exit cavity with the main passage inflow near the blade pressure side, then re-enters the main passage near the blade suction side, which leads to a significant reduction in mixing loss. By increasing the leakage mass fraction, the mixing of the leakage jet inside the exit cavity decreases. At high leakage mass fractions, the leakage jet leaves the exit cavity approximately unmixed, which increases the mixing loss and enhances the secondary flow upstream of the subsequent blade row. The leakage mass flow through the inlet cavity removes some of the rotor inflow boundary layer, preventing this slow fluid from entering the rotor passage. This leads to a reduction in the casing passage vortex at high clearance ratios. As the leakage mass fraction increases, the positive effect of the boundary layer removal increases, however the net secondary flow in the subsequent blade row increases due to the interaction between this strong leakage jet and the main passage flow. The 90^o degree leakage jet with circumferentially non-uniform injection pushes the low momentum fluid from the endwall towards the mid-span passage near the blade suction side, causing a further deceleration for the rotor trailing edge wake that results in the blockage of the main passage flow on the suction side, near the tip. Also, the radial injection causes a flow separation at the shroud cavity downstream corner, which leads to the thickening of the boundary layer and enhances the secondary flow in the downstream blade row. Both effects of the 90^o injection angle cause a radial shift in the mass flow distribution.

The leakage flow over the shroud keeps its swirl component since it does not do any work. The high swirl component of the leakage flow mixing with the turned flow through the rotor causes a negative incidence angle that affects the downstream blade row. At the moderate leakage mass fraction, as in test case 1 of table 6-2, the shroud exit cavity shows an inflow from the main passage close to the shroud trailing edge near the blade pressure side. This flow re-enters with the leakage jet close to the shroud casing near the blade suction side, adding a sheet of streamwise vorticity to the passage vortex near the blade trailing edge tip.

Controlling the radial component of the leakage flow by reducing the injection angle appears to be a promising concept to control most of the adverse effects of the leakage flow as summarized below:

- Reducing the injection form 90^o to 30^o leads to a reduction in entropy mixing loss coefficient by up to 24.7% and this reduction gives a 0.2% increase in the rotor static to static efficiency. This efficiency gain is expected to increase with further decrements in the leakage injection angle.

- By using a 30^o injection angle, the negative incidence angle induced by the leakage jet mixing with the main passage flow and the relative helicity (secondary flow marker) decrease.
- The blockage effect on the suction side due to the radial injection and its transport of the endwall boundary layer fluid radially downward decrease as the injection angle decreases.
- By using a 30^o injection angle, the flow separation downstream of the exit cavity is approximately eliminated.

7-4 Further research recommendations

- The CFD prediction can be further improved by performing a time-resolved simulation of the whole stage.
- The effect of the stator-rotor interaction and the wake transport through the stage can be addressed as this is a known source of loss.
- Further CFD research can investigate the control of the swirl component by using turning blades installed at the exit cavity, to align the leakage flow with the main passage flow. This concept can lead to a reduction in the incidence angle, affecting the downstream blade row.
- Other types of labyrinth can be considered, with features such as shroud leading and trailing edge protrusion.
- The non-uniform leakage flow injection at the exit cavity can be controlled by increasing the resistance near the suction side, using, for instance, a non-axisymmetry exit cavity opening.

References

Adamczyk, J. J. (1985) "Model Equation for Simulating Flows in Multistage Turbomachines," *Paper 85-GT-226, ASME*.

Adjlout, L., and Dixon, S. L. (1992) "Endwall Losses and Flow Unsteadiness in a Turbine Blade Cascade," *Trans. ASME, J. Turbomachinery*, Vol. 114, pp. 191-197.

Anker, J. E., Mayer, J. F., and Casey, M. V. (2005) "The Impact of Rotor Labyrinth Seal Leakage Flow on the Loss Generation in an Axial Turbine," Proc. IMechE, Vol. 219, Part A: J. Power and Energy.

Apsley, D. D., and Leschziner, M. A. (2001) "Investigation of Advanced Turbulence Models for the Flow in a Generic Wing-Body Junction," *Flow Turb. Combust.*, Vol. 67, pp. 25-55.

Arnone, A., and Pacciani, R. (1995) "Rotor-Stator Interaction Analysis Using the Navier–Stokes Equations and a Multigrid Method," *Paper 95-GT-117, ASME*

Aunapu, N. V., Volino, R. J., Flack, K. A., and Stoddard, R. M. (2000) "Secondary Flow Measurements in a Turbine Passage With Endwall Flow Modification," *J. Flow Measures and instrumentation*, Vol. 122, pp. 651-658.

Belhoucine, L., Deville, M., Elazehari, A.R., Bensalah, M.O. (2004) "Explicit Algebraic Reynolds Stress Model of Incompressible Turbulent Flow in Rotating Square Duct," *Comput. Fluids*, Vol. 33, pp. 179–199.

Benner, M. W., Sjolander, S. A., and Moustapha, S. H. (2004) "The Influence of Leading-Edge Geometry on Secondary Losses in a Turbine Cascade at the Design Incidence," *Trans. ASME, J. Turbomachinery*, Vol. 126, pp. 277-287.

Bennett, W. P. (2005) "A Time Accurate Computational Analysis of Two-Dimensional Wakes," *PhD Thesis, University of Leicester*.

Binder, A., Forster, W., Mach, K., and Rogge, H. (1987) "Unsteady Flow Interaction Caused by Stator Secondary Vortices in a Turbine Rotor," *Trans. ASME, J. Turbomachinery*, Vol. 109, pp. 251-257.

Binder, A., Schroeder, T., and Hourmuziadis, J. (1989) "Turbulence Measurements in a Multistage Low-Pressure Turbine," *Trans. ASME, J. Turbomachinery*, Vol. 111, pp. 153-161.

Bindon, J. P., and Morphis, G. (1992) "The Development of Axial Turbine Leakage Loss for Two Profiled Tip Geometries Using Linear Cascade Data," *Trans. ASME, J. Turbomachinery*, Vol. 114, pp. 198-203.

Blazek, J. (2001) *Computational Fluid Dynamics: Principles and Applications*: Elesevier.

Brear, j., Hodson, H., Gonzalez, P., and Harvey, N. W. (2002) "Pressure Surface Separations in Low-Pressure Turbines Part I: Midspan Behavior," *Trans. ASME, J. Turbomachinery*, Vol. 124, pp. 393-401.

Brear, j., Hodson, H., Gonzalez, P., and Harvey, N. W. (2002) "Pressure Surface Separations in Low-Pressure Turbines Part II: Interaction With the Secondary Flow," *Trans. ASME, J. Turbomachinery*, Vol. 124, pp. 402-409.

Chaluvadi, V. S. P. (2000) "Blade - Vortex Interactions in High Pressure Steam Turbines," *PhD thesis, University of Cambridge*.

Chaluvadi, V. S. P., Kalfas, A., I., Hodson, H., P., Ohyama, H., and Watanabe, E. (2003) "Blade Row Interaction in a High Pressure Steam Turbine," *J. Flow Measures and instrumentation*, Vol. 125, pp. 14-24.

Chaluvadi, V. S. P., Kalfas, A., I., and Hodson, H., P. (2004) "Vortex Transport and Blade Interactions in High Pressure Turbines," *Trans. ASME, J. Turbomachinery*, Vol. 126, pp. 395-405.

Chernobrovkin, A., and Lakshminarayana, B. (1999) "Turbulence Modeling and Computation of Viscous Transitional Flows for Low Pressure Turbines," *J. Fluid Mech.*, Vol. 121, p 824.

Chima, R. V. (1998) "Calculation of Multistage Turbomachinery Using Steady Characteristic Boundary Conditions," *Paper 98-0968, AIAA*.

Dahlström, S., and Davidson, L. (2003) "Hybrid RANS/LES Employing Interface Condition with Turbulent Structure," *Turbulence Heat and Mass Transfer*, Vol. 4, pp. 689-696.

Dawes, W. N. (1990) "Towards Improved Throughflow Capability: The Use of Viscous Flow Solvers in a Multistage Environment," *Paper 90-GT-18, ASME*

Denecke, J., Schramm, V., Kim, S., and Witting, S. (2003) "Influence of Rub-Grooves on Labyrinth Seal Leakage," *Trans. ASME, J. Turbomachinery*, Vol. 125, pp. 387-393.

Denton, J., and Johnson, C. (1976) "Measurements of the Flow Around a Turbine Rotor Tip Seal," *ACR34406*.

Denton, J., and Johnson, C. (1976) "Tip Leakage Loss of Shrouded Turbine Blades," *CEGB Report R/M/N848*.

Denton, J. D. (1983) "An Improved Time Marching Method for Turbomachinery Flow Calculations," *Trans. ASME, J. Eng. for Power*, Vol. 105, pp. 514-524.

Denton, J. D. (1990) "The Calculation of Three Dimensional Viscous Flow Through Multistage Turbomachines," *Paper 90-GT-19, ASME*.

Denton, J. D. (1992) "The Calculation of Three-Dimensional Viscous Flow Through Multistage Turbomachines," *Trans. ASME, J. Turbomachinery*, Vol. 114, pp. 18-26.

Denton, J. D. (1993) "Loss Mechanisms in Turbomachines," *Trans. ASME, J. Turbomachinery*, Vol. 115, pp. 621-656.

Devenport, W. J., and Simpson, R. L. (1990) "Time-Dependent and Time-Averaged Turbulence Structure Near the Nose of a Wing-Body Junction," *J. Fluid Mech.*, Vol. 210, pp. 23-55.

Dishart, P. T., and Morre, J. (1990) "Tip Leakage Losses in a Linear Turbine Cascade," *Trans. ASME, J. Turbomachinery*, Vol. 112, pp. 599-608.

Dutta, S., Anderson, M., Han, J.C. (1996) "Prediction of Turbulent Heat transfer in Rotating Smooth Square Ducts," *Int. J. Heat Mass Transfer*, Vol. 39, pp. 2505–2514.

Eckerle, W. A., and Awad, J. K. (1991) "Effect of Free Stream Velocity on the Three-Dimensional Separate Flow Region in Front of a Cylinder," *Trans. ASME, J. Fluids Engineering*, Vol. 113, pp. 37-44.

Egli, A. (1935) "The Leakage of Steam Through Labyrinth Seals," *Trans. ASME*, Vol. 57, pp. 115-122.

El-Dosoky, M. F., Rona, A., and Gostelow, J. P. (2007) "An Analytical Model for Over-Shroud Leakage Losses in a Shrouded Turbine Stage," *Paper GT2007-27786, ASME*

Emunds, R., Jennions, I. K., Bohn, D., and Gier, J. (1999) "The Computation of Adjacent Blade-Row Effects in a 1.5-Stage Axial Flow Turbine," *Trans. ASME, J. Turbomachinery*, Vol. 121, pp. 1-10.

Fleming, J. L., Simpson, R. L., Cowling, J. E., and Devenport, W. J. (1993) "An Experimental Study of a Turbulent Wing-Body Junction and Wake Flow," *Exp. Fluids*, Vol. 14, pp. 366-378.

Fridh, J. A. (2002) "Experimental Configurations and Partial Admission," *Tech. rep. 2003-4767, SNEA project P12457-2*.

Fu, S., Xiao, Z., Chen, H., Zhang, Y., and Huang, J. (2007) "Simulation of Wing-Body Junction Flows With Hybrid RANS/LES Methods," *Int. J. Heat and Fluid Flow*, Vol. 28, pp. 1379-1390.

Gallus, H. E., Zeschky, J., and Hah, C. (1995) "Endwall and Unsteady Flow Phenomena in an Axial Turbine Stage," *Trans. ASME, J. Turbomachinery*, Vol. 117, pp. 562-570.

Gavrilakis, S. (1992) "Numerical Simulation of Low-Reynolds Number Turbulent Flow Through a Straight Square Duct.," *J. Fluid Mech.*, Vol. 244, pp. 101-129.

Gbadebo, A. S., Cumpsty, A. N., and Hynes, P. T. (2006) "Interaction of Tip Clearance Flow and Three-Dimensional Separations in Axial Compressors," *Paper GT2006-90071, ASME*.

Geir, J., Stubert, B., Brouillet, B., De Vito, L. (2003) "Interaction of Shroud Leakage Flow and Main Flow in a Three-Stage LP Turbine," *Paper GT-2003-38025, ASME*.

Giles, M. B. (1988) "Stator/Rotor Interaction in a Transonic Turbine," *Paper 88-3093, AIAA*

Giles, M. B. (1990) "Nonreflecting Boundary Conditions for Euler Equation Calculations," *AIAA J.*, Vol. 28, pp. 2050-2058.

Goldstein, R. J., and Spores, R. A. (1988) "Turbulent Transport on the Endwall in the Region Between Adjacent Turbine Blades," *Trans. ASME, J. Heat Transfer*, Vol. 110, pp. 862-869.

Gregory-Smith, D. G., and Graves, C. P. (1983) "Secondary Flows and Losses in a Turbine Cascade ": AGARD-CP-351.

Gregory-Smith, D. G., and Cleak, J. G. E. (1992) "Secondary Flow Measurements in a Turbine Cascade with High Inlet Turbulence," *Trans. ASME, J. Turbomachinery*, Vol. 114, pp. 173-183.

Griffin, P. C., and Davies, M. R. D. (2004) "'Aerodynamic Entropy Generation Rate in a Boundary Layer With High Free Stream Turbulence," *Trans. ASME, J. Fluids Engineering*, Vol. 126, pp. 700-703.

Hall, E. J. (1997) "Aerodynamic Modeling of Multistage Compressor Flow-fields," *Paper 97-GT-344, ASME*

Harrison, S. (1990) "Secondary Loss Generation in a Linear Cascade of High-Turning Turbine Blades," *Trans. ASME, J. Turbomachinery*, Vol. 112, pp. 618-624.

Harrison, S. (1992) "The Influence of Blade Lean on Turbine Losses," *Trans. ASME, J. Turbomachinery*, Vol. 114, pp. 184-190.

Harten, A. (1983) "High Resolution Schemes for Hyperbolic Conservation Laws," *J. Comp. Phys.*, Vol. 49, pp. 357-393.

Harten, A., and Hyman, J. M. (1983) "Self Adjusting Grid Methods for One-Dimensional Hyperbolic Conservation Laws," *J. Comp. Phys.*, Vol. 50, pp. 235-269.

Hartland, J. C., Gregory-Smith, D. G., Harvey, N. W., and Rose, M. G. (2000) "Nonaxisymmetric Turbine End Wall Design: Part II- Experimental Validation," *Trans. ASME, J. Turbomachinery*, Vol. 122, pp. 286-293.

Harvey, N. W., Rose, M G., Taylor, M D., Shahpar, S., Hartland, J., and Gregory-Smith, D. G. (2000) "Nonaxisymmetric Turbine Endwall Design: Part I - Three-Dimensional Linear Design System," *Trans. ASME, J. Turbomachinery*, Vol. 122, pp. 278-285.

Harvey, N. W., Ramsden, K. (2001) "A Computational Study of a Novel Turbine Rotor Partial Shroud," *Trans. ASME, J. Turbomachinery*, Vol. 123, pp. 534-543.

Hawthrone, W. R. (1955) "Rotational Flow Through Cascades," *J. Mech. and Applied Math.*, Vol. Vol. 3.

Hellsten, A. (1998) "Some improvements in Menter's k-ω SST turbulence model," *Paper 98-2554, AIAA*

Helmers, L., Johnsson, R., and Trolheden,S. (2003) "'Modelling Turbine Performance at Large Tip Clearance of Unshrouded Rotor Cascades," *Paper 2003-4767, AIAA*.

Hermanson, K., S., and Thole, K., A. (2002) "Effect of Nonuniform Inlet Conditions on Endwall Secondary Flows," *Trans. ASME, J. Turbomachinery*, Vol. 124, pp. 623-631.

Heyes, F. J. G., Hodson, H. P., and Dailey, G. M. (1992) "The Effect of Blade Tip Geometry on the Tip Leakage Flow in Axial Turbine Cascades," *Trans. ASME, J. Turbomachinery*, Vol. 114, pp. 643-651.

Hirsch, C. (1990) *Numerical Computation of Internal and External Flows Vol. 2*: Wiley Series in Numerical Methods in Engineering.

Hodson, H. P., Howell, R. J. (2005) "Blade Row Interactions, Transition, and High-Lift Aerfoils in Low-Pressure Turbine," *Annu. Rev. Fluid Mech.*, pp. 71-98.

Hodson, H. P., and Dominy, R. G. (1987) "The Off-Design Performance of a Low-Pressure Turbine Cascade," *Trans. ASME, J. Turbomachinery*, Vol. 109, pp. 201-209.

Horlock, J. H. (1966) *Axial flow turbines: fluid mechanics and thermodynamics*: Butterworths.

Huser, A., and Biringen, S. (1993) "Direct Numerical Simulation of Turbulent Flow in a Square Duct," *J. Fluid Mech.*, Vol. 257, pp. 65-95.

Ince, N. (2008) "Steady simulation of 1.5-StageAxial Flow Turbine": Private communication.

Ingram, G., Gregory-Smith, D., and Harvey, N. (2005) "Investigation of a Novel Secondary Flow Feature in a Turbine Cascade With End Wall Profiling," *J. Flow Measures and instrumentation*, Vol. 127, pp. 209-214.

Jakirlić, S., and Hanjalić, K. (1995) "A Second Moment Closure for Non-Equilibrium and Separating High and Low-Re Number Flows," *Proceedings of 10th Symposium on Turbulent Shear Flows, Pennsylvania State University*, pp. 23.25–23.30.

Jones, D. A., and Clarke, D. B. (2005) "Simulation of a Wing-Body Junction Experiment using the Fluent Code," *DSTO-TR-1731*.

Jorgensen, P. C. E., and Chima, R. V. (1989) "An Unconditionally Stable Runge-Kutta Method for Unsteady Flows," *NASA TM 101347*.

Jorgeson, P. C. E., and Chima, R. (1988) "An Explicit Runge–Kutta Method for Unsteady Rotor/Stator Interaction," *Paper 88-0049, AIAA*

Kermani, M. J., and Plett, E. G. (2001) "Modified Entropy Correction Formula for the Roe," *Paper 2001-0083, AIAA*

Klein, A. (1966) "Investigation of the Entry Boundary Layer on the Secondary Flows in the Blading of Axial Turbines," *BHRAT 1004*.

Kopper, F. C., and Milano, R. (1981) "Experimental Investigation of Endwall Profiling in a Turbine Vane Cascade," *AIAA J.*, Vol. 19, pp. 1033-1040.

Korakianitis, T. (1992) "Blade-Loading Effects on the Propagation of Unsteady flow and on Forcing Function in Axial-Turbine Cascade," *J. Phys. III*, Vol. 2, pp. 507-525.

Kunz, R. F., and Lakshminarayana, B. (1992) "Three-Dimensional Navier-Stokes Computation of Turbomachinery Flows Using an Explicit Numerical Procedure and a Coupled K-ε Turbulence Model," *Trans. ASME, J. Turbomachinery*, Vol. 114, pp. 627-642.

Lampart, P. (2000) "The Application of Stator Blade Compound Lean at Root to Increase the Efficiency of LP Turbine Stages from Low to Nominal Load," *Int. Joint Power Generation Conference*.

Langston, L. S., Nice, M. L., and Hooper, R. M. (1977) "Three-Dimensional Flow Within a Turbine Blade Passage," *Trans. ASME, J. Eng. for Power*, Vol. 99, pp. 21-28.

Langston, L. S. (2000) "Secondary Flows in Axial Turbines - A Review," *ANNALS of the New York Academy of Sciences*, pp. 11-26.

Lee, J. (2006) "Development of an Efficient Viscous Approach in a Cartesian Grid Framework and Application to Rotor-Fuselage Interaction," *PhD thesis, Georgia Institute of Technology*.

Manna, M. (1992) "A Three Dimensional High Resolution Upwind Finite Volume Euler Solver," *von Karman Institute for Fluid Dynamics, Technical Note 180*.

Martelli, F. (2000) "Unsteady Flow Modeling in Turbine Stage," *ANNALS of the New York Academy of Sciences*, pp. 80-94.

Mårtensson, G.E., Brethouwer, G., Johansson, A.V. (2005) "Direct numerical simulation of rotating turbulent duct flow," *Proc. TSFP5*, vol. 3, pp. 911–916.

Matsunuma, T., and Tsutsui, Y. (2000) "LDV Measurements of Wake-Induced Unsteady Flow within a Turbine Rotor Cascade," *10th Int. Symp. Applications of Laser Techniques to Fluid Mechanics*.

McCarter, A., Xiao, X., and Lakshminarayana, B. (2001) "Tip Clearance Effects in Turbine Rotor: Part II-Velocity field and Flow physics," *Trans. ASME, J. Turbomachinery*, Vol. 123, pp 305-313.

McKeel, S. A. (1996) "Numerical Simulation of the Transition Region in Hypersonic Flow," *PhD thesis, Virginia polytechnic institute and state university*.

Menter, F. R. (1992) "Improved Two-Equation k-ω Turbulence Models for Aerodynamic Flows," *NASA TM-103975*.

Miller, R. J., Moss, R. W., Anisworth, R. W., and Horwood, C. K. (2003) "Time-Resolved Vane-Rotor Interaction in a High-Pressure Turbine Stage," *J. Flow Measures and instrumentation*, Vol. 125, pp. 1-13.

Miller, R. J., Moss, R. W., Anisworth, R. W., and Harvey, N. W. (2003) "Wake, Shock, and Potential Field Interactions in 1.5 Stage Turbine- Part I: Vane-Rotor and Rotor-Vane Interaction," *J. Flow Measures and instrumentation*, Vol. 125, pp. 33-39.

Miller, R. J., Moss, R. W., Anisworth, R. W., and Harvey, N. W. (2003) "Wake, Shock, and Potential Field Interactions in 1.5 Stage Turbine- Part II: Vane- Vane Interaction and Discussion of Results," *J. Flow Measures and instrumentation*, Vol. 125, pp. 40-47.

Moore, H., and Gregory-Smith, D. G. (1996) "Transition effects on Secondary Flows in a Turbine Cascade.," *Paper 96-GT-100, ASME*.

Ni, R. H., and Bogoian, J. C. (1989) "Predictions of 3-D Multi-Stage Turbine Flow Fields Using a Multiple-Grid Euler Solver," *Paper 89-0203, AIAA*.

Ölçmen, S. M., and Simpson, R. L. (1995) "An Experimental Study of a Three-Dimensional Pressure-Driven Turbulent Boundary Layer," *J. Fluid Mech.*, Vol. 290, pp. 225-262.

Ölçmen, S. M., and Simpson, R. L. (2006) "Some Feature of a Turbulent Wing-Body Junction Vortical Flow," *Int. J. Heat and Fluid Flow*, Vol. 27, pp. 980-993.

Paciorri, R., Bonfiglioi, A., Dimascio, A., and Favini, B. (2005) "RANS simulations of a junction flow," *Int. J. Comp. Fluid Dynamics*, Vol. 19, No. 2, pp. 179-189.

Paik, J., Escauriaza, C., and Sotiropoulos, F. (2007) "On the Bimodal Dynamics of the Turbulent Horseshoe Vortex System in a Wing-Body Junction," *Phys. of Fluids*, Vol. 19.

Pallares, J., and Davidson, L. (2002) "Large-Eddy Simulations of Turbulent Heat Transfer in Stationary and Rotating Square Ducts," *Phys. Fluids*, Vol. 14, pp. 2804–2816.

Pallares J., and Davidson L. (2000) "Large-Eddy Simulations of Turbulent Flow in a Rotating Square Duct," *Phys. Fluids*, Vol. 12, pp. 2878-2894.

Parneix, S., Durbin, P. A., and Behnia, M. (1998) "Computational of 3-D Turbulent Layers Using the V2F Model," *Flow Turb. and Combust.*, Vol. 60, pp. 19-46.

Payne, S., Ainsworth, R., Miller, R., Moss, R., and Harvy, N. (2003) "Unsteady loss in High Pressure Turbine Stage," *Int. J. Heat and Fluid Flow*, Vol. 24, pp. 698-708.

Pfau, A., Treiber, M., Sell, M., and Gyarmathy, G. (2001) "Flow Interaction From the Exit Cavity of an Axial Turbine Blade Row Labyrinth Seal," *Trans. ASME, J. Turbomachinery*, Vol. 123, pp. 342-352.

Pfau, A. (2003) "Loss Mechanisms in Labyrinth Seals of Shrouded Axial Turbines," *PhD thesis, SWISS FEDERAL INSTITUTE OF TECHNOLOGY ZURICH*.

Qin, Z., and Pletcher, R. H. (2006) "Large Eddy Simulation of Turbulent Heat Transfer in a Rotating Square Duct," *Int. J. Heat Mass Transfer*, Vol. 27, pp. 371–390.

Rao, K., and Delaney, R. (1990) "Investigation of Unsteady Flow Through Transonic Turbine Stage, Part I: Analysis," *Paper 90-2408, AIAA*.

Rhode, D. L., Johnson, J. W., and Broussard, D. H. (1997) "Flow Visualization and Leakage Measurements of Stepped Labyrinth Seals: part 1- Annular Groove," *Trans. ASME*, *J. Turbomachinery*, Vol. 119, p 839– 843.

Rhode, D. L., Younger, J. S., and Wernig, M. D. (1997) "Flow Visualization and Leakage Measurements of Stepped Labyrinth Seals: part 2- Sloping Surfaces," *Trans. ASME, J. Turbomachinery*, Vol. 119, pp. 844-848.

Roe, P. L. (1981) "Approximate Riemann Solvers, Parameter Vectors, and Difference Schemes," *J. Comp. Phys.*, Vol. 43, pp. 357–372.

Rokni, M., Olsson, C., and Sunden, B. (1998) "Numerical and Experimental Investigation of Turbulent Flow in a Rectangular Duct," *Int. J. Num. Meth. Fluids*, Vol. 28, pp. 225–242.

Rose, M. G., Harvy, N. W. (2000) "Turbomachinery Wakes: Differential Work and Mixing Losses," *Trans. ASME, J. Turbomachinery*, Vol. 122, pp. 68-77.

Rosic, B., Denton, J. D., and Pullan, G. (2006) "The Importance of Shroud Leakage Modeling in Multistage Turbine Flow Calculations," *Trans. ASME, J. Turbomachinery*, Vol. 128, pp. 699-707.

Rosic, B., Denton, J. D., Curtis, E. M., and Peterson, A. T. (2007) "The Influence of Shroud and Cavity Geometry on Turbine Performance: An Experimental and Computational Study, Part II: Exit Cavity Geometry," Paper GT2007-27770, ASME.

Rosic, B., Denton, J. D., and Curtis, E. M. (2007) "The Influence of Shroud and Cavity Geometry on Turbine Performance: An Experimental and Computational Study, Part I: Shroud Geometry," Paper GT2007-27769, ASME.

Rumsey, C., Allmaras, S., Alonso, J., Bush, B., et al. (2005) "The CFD General Notation System –Standard Interface Data Structures," AIAA Recommended Practice, No. R-101A-2005, Published by the American Institute of Aeronautics and Astronautics, Reston, VA, USA.

Sauer, H., Muller, R., and Vogeler, K. (2000) "Reduction of Secondary Flow Losses in Turbine Cascades by Leading Edge Modifications at the Endwall," *Paper 2000-GT-473, ASME*.

Schlienger, J., Pfau, A., Kalfas, A. I., and Abhari, R. S. (2003) "Effects of Labyrinth Seal Variation on Multistage Axial Turbine Flow," *Paper GT2003-38270, ASME*

Senoo, Y. (1958) "The Boundary Layer on the Endwall of a Turbine Nozzle Cascade," *Trans. ASME, J. Eng. for Power*, Vol. 80.

Shapiro, A. H. (1953) *The Dynamics and Thermodynamics of compressible Fluid Flow*: Ronald Press, New York.

Sharma, O. P., and Butler, T. L. (1987) "Prediction of Endwall Losses and Secondary Flows in Axial Flow Turbine cascade," *Trans. ASME, J. Turbomachinery*, Vol. 109, pp. 229-236.

Shih, T. P., and Lin, Y. L. (2003) "Controlling Secondary-Flow Structure by Leading-Edge Airfoil Fillet and Inlet Swirl to Reduce Aerodynamic Loss and Surface Heat Transfer," *Trans. ASME, J. Turbomachinery*, Vol. 125, pp. 48-56.

Sieverding, C. H. (1985) "Recent Progress in the understanding of Basic Aspects of Secondary Flows in Turbine Blade Passage," *Trans. ASME, J. Turbomachinery*, Vol. 107, pp. 248-257.

Sieverding, C. H, and Van den Bosche (1985) "The used of colored Smoke to Visualize Secondary Flows in a Turbine-Blade Cascade," *J. of Fluid Mech.*, Vol. 134, pp. 85-89.

Simpson, R.L. (2001) "Junction Flows," *Ann. Rev. Fluid Mech.*, Vol. 33, pp. 415-443.

Sjolander, S. A., and Amrud, K. K. (1987) "Effects of Tip Clearance on Blade Loading in a Planar Cascade of Turbine Blades," *Trans. ASME, J. Turbomachinery*, Vol. 109, pp. 237-245.

Song, B. H., Song, S. J. (2004) "Lateral Forces From Single Gland Rotor Labyrinth Seals in Turbines," *Trans. ASME, J. Turbomachinery*, Vol. 126, pp. 626-634.

Swanson, R. C., and Turkel, E. (1997) "Multistage Schemes with Multigrid for Euler and Navier-Stokes Equations, Component and Analyses," *NASA TP 3631*.

Sweby, P. K. (1984), "High resolution schemes using flux limiters for hyperbolic conservation laws," *SIAM J. Num. Analysis*, Vol. 21, pp. 995–1011.

Tallman, J., and Lakshminarayana, B. (2001) "Numerical Simulation of Tip Leakage Flows in Axial Flow Turbines, With Emphasis on Flow Physics: Part I-Effect of Tip Clearance Height," *Trans. ASME, J. Turbomachinery*, Vol. 123, pp. 314-323.

Tallman, J., and Lakshminarayana, B. (2001) "Numerical Simulation of Tip Leakage Flows in Axial Flow Turbines, With Emphasis on Flow Physics: Part II-Effect of Outer Casing Relative Motion"," *Trans. ASME, J. Turbomachinery*, Vol. 123, pp. 324-333.

Toro, E. F. (1999) *Riemann Solvers and Numerical Methods for Fluid Dynamics: a Practical Introduction*: Springer Publications, 2nd ed.

Traupel, W. (1973) *Thermische turbomaschinen*: SpringerVerlag, Berlin.

Urner, G. (1997) "Pressure Loss of Orifice Plates According to ISO 5167-1," *J. Flow Measures and instrumentation*, Vol. 8.

Van Leer, B. (1979) "Towards the Ultimate Conservative Difference Scheme V. A Second-Order Sequel to Godunov's Method," *J. Comp. Phys.*, Vol. 32, pp. 101–136.

Vogt, H.-F., and Zippel M. (1996) "Sekundarstromungen in Turbinengittern mit geraden und gekrummten Schaufeln; Visualisierung im ebenen Wasserkanal," *Forschung im Ingenieurwesen – Engineering Research, no. 9*, Vol. 62, pp. 247 – 253.

Volino, R. (2002) "Separated Flow Transition Under Simulated Low-Pressure Turbine Airfoil Conditions-Part: 1: Mean Flow Turbulence Statistics," *Trans. ASME, J. Turbomachinery*, Vol. 124, pp. 645-655.

Volino, R. (2002) "Separated Flow Transition Under Simulated Low-Pressure Turbine Airfoil Conditions-Part: 2: Turbulence Spectra," *Trans. ASME, J. Turbomachinery*, Vol. 124, pp. 656-664.

Volmar, T. W., Brouillet, B., Gallus, H. E., and Benetschik, H. (1998) "Time Accurate 3D Navier-Stokes Analysis of a 1 1/2-Stage Axial Turbine," Paper 98-3247, AIAA.

Wallis, A. M., Denton, J. D., and Demargne, A. A. (2001) "The Control of Shroud Leakage Flows to Reduce Aerodynamic Losses in a Low Aspect Ratio, Shrouded Axial Flow Turbine," *Trans. ASME, J. Turbomachinery*, Vol. 123, pp. 334-341.

Walraevens, R. E., and Gallus, H. E. (1995) "Stator-Rotor-Stator Interaction in an Axial Flow Turbine and its Influences on Loss Mechanisms," *AGARD 571*.

Walsh, J. A., and Gregory-Smith, D. G. (1990) "Inlet Skew and the Growth of Secondary Losses and Vorticity in a Turbine Cascade," *Trans. ASME, J. Turbomachinery*, Vol. 112, pp. 633-642.

Wang, H.P., Olson, S.J., Goldstein, R.J., and Eckert, E.R.G. (1997) "Flow Visualization in a Linear Turbine Cascade of High Performance Turbine Blade," *Trans. ASME, J. Turbomachinery*, Vol. 119, pp. 1-8.

Wilcox, D. C. (1993) *Turbulence Modelling for CFD*: Griffin Printing, Glendale, California, USA.

Wilcox, D. C. (2002) *Turbulence Modelling for CFD*: Second ed., DCW Industries Inc., California, USA.

Xiao, X., McCarter, A., and Lakshminarayana, B. (2001) "Tip Clearance Effects in Turbine Rotor: Part I- Pressure Field and Loss," *Trans. ASME, J. Turbomachinery*, Vol. 123, pp. 296-304.

Yamamoto, A. (1987) "Production and Development of Secondary Flows and Losses in Two Types of Straight Turbine Cascades: Part I- A Stator Case," *Trans. ASME, J. Turbomachinery*, Vol. 109, pp. 186-193.

Yamamoto, A. (1987) "Production and Development of Secondary Flows and Losses in Two Types of Straight Turbine Cascades: Part II- A Rotor Case," *Trans. ASME, J. Turbomachinery*, Vol. 109, pp. 194-200.

Yao, J., Jameson, A., and Alonso, J. (2000) "Development and Validation of a Massively Parallel Flow Solver for Turbomachinery Flows," Paper 00-0882, AIAA.

Yao, J., Davis, R. L., Alonso, J. J., and Jameson, A. (2001) "Unsteady Flow Investigations in an Axial Turbine Using the Massively Parallel Flow Solver TFLO," Paper 2001–0529, AIAA.

Yaras, M. I., Sjolander, S. A. (1990) "Development of the Tip Leakage Flow Downstream of a Planar Cascade of Turbine Blades: Vorticity Field," *Trans. ASME, J. Turbomachinery*, Vol. 112, pp. 609-617.

Yaras, M. I., Sjolander, S. A. (1992) "Effects of Simulated Rotation on Tip Leakage in a Planar Cascade of Turbine Blades: Part I- Tip Gap Flow," *Trans. ASME, J. Fluids Engineering*, Vol. 114, pp. 652-659.

Young, J. B., and Horlock, J. H. (2006) "Defining the Efficiency of a Cooled turbine," *Trans. ASME, J. Turbomachinery*, Vol. 128, pp. 658-667.

Zeschky, J., and Gallus, H. E. (1993) "Effects of Stator Wakes and Spanwise Nonuniform Inlet Conditions on the Rotor Flow of an Axial Turbine Stage," *Trans. ASME, J. Turbomachinery*, Vol. 115, pp. 128-136.